
8-2021

Quantitative Magnetic Resonance Imaging for the Early Prediction of Treatment Response in Triple Negative Breast Cancer

Benjamin C. Musall

Follow this and additional works at: https://digitalcommons.library.tmc.edu/utgsbs_dissertations



Part of the [Oncology Commons](#), [Other Medical Sciences Commons](#), [Other Physics Commons](#), and the [Radiology Commons](#)

Recommended Citation

Musall, Benjamin C., "Quantitative Magnetic Resonance Imaging for the Early Prediction of Treatment Response in Triple Negative Breast Cancer" (2021). *Dissertations and Theses (Open Access)*. 1113.
https://digitalcommons.library.tmc.edu/utgsbs_dissertations/1113

This Dissertation (PhD) is brought to you for free and open access by the The University of Texas MD Anderson Cancer Center UTHealth Houston Graduate School of Biomedical Sciences at DigitalCommons@TMC. It has been accepted for inclusion in Dissertations and Theses (Open Access) by an authorized administrator of DigitalCommons@TMC. For more information, please contact digcommons@library.tmc.edu.

Quantitative Magnetic Resonance Imaging for the Early Prediction of Treatment Response
in Triple Negative Breast Cancer


By

Benjamin Charles Musall, S.M.S.

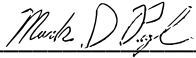
APPROVED:



Advisory Professor: Jingfei Ma, Ph.D.



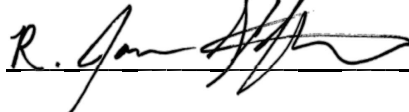
Gaiane M. Rauch, M.D. Ph.D.



Mark D. Pagel, Ph.D.



Ken-Pin Hwang, Ph.D.



R. Jason Stafford, Ph.D.



Steven H. Lin, M.D. Ph.D.

APPROVED:

Dean

The University of Texas MD Anderson Cancer Center UTHealth Graduate School of Biomedical Sciences

Quantitative Magnetic Resonance Imaging for the Early Prediction of Treatment Response
in Triple Negative Breast Cancer

A DISSERTATION

Presented to the Faculty of

The University of Texas

MD Anderson Cancer Center UTHealth

Graduate School of Biomedical Sciences

in Partial Fulfillment

of the Requirements

for the Degree of

DOCTOR OF PHILOSOPHY

By

Benjamin C. Musall, S.M.S.

Houston, Texas, United States of America

August 2021

Dedication

To my family; I love you very much.

Acknowledgements

I have received incredible and extensive support during my doctoral study. I am extremely grateful to the people who contributed to my personal development and to the work presented in this dissertation.

First, I must thank my advisor, Dr. Jingfei Ma. He is a brilliant scientist and teacher. He has spared no effort in my training and has been a powerful advocate on my behalf. I most admire his etiquette and his uncompromising scientific rigor. I hope to uphold his ideals in my career and to pay forward his generosity to the coming generation.

Thank you to my advisory committee: Maia Rauch, Marty Pagel, Ken Hwang, Jason Stafford, and Steven Lin. I have been especially fortunate to learn and receive direction from such an accomplished and helpful group of senior colleagues. I must specifically thank Maia and Marty for the many helpful hours they have spent mentoring me outside of our shared work. Additional thanks are also due to Marty for his careful editing of this dissertation.

Thank you to current and former members of the MR Applications Laboratory: Dante Son, Hao Song, Jeremiah Sanders, Zijian Zhou, and Bikash Panthi. Your support has been invaluable, and your candor and humor have supported me through much. I will remember working with each of you fondly.

Thank you to my radiologist collaborators in breast imaging for your support and for sharing your zeal for patient care with me: Beatriz Adrada, Rosalind Candelaria, Wei Yang, Abeer Abdelhafez, Nabil Elshafeey, Rania Mohamed, Medine Boge, Hagar Mahmoud, Ayah Mugahid, and many others.

Thank you to Bud Wendt, Frances Quintana, Anne Baronitis, Betsy Kindred, Brandy Koopman, and Marnie Copeland for your wonderful support.

Quantitative Magnetic Resonance Imaging for the Early Prediction of Treatment Response
in Triple Negative Breast Cancer

Benjamin C. Musall

Advisory Professor: Jingfei Ma, Ph.D.

Abstract

Triple Negative Breast Cancer (TNBC) is an aggressive subtype of breast cancer which lacks upregulated hormone receptors. Because of this, it is not vulnerable to clinically available targeted therapies. When treated with standard of care neoadjuvant systemic therapy (NAST), TNBC only shows approximately a 40% rate of pathologic complete response (pCR). A biomarker which could predict TNBC response to NAST early during treatment would be useful, as it would allow for non-responders to be triaged to alternative therapies and potentially allow for the treatment of responders to be de-escalated.

Quantitative Magnetic Resonance Imaging (MRI) may be used to probe and measure aspects of the perfusion, diffusion, and mechanical properties of a cancer and its surroundings. In the research setting, several quantitative MRI biomarkers have shown potential for early prediction of response in breast cancer. However, TNBC shows a unique image phenotype on both conventional MRI and MRI biomarkers of response. Several MRI biomarkers of response which show promise in other breast cancer subtypes are not useful for predicting response in TNBC. This, in combination with the clinical needs of TNBC, warrants the development of MRI biomarkers of response that are specific to TNBC. This rational supports a large, ongoing prospective trial of TNBC patients at our institution who underwent longitudinal multiparametric MRI at pretreatment, after 2 cycles of NAST and after 4 cycles of NAST. In this dissertation, MRI biomarkers from diffusion MRI, dynamic contrast-enhanced (DCE) MRI, and

magnetic resonance elastography (MRE) were developed and applied as predictors of NAST response in the prospective trial cohort.

First, aspects of the tumor necrosis on pretreatment diffusion MRI and DCE MRI were investigated as potential predictors of response. Our study established that no associations were present between tumor necrosis and the treatment response in our study population, thus served as a caution in the field for physicians considering necrosis on MRI as a possible negative predictive biomarker.

Second, functional tumor volume (FTV), an existing biomarker of response in breast cancer based on DCE MRI contrast thresholds, was optimized for early prediction of NAST response in TNBC. Fast DCE MRI from pretreatment and cycle 4 MRI scans was leveraged to find an optimal contrast timing to improve the predictive performance of FTV. FTV contrast thresholds optimized over the TNBC cohort paralleled TNBC subtype analysis presented by other groups in previous reports. This external validation further supports the use of a TNBC-specific FTV tuning for prediction of NAST response.

Third, diffusion MRI measurements in the peritumoral region were developed and applied as predictors of NAST response. We found that maximum diffusion and the standard deviation of diffusion in peritumoral regions including fatty tissues were useful for prediction of NAST response.

Finally, a convolutional neural network (CNN)-based MRE inversion algorithm was developed for improved spatial resolution of breast cancer MRE. Because acquisition of ground truth MRE data is impossible, simulating MRE data via finite volume methods (FVM) was substituted in CNN training. The CNN-based inversion algorithm was validated through gel phantom measurements. Validation on *in vivo* breast MRE was performed by comparing stiffness measurements from different breast tissues between the CNN-based algorithm and the existing vendor algorithm. Both algorithms were able to effectively

distinguish between the tumor and other breast tissues, though only the vendor algorithm was able to distinguish between fatty tissue and fibroglandular tissue.

In conclusion, quantitative MRI biomarkers of breast cancer were developed and show promise for early prediction of NAST response in TNBC. MRI biomarkers of necrosis were not seen to be useful, while TNBC-tuned FTV and diffusion MRI of the peritumoral region showed promise for this purpose. A CNN-based inversion algorithm shows potential for MRE with improved spatial resolution, though additional development is required.

Table of Contents

Approvals Page	i
Title Page	ii
Dedication	iii
Acknowledgements	iv
Abstract	v
Table of Contents	viii
List of Figures.....	xi
List of Tables.....	xiii
List of Abbreviations.....	xv
Chapter 1 – Introduction	1
1.1 Statement of Problem	1
1.1.1 General Problem.....	1
1.1.2 Specific Problem	2
1.1.3 Organization of Dissertation.....	4
1.2 Triple Negative Breast Cancer (TNBC)	6
1.2.1 Epidemiology	6
1.2.2 Diagnosis of TNBC.....	7
1.2.3 Treatment of TNBC.....	10
1.2.4 Prediction of NAST Response	11
1.2.5 ARTEMIS – A Robust TNBC Evaluation FraMework to Improve Survival (Trial NCT02276443)	12
1.3.1 The Nuclear Magnetic Resonance Phenomena (B_0).....	15
1.3.2 Radiofrequency Excitation (B_1) and Decay	17
1.3.3 Refocusing, Echoes, and Repeat Acquisition.....	21
1.3.4 Imaging with Gradient Fields (G_x , G_y , G_z).....	22
1.3.5 Basic Image Contrast	26
1.3.6 Basic Acquisition Techniques	29
1.4 Quantitative MRI Modalities	32
1.4.1 Dynamic Contrast Enhanced (DCE) MRI	32
1.4.2 Diffusion Weighted Imaging (DWI).....	36
1.4.3 Magnetic Resonance Elastography (MRE).....	39
1.5 MRI of TNBC	48

1.5.1 Clinical MRI of TNBC Subtype	48
1.5.2 Semi-quantitative and Quantitative MRI - TNBC Subtyping.....	51
1.5.3 MRI for Early Prediction of Treatment Response in TNBC	54
1.6 Hypothesis and Specific Aims	58
1.6.1 Hypothesis	58
1.6.2 Specific Aim 1 (SA1)	58
1.6.3 Specific Aim 2 (SA2)	58
Chapter 2 – Tumor Necrosis by Pretreatment Breast MRI: Association with Neoadjuvant Systemic Therapy Response in Triple-negative Breast Cancer	60
2.1 Abstract [<i>Necrosis for TNBC Response</i>]	60
2.2 Introduction [<i>Necrosis for TNBC Response</i>]	61
2.3 Methods [<i>Necrosis for TNBC Response</i>]	63
2.4 Results [<i>Necrosis for TNBC Response</i>]	69
2.5 Discussion [<i>Necrosis for TNBC Response</i>].....	76
2.6 Conclusion [<i>Necrosis for TNBC Response</i>]	79
2.6 Acknowledgements [<i>Necrosis for TNBC Response</i>].....	79
Chapter 3 – Functional Tumor Volume by Fast Dynamic Contrast-Enhanced MRI for Predicting Neoadjuvant Systemic Therapy Response in Triple-Negative Breast Cancer	81
3.1 Abstract [<i>FTV for TNBC Response</i>].....	81
3.2 Introduction [<i>FTV for TNBC Response</i>]	82
3.3 Methods [<i>FTV for TNBC Response</i>].....	84
3.4 Results [<i>FTV for TNBC Response</i>].....	89
3.5 Discussion [<i>FTV for TNBC Response</i>]	96
3.6 Conclusion [<i>FTV for TNBC Response</i>].....	99
Chapter 4 – Quantitative Apparent Diffusion Coefficients from Peritumoral Regions as Early Predictors of Treatment Response to Neoadjuvant Systemic Therapy in Triple Negative Breast Cancer	100
4.1 Abstract [<i>Peritumoral ADC for TNBC Response</i>]	101
4.2 Introduction [<i>Peritumoral ADC for TNBC Response</i>]	102
4.3 Methods [<i>Peritumoral ADC for TNBC Response</i>].....	103
4.4 Results [<i>Peritumoral ADC for TNBC Response</i>]	107
4.5 Discussion [<i>Peritumoral ADC for TNBC Response</i>]	113
4.6 Acknowledgements [<i>Peritumoral ADC for TNBC Response</i>].....	116
Chapter 5 – A Novel Convolutional Neural Network Inversion Algorithm for Magnetic Resonance Elastography of Breast Cancer	117

5.1 Introduction [<i>CNN-based Inversion Algorithm</i>].....	118
5.1.1 Magnetic Resonance Elastography in Cancer	118
5.1.3 Convolutional Neural Networks (CNNs)	120
5.1.4 Finite Volume Methods (FVM)	122
5.2 Simulated MRE, CNN Inversion, and Phantom Validation [<i>CNN-based Inversion Algorithm</i>]	125
5.2.1 MRE Simulation by Finite Volume Analysis	125
5.2.2 Synthetic MRE Dataset	128
5.2.3 CNN-Based Inversion	132
5.3 <i>In Vivo</i> Breast Cancer MRE Validation [<i>CNN-based Inversion Algorithm</i>]	135
5.3.1 MRE Dataset and Radiologist Interpretation	135
5.3.2 Comparing CNN-Stiffness with Vendor Algorithm	136
5.4 Discussion [<i>CNN-based Inversion Algorithm</i>]	139
Chapter 6 – Future Directions	141
6.1 Potential Clinical Adaptation and Possible Refinement of Dissertation Projects	141
6.1.1 Potential Improvements to <i>Chapter 2 – Tumor Necrosis by Pretreatment Breast MRI: Association with Neoadjuvant Systemic Therapy Response in Triple-negative Breast Cancer</i>	141
6.1.2 Potential Improvements to <i>Chapter 3 – Functional Tumor Volume by Fast Dynamic Contrast-Enhanced MRI for Predicting Neoadjuvant Systemic Therapy Response in Triple-Negative Breast Cancer</i>	142
6.1.3 Potential Improvements to <i>Chapter 4 – Quantitative Apparent Diffusion Coefficients from Peritumoral Regions as Early Predictors of Treatment Response to Neoadjuvant Systemic Therapy in Triple Negative Breast Cancer</i>	143
6.1.4 Potential Improvements to <i>Chapter 5 – A Novel Convolutional Neural Network Inversion Algorithm for Magnetic Resonance Elastography of Breast Cancer</i>	145
6.2 Combinations of Biomarkers for Prediction of Response	146
Appendix A. Multivariate Model Parameters from Chapter 4 – Quantitative Apparent Diffusion Coefficients from Peritumoral Regions as Early Predictors of Treatment Response to Neoadjuvant Systemic Therapy in Triple Negative Breast Cancer	148
References	153
Vita	189

List of Figures

Figure 1 PubMed search results by year for the query "cancer + prediction of treatment response."	2
Figure 2 A graphical depiction of an MRI biomarker for early prediction of treatment response to support triage to improve patient outcome.....	13
Figure 3 ARTEMIS trial care pathway with longitudinal MRI.....	14
Figure 4 T1 and T2 versus molecular tumbling rate.....	20
Figure 5 Simulated free induction decay (FID) for normal breast fibroglandular tissue (FGT) with $T2^* = 23.2$ ms and $T2 = 46.0$ ms.....	21
Figure 6 Graphical explanation of spatial encoding of MRI signal through application of a linear gradient field.....	23
Figure 7 Two cases of spin distribution with $2/\text{FOV}$ spatial frequency. (A) Spins are located on 0-phase lines and (B) spins are spread evenly across the phase cycle.	24
Figure 8 Segmentation of k-space for demonstration of low (inner k-space) and high spatial frequency content (outer k-space).	27
Figure 9 Example of contrast-enhanced spoiled GRE MRI (left) compared with SE-ssEPI diffusion MRI (right) in a 40-year-old woman with TNBC in her left breast. Distortion of the tumor and fibroglandular tissue can be seen. This EPI image has already undergone geometric correction by the vendor, as is evident in the uneven boundary on the left of the image.	31
Figure 10 Contrast enhancement patterns in DCE: persistent pattern (Pattern I, red), plateau pattern (Pattern II, blue), and washout pattern (Pattern III, black).	34
Figure 11 Basic pulse sequence diagram for SE-ssEPI with diffusion encoding in the y-direction.	38
Figure 12 Depiction of (A) Longitudinal and (B) Shear Waves from a Harmonic Oscillator	40
Figure 13 Depiction of response of a voxel of material in response to (A) a normal force and (B) a shear force.....	41
Figure 14 Pulse sequence diagram for MRE with a GRE sequence. Simplified 1-1 bipolar MEGs are shown.	45
Figure 15 Examples of MRE wave images for a homogenous gel phantom. T1-weighted magnitude image (left) and the corresponding MRE phase image sensitized to motion in the y-direction (right) are shown.	46
Figure 16 Inclusion criteria and assignment of analysis for each group.	64
Figure 17 Necrosis in a 35-year-old woman with TNBC of the left breast. (a) Axial fat-suppressed early-phase dynamic contrast-enhanced image shows central non-enhancing area representing necrosis (arrow). (b) Axial fat-suppressed T2-weighted image shows necrosis as central area of high signal intensity (arrow). (c) Axial apparent diffusion coefficient map shows shine-through corresponding to central area of necrosis (arrow) seen on dynamic contrast-enhanced and T2-weighted imaging.....	66
Figure 18 Segmentation technique in a 60-year-old woman with TNBC of the right breast. Axial dynamic contrast-enhanced early phase fat-suppressed images with whole tumor (a), tumor without necrosis (b), and necrosis only (c) segmentations, as well as corresponding apparent diffusion coefficient maps (d, e, f).	67
Figure 19 Necrotic index carcinoma with a pathological complete response after neoadjuvant systemic therapy in a 46-year-old woman with TNBC of the right breast. The volume of necrotic material was 10 cm^3 , and the percent of the total tumor volume occupied by necrosis was 17%. (a) Axial fat-suppressed	

early-phase dynamic contrast-enhanced image shows central non-enhancing area representing necrosis (arrow). (b) Axial fat-suppressed T2-weighted image shows necrosis as central area of high signal intensity (arrow). (c) Axial apparent diffusion coefficient map shows shine-through corresponding to central area of necrosis (arrow).	72
Figure 20 Necrotic index carcinoma with pathological non-complete response after neoadjuvant systemic therapy in a 30-year-old woman with TNBC of the left breast. The volume of necrotic material was 4 cm ³ , and the percent of the total tumor volume occupied by necrosis was 17%. (a) Axial fat-suppressed early-phase dynamic contrast-enhanced image shows central non-enhancing area representing necrosis (arrow). (b) Axial fat-suppressed T2-weighted image shows necrosis as a central area of high signal intensity (arrow). (c) Axial apparent diffusion coefficient map shows shine-through corresponding to central area of necrosis (arrow).....	72
Figure 21 Clustering of necrosis volume or NV _{DCE} (a), and necrosis-only volume as a percent of total tumor volume or %NV _{DCE} (b), by dynamic contrast enhanced MRI associated with response to neoadjuvant systemic therapy. There is no difference between TNBC patients with and without pathologic complete response (pCR).	75
Figure 22 Examples of tumor volume measurements in a 52-year-old woman with triple-negative breast cancer in her left breast: (A) tumor volume dimensions, (B) segmented enhanced tumor volume, and (C) enhancement threshold-based functional tumor volume in blue at percentage enhancement >130% and signal enhancement ratio >1.1.....	86
Figure 23 Map of fast dynamic contrast-enhanced MRI data flow, processing, and segmentation for volume measurements: (A) tumor volume by 3D measurements (TV), (B) enhanced tumor volume (ETV) and functional tumor volume (FTV) from early phase segmentations, with percentage enhancement (PE) and signal enhancement ratio (SER) thresholds applied for FTV, and (C) FTV with optimization of early phase timing.	87
Figure 24 Comparison of tumor volume (TV) by 3D measurements from early phase and late phase measurements (A,C,E) and enhanced tumor volume (ETV) from 1-minute and 2.5-minute early phase timings (B,D,F) between patients who had a pathologic complete response (pCR) and those who did not, at the baseline (BL) scan (A,B), cycle 4 (C4) scan (C,D), and %C4/BL (E,F).	93
Figure 25 Comparison of functional tumor volume (FTV) optimization contour plots between 1-minute and 2.5-minute early phase timings for the baseline (BL) scan (A), cycle 4 (C4) scan (C), and %C4/BL (E). Peak AUC for each plot is marked with a red dot. Dot plots are also shown, comparing optimal FTV between patients who had a pathologic complete response (pCR) and those who did not for each early phase timing at BL scan (B), C4 scan (D), and %C4/BL (F).	95
Figure 26 Comparison of functional tumor volume (FTV) optimization contour plots between different early phase timings for FTV _{Opt} at baseline (BL) scan (A), cycle 4 (C4) scan (B), and the relative change (%C4/BL) between the two scans (C). AUC = area under the receiver operating characteristic curve, PE = percentage enhancement, SER = signal enhancement ratio.	96
Figure 27 Peritumoral region segmentation technique in a 48-year-old woman with triple-negative breast cancer of the right breast. A, ADC map showing known 4.8 cm cancer at 9 o'clock position 8 cm from the nipple (red arrow). B, ADC maps with fat-inclusive peritumoral regions. C, ADC maps with fat-exclusive peritumoral regions. The solid red line in B and C show the tumor boundary; the outer lines show boundaries of different peritumoral region thicknesses: solid yellow line - 20 mm, the inner dashed orange line - 15 mm, dashed red line - 10 mm, and dashed maroon line - 5 mm.....	105

Figure 28 Dot plots and Mann Whitney p-values of the 4 top-performing peritumoral region (PTR) apparent diffusion coefficient (ADC) features compared using the area under the receiver operating characteristic curve (AUC) between patients with a pathologic complete response (pCR) and without a pCR (“non-pCR”) for both the training and testing sets. A, Cycle 4 fat-inclusive (FI) 20-mm ADC standard deviation (SD). B, Cycle 4 FI 15-mm ADC SD. C, Cycle 4 FI 5-mm ADC maximum. D, Cycle 2 FI 20-mm ADC Maximum.	111
Figure 29 Examples of poor anatomy visualization in MRE stiffness maps from the vendor inversion algorithm. In row 1 and row 3, FGT is poorly visualized. In row 2, the tumor (red arrow) does not show high stiffness in the vendor stiffness map. This is despite showing relatively homogenous grayscale values on the wave image that would correspond to a higher wavespeed and higher stiffness.	117
Figure 30 Number of PubMed results by year for publications mentioning CNNs and the word “image”.	122
Figure 31 Y-velocity map 100 Hz shear wave propagation from the left side of a homogenous medium (40x40cm, 512x512 grid, $\rho = 1000 \text{ kg/m}^3$, $\mu = 1 \text{ kPa}$). The simulation was evolved to $t = 0.0833$ seconds. The shear wavelength and wave speed were as expected. Color scale was set with a small window to exaggerate the peaks and troughs of the waveform.	126
Figure 32 Y-velocity maps from 100 Hz shear wave propagation from the left side of a homogenous medium (40x40cm, 512x512 grid, $\rho = 1000 \text{ kg/m}^3$) for two shear stiffnesses: 1kPa (left) and 4 kPa (right). The simulation was evolved to $t = 0.0833$ seconds. The shear wavelength and wave speed were as expected. Color scale was set with a small window to exaggerate wave period.	127
Figure 33 Y-velocity map from 100 Hz shear wave propagation from the left side of a homogenous medium (40x40cm, 512x512 grid, $\rho = 1000 \text{ kg/m}^3$, 1kPa) with a stiff circular insert (6 kPa). The shear wavelength was as expected. Color scale was set with a small window to exaggerate wave period. Longitudinal waves, which evolved from shear waves incident upon the interface of the two materials, can be seen at the right of the simulation. Reflected and refracted shear waves can also be seen.	128
Figure 34 Pseudo-code in Matlab 2018b for calculating the roundness of an object.	129
Figure 35 Procedurally generated stiffness geometries made from shapes within ADE20k.	130
Figure 36 Examples of output displacement maps from MRE simulation for two procedurally generated geometries. Both y (red) and x (blue) displacements are shown for six offsets along one frequency cycle are shown.	131
Figure 37 Optimization of rescale factor for conversion of CNN output to stiffness in Pa.	133
Figure 38 T1 magnitude images, unwrapped wave images, and vendor and CNN-based stiffness maps for the central three slices of the phantom scan.	134
Figure 39 Examples of tissue contouring for three patient pretreatment scans on T1-weighted MRE magnitude images.	136
Figure 40 Comparison of vendor and CNN-based stiffness maps for three patients. Tumors are shown with red arrows. For the third patient (row 3), the tumor is not visible on vendor stiffness maps but is clearly outlined in the stiffness map output by the CNN-based algorithm.	137
Figure 41 Dot plots showing distribution of stiffness values for vendor and CNN algorithms across different breast tissues in 20 TNBC patients.	138
Figure 42 Pearson correlation of tissue stiffness measurements between the vendor algorithm and the CNN algorithm. A single outlier patient with very high stiffnesses from the vendor algorithm on all tissues was excluded for correlations and plotting.	138

List of Tables

Table 1 T stage criteria for breast cancers ²⁵	8
Table 2 N stage criteria for breast cancers ²⁵	9
Table 3 Conversion table for TNM combinations into breast cancer stage ²⁵	10
Table 4 Common DCE semiquantitative metrics, their calculation, and an explanation of their meaning.	34
Table 5 Distinct TNBC clinical MRI features presented in literature	50
Table 6 Summary of literature findings for TNBC subtyping with PK analysis from DCE MRI	52
Table 7 Characteristics of 85 patients with triple negative breast cancer who received neoadjuvant systemic therapy	70
Table 8 T stage, nodal status, and pathologic complete response in 85 triple negative breast cancer patients and the subsets of patients with or without necrotic carcinomas.	73
Table 9 Logistic regression results for association analysis of pCR with presence of necrosis, T-stage, and pre-treatment nodal stage.	74
Table 10 DCE and DWI metrics from whole tumor, tumor without necrosis, and necrosis-only segmentations of necrotic carcinomas	76
Table 11 Characteristics of patients with triple-negative breast cancer who received neoadjuvant systemic therapy (n = 60).	90
Table 12 Longest diameter, tumor volume, and enhanced tumor volume measurements for patients who had a pathologic complete response (pCR) and those who did not.	92
Table 13 Functional tumor volume measurements in patients with and without pathologic complete response (pCR).	94
Table 14 Characteristics of all patients and patients in the training and the testing sets.	108
Table 15 Top performing peritumoral region apparent diffusion coefficient features by univariate analysis for prediction of a pathologic complete response	110
Table 16 Multivariate model results for prediction of pathologic complete response: apparent diffusion coefficient features with and without inclusion of segmented tumor volume	113
Table 17 Robustness of multivariate models with respect to variation in PTR thickness.....	113
Table 18 Comparison of tissue stiffness measurements between vendor and CNN-based algorithms..	138

List of Abbreviations

ADC	Apparent Diffusion Coefficient
AI	Artificial Intelligence
AIF	Arterial Input Function
AP	Antero-posterior
API	Application Programming Interface
ARC	Autocalibrating Reconstruction for Cartesian Imaging
ARTEMIS	A Robust TNBC Evaluation Framework to Improve Survival
AU	Arbitrary Units
AUC	Area Under the Receiver Operator Curve
AUC _{LL}	AUC Lower Limit
AUC _{UL}	AUC Upper Limit
BIRADS	Breast Imaging Reporting and Data System
BL	Baseline
BPE	Background Parenchymal Enhancement
CC	Cranio-caudal
CNN	Convolutional Neural Network
CPMG	Carr-Purcell-Meiboom-Gill
DAQ	Data Acquisition
DCE	Dynamic Contrast Enhanced
DCIS	Ductal Carcinoma In Situ
DICOM	Digital Imaging and Communications in Medicine
DISCO	Differential Subsampling with Cartesian Ordering
DNA	Deoxyribonucleic Acid
DW	Diffusion-Weighted
DWI	Diffusion-Weighted Imaging
EES	Extra-vascular Extra-cellular Space
EPI	Echo Planar Imaging
ER	Estrogen Receptor
ETV	Enhanced Tumor Volume
FCN	Fully Convolutional Network
FDA	Food and Drug Administration
FE	Fat-exclusive
FEM	Finite Element Methods
FFT	Fast Fourier Transform
FGT	Fibroglandular Tissue
FI	Fat-inclusive
FID	Free Induction Decay
FOV	Field of View
FSE	Fast Spin Echo
FT	Fourier Transform
FTV	Functional Tumor Volume

FVM	Finite Volume Methods
GBCA	Gadolinium-based Contrast Agents
GNU	GNU's Not Unix
GRE	Gradient Echo
HER	Human Epidermal Growth Factor Receptor
IDC	Invasive Ductal Carcinoma
IHC	Immunohistochemical
ISMRM	International Society of Magnetic Resonance in Medicine
IVIM	Intravoxel Incoherent Motion
LD	Longest Diameter
LFE	Local Frequency Estimation
LRRM	Linear Reference Region Model
MC	Monotized Central Difference
MEG	Motion Encoding Gradients
MR	Magnetic Resonance
MRE	Magnetic Resonance Elastography
MRI	Magnetic Resonance Imaging
MS	Maximum Slope
NAST	Neoadjuvant Systemic Therapy
NEX	Number of Excitations
NME	Non-mass enhancing
NMR	Nuclear Magnetic Resonance
NV	Necrotic Volume
NVDCE	Necrotic Volume on DCE
NV _{DWI}	Necrotic Volume on DWI
PACS	Picture Archiving and Communication System
PDE	Partial Differential Equation
PE	Percentage Enhancement
PG	Procedurally Generated
PK	Pharmacokinetic
PTR	Peritumoral Region
RECIST	Response Evaluation Criteria in Solid Tumors
RF	Radiofrequency
ROI	Region of Interest
SD	Standard Deviation
SE	Standard Error
SER	Signal Enhancement Ratio
SNR	Signal to Noise Ratio
TE	Time of Echo
TIL	Tumor Infiltrating Lymphocytes
TNBC	Triple Negative Breast Cancer
TNM	Tumor Node Metastasis
TR	Time of Repetition
TTP	Time to Peak

TTV	Total Tumor Volume
TTV _{DCE}	Total Tumor Volume on DCE
TTV _{DWI}	Total Tumor Volume on DWI
TV	Tumor Volume
TV _{DCE}	Tumor Volume on DCE
TV _{DWI}	Tumor Volume on DWI

Chapter 1 – Introduction

1.1 Statement of Problem

1.1.1 General Problem

In general, cancers are treated according to their diagnoses. After lesion discovery, a cancer is confirmed by biopsy and then staged through diagnostic exams. Basic histological parameters from the biopsy sample are used to characterize the cancer's cellular grade. Imaging may then be used to determine the size and extent of the cancer. These simple measures are combined into a staging specific to the anatomic site of the primary lesion. So far, most clinically used treatments are optimized for patient response based on the cancer staging.

Patients with low-stage, localized disease (stage 0 and early stage 1) may sometimes be cured with surgery, while patients with late stage 4 disease (the so-called “advanced setting”) have few treatment options and, tragically, are consigned to palliative care. In between these extremes are the intermediate stages, which are sometimes combined with low-stage disease in the so-called “early setting”. Early setting cancers are treated with curative intent and may use a combination of therapies to optimally treat the primary site and control recurrence. In most cancers, only a subset of early setting patients will show complete response to treatment prescribed based on staging. This occurs because vulnerability to treatment is heterogenous within a given cancer stage due to the varying cancer biology.

This limitation has been recognized for decades, and, to further cancer care, a new paradigm has arisen: therapy targeted towards specific molecular alterations in cancer. Novel targeted therapeutics from basic research may serve the individualized care paradigm but are limited to application in cancers which express the target of interest. This targeted therapy paradigm therefore requires support through effective characterization of cancers by advanced diagnostics¹.

Cancer biomarkers, including those from molecular analysis of tumor samples and *in vivo* medical imaging, can offer various information on the dysregulated biology of a specific cancer. These biomarkers might identify an aspect of the disease that would make it vulnerable or resistant to a given therapeutic agent. Alternatively, a biomarker might also track an aspect of the disease which is indicative of response early during the conventional treatment. This concept, early prediction of treatment response, is highly desirable as it would allow for triage of non-responsive cancers to alternative therapies. It also potentiates de-escalation of treatment for responsive cancers. In PubMed, the search term “cancer + prediction of treatment response” produced over 4,500 results from the year 2020 alone.

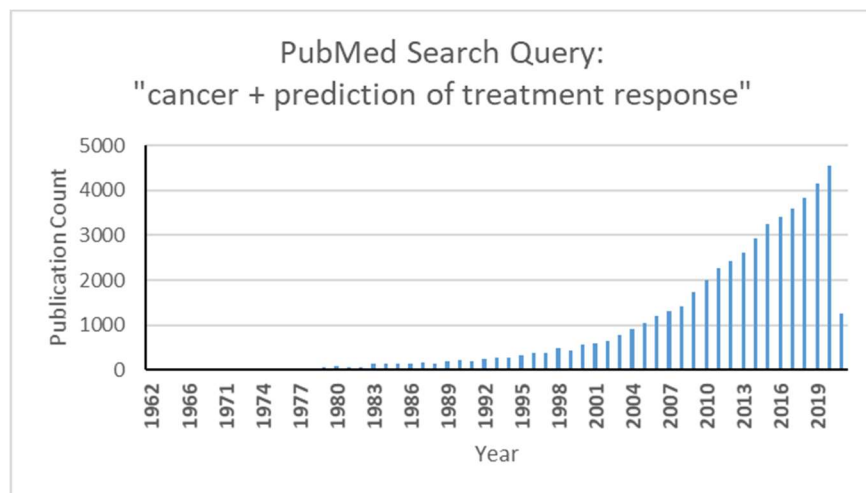


Figure 1 PubMed search results by year for the query "cancer + prediction of treatment response."

1.1.2 Specific Problem

Triple negative breast cancer (TNBC) is a hormonal subtype of breast cancer with a poor prognosis. TNBC lacks upregulated hormonal receptors common to other breast cancer subtypes.

Standard of care treatment for early setting TNBC is neoadjuvant systemic therapy (NAST) followed by

definitive surgery. Through analysis of surgical specimens, it has been found that only ~40% of TNBCs have pathologic complete response (pCR) from NAST alone. Although TNBC shows a slightly higher rate of pCR from NAST in comparison to other breast cancer subtypes (approximately 40% vs. 30% complete response), it is not vulnerable to the targeted therapies which have greatly improved the outcome of other breast cancers. Additionally, development of a targeted therapy for TNBC has proven difficult².

As with all cancers, early prediction of NAST response in TNBC would support triage for individualized care. However, prediction of response is additionally desirable as a clinical tool to support development of new targeted therapies for TNBC. By predicting patient outcome and testing novel therapeutics exclusively in predicted non-pCR, good response in those patients may be better attributed to the novel agent.

A biomarker's capability to characterize a cancer is attenuated by a few important factors: (1) evolution of a cancer's biology during treatment, (2) biological heterogeneity within a given cancer, and (3) specificity to a biologic pathway. To mitigate the impact of (1), a biomarker could be acquired longitudinally alongside treatment to track changes in cancer characteristics³. While molecular biomarkers obtained by biopsy are highly specific, solving (3), they are confounded by a sampling bias, as the biopsy-sampled region of the cancer may differ from other regions⁴. Although imaging is less specific to biological pathways, it may be sensitized to relevant tissue contrasts and may mitigate (2) by supplementing molecular biomarkers through sampling (imaging) of an entire tumor and its surroundings.

Magnetic resonance imaging (MRI) may be sensitized to several tissue contrasts which may be of interest for early prediction of treatment response, including perfusion, water diffusion in tissue, and tissue stiffness. These contrasts may be extended to quantitative measurements through advanced MRI

modalities. Measurements of these properties, and their changes across treatment, have previously been proposed for early prediction of treatment response in breast cancer.

TNBC is known to display a unique imaging phenotype on both conventional imaging and research imaging for prediction of response. Existing imaging biomarkers of breast cancer may be refined for use in TNBC. In addition, other useful measurements might also be proposed for prediction of response in TNBC. This thesis concerns the development and validation of established and novel quantitative MRI biomarkers for prediction of treatment response in TNBC.

1.1.3 Organization of Dissertation

The four projects in this thesis, which are encapsulated in the later chapters, each contain elements of biomarker development and validation. To distinguish numbered sections, the chapter subheadings are denoted with shorthand headings:

Chapter 2 – Tumor Necrosis by Pretreatment Breast MRI: Association with Neoadjuvant Systemic Therapy Response in Triple-negative Breast Cancer

- ***Necrosis for TNBC Response***

Chapter 3 – Functional Tumor Volume by Fast Dynamic Contrast-Enhanced MRI for Predicting Neoadjuvant Systemic Therapy Response in Triple-Negative Breast Cancer

- ***FTV for TNBC Response***

Chapter 4 – Quantitative Apparent Diffusion Coefficients from Peritumoral Regions as Early Predictors of Treatment Response to Neoadjuvant Systemic Therapy in Triple Negative Breast Cancer

- ***Peritumoral ADC for TNBC Response***

Chapter 5 – A Novel Convolutional Neural Network Inversion Algorithm for Magnetic Resonance Elastography of Breast Cancer

- ***CNN-based Inversion Algorithm***

In each project chapter, the specific concepts and relevant literature are introduced and discussed. However, the level of background in each chapter is insufficient for a general audience. Furthermore, the novel imaging techniques applied in this thesis may be unfamiliar to medical practitioners or experts in adjacent fields. To improve presentation, the dissertation begins with a comprehensive low- to mid-level background of both TNBC and MRI. Specifically, TNBC oncology, the fundamentals of MRI, quantitative MRI modalities, and MRI of TNBC are reviewed.

After this introduction, the Hypothesis and Specific Aims underlying the dissertation work are introduced. The placement of individual projects into this manifold is made clear with sub-Aims.

The dissertation is completed by a future directions chapter. This section considers potential clinical adaptation of the biomarkers, potential improvements to the biomarkers, and their possible combination in multifeatured predictive models.

1.2 Triple Negative Breast Cancer (TNBC)

1.2.1 Epidemiology

TNBC is a breast cancer immunohistochemical (IHC) subtype that is aggressive and has a relatively poor prognosis⁵. TNBCs differ from other breast cancers in that they do not express estrogen receptor (ER) or progesterone receptor (PgR), and they additionally do not overexpress human epidermal growth factor receptor 2 (HER2; hence “triple-negative”). Of the 298,937 cases of breast cancer diagnosed in 2010, 13% were TNBCs⁶. Breast cancers in non-Hispanic black and Hispanic patients are more likely to be TNBC. In comparison to other IHC subtypes, a greater fraction of TNBC affects younger women.

IHC subtyping of breast cancers is useful for assigning targeted treatment but is only one of many efforts to subtype breast cancers. IHC subtyping was preceded by a popular system of molecular characterization based on genetic profiling, which grouped breast cancers into four main intrinsic molecular subtypes: Luminal A, Luminal B, HER-2 enriched, and Basal-like^{7,8}. Based on their gene expression, the lineage of these subtype groups may be attributed to certain cells. One of these intrinsic subtypes, basal-like cancers, arise from the basal epithelial cell layer in mammary glands. This is indicated by their unique expression of various keratins and other structural proteins used by basal cells. A majority of TNBCs are the Basal-like intrinsic subtype, and, conversely, a majority of Basal-like cancers are TNBC^{9,10}. Exact numbers for this overlap vary depending on definitions and testing methods¹¹.

TNBCs are known to be aggressive, meaning that they present with a higher cellular grade, grow faster, are more likely to recur quickly, and affected patients exhibit shorter survival after development of metastases^{5,12}. These observations parallel the upregulation of Ki-67 in TNBC, which is an indicator of cell proliferation seen on IHC assays. This is seen in more than half of TNBC cancers, which is a greater fraction compared to other IHC subtypes^{5,13}.

In comparison to other IHC subtypes, TNBC has the lowest 5-year relative survival across all stages of disease (77% vs. 90% for TNBC and all-comers, respectively)¹⁴. This is due in part to the aggressive nature of TNBC and the resulting higher likelihood of discovery at a later stage⁵. However, this disparity is even more dire in breast cancers with regional (65% vs. 86%) and distant (11.5% vs. 28.1%) spread¹⁴. These disparities arise in part due to several breakthroughs in targeted therapies for other IHC subtypes. Anti-hormone therapies which reduce hormone-receptor activation in ER and PgR positive subtypes have greatly improved outcome in these IHC subtypes at all stages¹⁵. Trastuzumab, a targeted therapy which interferes with biological processes in HER2 positive cancer cells and recruits immune cells towards their destruction¹⁶, has shown unprecedented success in treating HER2 breast cancers of all stages¹⁷.

TNBC has thus far presented a continuing challenge for development of targeted therapies^{2,18,19}. Recent gene-profiling research has revealed TNBC is not a single entity but may be grouped into further subtypes²⁰⁻²².

1.2.2 Diagnosis of TNBC

After a suspicious finding on screening mammography or presentation of clinical symptoms, a patient will undergo diagnostic breast exams²³. This will include clinical examination by palpation of breasts and axillary lymph nodes as well as medical imaging. Imaging will include diagnostic mammography and ultrasound of the breast and lymph nodes. Sometimes, magnetic resonance imaging (MRI) will be used for screening or to clarify findings, particularly in patients with dense breasts which may occlude lesions on mammography²⁴. Finally, after diagnostic exams, the breast cancer will be confirmed on histopathology through biopsy of suspicious areas.

A confirmed cancer will then be classified based on its physical extent. Using imaging, the TNM (tumor, node, metastasis) categories will be determined²⁵. The T stage is dependent on the size and extent of the primary lesion on imaging Table 1

Table 1 T stage criteria for breast cancers²⁵

T Category	T Criteria
TX	Primary tumor cannot be assessed
T0	No evidence of primary tumor
Tis (DCIS)	Ductal carcinoma in situ (DCIS)
Tis (Paget)	Paget disease of the nipple NOT associated with invasive carcinoma or DCIS
T1	Tumor \leq 20 mm in greatest dimension
T1mi	Tumor \leq 1 mm in greatest dimension
T1a	Tumor $>$ 1 mm but \leq 5 mm in greatest dimension
T1b	Tumor $>$ 5 mm but \leq 10 mm in greatest dimension
T1c	Tumor $>$ 10 mm but \leq 20 mm in greatest dimension
T2	Tumor $>$ 20 mm but \leq 50 mm in greatest dimension
T3	Tumor $>$ 50 mm in greatest dimension
T4	Any size with extension to chest wall or skin
T4a	Extension to chest wall
T4b	Ulceration, nodules or edema (including peau d'orange) of skin
T4c	Both T4a and T4b
T4d	Inflammatory carcinoma

N-stage is determined by examining the number of involved lymph nodes. This may be done clinically or with imaging and may further be confirmed through biopsy and histopathology. N staging for clinical/imaging-base lymph node assessment is show in Table 2.

Table 2 N stage criteria for breast cancers²⁵

N Category	N Criteria
NX	Regional lymph nodes cannot be assessed
N0	No regional lymph node metastases
N1	Metastases to movable ipsilateral level I and II axillary lymph node(s)
N1mi	Micrometastases (approximately 200 cells, > 0.2 mm, but < 2.0 mm)
N2	Metastases in ipsilateral level I and II axillary lymph nodes that are clinically fixed or matted; <i>or</i> in ipsilateral internal mammary lymph nodes in the absence of axillary lymph node metastases
N2a	Metastases in ipsilateral level I and II axillary lymph nodes fixed to one another (matted) or to other structures
N2b	Metastases only in ipsilateral internal mammary lymph nodes in the absence of axillary lymph node metastases
N3	Metastases in ipsilateral infraclavicular (level III axillary) lymph node(s) with or without level I and II axillary lymph node involvement; <i>or</i> in ipsilateral internal mammary lymph node(s) with level I and II axillary lymph node metastases; <i>or</i> metastases in ipsilateral supraclavicular lymph node(s) with or without axillary or internal mammary lymph node involvement
N3a	Metastases in ipsilateral infraclavicular lymph node(s)
N3b	Metastases in ipsilateral internal mammary lymph node(s) and axillary lymph node(s)
N3c	Metastases in ipsilateral supraclavicular lymph node(s)

Finally, M is determined, is a binary measure determined by presence (M1) or lack (M0) of distant metastases. These may then be combined in TNM tumor staging Table 3.

Table 3 Conversion table for TNM combinations into breast cancer stage²⁵

T	N	M	Stage Group
Tis	N0	M0	0
T1	N0	M0	IA
T0	N1mi	M0	IB
T1	N1mi	M0	IB
T0	N1	M0	IIA
T1	N1	M0	IIA
T2	N0	M0	IIA
T2	N1	M0	IIB
T3	N0	M0	IIB
T1	N2	M0	IIIA
T2	N2	M0	IIIA
T3	N1	M0	IIIA
T3	N2	M0	IIIA
T4	N0	M0	IIIB
T4	N1	M0	IIIB
T4	N2	M0	IIIB
Any T	N3	M0	IIIC
Any T	Any N	M1	IV

While staging is the same for all breast cancers, it should be combined with the cellular grade and receptor status to determine an optimal course for disease management. The cellular grade, ER, pGR, and HER2 status will be obtained from a biopsy sample with IHC staining and histopathological interpretation. It is at this point in care that a TNBC would be recognized and managed accordingly.

1.2.3 Treatment of TNBC

After its diagnosis, TNBC is handled distinctly from other IHC subtypes. Disease management is considered in the context of the cancer stage, patient age (young patients may later face fertility issues

from some chemotherapy treatments), the general health of the patient, and the patient's menopausal status.

For early setting (stages I through III) TNBC patients with sufficient general health, standard of care treatment begins with neoadjuvant systemic therapy (NAST) consisting of dose-dense anthracycline-based chemotherapy followed by taxane²³. These chemotherapies are systemic, non-targeted therapies which preferentially harm cancer cells due to their fast reproduction rate. Anthracyclines are bacteria-derived drugs which interrupt DNA replication²⁶. Taxanes, originally identified in yew trees, halt cell reproduction through disruption of the mitotic spindle, which is the machine responsible for separating chromosomes for cell division²⁶. The term dose-dense is used to indicate a faster rate of delivery for chemotherapies. In the case of TNBC, dose-dense chemotherapy is delivered biweekly instead of monthly.

After completion of NAST, patients undergo surgical removal of their cancer. This may be either segmentectomy (breast-conserving surgery) or mastectomy. The surgical specimen is examined for viable cancer cells. If the patient has no viable cancer cells, they are considered pCR. In the case that viable cells are seen on histopathology, the patient is considered non-pCR.

Although pCR does not carry the direct clinical importance of long-term outcome measures, it is still considered an important clinical endpoint and may act as a surrogate for survival^{27,28}. Non-pCR patients may undergo additional treatment to mitigate recurrence or treat remaining cancer, while both pCR and non-pCR are placed under observation in case of recurrence.

1.2.4 Prediction of NAST Response

Currently, there are no accepted biomarkers for prediction of treatment response in TNBC. However, this is an area of active research. Many molecular biomarkers (from gene profiling or IHC) have been proposed for prediction of pCR to NAST.

Higher Ki67 expression at pretreatment is seen to correlate with pCR^{29,30}. The level of tumor-infiltrating lymphocytes (TIL), which are the lymphocyte-type immune cells which invade tumor tissue, has been shown to correlate strongly with pCR^{31,32}. Subtype-scores on PAM50, a multi-gene genetic assay which is used for characterization of intrinsic molecular subtypes in breast cancer, have also been shown to correlate with pCR³³. Specifically, basal-like TNBC is seen to have a higher rate of pCR³⁰, though TNBC with high proliferation score or low luminal A signature have also been shown to have higher rate of pCR³³. Besides these more popular assays, many novel molecular biomarkers of response in TNBC have also been proposed. These are summarized in a recent review by Chica-Parrado et al³⁴.

Proposed MRI biomarkers of response in TNBC are reviewed in detail in 1.5.3 MRI for Early Prediction of Treatment Response in TNBC.

1.2.5 ARTEMIS – A Robust TNBC Evaluation Framework to Improve Survival (Trial NCT02276443)

ARTEMIS (A Robust TNBC Evaluation Framework to Improve Survival) is a clinical trial conducted as part of the MD Anderson Cancer Center Moonshots Program in Breast Cancer. ARTEMIS seeks to identify targets for novel therapies in TNBC medicine and to develop molecular and imaging biomarkers of response. More specifically, ARTEMIS seeks to use imaging biomarkers to as early predictors of response after delivery of anthracycline-based chemotherapy and then assign a targeted therapy based on molecular characterization for predicted non-responders. A graphical depiction of this triage strategy may be seen in Figure 2. The imaging arm of this trial includes both ultrasound and MRI modalities, though the ultrasound arm is beyond the scope of this dissertation.

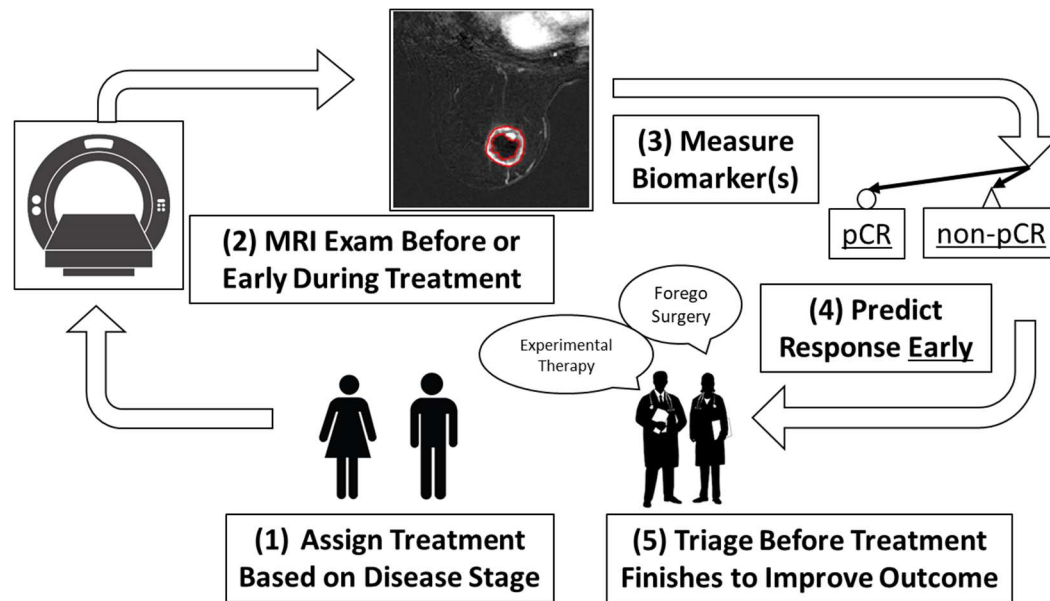


Figure 2 A graphical depiction of an MRI biomarker for early prediction of treatment response to support triage to improve patient outcome.

All patients received NAST consisting of dose-dense doxorubicin and cyclophosphamide (anthracycline-based chemotherapy) for 4 cycles followed by paclitaxel (a taxane chemotherapy drug), which was given every 2 weeks for 4 cycles or weekly for a total of 12 doses. MRI scans are performed at baseline (BL scan), after 2 cycles of dose-dense doxorubicin and cyclophosphamide (C2 scan), after 4 cycles of dose-dense doxorubicin and cyclophosphamide (C4 scan), and after completion of NAST but before surgery (preS scan). After completion of treatment, the patient undergoes definitive surgery. Through histopathologic examination of the surgical specimen, patients are determined as pCR if the specimen has no viable cancer cells, and non-pCR if the specimen contains any viable cancer cells. A protocol timeline for a patient undergoing longitudinal MRI alongside treatment is shown in Figure 3.

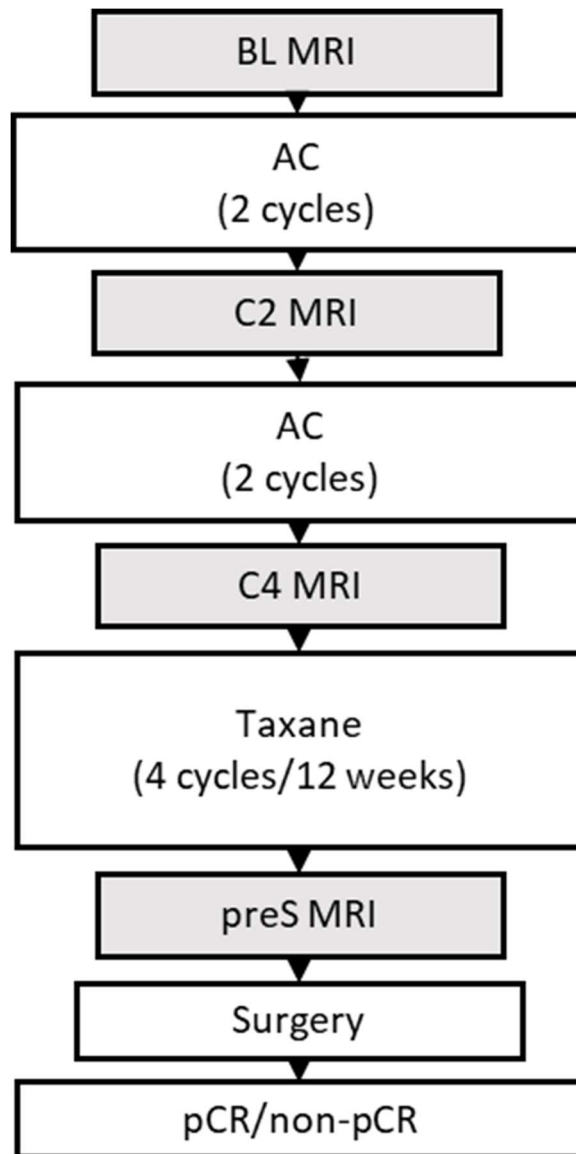


Figure 3 ARTEMIS trial care pathway with longitudinal MRI.

The longitudinal multiparametric MRI in ARTEMIS applies a variety of quantitative MRI modalities. The fundamentals of those relevant to this dissertation are covered in *1.4 Quantitative MRI Modalities*, while the specifics of the individual quantitative MRI series are covered later in the relevant project chapters. ARTEMIS patients were included in all chapters, however, a subset of retrospective clinical patients were also included in *Chapter 2 – Tumor Necrosis by Pretreatment Breast MRI: Association with Neoadjuvant Systemic Therapy Response in Triple-negative Breast Cancer*.

1.3 Fundamentals of Magnetic Resonance Imaging

Magnetic Resonance Imaging (MRI) is a medical imaging modality which uses magnetic fields to align and localize the magnetic moments arising from non-zero atomic nuclear spin. MRI is most commonly used to measure the signal from protons (^1H) due to their abundance in water and organic media, though other nuclei are areas of active research. The magnetic signal from protons is inherently sensitive to the local chemical environment and may also be sensitized to other factors such as motion or chemical exchange. This rich domain of sensitivities offers unique contrasts between tissues, making both nuclear magnetic resonance (NMR) and MRI powerful scientific and medical tools. It is therefore unsurprising that discoveries in magnetic resonance and MRI have resulted in five Nobel Prizes (two in physics, two in chemistry, and one in medicine).

In medicine, MRI is used commonly to assess and diagnose diseases affecting soft tissues. In the United States of America, from 2013 to 2016, MRI procedures were conducted at a rate of 118 per 1000 people annually³⁵. MRI does not utilize ionizing radiation and offers 3D imaging that may be obtained from an arbitrary viewing angle. However, MRI is relatively slow and expensive. These limitations are imposed by the MRI experiment and the high cost of superconducting magnets. Development efforts in MRI acquisition techniques and hardware design have been bolstered by the recent advent of deep learning algorithms and continual improvements in materials science technology. The resulting advances will continue to ameliorate MRI's speed and cost limitations. These improvements, in combination with new medical applications and rising global wealth and healthcare access, give MRI a strong growth trajectory for the recent future.

1.3.1 The Nuclear Magnetic Resonance Phenomena (B_0)

In 1938, Isidor Rabi found that this quantum nuclear spin could discretely absorb energy from an oscillating magnetic field³⁶. This phenomenon is referred to generally as nuclear magnetic resonance, or

NMR. The magnetic moment arises from a fundamental quantum property called spin, as if there were a “spinning charge” in the quantum object with a given angular momentum that produces a magnetic field. This is analogous to a conductive loop with some current, though the underlying phenomena is not a spinning charge and is instead fundamental. We now know this stems from elementary particles called quarks, though it is only observable in quark groupings whose spins sum to a non-zero moment.

Non-zero magnetic moments occur in several atomic isotopes. When considering these isotopes for NMR applications, it is useful to consider the isotopic abundance in nature, the strength of their magnetic dipole moment, and the elemental abundance in biology/tissue. With respect to these factors, protons (^1H) produce strong signal and are abundant in both nature (99.98% of hydrogen atoms) and biology in the form of water and organic chemicals.

In applied NMR, the measured signal is the net signal from all non-zero magnetic moments in a sample or subject. In the presence of an external magnetic field and at extremely low temperatures, the magnetic moments will align so that their dipoles are parallel to the external field. However, at physiological temperatures, the thermal energy is sufficient to induce transition between parallel and anti-parallel alignments. Two protons who take on opposite alignments will cancel and result in a net zero magnetic field. However, a slight preference for parallel alignment remains for magnetic fields of sufficient strength. This net magnetization is described by the following equation:

Equation 1:
$$\frac{N_{\text{Parallel}}}{N_{\text{Anti-parallel}}} = \exp\left(-\frac{\Delta E}{kT}\right)$$

where $N_{\text{Parallel}}/N_{\text{Anti-parallel}}$ is the ratio of magnetic moments expressing the two alignments, ΔE is the energy needed to transition between the parallel and anti-parallel states, k is the Boltzmann constant ($1.381 \times 10^{-23} \text{ J/K}$), and T is the temperature in Kelvin (310 K in physiological conditions). Solution of this reveals that at 1.5 T, there are about 10 extra parallel spins per million. Because of this, NMR/MRI has a

poor absolute sensitivity. However, the proton density in water and tissue is sufficient to create measurable (and useful) net magnetization (M_0) in spite of this.

NMR magnetic moments are not static and instead precess around the axis of the external field. By convention, this is chosen to be the z-axis. The frequency of this precession, ω , is called the Larmor frequency. The Larmor frequency is related to the strength of the external field (B_0) and may be calculated for a quantum object using its gyromagnetic ratio, γ .

Equation 2: $f = \frac{\gamma B_0}{2\pi}$

For ^1H in a 1.5 T MRI scanner, the Larmor frequency is 63.86 MHz. This is considered to be in the frequency domain of radiowaves on the electromagnetic spectrum.

Non-zero magnetic moments may also occur in molecules due to unpaired electrons in the orbitals of their constituent atoms. Some of these strongly affect nearby molecules, forming a basis for the effects of MR contrast agents and some *in vivo* contrasts.

1.3.2 Radiofrequency Excitation (B_1) and Decay

By playing a radiofrequency (RF) pulse at the Larmor frequency, it is possible to excite spins aligned with B_0 and tip them into the transverse plane (x-y plane). The degree to which these spins are tipped is called the “flip angle,” and it is dependent on the strength and duration of the RF pulse:

Equation 3: $\alpha = \gamma B_1 \tau$

where α is the flip angle, γ is the gyromagnetic ratio, B_1 is the RF amplitude, and τ is the RF duration.

From their steady-state alignment, a 90-degree flip angle would tip spins entirely into transverse plane, while a 180-degree flip angle would invert them. In this excited state, spins continue to precess around the z-axis at the Larmor frequency.

While tipped into the transverse plane, the net signal of these spins may be captured using an array of conductive coils placed perpendicular to the transverse plane. The time-varying magnetic field produced by the combined magnetic moment of the sample in the transverse plane (M_{xy}) induces current in the coils. This forms the basis of NMR signal measurement.

It is useful to consider a spin in the rotating frame of reference, where its vector relative to the Larmor frequency with a certain phase is considered. After excitation from rest, the spins in the sample will initially be in the transverse plane and will be pointing in the same direction (forming a coherent M_{xy}). Signal collected from coils varies sinusoidally in time with the Larmor frequency of the sample as M_{xy} rotates. A sample whose spins have varying Larmor frequencies will produce a composite signal whose components de-phase with time. The transverse signal and its inter-spin coherence will also decay naturally through several fundamental processes (termed T1, T2 and T2*) in a pattern known as free induction decay (FID).

The z-component of the M_0 will recover through a mechanism known by several names: longitudinal relaxation, spin-lattice relaxation, or T1 relaxation. Fundamentally, T1 relaxation represents thermal energy transfer from excited spins into their surroundings. This transfer depends on the size and movement of the spin's molecule. The frequency with which the molecule "tumbles" and thereby interacts with other molecules determines the likelihood of thermal energy transfer to the surroundings. A molecule whose interactions happen to occur at a rate similar to the Larmor frequency shows more efficient energy transfer and thereby exhibit shorter T1 relaxation. Large, bound molecules or small, free molecules have tumbling rates further from the Larmor frequency, and therefore have longer T1 relaxation times in comparison to a molecule tumbling at the Larmor frequency. Recovery of the longitudinal component of M_0 after excitation from a resting state can be described by the following equation:

Equation 4: $M_z = M_0 \left[1 - \exp\left(-\frac{t}{T_1}\right) \right]$

where M_z is the longitudinal magnetization, M_0 is the net magnetic moment, t is time, and T_1 is the longitudinal relaxation time. When a single T_1 time has passed after excitation from rest, approximately 63% of M_z will have recovered in the sample. T_1 relaxation time is proportional to the cubic root of the B_0 field.

A second type of relaxation called spin-spin relaxation, transverse relaxation, or T_2 relaxation also occurs. After initial excitation from rest with an RF pulse, all spins in the sample will produce a coherent signal of equal phase respect to their procession. However, due to T_2 processes, different phase evolutions will occur in spins with time, resulting in loss of coherence (dephasing) and decay in detectable signal with time. After a 90-degree RF excitation from rest, transverse signal decay due to T_2 coherence loss can be described by the following equation:

Equation 5: $M_{xy} = M_0 \exp\left(-\frac{t}{T_2}\right)$

where M_{xy} is the transverse magnetization, M_0 is the total magnetization, t is time, and T_2 is the T_2 relaxation time. Neglecting inhomogeneities, after a single T_2 time has passed, approximately 37% of the transverse magnetization will remain coherent. T_2 relaxation is not very dependent on the B_0 field.

Like T_1 relaxation, T_2 relaxation is partly due to thermal energy loss from excited spins returning to their lower energy resting state. This occurs unevenly among the spins and results in a lack of coherence. T_2 relaxation is also impacted by direct local transfer of energy between spins as well as slight differences in local magnetic fields on the molecular level, which would create small variations in the rate of precession that would incur phase differently. The efficiency and likelihood of this spin-spin energy transfer is also dependent on the tumbling rate; however, spin-spin energy transfer is most efficient in large, bound molecules (lower T_2 relaxation time) and decreases monotonically as molecules

become smaller and free. Because T2 is fueled by both T1 relaxation and additional sources, it is always shorter than T1. A visualization comparing of T1 and T2 relaxation times relative to tumbling rate can be seen in Figure 4.

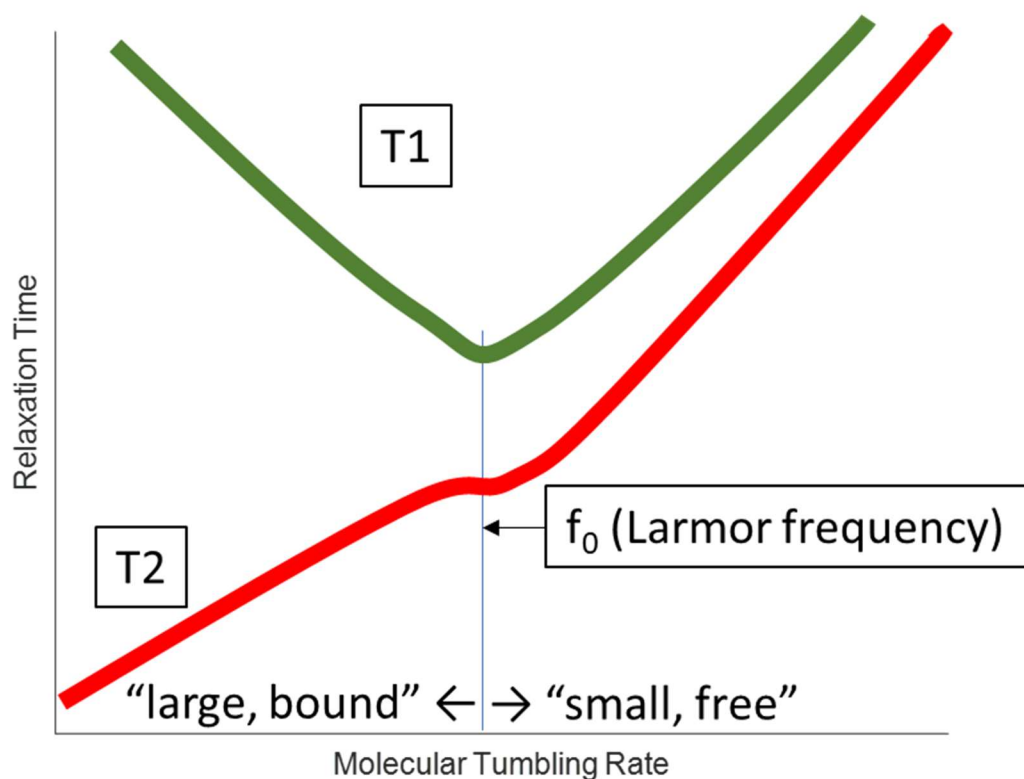


Figure 4 T1 and T2 versus molecular tumbling rate.

In FID, dephasing is additionally accelerated by inhomogeneity in B_0 . B_0 inhomogeneities may be inherent in the field but are additionally caused by modulations of the magnetic field from diamagnetic and paramagnetic effects in the sample. This accelerated decay is called $T2^*$, and it is a reversible property, whereas T2 is irreversible. FID signal decay in the $T2^*$ envelope can be seen in Figure 5.

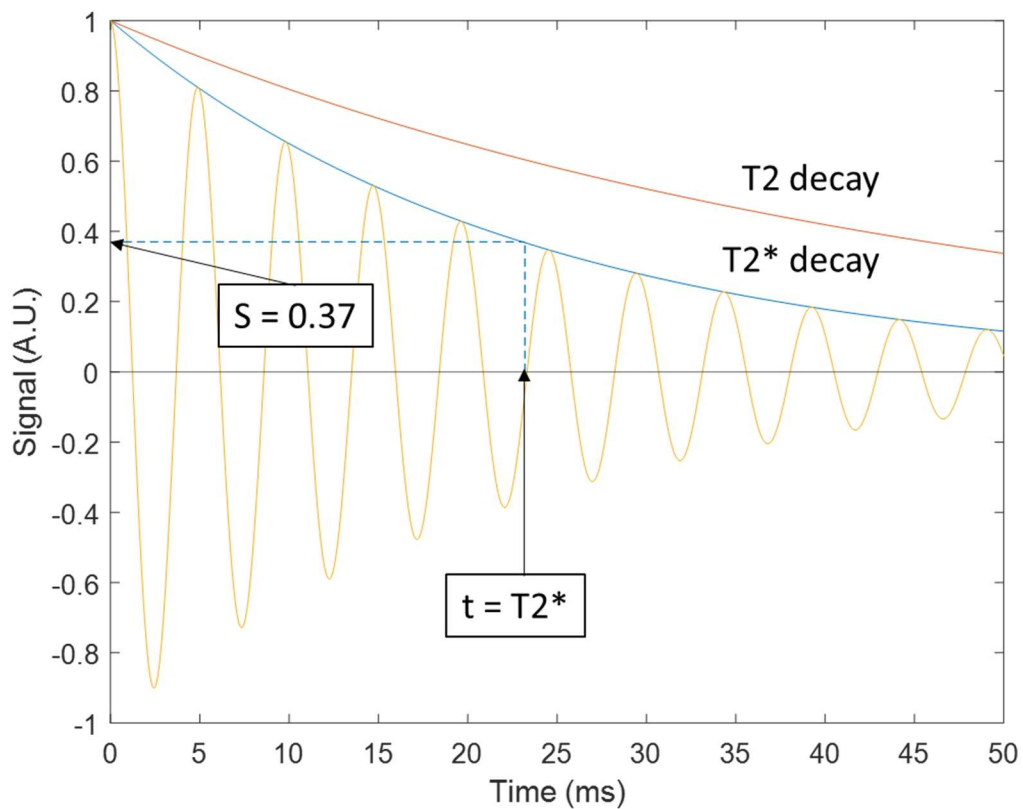


Figure 5 Simulated free induction decay (FID) for normal breast fibroglandular tissue (FGT) with $T2^* = 23.2$ ms and $T2 = 46.0$ ms.

1.3.3 Refocusing, Echoes, and Repeat Acquisition

After excitation, spins will naturally decay in an FID according to $T2^*$. It is possible to extend this to pure $T2$ decay through application of a transverse 180-degree RF pulse, also called a refocusing pulse. This refocusing pulse, when applied at time τ after excitation, will invert the phase incurred between the RF pulses. After time τ has elapsed after the refocusing pulse, the spins will again incur the same phase as before. However, this phase will be incurred in the opposite direction, with the result of “rewinding” the phase incurred before the refocusing pulse. This results in re-coherence in the form of a Hahn echo or “spin-echo” (SE). SE magnitude is governed by $T2$ decay rather than $T2^*$ decay, as the reversible sources of phase are rewound.

Repeated acquisition of a set of NMR data may be used for signal averaging, where multiple redundant acquisitions are acquired and the signal-to-noise ratio (SNR) increases in the following manner:

Equation 6: $\text{SNR} \propto \sqrt{NEX}$

where NEX is the number of excitations.

1.3.4 Imaging with Gradient Fields (G_x , G_y , G_z)

Localization in z-direction (slice-selection)

When a magnetic field gradient is imposed upon the subject, the Larmor frequency of the spins will vary spatially across the subject. By “playing” an RF pulse with a narrow frequency bandwidth while simultaneously applying a linear gradient field, RF excitation may be limited to a “slice” of the subject with Larmor frequencies matching the narrow bandwidth of the RF pulse. This slice-selection process is often depicted as the mechanism of localization in the z-axis, with the gradient field G_z applied parallel to the bore of the MRI and B_0 . In practice, gradient fields may be applied at any angle in an MRI and the slice-selection direction may be chosen arbitrarily.

Spatially Encoded Signal

In-plane spatial encoding of an excited slice is also accomplished through application of gradient fields (G_x , G_y), but they are instead applied during signal readout or data acquisition (DAQ). Application of a linear gradient field after excitation causes dephasing of spins due to the spatial variation of the Larmor frequency in the subject. Because phase is cyclic, spin coherence will occur cyclically across the spatially varying Larmor frequencies after evolution during an applied gradient.

The spatial distance over which a single phase-cycle evolves may be considered as a spatial frequency (in units of cycles per length) and the resulting partially coherent signal is said to be encoded with this spatial frequency, k (Equation 7).

Equation 7: $k_r(t) = \gamma \int_0^t G_r(x, t) dt$

The signal, thus encoded, is related to the spatial variation of spins along the direction of encoding within the subject.

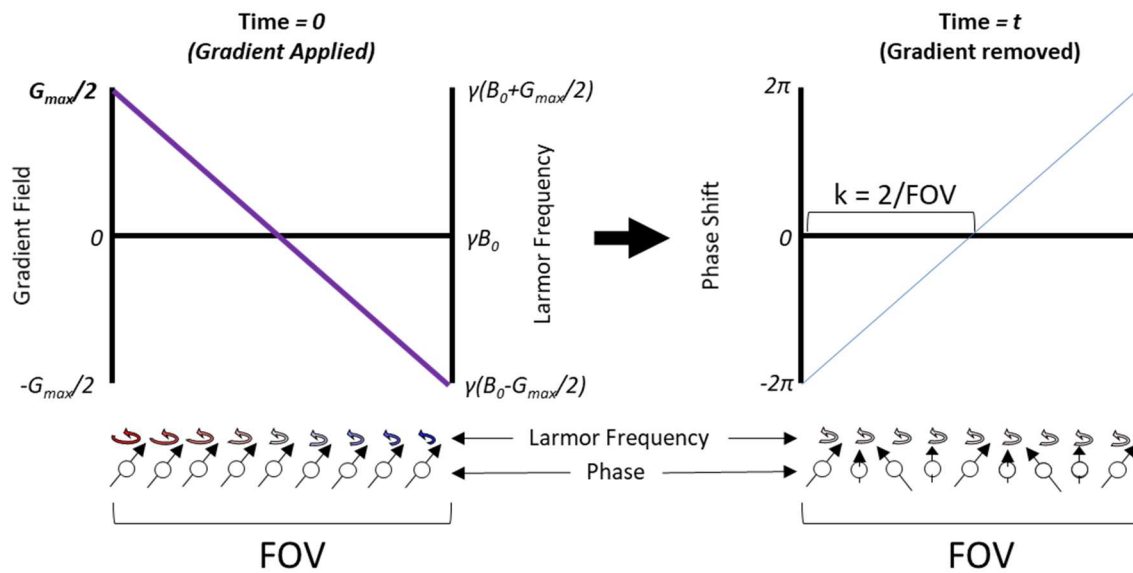


Figure 6 Graphical explanation of spatial encoding of MRI signal through application of a linear gradient field.

The effect of spatial encoding on the acquired signal is easiest to consider in two extreme cases. In the case that the spatial distribution of spins was such that spins were only located at the 0 phase indices (Figure 7A), the coherent signal would be maximized and equivalent to the signal without any gradient spatial encoding. If the subject's spin were distributed evenly across all phases (Figure 1B) the net signal would be 0 due to equal density of signal at all phase offsets.

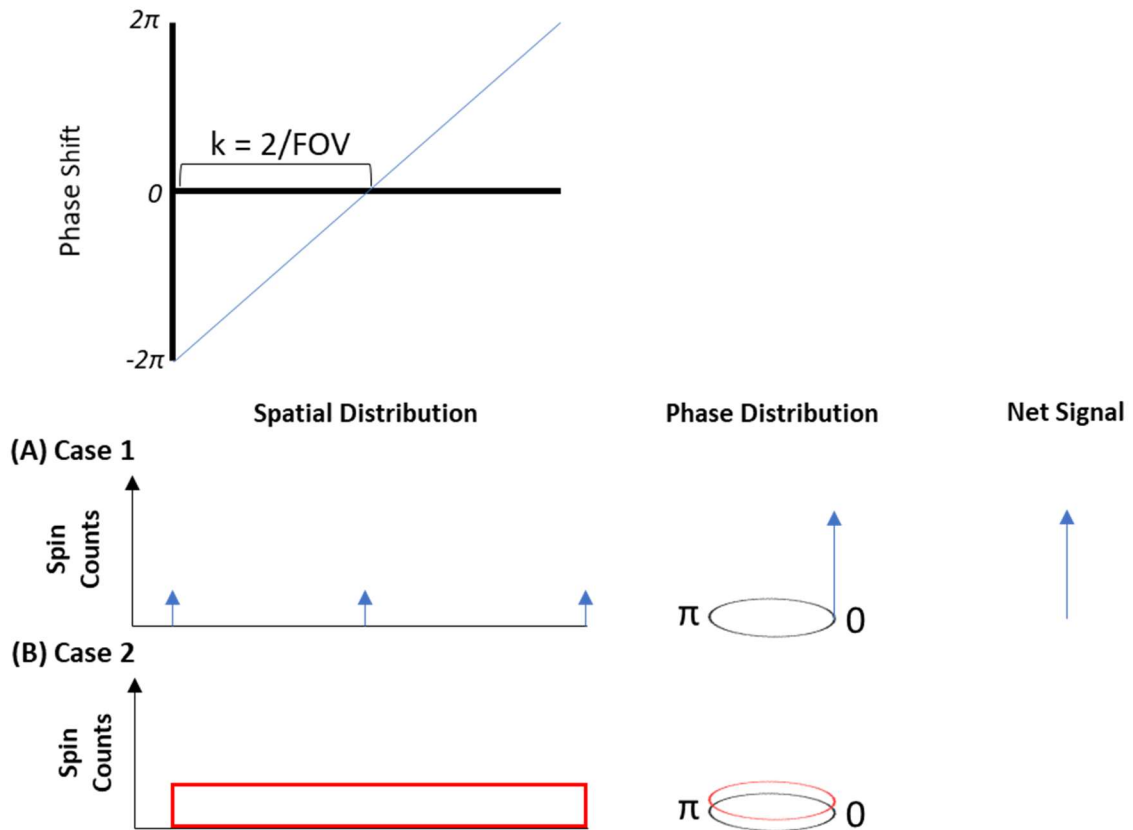


Figure 7 Two cases of spin distribution with $2/\text{FOV}$ spatial frequency. (A) Spins are located on 0-phase lines and (B) spins are spread evenly across the phase cycle.

In vivo, MRI scans will always contain non-symmetric spatial distribution of spins across a subject's anatomy. Thus, a net signal would always be produced when encoding with an arbitrary spatial frequency from an arbitrary direction.

With the inverse Fourier Transform (FT), we are able to recompose the acquired MRI signal from a function of spatial frequency into a function of space. For the 1D case, the inverse FT would be as follows:

Equation 8:
$$F(x) = \frac{1}{2\pi} \int_{-\infty}^{\infty} f(\omega) e^{-i\omega x} d\omega$$

where $F(x)$ is the spin distribution as a function of space, ω is the spatial frequency, and $f(\omega)$ is the proton distribution as a function of spatial frequency.

This may be extended to an arbitrary dimension. 1D, 2D, and 3D FTs are used regularly in MRI, though for digitized, discrete signal they are performed as Fast Fourier Transforms (FFTs) and inverse FFT (iFFTs). FFTs and iFFTs are a class of algorithm developed for rapid FT processing of digitized signal. When applied to acquired MRI signal, they convert digitized signal from time domain (k-space) into an image.

In k-space, spatial direction is conserved but mirrored. Signal with no spatial encoding would correspond to the origin of k-space, while increasing distance from the origin corresponds to increasing spatial frequency. K-space has Hermitian symmetry.

Frequency and Phase Encoding

In Cartesian MRI acquisition, sampling is split into a continuously-sampled dimension and an iteratively-sampled dimension. By convention, these are assigned to the remaining spatial encoding axes (x and y dimensions, respectively).

The continuously-sampled dimension is assigned to the x-dimension by convention (perpendicular to the MRI bore and parallel to the ground) and is said to be frequency encoded. DAQ is performed as application of the x-gradient field (G_x) sweeps across k-space through a range of spatial encodings for a single direction. This line of k-space is split into n_s samples with digitization of the signal. The dwell time, t_d , is the DAQ time per sample, where each sample is a point in k-space across the frequency-encoded line. t_d is the inverse of the receiver bandwidth (rBW) of a single pixel in image space:

Equation 9: $rBW_{pixel} = \frac{1}{t_d} = \frac{n_s}{\text{sampling time}}$

In MRI, rBW for an entire k-space line values range from 1 to 100 kHz. This quantity is distinct from the extent of sampled k-space, which would additionally depend on the strength of the gradient:

Equation 10 $k_{max} = \gamma \int_0^\delta G(t)dt$

where k_{max} is the edge of acquired k-space and δ is the gradient duration during readout. This, in combination with n_s , determines the field of view (FOV) of the acquired image:

Equation 11: $FOV_x = \frac{1}{k_x} = \frac{2n_s}{k_{max}}$

Because there is no spatial encoding after excitation from rest, an initial shift to one edge of k-space is performed before frequency encoding so that k-space may be swept across with a single frequency encoding line.

Phase encoding, which extends sampling across the y-axis, is also performed as a pre-DAQ shift. Before DAQ, a discrete shift in the y-axis of k-space is induced through application of G_y . Through iterative acquisition of frequency encoding lines with varied phase encodings, 2D k-space may be sampled.

3D localization may be achieved with 3D k-space acquisition or 2D k-space acquisition combined with slice-selection. 3D k-space acquisition may be achieved by simply adding another phase encoding dimension.

1.3.5 Basic Image Contrast

Contrast Weighting

While acquiring k-space, the DAQ timing may be chosen to emphasize contrast between tissues based on one or more aspects of their decay. In particular, the DAQ timing for central k-space must be considered. The low spatial frequency content at the center of k-space hold a majority of the image contrast, while the high spatial frequency region in outer k-space carries the fine detail and edge information of the image (Figure 8).

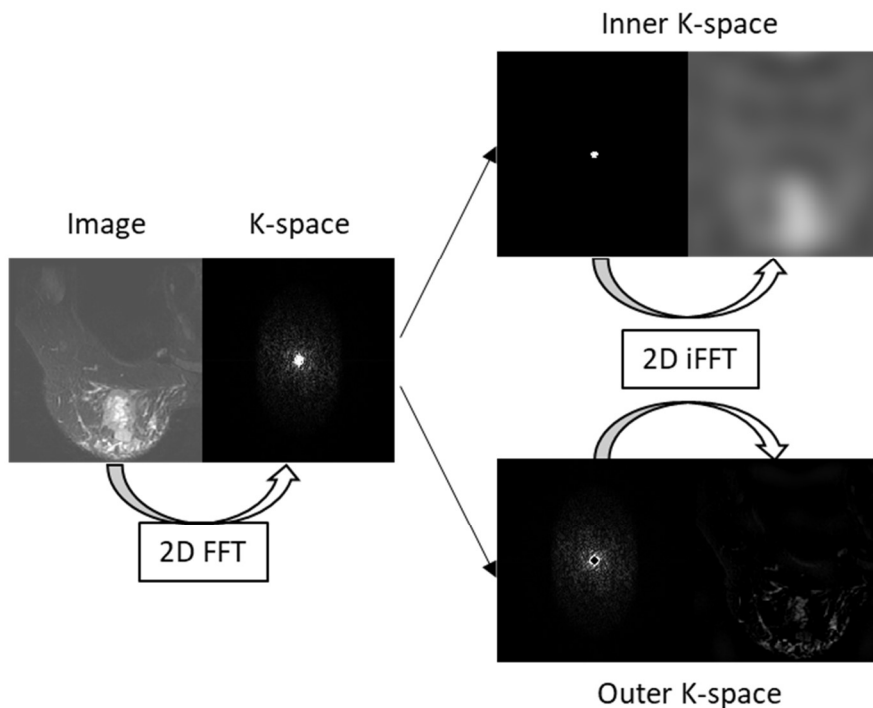


Figure 8 Segmentation of k-space for demonstration of low (inner k-space) and high spatial frequency content (outer k-space).

In acquisitions where a single line of k-space is acquired for each excitation, the contrast timing for when the center of k-space is acquired may be referred to as the echo timing (TE). For SE, DAQ and the timing of the SE are typically centered on one another to maximize signal. This is the source of the term TE.

For non-SE acquisition, the sweep of one frequency encoding line across k-space will result in maximal signal at the center of k-space (where there is no spatial encoding in the frequency direction) and decreasing signal from the center to either side. This phenomenon has a similar appearance to a spin echo and is termed a gradient echo (GRE).

In addition to TE, the repetition time (TR) of repeated excitation must be considered for image contrast weighting. If longitudinal relaxation is not allowed to completely recover by T1 decay, then the

amount of available magnetization for excitation is reduced. By shortening TR and repeating acquisition without complete T1 relaxation, this phenomenon may be leveraged to create images with T1-weighting.

If TR is long (>1000 ms), and TE is long (50-100 ms), transverse relaxation may evolve to create contrast between tissues, creating T2-weighted images for SE acquisitions and T2*-weighted images for GRE acquisitions.

With short TE and long TR, transverse relaxation does not have time to evolve before the TE and longitudinal relaxation is kept similar between tissues with different T1 relaxation times. This creates weighting based on proton density. Generally, T2-weighting is most useful for visualizing pathology, though T1-weighting also has several uses in medicine. Proton density weighting is not frequently used.

TE and TR should be held constant over repeat acquisitions if another source of contrast is desired from a preparation module used before imaging. This will best isolate the prepared contrast as the intrinsic decay is held consistent between acquisitions. TR is generally chosen to be long for these alternate contrast sources to maximize available signal after a time- or signal-expensive preparation module.

Fat Suppression

For many MRI applications, it is useful to suppress signal from fat and thereby improve the conspicuity of possible pathologies that are adjacent or overlapping with fat. This may be done by leveraging either the difference in T1-relaxation properties between water and fat or their difference in Larmor frequencies. The methods applied in this dissertation rely on differences in Larmor frequencies for fat suppression.

The difference between a spin's Larmor frequency and that of a standard spin is called the chemical shift. In MRI, water is taken as the standard and is said to have a chemical shift of 0 parts per

million (ppm). The chemical shift of fat is 3.5 ppm away from the Larmor frequency of water. Because the Larmor frequency of water is dependent on B_0 , the chemical shift in terms of frequency also is dependent on B_0 . At 3T, where water takes a Larmor frequency of 128 MHz, the chemical shift of fat is about 440 Hz.

One popular method for suppression fat is through the use of a spectral saturation pulse³⁷. By selectively exciting fat with a narrowband RF pulse and forcing it to dephase, fat signal may be minimized in the following acquisition. This technique is limited by B_1 and B_0 heterogeneity, which would cause uneven fat suppression throughout the acquired image.

Another more advanced method is the Dixon technique³⁸. It is possible to create a water-only image through linear combination of two acquired images: one with fat and water in-phase and the second with a gradient readout offset chosen to induce a 180-degree phase shift in fat relative to water. While this technique is also vulnerable to B_0 heterogeneity, this may be ameliorated with various techniques that leverage the phase of the two images to correct inconsistencies caused by B_0 heterogeneity³⁹.

1.3.6 Basic Acquisition Techniques

Spoiled Gradient Echo (GRE)

In spoiled GRE, continual excitation and acquisition with incomplete longitudinal recovery between TRs is performed. To avoid coherent signal from previous echoes, signal from previous excitations is made incoherent through RF phase scrambling. Spoiled GRE protocols are typically used for T1-weighted imaging with short TE (<10 ms) and short TR (<20 ms). They may also be used also be used for MRI with proton density weighting and T2* weighting.

In T1-weighted spoiled GRE with short TR, T1 recovery is cut short. This lowers available signal for excitation into the transverse plane. At steady state for a tissue with given T2* and T1, the repeated GRE experiment will result in signal as follows:

Equation 12
$$S = S_0 \frac{\sin \alpha (1 - e^{-TR/T1})}{(1 - (\cos \alpha) e^{-TR/T1})} e^{-TE/T2^*}$$

Fast Spin Echo (FSE)

Through continued application of refocusing pulses in a single TR, an SE sequence can be extended to create multiple sequential SEs. Because this allows for multiple frequency-encoded readouts during a single TR, this imaging technique is called fast spin echo (FSE). In clinical imaging, as many as 30 echoes might be acquired per TR in conventional imaging. This enables strong acceleration of T2-weighted imaging.

Although FSE is used for T2-weighted imaging, it is said to not contain pure T2 contrast because TE is variable between frequency-encoded lines of k-space and because the refocusing pulses are less than 180 degrees. FSE may instead be described with an effective TE, which is calculated based on the timing of phase encoding lines which sample the center of k-space.

Echo Planar Imaging (EPI)

Through the use of strong, rapidly changing gradients, it is possible to quickly navigate a raster trajectory in k-space and capture multiple lines after a single excitation. This may even cover the entirety of k-space through single-shot echo planar imaging (ssEPI). Rapid navigation is necessary to cover the entirety of k-space while maintaining good signal from a single echo. This requires powerful and precise gradients.

Off-resonance artifacts and imperfection in the gradient waveform may cause phase shifts during the EPI readout. These phase errors accumulate across an EPI readout and result in image distortion. The degree of distortion for a given phase error increases with the length of the EPI readout

(also called echo train length). Distortion from EPI acquisition on diffusion MRI can easily be seen when compared to the spoiled GRE contrast-enhanced images of the same breast anatomy in Figure 9.

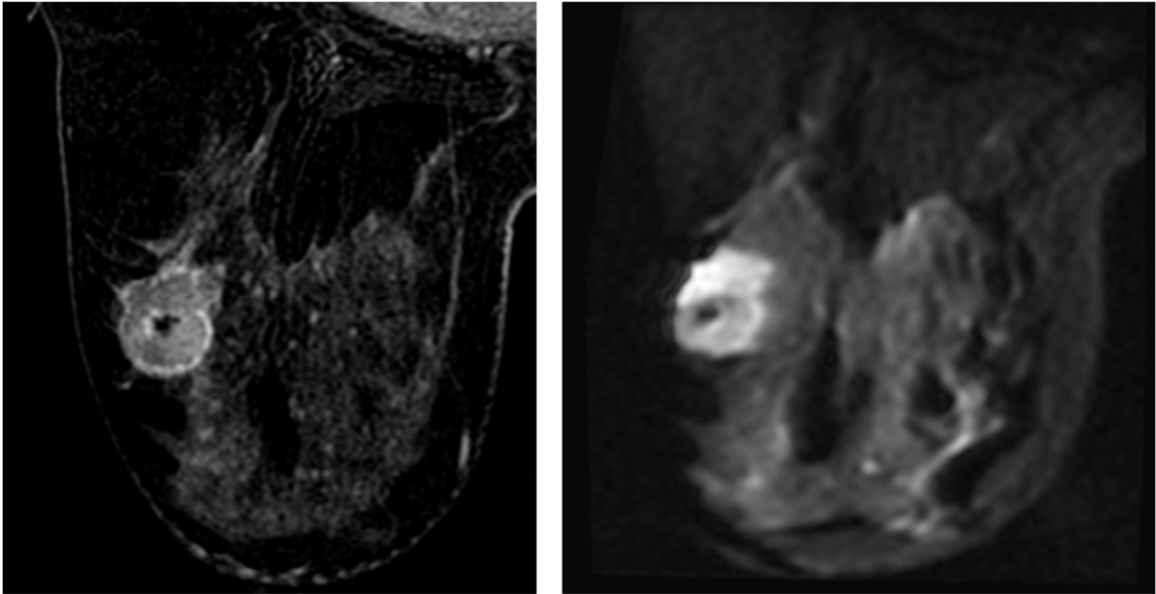


Figure 9 Example of contrast-enhanced spoiled GRE MRI (left) compared with SE-ssEPI diffusion MRI (right) in a 40-year-old woman with TNBC in her left breast. Distortion of the tumor and fibroglandular tissue can be seen. This EPI image has already undergone geometric correction by the vendor, as is evident in the uneven boundary on the left of the image.

1.4 Quantitative MRI Modalities

This section serves to introduce the MRI modalities applied in this dissertation. For each modality, a basic introduction is followed by explanation of the contrast sensitization as well as modeling of the contrast for quantization.

1.4.1 Dynamic Contrast Enhanced (DCE) MRI

DCE MRI is an MRI modality in which imaging is repeated to track the dynamics of tissue enhancement from an injected contrast agent. Changes in contrast throughout time vary according to vascular perfusion of the injected agent. This perfusion contrast is useful for visualizing and clarifying pathology that is unclear or occult on conventional T1 and T2 weighted imaging. Through modeling of contrast transport, it is possible to estimate vascular properties in tissue.

Contrast Agents

A majority of clinical DCE MRI uses Gadolinium-based contrast agents (GBCAs). Gd is paramagnetic and strongly interacts with surrounding water molecules through dipole-dipole interactions. These interactions shorten both the T1 and T2 relaxation times of the water's protons. In a spoiled GRE sequence, shortened T1 creates positive enhancement (increased signal) in accordance with Equation 12. By convention, the term DCE MRI is used to refer to MRI acquisitions which track T1 changes.

In tissues with leaky vasculature (such as cancers and damaged tissue), GBCAs move from vasculature into the extravascular extracellular space (EES). After some time, they are eventually reabsorbed into the blood. At a given time, DCE enhancement is roughly proportional to the concentration of contrast agent within the tissue:

Equation 13:
$$\frac{1}{R1_{effective}(t)} = \frac{1}{R1_{Tissue}} + c(t)r1_{GBCA}$$

where $R1$ is the inverse of $T1$, $c(t)$ is the concentration of the contrast agent as a function of time, and $r1$ is the induced change in effective $R1$ per mole concentration of the contrast agent. $r1$ values vary between GBCAs. Gadbutrol, a GBCA indicated for use in breast MRI, has an $r1$ value of 3.6 L/mmol·s at 3T⁴⁰. GBCA enhancement is strong and may result in signal enhancement of greater than 200% in voxels with vasculature or well-perfused tissue. Mapping of underlying $T1$ values of voxels allows for direct estimation of contrast concentration.

As with many types of MRI, DCE MRI acquisition must be balanced between degree of contrast characterization (in this case, dynamic changes in enhancement) and the spatial extent and resolution. The sampling rate of contrast enhancement curves is referred to as the temporal resolution of DCE. This is the time during which the entire imaged volume, or one DCE “phase,” is sampled. Higher temporal resolution is needed for estimation of tissue perfusion properties in quantitative DCE MRI.

Qualitative DCE MRI

In qualitative DCE MRI, phases may be interpreted qualitatively in an indirect manner, where a radiologist would make interpretations while looking simultaneously at different phase timings or subtractions of phases to show difference in enhancement over time. DCE enhancement may also be interpreted in a direct manner through visualization of enhancement curves from an ROI or voxel.

The enhancement curves of most tissues can be considered as one of three archetypal patterns which occur in the ~ 15 minutes after injection. The first, pattern I or a persistent pattern, is characterized by a continual slow rise of contrast enhancement. Pattern II, also called the plateau pattern, show an early rise in enhancement followed by a plateau. Pattern III, the washout pattern, is characterized by rapid early contrast uptake followed by rapid washout of contrast. A basic depiction of these patterns can be seen in Figure 10.

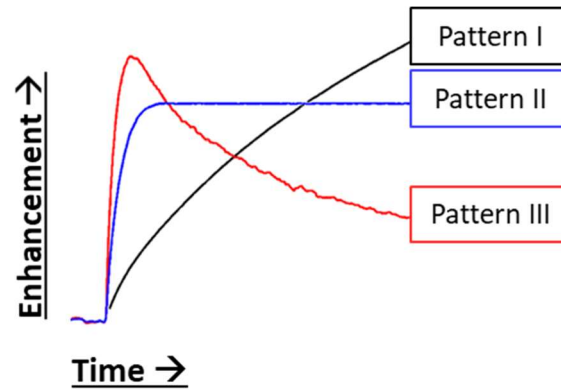


Figure 10 Contrast enhancement patterns in DCE: persistent pattern (Pattern I, red), plateau pattern (Pattern II, blue), and washout pattern (Pattern III, black).

Semi-quantitative DCE MRI

By taking basic measurements of the DCE curve shape, it is possible to assess the degree to which an enhancement curve fits an archetypal enhancement pattern. In general, these empiric, semi-quantitative metrics are chosen to assess rapidity of enhancement and degree of washout. A listing of common DCE semiquantitative metrics is shown in Table 4.

Table 4 Common DCE semiquantitative metrics, their calculation, and an explanation of their meaning.

Metric Name	Calculation	Explanation
TTP - Time to Peak	$[\sim, TTP] = \max (curve(S, t))$	Rapid enhancement and washout pattern
PE _t - Percentage Enhancement at time t	$PE(t) = \frac{S(t) - S_{mask}}{S_{mask}}$	Perfusion level at time t
SER - Signal Enhancement Ratio	$SER = \frac{S_{Early} - S_0}{S_{Late} - S_0}$	Degree of washout (positive SER) between early and late phases
iAUC _t - Initial Area Under curve up to time t	$IAUC_{t=t} = \int_0^{t=t} S(t)dt$	Amount of perfusion up to some timing after injection
MS	$\max \left(\frac{dS}{dt} \right)$	Speed of enhancement

Quantitative DCE MRI

Through parametric modeling and assumptions of contrast flow behavior, pharmacokinetic (PK) analysis contrast transport rates between tissues may be accomplished. This perfusion quantification typically concerns the concentration-agnostic rate of contrast transport from blood to EES (k_{trans}). The coefficient for the reverse process (k_{ep}) may also be calculated.

A two-compartment PK model considering these processes, also called Tofts model, is formulated as follows⁴¹:

Equation 14: $\frac{dC_t}{dt} = k_{trans}C_p - k_{ep}C_t$

where C_t is the contrast concentration in tissue, k_{trans} is the transfer coefficient from vasculature to EES, C_p is the concentration, and k_{ep} is the transfer constant from tissue to vasculature. The ratio of k_{trans}/k_{ep} , v_e , is the EES fractional volume. C_t may be measured directly with MRI, and C_p can be measured or estimated in several fashions. With this information and variational methods, transfer constants can be estimated to best describe the kinetic curve.

Toft's model may also be extended to include contributions from intra-voxel capillaries, which is thought to be useful for well-perfused tissues⁴². A variety of variational methods have been proposed for fitting the DCE enhancement curve to these models.

Compartmental models require accurate temporal tracking or modeling of blood contrast concentration in the tissue of interest. Several strategies have been proposed for this, such as tracking the most enhancing voxels in an imaged volume (assumed to correspond to blood vessels), directly measurement with an ROI on a nearby blood vessel⁴³, or use of a population-based model⁴⁴.

Alternatively, a tissue with known enhancement characteristics can be used as a reference in place of the AIF^{45,46}. These so-called reference-region models (RRMs) may be linearized (LRRM) to improve stability and allow for imaging with relaxed restraints on temporal resolution⁴⁷.

Finally, to account for differences between tissue of interest and region of blood concentration measurement, contrast delivery time may be estimated with blood vessel mapping techniques in combination with ultrafast MRI⁴⁸.

1.4.2 Diffusion Weighted Imaging (DWI)

Diffusion Weighted Imaging (DWI) is an MRI modality where the MRI signal is sensitized to the microscopic diffusion motion of water through application of strong motion encoding gradients (MEGs). Contrast is seen between tissues due to their differential hindrance of water diffusion. This diffusion contrast varies between types of normal tissue and is altered in several pathologies. In solid cancers, the rapid reproduction of cells creates high cellular density, hindering water diffusion. In regions of pathologic edema with little structure, or in cerebrospinal fluid, water may diffuse more freely.

Brownian Motion and the Diffusion Coefficient

Diffusion, an expression of entropy in the form of Brownian motion, was first observed as the random motion of pollen particles on the surface of water. In both this case and the general one, particles dissolved in a solvent are seen to move about in random directions at varying speeds in a “random walk”. This natural process occurs in all mixtures and is brought about by the microscopic kinetic interactions of a particle with its solvent media. There are many possible paths a molecular might take during its “random walk”. In terms of transport between two points, most of these paths are indirect and might be considered as an “inefficient” means of locomotion. In this sense, diffusion may be said to be a slow process.

Diffusion may be characterized with a propagator function $P(r)$, which is a probability density function describing the likelihood that the molecule would move to the spatial position r in a given amount of time. After a given diffusion/mixing time (Δ), $P(r)$ takes on a Gaussian distribution with respect to the magnitude of r if the media is unbound $P(r)$ is isotropic with respect to the direction of r in

a homogenous media. Unlike linear motion, the rate at which a molecule diffuses is described in units of (length²/time):

Equation 15: $D = \frac{\langle r^2 \rangle}{2t}$

where D is the diffusion coefficient, t is time, and r^2 is the mean-squared displacement of a particle from its original position.

MRI allows for direct measurement of D through repeated DWI with varied levels of diffusion sensitization. However, water protons in tissue are present in heterogenous environments which include barriers such as cell walls, large macromolecules, and other structures. These structures may hinder (slow) or restrict (prevent) water diffusion. Additionally, the voxel spins may also experience microscopic intra-voxel motion in tissue capillaries. In light of these phenomena, MRI-measured diffusion is not truly D . In recognition of this, the measured quantity is instead referred to as the Apparent Diffusion Coefficient (ADC).

Typically, DWI is performed as fat-suppressed SE in combination with ssEPI. Because diffusion weighting reduces signal, it is advantageous to select a long TR to maximize available M_0 for each excitation. SE improves signal by extending decay to the T2 envelope, which maximizes signal at TE. DWI requires a later (>50 ms) TE because powerful MEGs must have time to encode motion on a microscopic scale after excitation. Because it has long TR and long TE, DWI acquired in this manner can be said to have T2-weighting in addition to diffusion weighting.

Diffusion Encoding

For SE-ssEPI acquisition, diffusion MEGs are placed on either side of the refocusing pulse. A basic pulse sequence diagram of this can be seen in Figure 11.

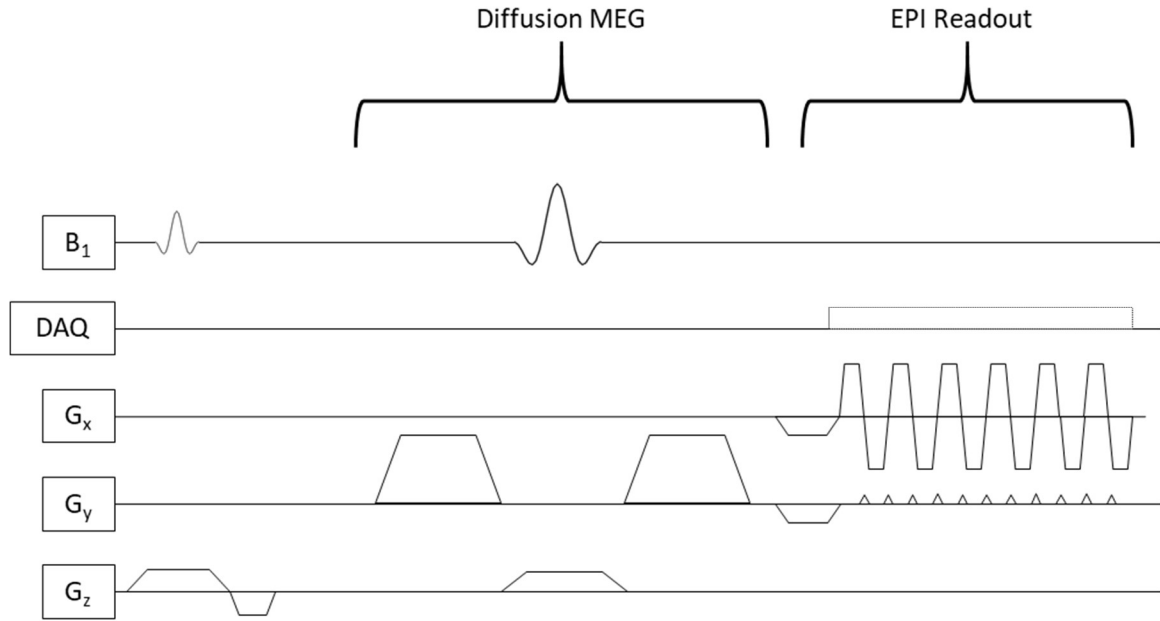


Figure 11 Basic pulse sequence diagram for SE-ssEPI with diffusion encoding in the y-direction.

Like other spatial encoding, the degree of diffusion-weighting from MEGs is dependent on the duration and magnitude of the applied spatial gradient field. In DWI, the degree of diffusion weighting may be expressed as the “b-value,” which can be calculated for a given gradient as follows:

$$\text{Equation 16: } b \text{ (s/mm}^2\text{)} = \gamma^2 G^2 \delta^2 (\Delta - \delta/3)$$

where γ is the gyromagnetic ratio, G is the gradient magnitude, δ is the gradient duration, and Δ is the time elapsed between the MEGs (mixing time).

Diffusion Modeling

For a voxel of tissue with a given ADC that exhibits isotropic Gaussian diffusion, the MR signal will decrease exponentially with increasing diffusion weighting:

$$\text{Equation 17: } S = S_0 e^{-b \cdot \text{ADC}}$$

where b is the b-value, ADC is the apparent diffusion coefficient of the voxel, and S_0 is the signal without diffusion weighting. This equation is called the mono-exponential model of diffusion. ADC may be estimated through measurement of MRI signal at two diffusion weightings, neither of which must

necessarily be b_0 (no diffusion weighting). Signal measurements may also be taken at several diffusion weightings, and variational methods such as least-squares algorithms may be used to estimate an ADC that best fits the monoexponential model.

While all tissues show exponential signal decay to some extent, it has been shown that this behavior diverges at low and high b -values due to intravoxel flow and non-Gaussian diffusion, respectively. A variety of diffusion models have been proposed to best explain signal variation with respect to diffusion weighting and direction. These are extended from the mono-exponential model of isotropic Gaussian diffusion, and additional model parameters are included to account for capillary flow and microscopic barriers which would impact signal. These models are beyond the scope of this thesis. To avoid the effects of capillary flow on diffusion acquisition at low b -values, a b -value greater than 100 s/mm^2 may be chosen. This approach was taken in the ARTEMIS DWI scans.

Directional variation in diffusion (anisotropy) are also present in many tissues. Through sufficient sampling of this directional dependence, this may be characterized and modeled. This is also beyond the scope of this dissertation.

1.4.3 Magnetic Resonance Elastography (MRE)

Magnetic Resonance Elastography (MRE) is a phase-contrast modality which tracks externally-induced motion in tissue and inverts the imaged mechanical waves into the underlying tissue stiffness. MRE is an emerging MRI modality which was initially proposed in 1995⁴⁹. Thus far, its only clinically indicated use is for assessment of chronic liver disease⁵⁰. It has been shown to correlate well with histopathology levels of liver fibrosis⁵¹.

In the research setting, cancer tumors of several types have been shown to be stiffer in comparison to normal tissue⁵². In preliminary reports, measures of tumor stiffness have been shown to correlate with histopathology measures such as tumor grade⁵³ and intratumoral T lymphocytes⁵⁴.

Mechanical Wave Propagation

Mechanical waves are a form of energy transmission through matter in the form of oscillatory motion. They include natural phenomena such as seismic waves, sound waves, and ocean waves. Like in seismology other areas of science, examining wave behavior may give us insight into the propagation media.

In solid bulk matter, waves of both longitudinal and transverse motion may propagate. Longitudinal waves (also called compression waves, pressure waves, or P waves) create compression and rarefaction of the solid in the direction of propagation (Figure 12A). Transverse waves (also called shear waves or S waves) create side-to-side shearing motion in the solid that is perpendicular to the direction of wave propagation (Figure 12B).

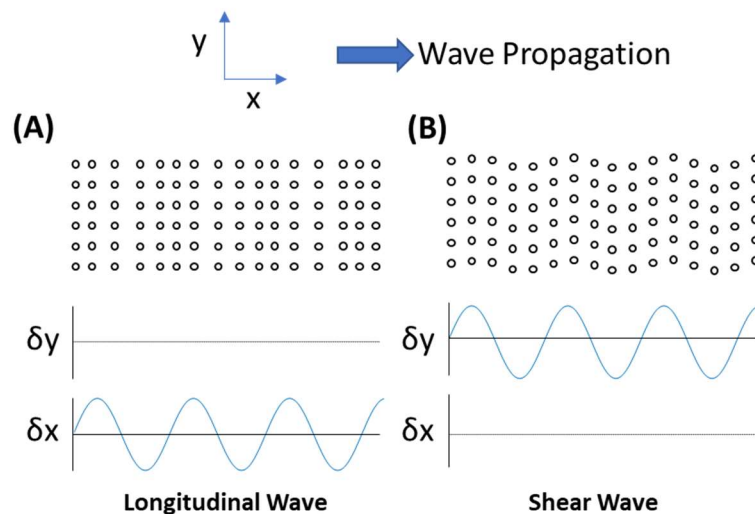


Figure 12 Depiction of (A) Longitudinal and (B) Shear Waves from a Harmonic Oscillator

The speed and amplitude (material displacement in the media, δ) of a propagating wave with a given energy is determined by the mechanical properties of the propagation media. These mechanical properties may be considered as the resistance of the media to deformation from wave forces. It is expedient to consider these waves as a balance of forces experienced by a small voxel of material in relation to its surroundings.

In longitudinal waves, the voxel experiences force normal to its surface in the direction of wave propagation (Figure 13A). In shear waves, the forces are parallel to the voxel face and perpendicular to the direction of wave propagation (Figure 13B).

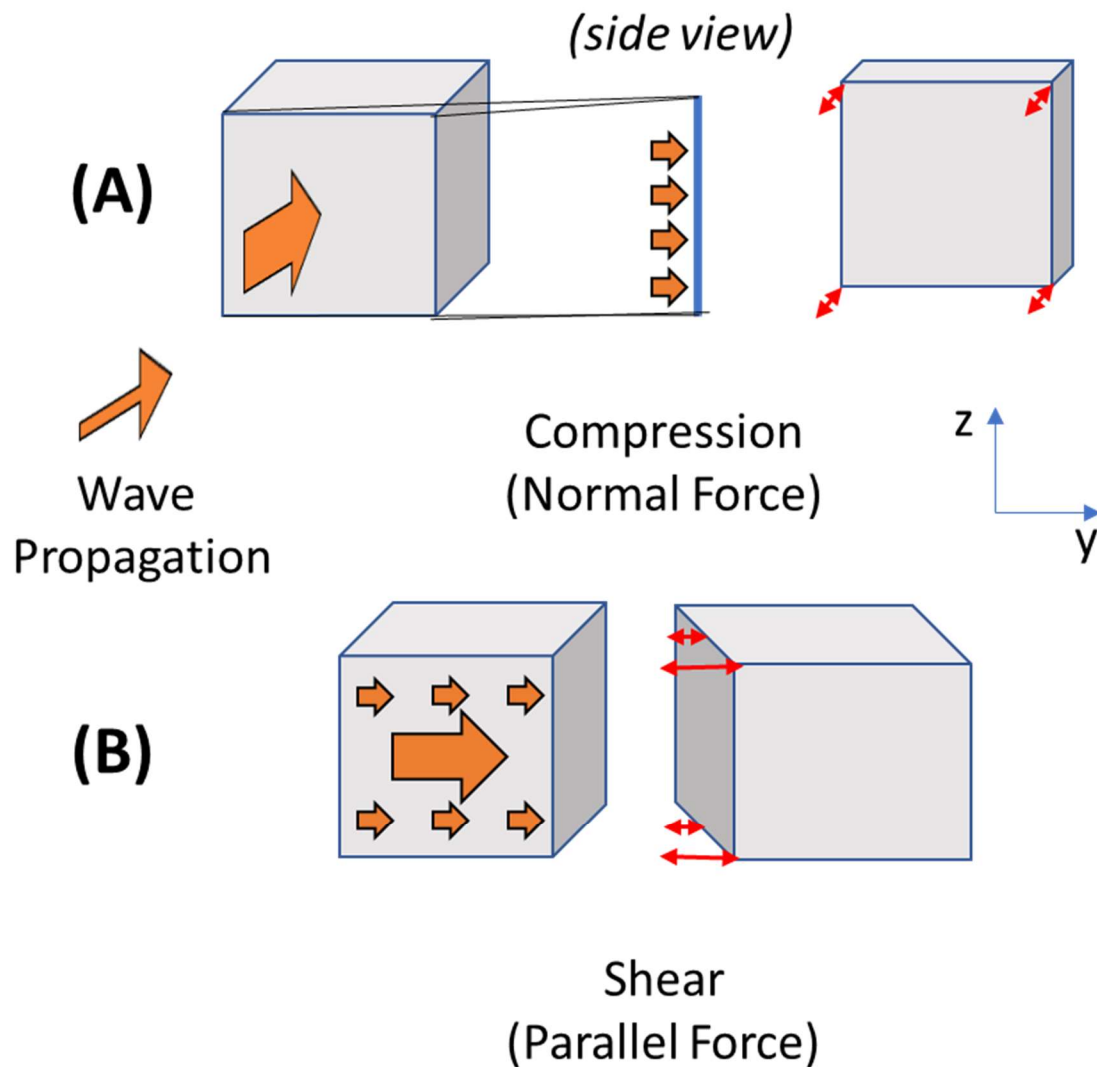


Figure 13 Depiction of response of a voxel of material in response to (A) a normal force and (B) a shear force.

In MRE, the forces applied to tissue are relatively small and do not result change the volume of a voxel of tissue (also called incompressibility). Instead, the tissue is deformed from its original shape. The

degree of deformation is related to the amount of applied force by the elastic moduli of the tissue. This relation is called the stress-strain relation. The strain is the differential of the displacement:

Equation 18: $\epsilon = \nabla \delta$

In two-dimensions, with static shear and normal forces, a voxel is deformed according to:

Equation 19: $\epsilon^{xx} = \frac{1}{E}\sigma^{xx} - \frac{\nu}{E}\sigma^{yy}$

Equation 20: $\epsilon^{yy} = \frac{1}{E}\sigma^{yy} - \frac{\nu}{E}\sigma^{xx}$

Equation 21: $\epsilon^{xy} = -2\mu\sigma^{xy}$

where ϵ_{xx} is the longitudinal strain in the x-direction, ϵ_{yy} is the longitudinal strain in the y-direction, ϵ_{xy} is the shear strain, σ_{xx} is the normal force applied to the x face, σ_{yy} is the normal force applied to the y face, σ_{xy} is the shear force, ν is Poisson's ratio, E is Young's modulus, and μ is the shear stiffness (also called Lamé's second parameter).

These static forces do not represent the standing mechanical waves of MRE, where oscillatory motion is induced until steady-state harmonic motion is observed. This steady-state occurs quickly⁵⁵, and both longitudinal and shear wave motion converge to the time-harmonic Navier-Stokes equation through a balance of the previously presented relations:

Equation 22: $\nabla \cdot (\mu(\nabla \vec{\delta} + \nabla \vec{\delta}^T)) + \nabla(\lambda \nabla \cdot \vec{\delta}) = -\rho \omega^2 \vec{\delta}$

Where ρ is the density and ω is the excitation frequency. The second parenthetical term of this equation is said to be the pressure term, which balances the forces of longitudinal waves.

Young's modulus is related to Lamé's first parameter, λ , with the following relation:

Equation 23: $\lambda = \frac{E\nu}{(1+\nu)(1-2\nu)}$

The speed (c) of longitudinal and shear waves are related to Lamé's parameters in the following manner:

Equation 24: $c_{longitudinal} = \sqrt{(\lambda + 2\mu)/\rho}$

Equation 25: $c_{shear} = \sqrt{\mu/\rho}$

It can be seen from these relations that longitudinal waves always travel faster than shear waves.

Importantly, this relationship between mechanical parameters and wavespeed is the basis of MRE: by measuring the wavespeed in tissue it is possible to estimate the material properties. Wavelength is related to both the wavespeed and frequency (which are material and input parameters, respectively).

Equation 26: $wavelength = \frac{c}{f}$

In Equation 26, the Greek letter lambda is not used for wavelength as it has already been designated as Lamé's first parameter.

In MRE, the tissue parameter of interest is usually the shear stiffness (μ). The reason for this is practical: for harmonic wave motion with frequencies that are compatible with MRI acquisition, shear waves travel at speeds such that the resulting wavelength is on the order of cm. This makes measurement of local wavelength across MR voxels feasible and allows estimation of shear stiffness. The speed of longitudinal waves is much greater, and the resulting long wavelengths make local wavelength measurement difficult.

Thus far, relations have been shown which describe mechanical waves in a solid material that is incompressible, elastic, and isotropic with respect to its mechanical properties. Although tissue is nearly incompressible, the other assumptions do not hold up as well.

Most tissues exhibit both elastic and viscous characteristics and may be described as viscoelastic. Their viscosity arises from the partial liquidity of tissue, which attenuates shear waves by

dissipating wave energy into fluid motion. Several rheological models of viscoelasticity have been proposed for MRE⁵⁶.

Anisotropic structure in tissue, such as that of white matter, also leads to anisotropic material properties^{57,58}.

MRE Acquisition

The purpose of acquisition in MRE is to induce and visualize mechanical waves. This occurs in 2 steps:

(1) Harmonic wave motion is induced through oscillation of a mechanical driver

To induce harmonic wave motion, an oscillating driver is coupled to the surface of the patient at or near the area of interest. This driver must be MRI compatible. Modern drivers have been developed to apply motion passively. This is accomplished by connecting the driver paddle to a sound wave generator via a pneumatic tube. The sound wave generator can then be placed away from the scanner. It is important to couple the passive driver well to the patient and near the anatomy of interest to ensure good wave penetration.

(2) MRI phase is sensitized to motion and wave images are acquired

Bipolar MEGs are synchronized with the frequency cycle of the driver and applied before readout to alter the MRI phase according to tissue motion. The relationship for this process is as follows:

Equation 27:
$$\phi(\vec{r}, \theta) = \frac{\gamma NT(\vec{G} \cdot \vec{\xi}_0)}{2} \cos(\vec{k} \cdot \vec{r} + \theta)$$

where ϕ is the MRI phase, r is the position vector of the spins, θ is the MEG offset from motion cycle, γ is the gyromagnetic ratio, N is the number of bipolar MEGs, T is the period of one motion cycle, G is the gradient amplitude, ξ is the maximum displacement, and k is the wave number. Depiction of these components in a pulse sequence diagram can be seen in Figure 14.

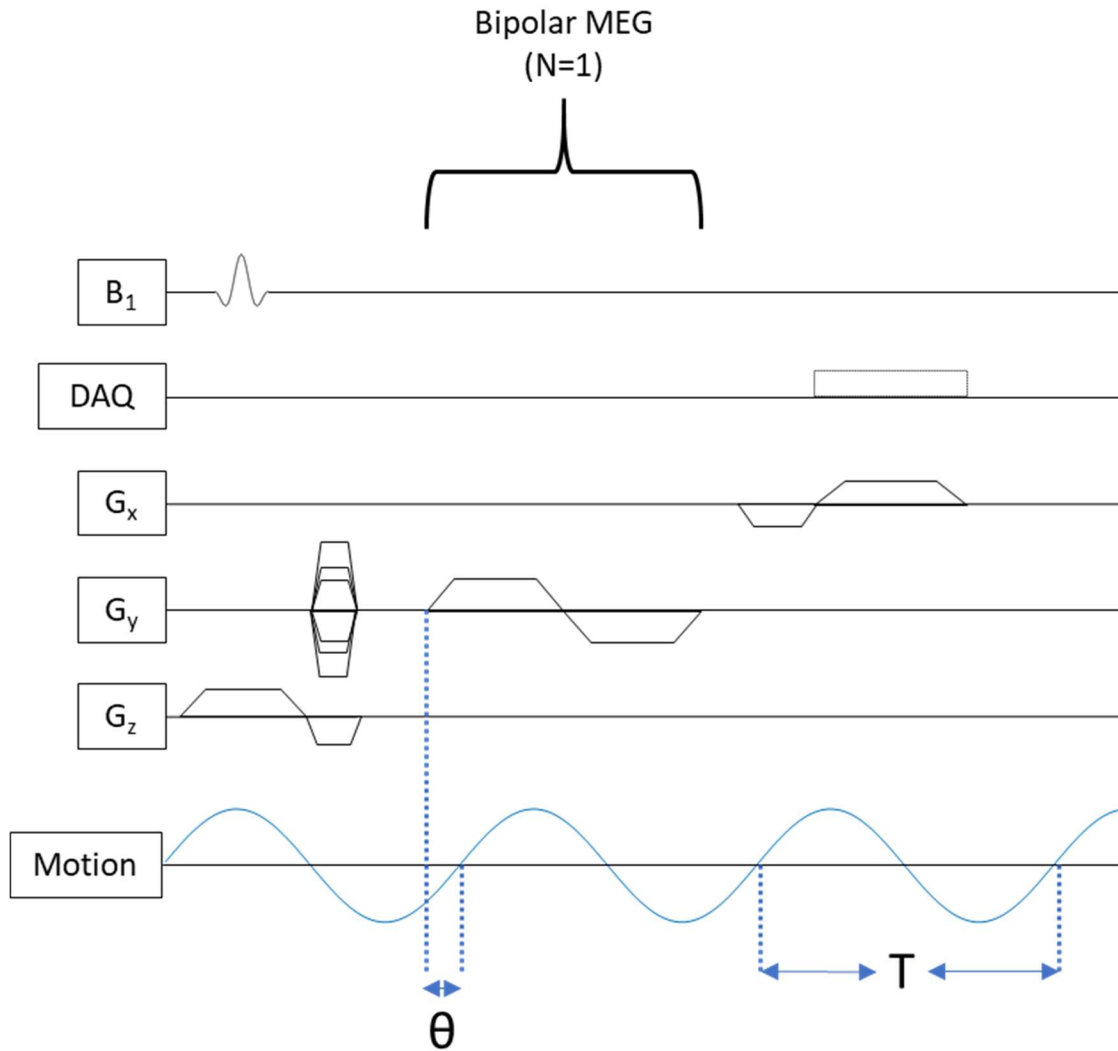


Figure 14 Pulse sequence diagram for MRE with a GRE sequence. Simplified 1-1 bipolar MEGs are shown.

MRE can detect motion on the order of hundreds of nm. It is typically used with displacements on the order of 10-100 μm . Acquisitions image harmonic waves with several frequency offsets and with different MEG directions. Additionally, each individual offset will be re-acquired with reversed MEG encoding and subtracted to remove underlying phase errors due to inhomogeneities.

After imaging in this manner using a fast acquisition sequence, the resulting phase images are called wave images. Examples of wave images for a homogenous gel phantom are shown in Figure 15.

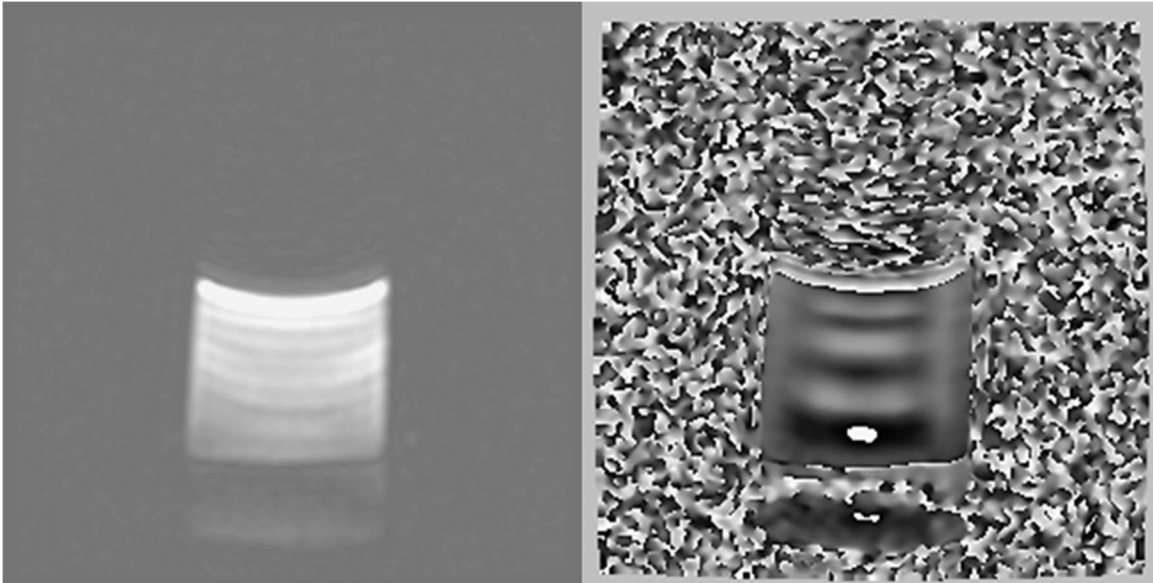


Figure 15 Examples of MRE wave images for a homogenous gel phantom. T1-weighted magnitude image (left) and the corresponding MRE phase image sensitized to motion in the y-direction (right) are shown.

Finally, it is possible to acquire MRE across multiple frequencies or with mismatched MEG and excitation frequencies in so-called partial encoding. This advanced work is beyond the scope of this dissertation.

MRE Inversion

After wave images are obtained, the underlying material properties may be estimated through a process called inversion. This is referred to as the inversion problem because it requires finding the inverse solution to the Navier-Stokes equation (Equation 22). Instead of the forward problem, which would solve for the variables of a differential equation from its coefficients and boundary conditions, the coefficients are inverted from the measured variables (displacement) and assumed boundary conditions.

Different inversion methods are summarized well in a review by Fovargue et al⁵⁹. They suggest a useful phylogeny for MRE inversion algorithms according to their method for reaching a solution: iterative or direct.

Iterative inversion algorithms repeatedly solve the forward problem in an attempt to converge on mechanical properties that minimize error between estimated and acquired displacements across the domain^{60,61}. These methods typically designate various boundary conditions and construct of a discretized model of the system, such as with finite element methods (FEM). The underlying material properties are then converged upon through a variational method. More elaborate iterative models have been suggested, with advanced rheological models and discretization methods⁶². Iterative models are computationally expensive and may take a long time to run⁵⁹.

Direct inversion algorithms attempt to directly solve for stiffness on a local region of the acquired wave image. This may also involve numeric discretization techniques such as FEM for calculating local derivatives. The action of direct inversion algorithms may be described as the use of discrete kernels to calculate local derivatives. These derivatives may then be used to solve of measured displacements to solve for the shear stiffness of an individual voxel⁵⁹:

Equation 28:
$$\mu = \frac{-\rho\omega(\vec{\nabla}\delta)^T\vec{\delta}}{(\vec{\nabla}\delta)^T(\vec{\nabla}\delta)}$$

For direct inversion, some algorithms simply ignore the pressure term from longitudinal waves (Equation 28). Alternatively, some algorithms take the curl of the image before processing⁵⁹. This has the effect of eliminating the pressure term and isolating shear waves. However, applying the curl is an additional derivative and therefore further decreases SNR.

Another direct method, called Local Frequency Estimation (LFE), has also been used⁵⁹. This method leverages the differential response to two spatial filters to estimate the local wavelength and thereby estimate the underlying tissue stiffness⁶³.

Several k-space filtering techniques have also been proposed and applied in direct inversion⁶⁴. These methods seek to isolate portions of k-space with spatial frequencies corresponding to shear wave wavelengths, thereby emphasizing the contrast of interest for parameter estimation.

1.5 MRI of TNBC

Clinically, MRI of TNBC is interpreted by radiologists in a framework shared by all breast cancers. Qualitative assessment of breast cancers on MRI shows TNBC to have a unique image phenotype. This phenotype has also been observed in research studies with advanced MRI modalities and analyses. Because of this, MRI biomarkers proposed for use in breast cancer may require validation or adjustment for the TNBC subtype. This section first explains clinical MRI assessment of TNBC. This is followed by review of literature which compares image biomarkers between IHC subtypes, suggesting a unique image phenotype for TNBC. Finally, proposed MRI biomarkers of treatment response in TNBC are reviewed.

Studies comparing MRI biomarkers between the intrinsic molecular subtypes of breast cancer (Luminal A, Luminal B, etc.) are not included.

1.5.1 Clinical MRI of TNBC Subtype

Through field-wide efforts, radiologist interpretation of clinical breast MRI has been standardized under a definitive framework called the Breast Imaging Reporting and Data System (BIRADS)⁶⁵. (*Readers already familiar with BIRADS should skip to Table 5*). Because this dissertation concerns treatment response, this section ignores application of BIRADS for breast cancer screening and instead focuses on diagnostic application of BIRADS.

In its current fifth edition, BIRADS specifies the basic imaging protocol, defines sequential steps for interpretation and documentation, and standardizes image features (also called “signs”) into categories. The imaging protocol should include at least a bright-fluid sequence (Ex: T2-weighted FSE) and a GBCA contrast-enhanced spoiled GRE sequence with pre- and post-contrast imaging. Ideally, fat suppression should be applied for both sequences. After imaging, interpretation should take a series of steps.

After recognizing and documenting a patient's clinical history, the radiologist should visually estimate the breast composition in terms of the amount of fibroglandular tissue (FGT). This is highly variable between patients and should be classified as one of four ordinal categories: (1) Almost entirely fat, making up 10% of female breasts, (2) scattered FGT, making up 40% of female breasts, (3) heterogeneous FGT, making up 40% of female breasts, and (4) extreme FGT, making up 10% of female breasts⁶⁵. Younger and premenopausal patients are more likely to have a higher FGT breast composition⁶⁶.

FGT should then be considered for its enhancement during the contrast-enhanced sequence, which is referred to as background parenchymal enhancement (BPE). BPE is also divided into four ordinal categories: (1) Minimal, (2) Mild, (3) Moderate, and (4) Marked. BPE fluctuates with hormone levels and is mediated by menstrual cycle stage⁶⁷, hormone-replacement therapy⁶⁸, and age⁶⁹. Women with higher BPE have a higher risk of breast cancer^{70,71}.

Breast composition and BPE are important to note in interpretation because of their impact on diagnostic exams: higher FGT composition breasts have poorer image contrast on mammography and high BPE lessens contrast between FGT and enhancing pathology in contrast-enhanced breast MRI.

After classifying breast composition and BPE, the breasts, chest wall, and axilla are examined for abnormalities. Reports of abnormal findings should include lesion type (mass, non-mass enhancement, multi-focal disease), image artifacts, tissues invasion (chest wall, skin, etc.), abnormal lymph nodes, and other breast cancer associated features.

Masses are described by three types of modifiers: shape, margin, and internal enhancement characteristics. Mass shape may be oval, round, or irregular. Mass margins may be smooth, irregular, or spiculated. Mass internal enhancement may be homogenous, heterogeneous, or show rim enhancement. Visual depiction of these modifiers may be seen in the MRI BIRADS atlas⁶⁵.

It has also become common to report intra-tumoral high signal intensity on T2 (which corresponds to intra-tumoral necrosis⁷²) and high T2 signal intensity in the peritumoral region (which corresponds to peritumoral edema). Other imaging signs are also required in BIRADS, but their frequency is too low to support subtype comparisons.

Each breast cancer IHC subtypes may present with any of the listed clinical MRI signs and categories. However, several reports have compared distributions of these signs between IHC subtypes and found TNBC to have a unique distribution. These results are summarized in Table 5.

Table 5 Distinct TNBC clinical MRI features presented in literature

Image Feature	Distinct in TNBC Relative to other IHC Subtype?	N	Source
Breast Composition			
	Lower FGT more likely	2995 (225 TNBC)	⁷³ Mema et al. 2020
		214 (37 TNBC)	⁷⁴ Huang et al. 2020
	No difference	62 (31 TNBC)	⁷⁵ Angelini et al. 2018*
BPE			
	Lower more likely	2995 (225 TNBC)	⁷³ Mema et al. 2020
	No difference	62 (31 TNBC)	⁷⁵ Angelini et al. 2018*
		81 (15 TNBC)	⁷⁶ Kim et al. 2015
Mass vs. NME			
	Mass-only more likely	267 (24 TNBC)	⁷⁷ Dogan et al. 2018
		219 (69 TNBC)	⁷⁸ Negrão et al. 2019
		62 (31 TNBC)	⁷⁵ Angelini et al. 2018
		176 (59 TNBC)	⁷² Uematsu et al. 2009
		214 (37 TNBC)	⁷⁴ Huang et al. 2020
		200 (36 TNBC)	⁷⁹ Du et al. 2021
Mass Shape			
	Round/oval more likely	267 (24 TNBC)	⁷⁷ Dogan et al. 2018
		200 (36 TNBC)	⁷⁹ Du et al. 2021
Mass Margin			
	Circumscribed more likely	267 (24 TNBC)	⁷⁷ Dogan et al. 2018
		224 (39 TNBC)	¹³ Öztürk et al. 2020
		176 (59 TNBC)	⁷² Uematsu et al. 2009
Rim Enhancement			
	More likely	224 (39 TNBC)	¹³ Öztürk et al. 2020
		62 (31 TNBC)	⁷⁵ Angelini et al. 2018
		176 (59 TNBC)	⁷² Uematsu et al. 2009

		200 (36 TNBC)	⁷⁹ Du et al. 2021
Contrast kinetics			
	Washout more likely	224 (39 TNBC)	¹³ Öztürk et al. 2020
		176 (59 TNBC)	⁷² Uematsu et al. 2009
	Persistent more likely	176 (59 TNBC)	⁷² Uematsu et al. 2009
		214 (37 TNBC)	⁷⁴ Huang et al. 2020
Unifocal			
	More likely	224 (39 TNBC)	¹³ Öztürk et al. 2020
		62 (31 TNBC)	⁷⁵ Angelini et al. 2018
		176 (59 TNBC)	⁷² Uematsu et al. 2009
Intra-tumoral T2w Signal			
	High signal more likely	224 (39 TNBC)	¹³ Öztürk et al. 2020
		62 (31 TNBC)	⁷⁵ Angelini et al. 2018
		267 (24 TNBC)	⁷⁷ Dogan et al. 2018
		249 (24 TNBC)	⁸⁰ Yuen et al. 2020
Peritumoral Edema			
	More likely	294 (86 TNBC)	⁸¹ Song et al. 2017
		225 (77 TNBC)	⁸² Constantini et al. 2012

*Note: ⁷⁵Angelini et al. used an alternative categorization method for breast composition and BPE classification.

1.5.2 Semi-quantitative and Quantitative MRI - TNBC Subtyping

Semi-quantitative and quantitative MRI measurements have been proposed for a variety of applications in breast cancer medicine. These measurements are not standardized for widespread clinical use and therefore cannot be handily summarized in a single table like qualitative image signs. Scan protocols, measurement ROIs (whole tumor, single slice, etc.), parametric models, parameter estimation methods, and measurement methods (average, histogram metrics, radiomics, etc.) may impact results and are heterogeneous between these studies.

Measurements from the tumor, peritumoral region, and background parenchyma have been investigated for differences between IHC subtypes. Summaries of the literature investigating IHC subtype distinctions from these measurements are shown below. TNBC phenotype differences observed

in pursuit of the prediction of treatment response are reserved for section 1.5.3 *MRI for Early Prediction of Treatment Response in TNBC*.

DCE MRI

On semiquantitative DCE MRI, one study found that TNBC has higher MS^{83} in comparison to other IHC subtypes. Other studies have not shown a difference on semi-quantitative DCE in TNBC as compared with other subtypes^{76,84}.

Differentiation of IHC subtypes with PK analysis of tumors is controversial, with some studies indicating higher k_{ep} and lower v_e in TNBC, while others do not show a difference in PK parameters between subtypes. These literature findings are summarized in Table 6.

Table 6 Summary of literature findings for TNBC subtyping with PK analysis from DCE MRI

Finding	Patients	Study
K_{trans}		
No difference	200 (36 TNBC)	⁷⁹ Du et al. 2021
	37 (16 TNBC)	⁸⁵ Li et al. 2011
	68 (20 TNBC)	⁸⁶ Koo et al. 2012
	214 (37 TNBC)	⁷⁴ Huang et al. 2020
	81 (15 TNBC)	⁷⁶ Kim et al. 2015
K_{ep}		
Higher in TNBC	37 (16 TNBC)	⁸⁵ Li et al. 2011
	68 (20 TNBC)	⁸⁶ Koo et al. 2012
No difference	200 (36 TNBC)	⁷⁹ Du et al. 2021
	214 (37 TNBC)	⁷⁴ Huang et al. 2020
	81 (15 TNBC)	⁷⁶ Kim et al. 2015
v_e		
Lower in TNBC	37 (16 TNBC)	⁸⁵ Li et al. 2011
	68 (20 TNBC)	⁸⁶ Koo et al. 2012
No difference	200 (36 TNBC)	⁷⁹ Du et al. 2021
	214 (37 TNBC)	⁷⁴ Huang et al. 2020
	81 (15 TNBC)	⁷⁶ Kim et al. 2015

Differences between these studies might be attributed to differences in methods (DCE protocol, analysis software, AIF, etc.) and patient populations⁸⁷. However, the variable findings in Table 6 could also be expected based on the studies summarized in Table 5, which found that TNBC was more likely to show washout and persistent enhancement patterns relative to other IHC subtypes. The basic enhancement patterns hold information related to PK parameters⁸⁸, but the washout pattern and persistent pattern (both shown as more likely in TNBC relative to other IHC subtypes) would contribute inversely to PK coefficients. This would likely result in a wide range of PK parameters within TNBC as compared to other IHC subtypes.

Only one study has examined DCE MRI parameters of BPE for breast cancer subtyping. Kim et al. found that DCE parameters measured in FGT of the affected breast (ipsilateral parenchyma) were not different between TNBC and other IHC subtypes, although higher k_{trans} and lower $iAUC_{1-minute}$ was seen for the ipsilateral parenchyma of HER2-negative cancers⁷⁶.

Several groups have shown that DCE MRI radiomics of the tumor hold promise for differentiating IHC subtypes⁸⁹⁻⁹¹.

DWI MRI

A large body of work has been presented comparing biomarkers from diffusion weighted imaging between tumors of different breast cancer IHC subtypes. Average tumor ADC from the monoexponential model of diffusion has been shown by several groups to have broad overlap between IHC subtypes and is not useful for breast cancer subtyping on its own^{79,92-94}.

Intravoxel Incoherent Motion (IVIM), a diffusion model which includes additional parameters to account for greater signal loss at lower b-values from intravoxel capillary perfusion motion, has also been applied for TNBC subtyping. One study by Uslu et al. with 51 patients (11 TNBC) found that the perfusion contribution to low b-value signal loss in tumors was significantly lower in TNBC⁹⁵. They did

not find a difference in ADC between tumors of different IHC subtypes. The findings on perfusion contribution were paralleled by Zhao et al.; however, Zhao et al. additionally found that ADC from the IVIM model was lower in TNBC⁹⁶.

Several groups have examined radiomic features from the tumor on ADC maps for discrimination of TNBC subtype with varying results. Wang et al. examined histogram measures as well as 2nd and 3rd order radiomics from ADC maps of the entire tumor and found that TNBC could be discriminated from other subtypes with radiomic measures of intra-tumor heterogeneity and shape⁹². Leithner et al. found that 2nd order radiomic features from ADC and DCE MRI were good discriminants of the TNBC subtype from other IHC subtypes⁹⁷. However, in another report using ADC alone, Leithner et al. did not find a unique radiomic signature which could distinguish the TNBC subtype⁹⁸.

A summary of DWI in the peritumoral region of breast cancers is presented in *Chapter 4 – Quantitative Apparent Diffusion Coefficients from Peritumoral Regions as Early Predictors of Treatment Response to Neoadjuvant Systemic Therapy in Triple Negative Breast Cancer*.

MRE

MRE of breast cancer is not yet widely used. No studies yet exist which have compared MRE-measured tissue stiffness between breast cancer IHC subtypes.

A review of MRE in breast cancer can be found in *5.1.1 Magnetic Resonance Elastography in Cancer*.

1.5.3 MRI for Early Prediction of Treatment Response in TNBC

While a large number of MRI biomarkers have been proposed for early prediction of response in all-comers breast cancers, there are several papers which specifically investigate TNBC or contain IHC subtype analyses. Some biomarkers that show utility for early prediction of response in other subtypes have failed to show value for TNBC⁹⁹⁻¹⁰¹.

This section specifically reviews studies applying MRI for early prediction of pCR vs. non-pCR at surgery (i.e. only biomarkers assessed on pretreatment or mid-treatment MRI). Because prediction of pCR vs. non-pCR is a binary outcome, some of the following results will be expressed in Area Under the receiver operating Curve (AUC).

Qualitative Interpretation on Clinical MRI

Lineal measurements of tumor size on midtreatment clinical MRI shows good performance for early prediction of response in TNBC, with AUCs reported from 0.7 to 0.84¹⁰²⁻¹⁰⁸.

Visual assessment of necrosis and peritumoral edema have also been suggested as early predictors of response. These are reviewed in greater detail in *Chapter 2 – Tumor Necrosis by Pretreatment Breast MRI: Association with Neoadjuvant Systemic Therapy Response in Triple-negative Breast Cancer* and *Chapter 4 – Quantitative Apparent Diffusion Coefficients from Peritumoral Regions as Early Predictors of Treatment Response to Neoadjuvant Systemic Therapy in Triple Negative Breast Cancer*, respectively.

BPE, scored visually on DCE MRI, did not show promise for early prediction of treatment response in TNBC in one study¹⁰⁹.

DCE MRI

DCE MRI is most popularly used for the prediction of response in breast cancer in the form of Functional Tumor Volume (FTV). In this measurement, DCE enhancement curves are leveraged to find voxels matching DCE pattern I and their combined volume is used to predict response. FTV shows good performance for early prediction of response in TNBC and may be optimized for different IHC subtypes. This is discussed at length in *Chapter 3 – Functional Tumor Volume by Fast Dynamic Contrast-Enhanced MRI for Predicting Neoadjuvant Systemic Therapy Response in Triple-Negative Breast Cancer*.

In a brilliant report by Braman et al. that investigated intra- and peri- tumoral radiomics on pretreatment DCE MRI, TNBC was found to have a unique radiomic signature for predicting response¹¹⁰. This report showed cross-validated AUC of 0.93 for prediction of response in 47 TNBC patients. Another study examining intra-tumoral radiomics on DCE MRI found mediocre performance (AUC=0.68) from the pretreatment scan, though the radiomic methods were quite different in comparison to Braman et al.

In the ISPY-2 multicenter trial, quantitative BPE did showed mediocre performance for early prediction of response in TNBC¹⁰¹.

DWI

In the large, multicenter trial I-SPY 2, ADC did not show value for early prediction of response in TNBC (354 patients, 132 TNBC)⁹⁹. This was also seen in a separate study¹¹¹.

ADC of the peritumoral region for predicting treatment response is discussed in *Chapter 4 – Quantitative Apparent Diffusion Coefficients from Peritumoral Regions as Early Predictors of Treatment Response to Neoadjuvant Systemic Therapy in Triple Negative Breast Cancer*.

Combined Modalities

In the large, multicenter trial, I-SPY 2, ADC did not show added value to FTV for the early prediction of response in TNBC (354 patients, 132 TNBC)⁹⁹. Combination of FTV, longest tumor diameter, tumor sphericity (a 3D shape radiomic), and BPE showed improve prediction of response in TNBC as compared to FTV alone, though their individual contributions to the model were not reported¹⁰¹.

Liu et al. found that radiomics from T2-weighted images, ADC maps and contrast-enhanced MRI at pretreatment showed good performance for prediction of pCR (AUC>0.8) in several independent TNBC validation sets¹¹². They also found that a combined predictor from these modalities improved AUC across all IHC subtypes, however, they did not report if multi-modality prediction was specifically

important for TNBC. Another report investigated radiomics from T2-weighted imaging and contrast-enhanced MRI and found they were only useful for predicting response in non-TNBC breast cancers¹⁰⁰.

1.6 Hypothesis and Specific Aims

1.6.1 Hypothesis

Quantitative imaging biomarkers from magnetic resonance imaging acquired early during treatment are predictive of treatment response in triple negative breast cancer.

1.6.2 Specific Aim 1 (SA1)

(SA1) Develop analysis techniques for measurement of imaging biomarkers in breast cancer.

SA1.1: Develop quantitative DWI and semi-quantitative DCE biomarker measurements for assessment of TNBC intra-tumoral necrosis.

SA1.2: Develop methods for measurement of functional tumor volume (FTV) by fast DCE MRI in TNBC.

SA1.3: Develop measurement techniques for DWI-based biomarkers of peritumoral edema in TNBC.

SA1.4: Develop a convolutional neural network-based algorithm for wave image inversion in magnetic resonance elastography.

1.6.3 Specific Aim 2 (SA2)

(SA2) Validate imaging biomarkers in triple negative breast cancer patients.

SA2.1: Apply DWI and DCE biomarkers of necrosis in a retrospective cohort of TNBC patients and test for association with pCR.

SA2.2: Apply improved FTV measurements for discrimination of response in a prospective cohort of TNBC patients.

SA2.3: Apply DWI-based assessments of peritumoral edema in a prospective cohort of TNBC patients and test for discrimination of treatment response.

SA2.4: Validate novel MRE inversion algorithm by comparing stiffness measurements between breast tissue types in MRE of TNBC.

Chapter 2 – Tumor Necrosis by Pretreatment Breast MRI: Association with Neoadjuvant Systemic Therapy Response in Triple-negative Breast Cancer

This chapter is based upon the following article, published in Breast Cancer Research and Treatment¹¹³:

*Abdelhafez AH, *Musall BC, Adrada BE, Hess K, Son JB, Hwang KP, Candelaria RP, Santiago L, Whitman GJ, Le-Petross HT, Moseley TW, Arribas E, Lane DL, Scoggins ME, Leung JWT, Mahmoud HS, White JB, Ravenberg EE, Litton JK, Valero V, Wei P, Thompson AM, Moulder SL, Pagel MD, Ma J, **Yang WT, **Rauch GM. **Tumor necrosis by pretreatment breast MRI: association with neoadjuvant systemic therapy (NAST) response in triple-negative breast cancer (TNBC).** *Breast cancer research and treatment* 2020. doi: 10.1007/s10549-020-05917-7

*Dual first-author

**Dual last-author

2.1 Abstract [Necrosis for TNBC Response]

Purpose: To determine if tumor necrosis by pretreatment breast MRI and its quantitative imaging characteristics are associated with response to NAST in TNBC.

Methods: This retrospective study included 85 TNBC patients (mean age 51.8 ± 13 years) with MRI before NAST and definitive surgery during 2010–2018. Each MRI included T2-weighted, diffusion-weighted (DWI), and dynamic contrast-enhanced (DCE) imaging. For each index carcinoma, total tumor volume including necrosis (TTV), excluding necrosis (TV), and the necrosis-only volume (NV) were segmented on early-phase DCE subtractions and DWI images. NV and %NV were calculated. Percent enhancement on early and late phases of DCE and apparent diffusion coefficient were extracted from

TTV, TV, and NV. Association between necrosis with pathological complete response (pCR) was assessed using odds ratio (OR). Multivariable analysis was used to evaluate the prognostic value of necrosis with T stage and nodal status at staging. Mann-Whitney U-tests and area under the curve (AUC) were used to assess performance of imaging metrics for discriminating pCR vs. non-pCR.

Results: Of 39 patients (46%) with necrosis, 17 had pCR and 22 did not. Necrosis was not associated with pCR (OR, 0.995; 95% confidence interval [CI], 0.4-2.3), and was not an independent prognostic factor when combined with T stage and nodal status at staging ($P = .46$). None of the imaging metrics differed significantly between pCR and non-pCR in patients with necrosis ($AUC < 0.6$ and $P > .40$).

Conclusion: No significant association was found between necrosis by pretreatment MRI or the quantitative imaging characteristics of tumor necrosis and response to NAST in TNBC.

Keywords: Triple Negative Breast Cancer, Multiparametric MRI, Necrosis, Diffusion Weighted MRI, Neoadjuvant Therapy

2.2 Introduction [Necrosis for TNBC Response]

Triple-negative breast cancer (TNBC) accounts for approximately 20% of all breast cancers and is a subtype of breast cancer that lacks estrogen receptor, progesterone receptor, and HER2 expression¹¹⁴. Compared with other breast cancer subtypes, TNBC is more aggressive and is associated with a higher rate of relapse and a lower rate of overall survival^{109,115}. Patients with TNBC usually undergo neoadjuvant systemic therapy (NAST) for downstaging of disease to facilitate less invasive surgery. The extent of downstaging is used as a surrogate prognostic marker. Despite recent advances in breast cancer diagnosis and treatment, patients with TNBC tend to have a poor prognosis, with highly divergent response to treatment. Excellent response to NAST is seen in about half of the TNBC patients undergoing the treatment but weak or absent in the others^{109,114,116}.

Although still controversial, tumor necrosis detected at the histopathological evaluation has been proposed as a marker of poor prognosis in a variety of solid-organ malignancies¹¹⁷. A few studies have showed an association between tumor necrosis and poor treatment response and lower overall survival in colorectal and non-small cell lung cancer^{118,119}. However, such an association was not seen in renal cell carcinoma¹²⁰. In breast cancer studies that included all hormonal subtypes, conflicting findings have been reported. One study showed that the presence of tumor necrosis correlated with tumor grade¹²¹. Two studies showed that the presence of tumor necrosis was associated with aggressiveness and unfavorable long-term outcomes^{122,123}, while two other studies showed that the presence of tumor necrosis was associated with improved response to chemotherapy^{124,125}. Two additional studies showed no direct association between tumor necrosis and prognosis^{126,127}.

Compared to other breast cancer subtypes, TNBC is more likely to display necrosis with a reported incidence ranging from 35% to 56%^{72,128}. The propensity for necrosis in TNBC may be due to the tumor's aggressiveness (most TNBCs are of high grade) and increased mitotic activity (with high expression of proliferation marker Ki-67), characteristics that result in tumors outgrowing their blood supplies¹²⁹⁻¹³². Tumor necrosis in TNBC has been evaluated on MR imaging in prior studies^{72,109,133}, as MRI can provide a comprehensive evaluation of the tumor and the accompanying necrosis on the basis of their often vastly different diffusion, perfusion and T2 relaxation characteristics. However, few studies have evaluated tumor necrosis in TNBC as an independent prognostic factor and predictor of response to NAST^{109,133}. In prior MRI-based studies of the association between tumor necrosis and tumor response to NAST, necrosis was assessed qualitatively based on a single slice of T2-weighted imaging^{109,133}.

The objective of our study is to determine if tumor necrosis determined by pretreatment breast MRI and the quantitative imaging characteristics of tumor necrosis are associated with response to NAST in patients with TNBC.

2.3 Methods [*Necrosis for TNBC Response*]

Patients

This retrospective study was conducted in compliance with the Health Insurance Portability and Accountability Act. Institutional Review Board approval was obtained and written informed consent was waived. A single institutional research database was searched to identify adult women (age ≥ 18 years) with pathologically proven stage I-III TNBC (ER, PR, HER-2 negative) who underwent pretreatment breast MRI and NAST followed by definitive surgery during the period from April 2010 through December 2018 (Figure 16).

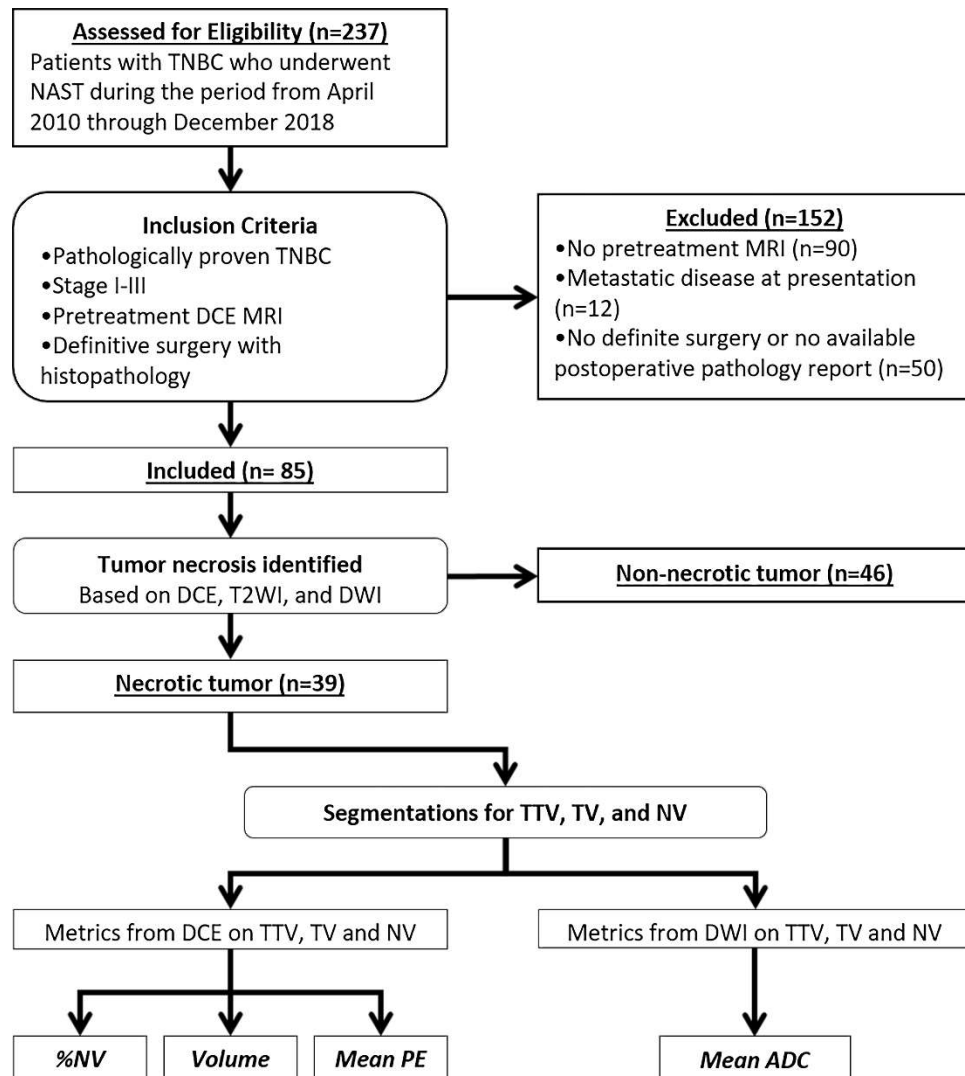


Figure 16 Inclusion criteria and assignment of analysis for each group.

Note – ADC = apparent diffusion coefficient, DCE = dynamic contrast-enhanced imaging, DWI = diffusion-weighted imaging, NAST = neoadjuvant systemic therapy, NV = necrosis-only volume, PE = percent enhancement, T2WI = T2-weighted imaging, TNBC = triple negative breast cancer, TTV= total tumor volume including necrosis, TV = tumor volume without necrosis

MRI acquisition

All MRI studies were performed at our institution using MRI scanners that were approved for clinical breast MRI. These included 1.5T scanners (Signa HDxt and Optima MR450w, GE Healthcare Technologies, Waukesha, WI) and 3T scanners (Signa Discovery MR750w, GE Healthcare Technologies, Waukesha, WI; Magnetom Skyra, Siemens Healthineers, Erlangen, Germany). All examinations were acquired with the patients in a prone position using dedicated eight-channel breast coils. The MRI protocol included bilateral axial non-contrast T1-weighted, axial fat-suppressed T2-weighted, pre-contrast axial diffusion-weighted imaging (DWI), axial dynamic contrast enhanced (DCE) pre-contrast and post-contrast fat-suppressed T1-weighted, and delayed post-contrast sagittal fat-suppressed T1-weighted imaging.

DCE imaging was performed with the following parameters: temporal resolution, 90-120 seconds; total acquisition time, 6-8 minutes; repetition time, 6.0 ms; echo time, 2.0 ms; flip angle, 10°; slice thickness, 2.5 mm; and matrix, 256-480 x 256-324. Each patient received 0.1 mmol/kg gadobutrol (Gadovist, Bayer HealthCare) intravenously at a rate of 2 cc/s with a power injector. For an adult woman weighing 77 kg (average in the United States), 15 mL of 500 nM gadbuterol would be injected over 7.5 s. Serial subtraction images were generated during post-processing. Maps of percent enhancement (PE) relative to the mask series were calculated for the early phase (PE1) at approximately 60 s after injection and the delayed phase (PE2) at approximately 6 minutes after injection.

Typical scan parameters for DWI were as follows: echo time, 66 ms; repetition time, 7500 ms; flip angle, 90°; slice thickness, 5 mm; and matrix, 128 x 128. At least two b-values were used, with the lowest b-value ranging from 0 s/mm² to 100 s/mm² and the highest b-value ranging from 800 s/mm² to 1000 s/mm². Apparent diffusion coefficient (ADC) maps were calculated from DWI using a mono-exponential model.

MRI interpretation and segmentation

The largest lesion identified on DCE images was considered the index carcinoma and was used in our analysis. T stage was determined on the basis of the longest tumor dimension. Axillary lymph node status was assessed at staging by ultrasound-guided biopsy of suspicious lymph nodes and at surgery by pathologic review of the surgical specimen and was classified as positive or negative.

On the basis of the morphologic features on MRI, the index carcinomas were classified as necrotic or non-necrotic. Tumors were classified as necrotic if they displayed all three of the following features by visual assessment: a non-enhancing central or paracentral area on DCE images, hyperintensity of this central area on axial fat-suppressed T2-weighted images, and hyperintensity of this central area on ADC maps (Figure 17).

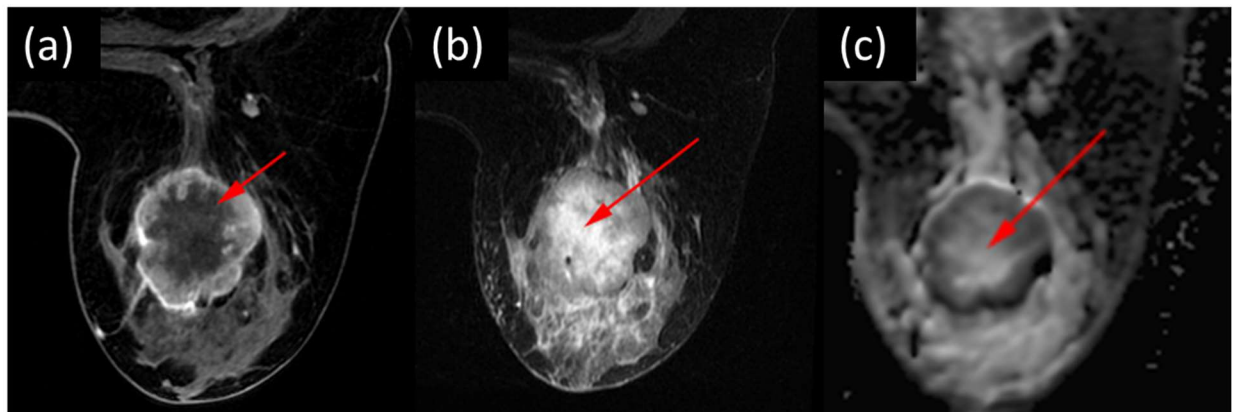


Figure 17 Necrosis in a 35-year-old woman with TNBC of the left breast. (a) Axial fat-suppressed early-phase dynamic contrast-enhanced image shows central non-enhancing area representing necrosis (arrow). (b) Axial fat-suppressed T2-weighted image shows necrosis as central area of high signal intensity (arrow). (c) Axial apparent diffusion coefficient map shows shine-through corresponding to central area of necrosis (arrow) seen on dynamic contrast-enhanced and T2-weighted imaging.

Quantitative image analysis of necrotic carcinomas was performed with Imager, an image visualization and processing software developed in-house. Imager was used for tumor contouring and analyses of a previously published work on esophageal cancer¹³⁴. Among many commonly useful utilities, Imager offers convenient DICOM image import from the patient PACS system, customizable

model fitting of the images, graphical user interface based manual and semi-automatic tumor segmentation and contouring, and easy export of the tumor ROI statistics and quantitative metrics including different radiomics features.

Two breast radiologists, both with at least 5 years of experience in breast MRI interpretation, were blinded to the patient outcome data and performed segmentation encompassing the tumor in all slices. Segmentations were further refined using the histogram thresholding in Imager to exclude voxels that were visually determined to be non-tumor by the radiologist. These segmentations were performed separately on both early DCE subtractions and ADC maps. All segmentations were reviewed and confirmed by both radiologists to avoid inter-reader bias. The segmented regions were the total tumor volume including necrosis (TTV), the tumor volume excluding necrosis (TV), and the necrosis-only volume (NV) (Figure 18).

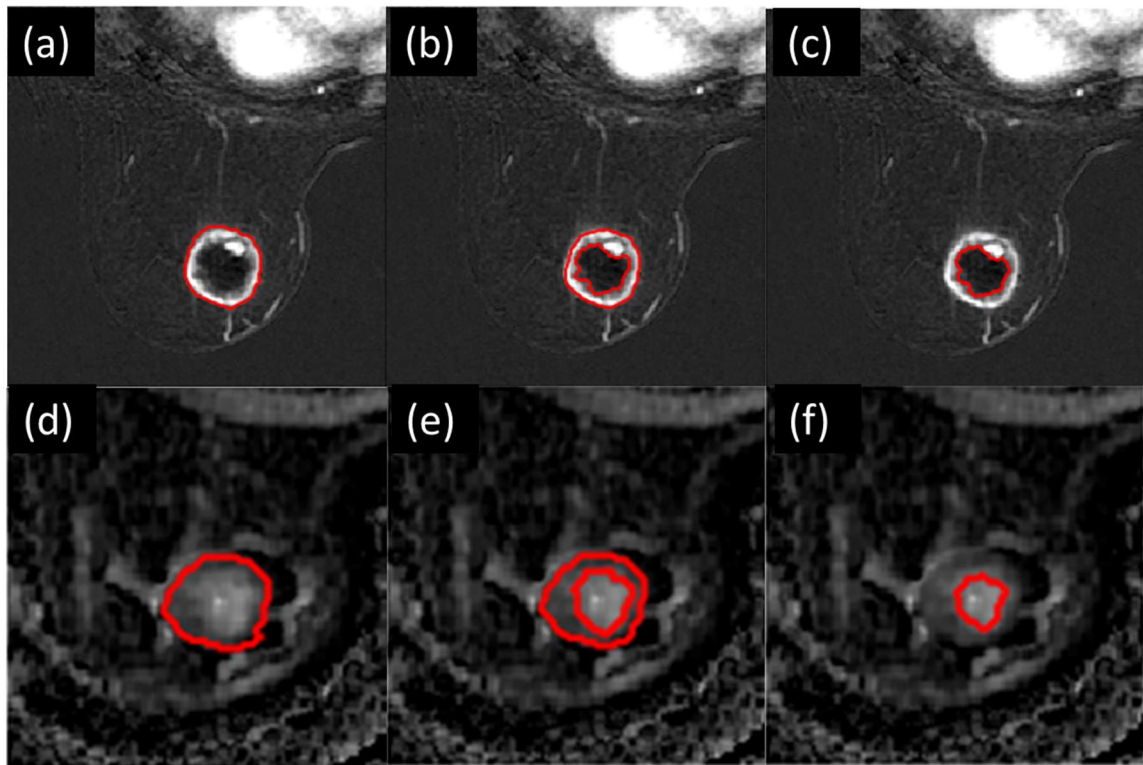


Figure 18 Segmentation technique in a 60-year-old woman with TNBC of the right breast. Axial dynamic contrast-enhanced early phase fat-suppressed images with whole tumor (a), tumor

without necrosis (b), and necrosis only (c) segmentations, as well as corresponding apparent diffusion coefficient maps (d, e, f).

For DCE, TV_{DCE} was manually defined as the fraction of the TTV_{DCE} with visual enhancement, which was assumed to correspond to viable tumor. The $\%NV_{DCE}$ was calculated from the extracted volumes as:

$$\text{Equation 29: } \%NV_{DCE} = 100\% * \frac{NV_{DCE}}{NV_{DCE} + TV_{DCE}}$$

PE1 and PE2 were calculated from voxel signal levels as:

$$\text{Equation 30: } PE1 = 100\% * \frac{S_{\text{early phase}} - S_{\text{mask phase}}}{S_{\text{mask phase}}}$$

$$\text{Equation 31: } PE2 = 100\% * \frac{S_{\text{delayed phase}} - S_{\text{mask phase}}}{S_{\text{mask phase}}}$$

where S is the signal level for each respective phase. Average PE1 and PE2 values were extracted from the tumor ROIs as determined on the early phase DCE images for TTV_{DCE} , TV_{DCE} , and NV_{DCE} .

On DWI, viable tumor tissue was visually identified as areas of restricted diffusion that displayed high signal intensity on high b-value images (i.e., 800 or 1000) with a corresponding low ADC signal intensity. The mean ADC values from TTV_{DWI} , TV_{DWI} , and NV_{DWI} segmentations were calculated. The quantitative ADC analysis was performed on subset of patients with necrotic carcinomas after exclusion of DW images with large clip artifact or DWI performed after contrast administration which may introduced error in ADC value assessment. However, all DW images were available for visual assessment for presence or absence of necrosis.

Response assessment

Patients were dichotomized into pathologic complete response (pCR) and non-pCR groups on the basis of findings from surgical histopathology. pCR was defined as absence of residual invasive

cancer with or without ductal carcinoma in situ in the breast and the absence of carcinoma in the sampled axillary lymph nodes.

Statistical analysis

A statistical association of the imaging parameters assessed on DCE imaging and ADC maps relative to pCR was performed using the statistics module in Matlab (version 2018b, Mathworks, Natick, MA). An odds ratio (OR) analysis was used to determine the value of necrosis as a predictor of response to NAST. Association of necrosis with T stage and nodal status was assessed using chi-squared test and OR, respectively. Separately, multiple logistic regression, using R Statistical Software (Foundation for Statistical Computing, Vienna, Austria), was used to create a model for predicting pCR with the following variables: presence of necrosis, T stage, and pretreatment axillary lymph node status. Mann-Whitney U test and the area under the receiver operator characteristic curve (AUC) were used to compare image metrics between the pCR and non-pCR groups. Finally, we performed power analyses to assess the power of our comparisons between measurements and pCR status. *P* values less than 0.05 were considered statistically significant. No correction was made for multiple comparisons.

2.4 Results [Necrosis for TNBC Response]

Patient characteristics

A total of 85 women met the selection criteria and were included in the study (Figure 16). Patient and tumor characteristics of these 85 women are presented in Table 7. The mean, median, and range of the patient age in years at diagnosis were 51.8 ± 13 , 51, 26-78, respectively. The median longest tumor diameter measured at DCE imaging was 3.8 cm (range, 1.3–9.8 cm).

Table 7 Characteristics of 85 patients with triple negative breast cancer who received neoadjuvant systemic therapy

Characteristic	Study Population	pCR	Non-pCR
No. of patients	85	37/85 (44)	48/85 (56)
<u>Age (years)</u>			
Mean \pm SD	51.8 \pm 13	54.3 \pm 13.8	49.9 \pm 12.39
Median (range)	51 (26-78)	57 (27-78)	47 (26-75)
<u>Longest tumor diameter (cm)</u>			
Mean \pm SD	4.57 \pm 2.9	3.6 \pm 2.18	5.3 \pm 3.3
Median (range)	3.8 (1.3-9.8)	3 (1.3-4.4)	4.25 (1.6-9.8)
<u>Tumor histological type</u>			
IDC grade II	10/85 (12)	2/37 (5)	8/48 (17)
IDC grade III	72/85 (85)	35/37 (95)	37/48 (77)
Metaplastic	3/85 (3)	0 /37(0)	3/48 (6)
<u>Necrotic tumor histological type</u>			
IDC grade II	5/85 (6)	1/37 (3)	4/48 (8)
IDC grade III	32/85 (38)	16/37 (43)	16/48 (33)
Metaplastic	2/85 (2)	0/37 (0)	2/48 (4)
<u>Tumor classification on DCE imaging</u>			
Non-necrotic (solid)	46/85 (54)	20/37 (54)	26/48 (54)
Necrotic	39/85 (46)	17/37 (46)	22/48 (46)
<u>Type of surgery</u>			
Total mastectomy	47/85 (55)	21/37 (57)	28/48 (58)
Conservative surgery	38/85 (45)	16/37 (43)	20/48 (42)

Note.—Data are number of patients (percent) unless otherwise indicated.

Regarding NAST, 76/85 (89%) of the 85 patients received standard chemotherapy consisting of doxorubicin and cyclophosphamide followed by paclitaxel, and 9/85 (11%) patients received a combination of doxorubicin and cyclophosphamide followed by paclitaxel and then followed by targeted therapy. The median number of cycles received was 6 (range, 4-8). Of the 85 patients, 47/85 (55%) underwent total mastectomy, and 38/85 (45%) underwent segmentectomy.

Thirty-seven patients 37/85 (44%) had pCR, and 48/85 (56%) did not; 39/85 (46%) patients had necrotic tumors and 46/85 (54%) patients had non-necrotic tumors (Table 8). Of 39 patients with necrotic carcinoma, 17/39 (44%) had pCR (Figure 19), and 22/39 (56%) did not (Figure 20).

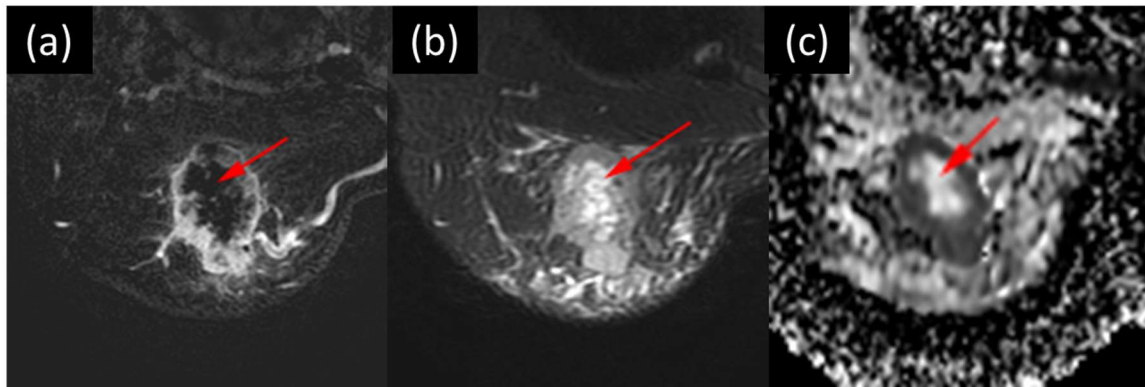


Figure 19 Necrotic index carcinoma with a pathological complete response after neoadjuvant systemic therapy in a 46-year-old woman with TNBC of the right breast. The volume of necrotic material was 10 cm³, and the percent of the total tumor volume occupied by necrosis was 17%. (a) Axial fat-suppressed early-phase dynamic contrast-enhanced image shows central non-enhancing area representing necrosis (arrow). (b) Axial fat-suppressed T2-weighted image shows necrosis as central area of high signal intensity (arrow). (c) Axial apparent diffusion coefficient map shows shine-through corresponding to central area of necrosis (arrow).

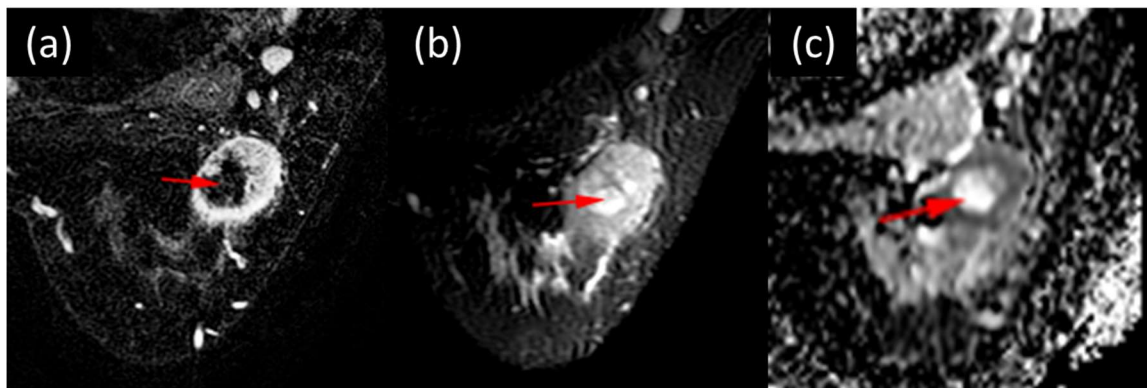


Figure 20 Necrotic index carcinoma with pathological non-complete response after neoadjuvant systemic therapy in a 30-year-old woman with TNBC of the left breast. The volume of necrotic material was 4 cm³, and the percent of the total tumor volume occupied by necrosis was 17%. (a) Axial fat-suppressed early-phase dynamic contrast-enhanced image shows central non-enhancing area representing necrosis (arrow). (b) Axial fat-suppressed T2-weighted image shows necrosis as a central area of high signal intensity (arrow). (c) Axial apparent diffusion coefficient map shows shine-through corresponding to central area of necrosis (arrow).

Table 8 T stage, nodal status, and pathologic complete response in 85 triple negative breast cancer patients and the subsets of patients with or without necrotic carcinomas.

Characteristic	Study Population (n = 85)	Necrotic Carcinomas (n = 39)	Non-necrotic Carcinomas (n = 46)	P-value
<u>T Stage</u>				0.07
T1	14/85 (16)	3/39 (8)	11/46 (24)	
T2	44/85 (52)	20/39 (51)	24/46 (52)	
T3	27/85 (32)	16/39 (41)	11/46 (24)	
<u>Nodal Status at Staging</u>				0.69
Positive	46/85 (54)	22/39 (56)	24/46 (52)	
Negative	39/85 (46)	17/39 (44)	22/46 (48)	
<u>Nodal Status at Surgery</u>				0.75
Positive	21/85 (25)	9/39 (23)	12/46 (26)	
Negative	64/85 (75)	30/39 (77)	34/46 (74)	
<u>pCR Status</u>				0.99
pCR	37/85 (44)	17/39 (44)	20/46 (43)	
Non-pCR	48/85 (56)	22/39 (56)	26/46 (57)	

Data are number of patients (percent), except for the p-value column. P-values comparing characteristic distributions between necrotic and non-necrotic patients used Chi-square test.

Association of Necrosis with T Stage, Axillary Nodal Status, and pCR

The frequency of tumor necrosis in the 85 patients with TNBC based on T stage, nodal status at staging and at surgery, and pCR is provided in Table 2. The likelihood of necrosis increased with increasing T stage (χ^2 (2, N=85) = 5.321, P = .070). No association was observed between the presence of necrosis and nodal status at staging (OR, 1.19; 95% confidence interval [CI]: 0.5-2.8) or nodal status at surgery (OR, 0.850; 95% CI: 0.3-2.3).

There was no association between the presence of necrosis and pCR (OR, 0.995; 95% CI: 0.4-2.3). Multiple logistic regression to predict pCR based on the presence of necrosis, T stage, and nodal status at staging showed that necrosis was not a significant independent prognostic factor of pCR status (P = .46, Table 9).

Table 9 Logistic regression results for association analysis of pCR with presence of necrosis, T-stage, and pre-treatment nodal stage.

Parameter	β	Standard Error	z-statistic	P-value	Exp(β) (Adjusted Odds Ratio)
Necrosis	0.36	0.49	0.74	0.46	1.44
T-stage (2)	-0.64	0.65	-0.98	0.33	0.53
T-stage (3)	-1.88	0.77	-2.45	0.014	0.15
Nodal Stage	-0.63	0.47	-1.34	0.18	0.53

Association of DCE imaging metrics with pCR in necrotic TNBC subset.

The mean NV_{DCE} was 5.9 cm³ (SD \pm 6.8 cm³) for the pCR group and 7.7 cm³ (SD \pm 10.8 cm³) for the non-pCR group. The mean % NV_{DCE} was 14% (SD \pm 12%) for the pCR group and 14% (SD \pm 10.4%) for the non-pCR group (6). There was no significant difference in the NV_{DCE} (AUC = 0.58; P = .37) and % NV (AUC = 0.50; P = .90) between the two groups (Figure 21).

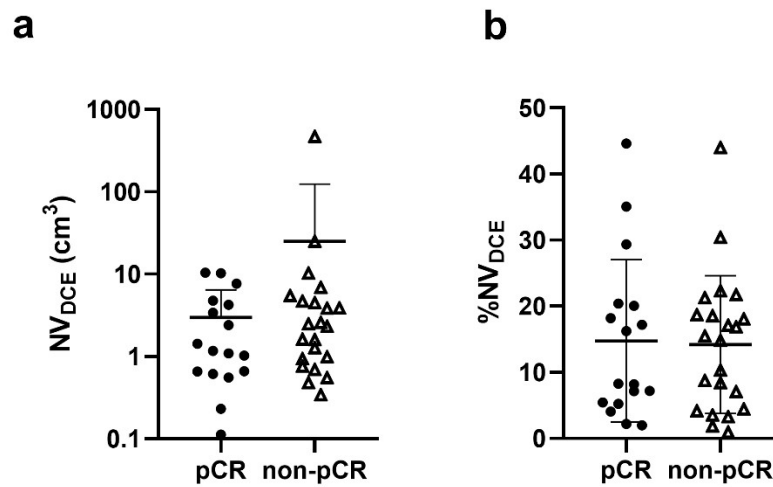


Figure 21 Clustering of necrosis volume or NV_{DCE} (a), and necrosis-only volume as a percent of total tumor volume or %NV_{DCE} (b), by dynamic contrast enhanced MRI associated with response to neoadjuvant systemic therapy. There is no difference between TNBC patients with and without pathologic complete response (pCR).

Among the necrotic index carcinomas, there were no differences between the pCR and non-pCR groups in PE1 and PE2 of the TTV_{DCE}, TV_{DCE} or NV_{DCE} (Table 4). At a significance level of 0.05, we can have 80% power to detect an AUC of ≥ 0.75 .

Association of DWI imaging metrics with pCR in necrotic TNBC subset

For quantitative evaluation of necrotic regions on DWI, 22/39 (56%) necrotic tumors in the study were included. The remaining 17 necrotic tumors were excluded for quantitative assessment of ADC value because the DWI showed severe clip-related metallic artifact or DWI were acquired after contrast agent administration, also were available for visual assessment for presence of necrosis. Of the 22 patients with necrotic index carcinomas and available for quantitative evaluation of ADC, 8/22 (36%) had pCR and 14/22 (64%) did not.

There were no differences between the pCR and non-pCR groups in the mean ADC for the TTV_{DWI}, TV_{DWI} or NV_{DWI} for necrotic tumors (Table 10). At a significance level of 0.05, we can have 80% power to detect an AUC of ≥ 0.84 .

Table 10 DCE and DWI metrics from whole tumor, tumor without necrosis, and necrosis-only segmentations of necrotic carcinomas

Metric	pCR	Non-pCR	AUC	P Value
DCE (N = 39)	N = 17/39 (44%)	N = 22/39 (56%)		
NV _{DCE} (cm ³)	5.9 ± 6.8	7.7 ± 10.8	0.59	.37
%NV _{DCE}	14 ± 12	14 ± 10.4	0.50	.99
PE1 TTV _{DCE}	189.2 ± 26	164.37 ± 58	0.51	.97
PE2 TTV _{DCE}	102 ± 12	183.77 ± 51	0.52	.83
PE1 TV _{DCE}	213.17 ± 30.42	184.8 ± 56	0.51	.97
PE2 TV _{DCE}	220.7 ± 14.8	202.6 ± 57	0.53	.77
PE1 NV _{DCE}	58.37 ± 45	64.45 ± 95	0.52	.81
PE2 NV _{DCE}	106.37 ± 67	133.35 ± 97	0.55	.62
DWI (N = 22)	N = 8/22 (36%)	N = 14/22 (64%)		
ADC TTV _{DWI} (10 ⁻³ mm ² /s)	1.26 ± 0.36	1.20 ± 0.22	0.53	.83
ADC TV _{DWI} (10 ⁻³ mm ² /s)	1.08 ± 0.23	1.13 ± 0.26	0.51	.97
ADC NV _{DWI} (10 ⁻³ mm ² /s)	1 ± 0.5	1.7 ± 0.3	0.53	.87

Data are mean ± standard deviation unless otherwise indicated.

2.5 Discussion [Necrosis for TNBC Response]

Our study did not find significant association between the presence of tumor necrosis by pretreatment MRI and response to NAST in patients with TNBC. In patients with necrotic index carcinomas, the necrosis-only volume, necrosis as a percent of the TTV, and quantitative perfusion and diffusion metrics were not significantly different between the patients with and without a pCR.

Tumor necrosis detected at histopathological evaluation has been investigated in multiple studies for different types of carcinomas and has been proposed as a poor prognostic factor in a variety of solid tumors, as it is thought to reflect chronic hypoxia and poor vascularity^{117,119,120,135}. Previous studies based on the review of pathological specimens have reported conflicting results regarding the association between tumor necrosis and overall survival in breast cancer. One study showed that tumor necrosis correlated with tumor grade but did not compare necrosis directly with outcome¹²¹. Two studies showed that tumor necrosis was associated with poor clinical outcomes and aggressive tumor biology, as well as decreased relapse-free survival and increased mortality^{122,125}. In an analysis of over 1200 patients with HER2-positive tumors, necrosis was not associated with overall survival, although

necrotic tumors represented only 9% of selected patients¹³⁶. In another cohort of 1850 patients of different hormonal subtypes, necrosis was associated with tumor characteristics suggesting poor outcome and was an independent adverse prognostic factor for disease-free survival¹¹⁵. It should be noted that in the aforementioned studies, necrosis rates were between 4.5% and 9%, which were substantially lower than those reported in other studies with a necrosis rate of up to 40% among different hormonal subtypes¹¹⁷. Some other studies do not demonstrate a clear correlation between tumor necrosis and prognosis in breast cancer^{126,127}.

A few studies have specifically evaluated the association between tumor necrosis seen at histopathological evaluation and prognostic outcomes in patients with TNBC. In a study of 154 patients with TNBC that examined age, clinical stage, Ki-67 proliferation index, tumor necrosis, lymph node status, and histological grade, tumor necrosis was found by univariate analyses to be a significant negative prognostic factor of relapse-free survival¹³⁷. A second study of 149 patients with TNBC showed better disease-free survival for smaller tumor size (≤ 2 cm) and absence of necrosis based on univariate analysis. However, a multivariable analysis of the same data revealed no statistically significant association between necrosis and disease-free survival¹³⁸. A third study of 87 TNBCs showed that pathologic characteristics, including necrosis, were not associated with overall prognosis¹³². In a cohort of 841 TNBCs, tumor necrosis was associated with mortality but was not a prognostic factor for recurrence¹²⁸.

Very few MRI-based studies have investigated whether necrosis predicts response of TNBC to NAST. In a study of 23 patients with TNBC, Kawashima et al.¹³³ sought to differentiate responders from non-responders to NAST and found that irregularly shaped mass and the presence of clear intratumoral necrosis were significantly associated with absence of response. However, 5 patients (21%) had necrotic index carcinomas in this study, which was substantially lower than the number and percentage of patients with necrotic carcinomas in our study (39 /46%), and is lower than the typical reported rate of

necrosis of up to 50% in TNBCs¹²⁸. More importantly, the response assessment in this study was based on response evaluation criteria in solid tumors (RECIST) rather than the pathological response at surgery, which is generally accepted as a potential surrogate marker for survival in TNBC²⁷. In another study of 132 patients with TNBC, Bae et al.¹⁰⁹ examined the association between pretreatment breast MRI features and pCR and recurrence-free survival and found that the absence of intratumoral T2 high signal intensity, representing necrosis, was associated with pCR. However, this association was not statistically significant. Furthermore, only 18 of the 132 patients (13%) had a pCR, which is substantially lower than the 44% rate of pCR seen in our study as well as the typical range of 33% to 45% among TNBC patients as reported by others¹³⁹⁻¹⁴². In comparison, our study population was more representative of the typical TNBC population in terms of their rates of pCR and necrosis. Further, our analysis included evaluation of quantitative imaging characteristics of necrosis in addition to the qualitative assessment of the presence of necrosis. One plausible hypothesis explaining the similar outcomes between necrotic and non-necrotic tumors observed in our study is that tissue hypoxia at the necrotic core may result in increased local angiogenic growth factors, making the tumor more aggressive but also more vulnerable to treatment due to improved perfusion and drug delivery. However further work is needed to investigate this hypothesis and other possible physiological changes in necrotic and non-necrotic tumors.

To the best of our knowledge, the association between necrotic carcinoma and nodal disease in TNBC has not been investigated. In our study, we found that necrosis was not significantly associated with nodal disease either at staging or at surgical pathology.

Our study differs from prior studies of necrosis on MRI as a predictive marker in TNBC in that we conducted a comprehensive quantitative analysis of tumors with and without necrosis as well as the necrotic region itself, on both DCE images and diffusion-weighted images, and tested association between these quantitative imaging metrics with pCR after NAST. In our analysis, we also focused on

necrosis as an independent predictor of treatment response and investigated the behavior of the solid and necrotic components of necrotic tumors both separately and in combination. In comparison, all the prior studies were based mainly on binary evaluation of presence or absence of necrosis on T2-weighted images.

Our study had several limitations. First, this is a retrospective study performed in a single institution with a relatively small patient population. Second, the segmentation of the different tissue volumes was performed by two breast radiologists in consensus, and we did not evaluate inter-observer variability in segmentation. Third, while all DWI images were available for visual assessment for presence or absence of necrosis, the quantitative ADC analysis was performed on a subgroup of necrotic lesions due to technical limitations. Finally, the NAST treatment protocols in our study population were heterogeneous as they depended on clinician preference, yet this heterogeneity reflects the adaptive design that is used in actual clinical practice for best patient outcome.

2.6 Conclusion [*Necrosis for TNBC Response*]

In conclusion, our study did not find significant associations between tumor necrosis by pretreatment MRI and the quantitative image characteristics of tumor necrosis and the response to NAST in TNBC patients. Our findings warrant further validation in larger population-based multi-institutional studies that evaluate not only response to NAST but also long-term outcomes.

2.6 Acknowledgements [*Necrosis for TNBC Response*]

We would like to thank Stephanie P. Deming from the Department of Scientific Publications, Research Medical Library, at The University of Texas MD Anderson Cancer Center for her assistance in editing and proofreading this document.

This study has received funding by the National Institutes of Health/National Cancer Institute (Cancer Center Support Grant P30 CA016672); specifically, resources from the Biostatistics Resource Group were used.

Chapter 3 – Functional Tumor Volume by Fast Dynamic Contrast-Enhanced MRI for Predicting Neoadjuvant Systemic Therapy Response in Triple-Negative Breast Cancer

This chapter is based upon the following article, published in the Journal of Magnetic Resonance Imaging:

Musall BC, Abdelhafez AH, Adrada BE, Candelaria RP, Mohamed RMM, Boge M, Le-Petross H, Arribas E, Lane DL, Spak DA, Leung JWT, Hwang K, Son JB, Elshafeey NA, Mahmoud HS, Wei P, Sun J, Zhang S, White JB, Ravenberg EE, Litton JK, Damodaran S, Thompson AM, Moulder SL, Yang WT, Pagel MD, Rauch GM, Ma J. **Functional tumor volumes by fast DCE MRI for predicting neoadjuvant systemic therapy response of triple-negative breast cancer.** *Journal of Magnetic Resonance Imaging*, accepted for publication (2021).

3.1 Abstract [FTV for TNBC Response]

BACKGROUND: Dynamic contrast-enhanced (DCE) MRI is useful for diagnosis and assessment of treatment response in breast cancer. Fast DCE MRI offers a higher sampling rate of contrast enhancement curves in comparison to conventional DCE MRI, potentially characterizing tumor perfusion kinetics more accurately for measurement of functional tumor volume (FTV) as a predictor of treatment response.

PURPOSE: To investigate FTV by fast DCE MRI as a predictor of neoadjuvant systemic therapy (NAST) response in triple-negative breast cancer (TNBC).

STUDY TYPE: Prospective

POPULATION/SUBJECTS: 60 patients with biopsy-confirmed TNBC between December 2016 and September 2020

FIELD STRENGTH/SEQUENCE: 3.0 T/3D fast spoiled gradient echo-based DCE MRI

ASSESSMENT: Patients underwent MRI at baseline and after 4 cycles (C4) of NAST, followed by definitive surgery. DCE subtraction images were analyzed in consensus by two breast radiologists with 5 (A.H.A.) and 2 (H.S.M.) years of experience. Tumor volumes (TV) were measured on early and late subtractions. Tumors were segmented on 1 and 2.5-minute early phase subtractions and FTV was determined using optimized signal enhancement thresholds. Interpolated enhancement curves from segmented voxels were used to determine optimal early phase timing.

STATISTICAL TESTS: Tumor volumes were compared between patients who had a pathologic complete response (pCR) and those who did not using the area under the receiver operating curve (AUC) and Mann-Whitney U test.

RESULTS: 26/60 patients (43%) had pCR. FTV at 1 minute after injection at C4 provided the best discrimination between pCR and non-pCR, with AUC (95% confidence interval [CI]) = 0.85 (0.74,0.95) ($P < 0.05$). The 1-minute timing was optimal for FTV measurements at C4 and for the change between C4 and baseline. TV from the early phase at C4 also yielded a good AUC (95%CI) of 0.82 (0.71,0.93) ($P < 0.05$).

DATA CONCLUSION: FTV and TV measured at 1 minute after injection can predict response to NAST in TNBC.

KEYWORDS

Triple-Negative Breast Cancer, DCE MRI, Functional Tumor Volume, Breast MRI, Treatment Response

3.2 Introduction [FTV for TNBC Response]

Triple-negative breast cancer (TNBC) accounts for approximately one-fifth of all breast cancers and is an aggressive subtype of the disease⁵. Unlike other subtypes of breast cancer, TNBC does not

respond to conventional hormone therapies and is typically treated with neoadjuvant systemic therapy (NAST)¹⁴³. Unfortunately, less than half of TNBC patients respond to NAST¹⁴³. Patients without a pathologic complete response (pCR) to NAST have a high risk of recurrence and poor prognosis¹¹⁶. Early prediction of NAST response in TNBC could be highly valuable because non-responders could be triaged to alternative treatments for better outcomes²⁰.

Dynamic contrast-enhanced (DCE) MRI has been reported useful for both initial diagnosis/staging and assessment of treatment response in breast cancer¹⁴⁴⁻¹⁴⁶. In general, malignant breast lesions are highly vascular and exhibit rapid early enhancement (wash-in) followed by a rapid loss of enhancement (wash-out) in DCE MRI. The volume of the tumor regions displaying this fast wash-in/wash-out pattern, as selected by semi-quantitative enhancement ratio thresholds applied to the early and late phases of a DCE scan, has been defined as the functional tumor volume (FTV)¹⁴⁷. FTV is assumed to represent the region of viable tumor cells and has been found useful for predicting treatment response^{145,148}. The definition of FTV is empirical and is adjusted to optimize its predictive performance through selection of optimal image enhancement thresholds¹⁴⁵. The optimal enhancement thresholds used for calculating FTV differ among different subtypes of breast cancer, including TNBC^{149,150}.

Several recent studies have shown that assessment of breast lesion perfusion, specifically with rapid sampling of contrast uptake after contrast injection, is useful for screening and diagnosis¹⁵¹⁻¹⁵³. Because of the requirements for a large imaging volume and high spatial resolution, the temporal resolution of breast DCE MRI is typically limited to approximately 90-120 seconds per phase^{152,154,155}. Newer imaging techniques, which apply higher acceleration by parallel imaging and/or data sharing, can enable fast DCE MRI and allow acquisition of a large imaging volume in under 20 s^{152,156}. These techniques offer substantially faster sampling of the contrast enhancement curves and potentially more accurate characterization of the tumor perfusion kinetics than conventional DCE MRI^{157,158}. One such method, Differential Sub sampling with Cartesian Ordering (DISCO), accelerates data acquisition by

sharing views in k-space between a central “a-region” and one or multiple under-sampled outer “b-regions”¹⁵⁹. For semi-quantitative analysis, most prior work on FTV as a predictor of treatment response has been performed using conventional DCE MRI acquisitions with an early phase acquired at approximately 2.5 minutes after injection of contrast agent^{99,147-150}. Two other studies used early phase images with a 2-minute and 1.5-minute delay after injection^{160,161}. Rapid tumor enhancement has been shown to correlate with microvessel density and aggressiveness, and assessment of enhancement early after contrast injection by fast DCE MRI may be useful for measuring FTVs^{83,151}.

This study aims to investigate FTV by fast DCE MRI as a predictor of neoadjuvant systemic therapy (NAST) response in triple-negative breast cancer (TNBC).

3.3 Methods [FTV for TNBC Response]

Patients

Treatment-naïve patients with biopsy-confirmed TNBC were enrolled between December 2016 and September 2020 in an Institutional Review Board–approved and Health Insurance Portability and Accountability Act–compliant prospective ongoing clinical trial (“A Robust TNBC Evaluation Framework to Improve Survival” [ARTEMIS]; NCT02276442). The study patients were prospectively monitored for response to NAST. TNBC was defined from standard pathologic assays as negative for ER and PR (<10% tumor staining) and negative for HER2 (IHC score <3, gene copy number not amplified). TNBC patients with clinical stage I-III who were scheduled to receive NAST with anthracycline/taxane based regimens were included in this study. Any patients with stage IV disease prior to initiation of treatment were excluded. All patients provided written informed consent.

All patients received NAST consisting of dose-dense doxorubicin and cyclophosphamide for 4 cycles followed by paclitaxel, which was given every 2 weeks for 4 cycles or weekly for a total of 12 doses. All patients underwent an MRI scan at baseline (BL) before the initiation of NAST and a second scan after 4 cycles (C4) of the treatment. The minimum BL tumor size in all patients was 1.0 cm as

measured by clinical diagnostic ultrasound, as patients who did not meet this criterion were usually sent directly to surgery. All patients underwent surgery after the completion of NAST. Pathologic findings from surgery were used to classify patients as pCR or non-pCR. pCR was defined as no residual invasive disease in the surgical specimen.

MRI Acquisition

All MRI scans were conducted with the patients in a prone position using a GE 3.0-T MR750w whole body scanner (Waukesha, WI) with an 8-channel phased array bilateral breast coil. Each MRI scan included an axial T_2 -weighted series and an axial fast DCE MRI series. The fast DCE MRI series used the DISCO sequence with bipolar readouts for two-point Dixon processing to produce water-only and fat-only images for each acquired image¹⁵⁹. Typical scan parameters for the DISCO series in this study were as follows: field of view = 34×34 cm, slice thickness/slice spacing = 3.0/-1.5 mm, flip angle = 12° , repetition time/echo time 1/echo time 2 = 7.4/1.1/2.3 ms, matrix = 320×320 , number of acquired slices = 60-115, in-plane spatial resolution = 0.6-0.8 mm, total acquisition time = 7 minutes, and Auto-calibrating Reconstruction for Cartesian imaging (ARC) factor = 3. DISCO parameters and typical phase timings were as follows: number of b-regions = 5, a-region fraction = 16%, time for fully sampled phase = 34 seconds, backwards view sharing, and time for DISCO accelerated phase = 11 seconds. After at least one mask phase was obtained, a single bolus of gadobutrol (Gadovist, Bayer HealthCare) contrast agent was injected (0.1 mL/kg at ~ 2 mL/second followed by saline flush) at the start of a DCE phase. Temporal resolution of the DISCO series had a median of 11 seconds and ranged from 8 seconds to 15.5 seconds, depending on the slice coverage.

MRI Analysis

Tumor size along the three orthogonal axes was measured separately on both early and late phase subtraction images. TV was calculated from the early and late phase measurements (TV_{Early} and TV_{Late}) as the ellipsoid of the three dimensions (Figure 22A, Figure 23A):

Equation 32: $TV = \frac{4}{3} \pi \times (AP/2) \times (CC/2) \times (TR/2)$

where AP, CC, and TR are the anteroposterior, craniocaudal, and transverse tumor dimensions, respectively. Additionally, the maximum of these three measurements was selected to represent the longest diameter (LD) of the tumor.

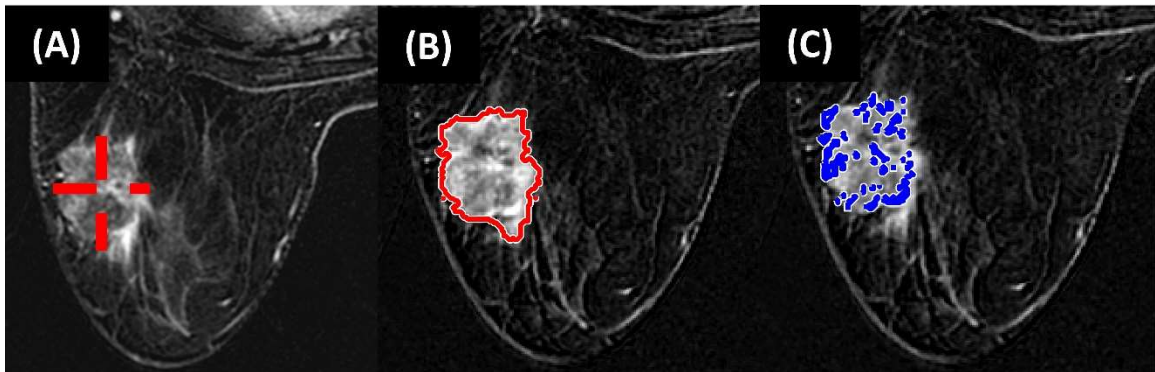


Figure 22 Examples of tumor volume measurements in a 52-year-old woman with triple-negative breast cancer in her left breast: (A) tumor volume dimensions, (B) segmented enhanced tumor volume, and (C) enhancement threshold-based functional tumor volume in blue at percentage enhancement >130% and signal enhancement ratio >1.1.

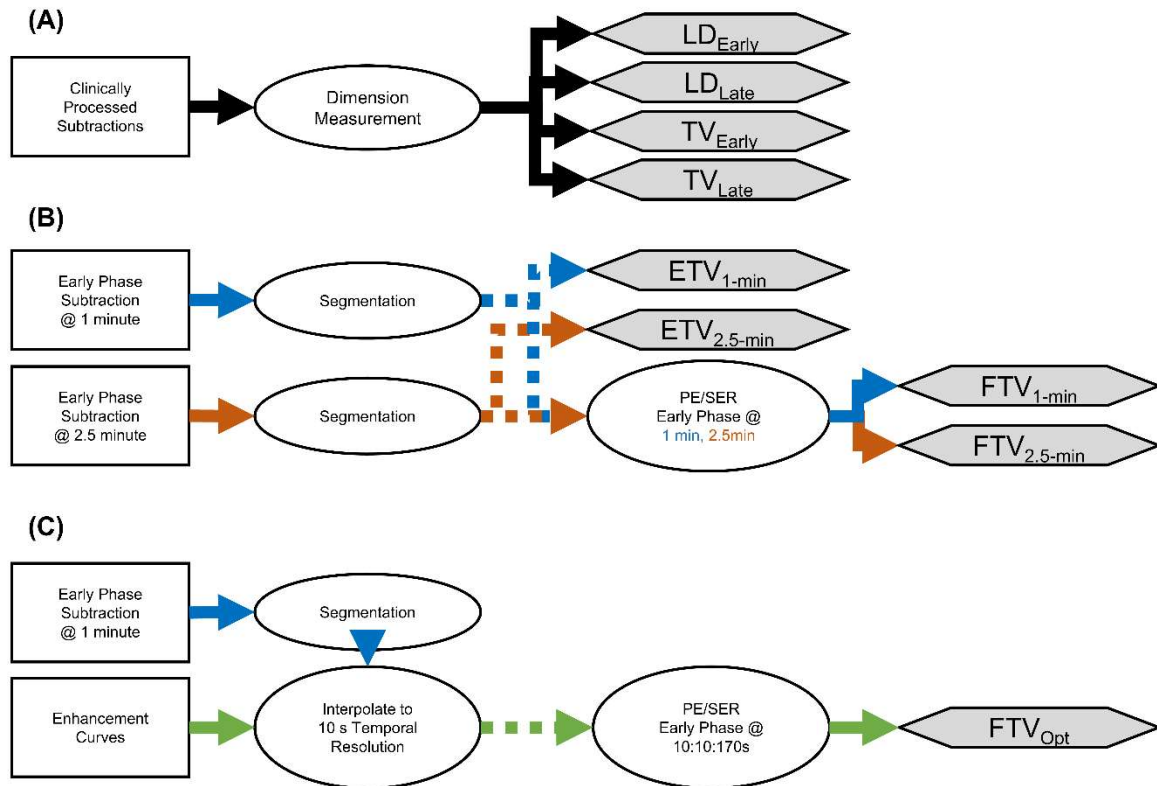


Figure 23 Map of fast dynamic contrast-enhanced MRI data flow, processing, and segmentation for volume measurements: (A) tumor volume by 3D measurements (TV), (B) enhanced tumor volume (ETV) and functional tumor volume (FTV) from early phase segmentations, with percentage enhancement (PE) and signal enhancement ratio (SER) thresholds applied for FTV, and (C) FTV with optimization of early phase timing.

Two sets of images from the DISCO fast DCE MRI acquisition were selected as an early phase for segmentation based on their timing after injection. The phase closest to 1 minute after injection was chosen to show tumor contrast as early as possible after injection while allowing for inter-patient variability in contrast arrival. The phase closest to 2.5 minutes after injection was chosen to match with the earlier studies of FTV as reported in the literature^{99,147-150}. The final phase of the DCE scan, approximately 6-7 minutes after injection, was selected as the late phase for analysis.

Two breast radiologists, with 5 (A.H.A.) and 2 (H.S.M.) years of experience in breast MRI interpretation, were blinded to the patient clinical outcomes and performed semi-automatic consensus segmentation that encompasses the tumor in all slices. Tumors were first manually segmented on both 1-minute and 2.5-minute early phase subtraction images separately using Imager, which is a graphic user

interface-based in-house software developed for image analysis. Imager features importing/exporting Digital Imaging and Communications in Medicine-compatible images as well as manual and semi-automatic contouring of image regions of interest ¹⁶². All segmentations were further refined by semi-automatic segmentation using the histogram thresholding in Imager to exclude voxels below enhancement thresholds that were visually determined to be non-tumor by the radiologists. All segmentations were reviewed and confirmed by both radiologists to avoid inter-reader bias. Care was taken to exclude necrotic regions and regions with artifacts from the biopsy clips within the tumors.

Segmented tumor volumes on 1-minute and 2.5-minute subtractions were first extracted as the enhanced tumor volume (ETV; Figure 22B, Figure 23B). FTV was defined as a subset of the ETV voxels that were above a set percentage enhancement (PE) threshold and below a set signal enhancement ratio (SER, Figure 23B) threshold ¹⁴⁷. PE and SER were defined as

$$\text{Equation 33: PE} = 100 \times \frac{S_{\text{Early}} - S_{\text{Mask}}}{S_{\text{Mask}}}$$

$$\text{Equation 34: SER} = \frac{S_{\text{Early}} - S_{\text{Mask}}}{S_{\text{Late}} - S_{\text{Mask}}}$$

where S_{Mask} , S_{Early} , and S_{Late} are the pixel intensity of the mask, early phase, and late phase images, respectively.

PE and SER thresholds were optimized to best discriminate between pCR and non-pCR patients by FTV (Figure 22C) with early phase timings of 1 and 2.5 minutes. This optimization was performed separately for BL and C4 scans as well as the relative change between BL and C4 (%C4/BL).

$$\text{Equation 35: \%C4/BL} = 100 \times \frac{C4 - BL}{BL}$$

Different combinations of PE thresholds (0% to 220%, in increments of 5%) and SER thresholds (0 to 2.0, in increments of 0.05) were evaluated for calculating FTVs. Contour plots of the area under the receiver operating characteristic curve (AUC) for discriminating pCR from non-pCR were generated for FTVs across a grid of PE and SER thresholds. Optimal PE/SER values were selected as those producing the

peak AUC on the contour plot, and optimized FTVs were extracted from all tumors using these thresholds (Figure 23B).

Fast DCE enhancement curves were then used to search for optimal early phase timing (FTV_{opt}). Voxel enhancement curves were extracted from the segmentations on the 1-minute subtractions and were then temporally linearly interpolated into a shared frame with a sampling rate of 10 seconds per phase (with $t = 0$ seconds at injection). Signal levels at early phase timings from 10 seconds to 240 seconds in increments of 10 seconds were used to repeat FTV calculations across PE and SER thresholds for each early phase timing (Fig. 2C). Optimal early phase timing and PE/SER thresholds were taken from the coordinate of the peak AUC of this search and were used to calculate FTV_{opt} .

Statistical analysis

For BL, C4, and %C4/BL, all volume measurements and LDs of the tumor were tested for their performance in discriminating pCR from non-pCR patients using the Mann-Whitney U Test and AUC in Matlab 2018b (Mathworks, Natick, MA). As the biomarkers in this study all measure tumor size and are highly positively correlated, the conventional Bonferroni procedure for correcting multiple comparisons would be overly conservative. Therefore, no correction was made for multiple comparisons. P values less than 0.05 were considered statistically significant.

3.4 Results [FTV for TNBC Response]

A total of 60 patients were enrolled, and their characteristics are provided in Table 11. Of the 60 patients, 26 (43%) had pCR and 34 (57%) did not have pCR.

Table 11 Characteristics of patients with triple-negative breast cancer who received neoadjuvant systemic therapy (n = 60).

Characteristic	No. (%)
Age	
Mean \pm SD	52 \pm 12 years
Median (range)	50. years (28-79 years)
Largest tumor diameter	
Mean \pm SD	4.6 \pm 2.9 cm
Median (range)	3.8 cm (1.3-9.8 cm)
Tumor stage	
I	7 (12)
II	36 (60)
III	17 (28)
T category	
1	11 (18)
2	37 (62)
3	11 (18)
4	1 (2)
N category	
0	34 (57)
1	19 (32)
2	1 (2)
3	6 (10)
Type of Surgery	
Total mastectomy	20 (33)
Conservative surgery	40 (67)
Treatment Response	
pCR	26 (43)
non-pCR	34 (57)

pCR = pathologic complete response, SD = standard deviation

The results from all volume measurements and LD, as compared between the pCR and non-pCR groups, are presented in

Table 12 and Table 13.

Table 12 Longest diameter, tumor volume, and enhanced tumor volume measurements for patients who had a pathologic complete response (pCR) and those who did not.

Measure	AUC [95% CI]	P	Mean ± SD	
			pCR	Non-pCR
BL Scan				
LD _{Early}	0.62 [0.47,0.76]	0.13	3.3 ± 1.7 cm	3.9 ± 1.8 cm
LD _{Late}	0.59 [0.45,0.74]	0.22	3.5 ± 1.6 cm	4.1 ± 1.8 cm
TV _{Early}	0.63 [0.49,0.77]	0.085	19 ± 37 cm ³	31 ± 49 cm ³
TV _{Late}	0.62 [0.48,0.77]	0.11	21 ± 37 cm ³	34 ± 53 cm ³
ETV _{1-min}	0.59 [0.45,0.74]	0.23	15 ± 31 cm ³	19 ± 24 cm ³
ETV _{2.5-min}	0.60 [0.46,0.75]	0.18	15 ± 36 cm ³	18 ± 22 cm ³
C4 Scan				
LD _{Early}	0.81 [0.70,0.93]	<0.05	0.80 ± 0.95 cm	2.3 ± 1.4 cm
LD _{Late}	0.78 [0.65,0.90]	<0.05	1.1 ± 1.0 cm	2.4 ± 1.5 cm
TV _{Early}	0.82 [0.71,0.94]	<0.05	0.74 ± 1.7 cm ³	7.7 ± 18 cm ³
TV _{Late}	0.82 [0.70,0.93]	<0.05	1.1 ± 2.3 cm ³	9.0 ± 19 cm ³
ETV _{1-min}	0.79 [0.70,0.92]	<0.05	0.65 ± 1.6	4.0 ± 7.5
ETV _{2.5-min}	0.79 [0.67,0.91]	<0.05	0.45 ± 1.0	3.9 ± 8.2
%C4/BL			% change	% change
LD _{Early}	0.76 [0.63,0.89]	<0.05	-71% ± 33%	-38% ± 33%
LD _{Late}	0.74 [0.62,0.87]	<0.05	-65% ± 31%	-36% ± 33%
TV _{Early}	0.77 [0.65,0.90]	<0.05	-91% ± 20%	-62% ± 46%
TV _{Late}	0.78 [0.67,0.90]	<0.05	-90% ± 14%	-59% ± 50%
ETV _{1-min}	0.77 [0.65,0.90]	<0.05	-93% ± 11%	-67% ± 37%
ETV _{2.5-min}	0.76 [0.63,0.88]	<0.05	-92% ± 15%	-66% ± 38%

AUC = area under the receiver operator characteristic curve, BL = baseline, CI = confidence interval, TV = clinical tumor volume, LD = longest diameter, C4 = cycle 4.

TV and LD performed best as predictors of treatment response when measured on the C4 scans (Table 12, Figure 24). Of these measurements, TV_{Early} at C4 performed best with an AUC (95% confidence interval [CI]) of 0.82 (0.71,0.94) ($P < 0.05$, Figure 24C). TV and LD performance also performed well at %C4/BL, and none of the measures reached statistical significance at BL (minimum $P = 0.085$). In all cases, TV and LD showed stronger performance when measured on the early phase in comparison to the measurement on the late phase.

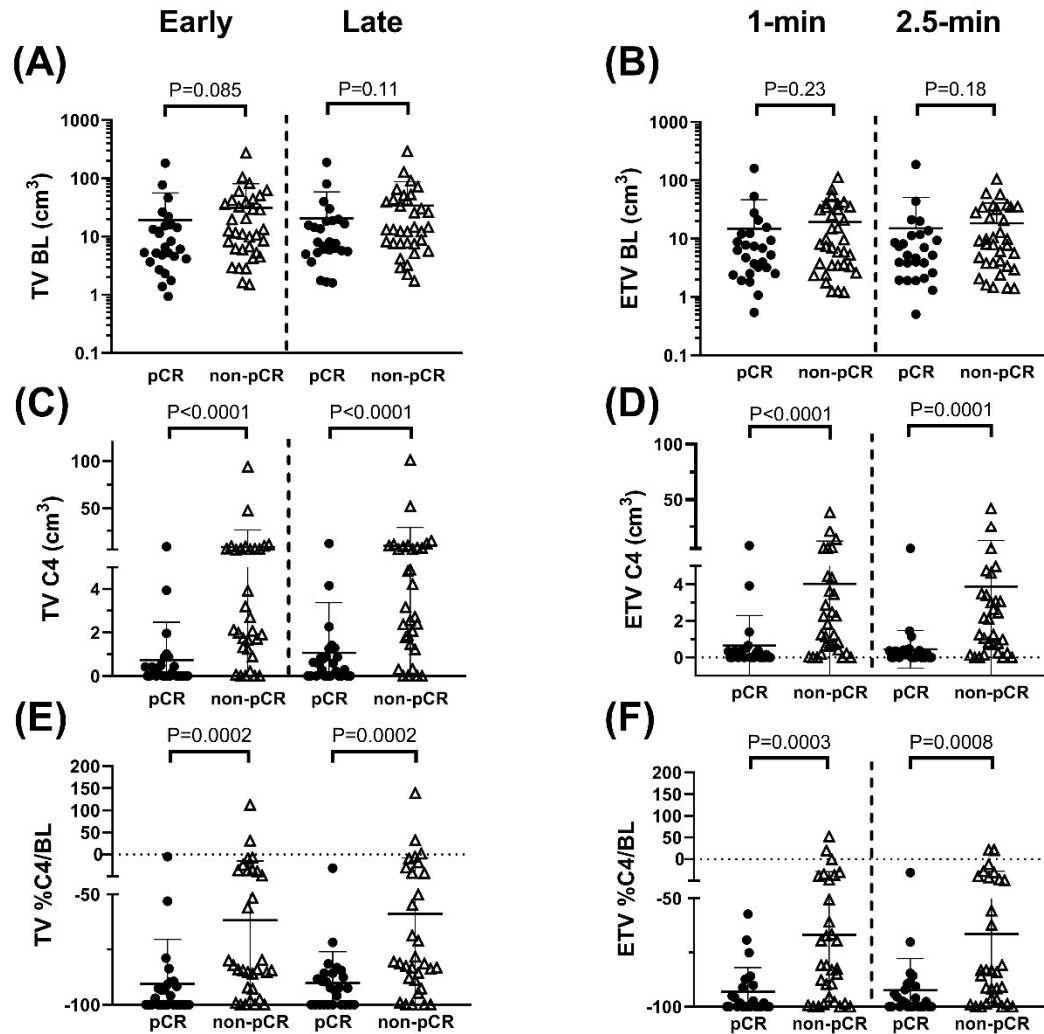


Figure 24 Comparison of tumor volume (TV) by 3D measurements from early phase and late phase measurements (A,C,E) and enhanced tumor volume (ETV) from 1-minute and 2.5-minute early phase timings (B,D,F) between patients who had a pathologic complete response (pCR) and those who did not, at the baseline (BL) scan (A,B), cycle 4 (C4) scan (C,D), and %C4/BL (E,F).

ETV showed good performance at the C4 scan and %C4/BL (Table 12, Figure 24D,F). Top performance from ETV was achieved with an early phase timing of 1 minute at the C4 scan, with AUC (95%CI) = 0.79 (0.67,0.92) ($P < 0.05$; Figure 24D). ETV did not reach a statistical significance at BL ($P = 0.23$ and 0.18 for the 1- and 2.5-minute early phase timings, respectively). Performance was similar between 1- and 2.5-minute early phase timings for all scans.

Table 13 Functional tumor volume measurements in patients with and without pathologic complete response (pCR).

Measure	Optimal threshold	AUC [95% CI]	P	Mean ± SD volume, cm ³	
				pCR	Non-pCR
BL Scan					
FTV _{1-min}	PE>0 SER>0	0.59 [0.45,0.74]	0.23	15 ± 31	19 ± 24
FTV _{2.5-min}	PE>0 SER>0	0.60 [0.46,0.75]	0.18	15 ± 35	18 ± 22
FTV _{Opt}	Early Phase=30 s PE>0 SER>1.3	0.69 [0.55,0.82]	<0.05	0.12 ± 0.34	0.32 ± 0.62
C4 Scan					
FTV _{1-min}	PE>40 SER>0.5	0.85 [0.74,0.95]	<0.05	0.12 ± 0.25	3.2 ± 6.2
FTV _{2.5-min}	PE>95 SER>0.8	0.83 [0.72,0.94]	<0.05	0.17 ± 0.47	2.7 ± 5.4
FTV _{Opt}	Early Phase=60 s PE>40 SER>0.35	0.85 [0.75,0.96]	<0.05	0.13 ± 0.26	3.5 ± 7.2
%C4/BL				% change	% change
FTV _{1-min}	PE>130 SER>1.1	0.82 [0.71,0.93]	<0.05	-99% ± 0.20%	-89% ± 7.0%
FTV _{2.5-min}	PE>120 SER>0.85	0.79 [0.66,0.91]	<0.05	-93% ± 24%	-62% ± 63%
FTV _{Opt}	Early Phase=60 s PE>115 SER>0.75	0.85 [0.74,0.95]	<0.05	-100% ± 1.7%	-47% ± 110%

Optimal thresholds, AUC performance, and P values for FTV measurements are shown in Table 13. Top AUC performance was shown at the C4 scan by FTV with a 1-minute early phase timing and optimal contrast thresholds of PE \geq 40% and SER \geq 0.5 (AUC [95% CI] = 0.85 [0.74,0.95], P < 0.05). FTV optimization contour plots at C4 showed a broad plateau near the origin, and higher AUC is visible for the 1-minute early phase timing across high performing PE/SER thresholds (Figure 25C, D). For %C4/BL, optimized FTV with a 1-minute early phase timing also performed better in terms of maximum AUC and in visual comparison of contour plots (Figure 25E, F). At BL, the FTV optimization contour plots were similar between the two sets of early phase images in terms of maximum AUC and contour shape

(Figure 25A), though peak performance was achieved for both early phase timings with PE/SER thresholds of 0/0 and no statistical significance was observed (minimum $P = 0.18$).

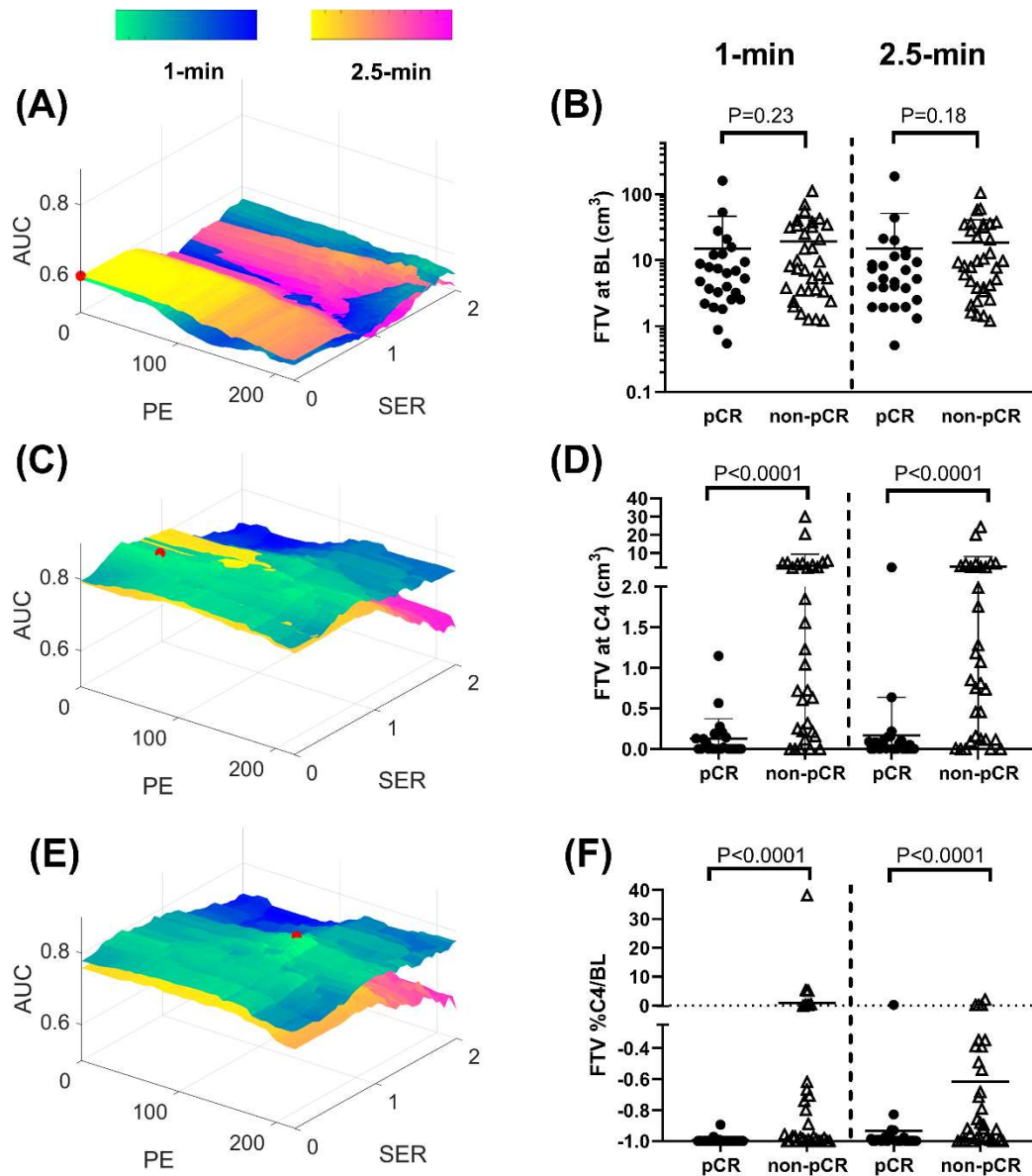


Figure 25 Comparison of functional tumor volume (FTV) optimization contour plots between 1-minute and 2.5-minute early phase timings for the baseline (BL) scan (A), cycle 4 (C4) scan (C), and %C4/BL (E). Peak AUC for each plot is marked with a red dot. Dot plots are also shown, comparing optimal FTV between patients who had a pathologic complete response (pCR) and those who did not for each early phase timing at BL scan (B), C4 scan (D), and %C4/BL (F).

Comparison of the AUC performance for different early phase timings can be seen in the contour plots in Figure 26A, C, and E, where contours corresponding to optimal early phase timings cover suboptimal early phase timings. From interpolated fast DCE MRI data, an optimal early phase timing was found to be 30 s for the BL scan, showing an AUC (95% CI) performance of 0.69 (0.55,0.82) ($p < 0.05$; Table 13, Figure 26A). Optimal FTV early phase timings were found to be 1 minute for both C4 and %C4/BL (Table 13, Figure 26B, C). For FTV_{Opt} at C4 and %C4/BL, optimal PE/SER thresholds and peak AUC were similar to those of FTV_{1-min} but were not identical as a result of the interpolation of the enhancement curves.

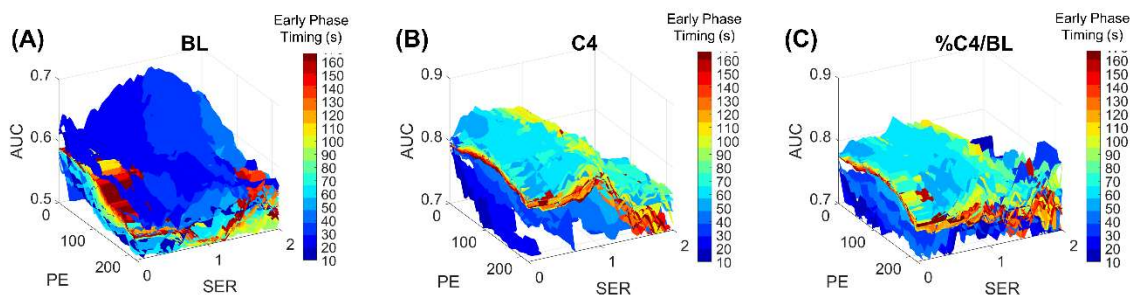


Figure 26 Comparison of functional tumor volume (FTV) optimization contour plots between different early phase timings for FTV_{Opt} at baseline (BL) scan (A), cycle 4 (C4) scan (B), and the relative change (%C4/BL) between the two scans (C). AUC = area under the receiver operating characteristic curve, PE = percentage enhancement, SER = signal enhancement ratio.

3.5 Discussion [FTV for TNBC Response]

Tumor volume measurements by fast DCE MRI at C4 and %C4/BL were found to be capable of discriminating between pCR and non-pCR to NAST in patients with TNBC. In comparison, tumor volume measurements at BL did not discriminate pCR from non-pCR to NAST, with the sole exception of FTV measured on an optimal early phase at 30 seconds after injection. The volume measurements extracted using enhancement thresholds showed stronger performance in comparison to volume measurements that did not use thresholds. Both ETV and optimized FTV showed stronger performance with an early phase timing of 1 minute compared with an early phase timing of 2.5 minutes. By leveraging

interpolated rapidly sampled fast DCE enhancement curves, the FTV_{Opt} experiment also showed an optimal early phase timing of 1 minute for both C4 and %C4/BL.

Much of the previous work investigating FTV as a predictor of treatment response in breast cancer preceded or stemmed from the multi-center I-SPY1 and I-SPY2 trials^{145,147-149,163,164}. Two of these studies applied FTV to predict pCR^{149,164}. Both studies used early phase timings of 2.5 minutes and with longitudinal imaging. The optimal contrast threshold values for %C4/BL FTV_{2.5-min} were similar to the thresholds used in these earlier studies, though the AUC performance in the earlier studies was slightly lower, likely due to their multi-center setting^{149,164}.

Two previous studies have optimized FTV contrast thresholds for the TNBC subtype^{149,150}. In a cohort of 30 TNBC patients, Li et al. examined change in FTV across 4 cycles of NAST as a predictor of pCR and found optimal thresholds of PE > 140% and SER > 0¹⁴⁹. Lo et al. examined changes in FTV after 1 cycle of NAST in a small TNBC subset (n = 11) and found that optimized contrast thresholds PE > 120% and SER > 1.4 best predicted recurrence-free survival¹⁵⁰. At %C4/BL, optimal PE thresholds for FTV_{1-min} and FTV_{2.5-min} in the current study were similar to contrast thresholds used in these earlier studies, and SER similar to Lo et al. was found to be useful.

Assessment of lesion enhancement early after injection by fast DCE MRI is useful for screening and diagnosis for breast lesions, and has been shown to correlate with both microvessel density and aggressiveness^{83,151-153}. The optimal FTV early phase timings of 30 s at BL and 1 minute at C4 and %C4/BL may leverage this correlation to measure the well-perfused volume of the tumor with aggressive characteristics.

Many of the previous studies used early phase timings of 2.5 minutes and a validated semi-automated segmentation tool^{99,148,149,163}. One of these studies examined FTV obtained using a manual segmentation method aided with visualization of SER maps and reported a slight improvement in predictive performance for volumes measured using this method¹⁶¹. Although segmentation in the

current study was performed on early phase subtractions by referencing PE instead of SER, the ETV measurements were similar to those reported by Henderson et al¹⁶¹. Because the setup and contrast injection protocols are fairly standardized across institutions and the semi-quantitative DCE MRI measurements have shown strong reproducibility, the FTV measurements in the current study were comparable to those obtained in other studies using a semi-automatic tool^{165,166}.

Limitations

There are some limitations to this current study. First, an inter-reader repeatability test of segmentation and its potential impact on the tumor volume measurements and their predictive performance was not performed. Second, the effect of interpolation on enhancement curves in the FTV_{Opt} analysis was not evaluated, though the results of this analysis would have been difficult to interpret because the actual temporal resolution of the dataset was not fixed and depended on the patient size. Third, the study was performed on a single scanner using a single imaging protocol. Nevertheless, the DISCO sequence used is widely available on the platform of one major vendor, and similar sequences are readily available on the platforms of the other vendors. Further, a prior study has found that the predictive value of FTV is stable with some variation in the imaging protocol¹⁶⁴. Therefore, the findings of the current study are expected to be reproducible and translatable, although additional studies would be helpful and multi-site, cross-platform validation is warranted. Finally, inter-patient variation in contrast arrival due to circulation differences among patients was not accounted for. Harmonizing contrast arrival at a nearby feeding vessel would reduce a source of potential timing variation, however, reliable identification of a feeding vessel is not always possible and the temporal resolution of the fast DCE MRI in this study was limited to ~11 s, which is too long to relative to the expected inter-patient differences in blood circulation.

3.6 Conclusion [*FTV for TNBC Response*]

Tumor volume measurements by fast DCE MRI were compared as discriminators of pCR and non-pCR in TNBC patients undergoing NAST. This study finds that selection of an early phase at 1 minute after contrast injection improves the predictive performance of FTV and TV measured after 4 cycles of NAST.

Chapter 4 – Quantitative Apparent Diffusion Coefficients from Peritumoral Regions as Early Predictors of Treatment Response to Neoadjuvant Systemic Therapy in Triple Negative Breast Cancer

This chapter is based upon the following article, which has been submitted to the Radiology: Imaging Cancer:

Musall BC, Adrada BE, Candelaria RP, Mohamed RMM, Abdelhafez AH, Son JB, Sun J, Santiago L, Whitman GJ, Moseley TW, Scoggins ME, Mahmoud HS, White JB, Hwang KP, Elshafeey NA, Boge M, Zhang S, Litton JK, Valero V, Tripathy D, Thompson AM, Yam C, Wei P, Moulder SL, Pagel MD, Yang WT, Ma J, Rauch GM. **Quantitative Apparent Diffusion Coefficients from Peritumoral Regions as Early Predictors of Response to Neoadjuvant Systemic Therapy in Triple-Negative Breast Cancer.** *In Submission.*

Key Results:

- Quantitative apparent diffusion coefficient maps features from peritumoral regions were predictive of response to neoadjuvant systemic therapy in triple-negative breast cancer
- Exclusion of fat-dominant regions from peritumoral regions did not improve the predictive performance of quantitative apparent diffusion coefficient map features

Summary Statement:

Features from quantitative apparent diffusion coefficient maps from the peritumoral regions after 2 and 4 cycles of neoadjuvant systemic therapy predicted pathologic complete response in triple-negative breast cancers.

4.1 Abstract [Peritumoral ADC for TNBC Response]

Background: Pathologic complete response (pCR) to neoadjuvant systemic therapy (NAST) in triple-negative breast cancer (TNBC) is a strong predictor of patient survival. Edema in the peritumoral region (PTR) has been reported to be a negative prognostic factor in TNBC.

Purpose: To determine if quantitative ADC features from PTRs on reduced field-of-view (rFOV) diffusion-weighted imaging (DWI) predict the response to NAST in TNBC.

Materials and Methods: This prospective study enrolled patients with biopsy-proven TNBC who underwent NAST and definitive surgery during 2015–2020. All patients had MRIs with rFOV DWI before and after 2 and 4 cycles of NAST. ADC histogram features were extracted from tumors and from PTRs of 5 mm, 10 mm, 15 mm, and 20 mm in thickness with inclusion and exclusion of fat dominant pixels. ADC features, individually in training and testing sets and combined in multivariate models with k-fold cross-validation, were tested for prediction of pCR using Mann Whitney U test and area under the receiver operating characteristic curve (AUC).

Results: One hundred eight women (median age [range], 52 [24-79] years) were included. Fifty-one patients (47%) had pCR, and 57 did not. Maximum ADC from PTR, measured after 2 and 4 cycles of NAST, was significantly higher in pCR patients. The top-performing feature for prediction of pCR was the standard deviation of the ADC from the 20-mm fat-inclusive PTR after cycle 4 of NAST (testing AUC: 0.84; 95% confidence interval: 0.69, 0.98; $P = 0.00012$). A multivariable model based on ADC features from fat-inclusive PTRs from a scan performed after cycle 2 of NAST showed top performance (AUC: 0.82; standard error: ± 0.08).

Conclusion: Quantitative apparent diffusion coefficient features from peritumoral regions are early predictors of the response to neoadjuvant systemic therapy in triple-negative breast cancer.

4.2 Introduction [Peritumoral ADC for TNBC Response]

Triple-negative breast cancer (TNBC) accounts for ~20% of all breast cancers. Compared to other types of breast cancer, TNBC is more aggressive and more likely to present as high grade and with nodal spread ¹⁶⁷. Owing to its lack of receptors, TNBC does not respond to conventional hormone-targeted therapies and is typically treated with neoadjuvant systemic therapy (NAST). Fewer than half of the patients with TNBC have a pathologic complete response (pCR) to NAST, and non-pCR status is a strong predictor of poor clinical outcome ¹¹⁶. Early prediction of the response to NAST is highly desirable as it could lead to improved patient outcome through triage of patients with incomplete or no response (“non-pCR”) to alternative treatments or triage of pCR patients to de-escalation of their treatment regimens ¹⁶⁸.

In breast cancer, the presence of peritumoral edema is known to correlate with poor outcome, such as lower distant-metastasis-free survival ⁸¹ and higher lymph node involvement ^{169,170}. MRI is capable of a multifaceted assessment of the peritumoral region (PTR) because edema manifests as hyperintensity on T2-weighted imaging ^{171,172}, enhancement on dynamic contrast-enhanced MRI ¹¹⁰, and high apparent diffusion coefficient (ADC) on diffusion-weighted imaging (DWI) ^{169,173}. Notably, the presence of peritumoral edema assessed on T2-weighted imaging has been reported to be a negative prognostic factor in breast cancer ^{81,170,174}. Peritumoral edema is seen more frequently in TNBC than in other types of breast cancer ^{81,82,175}, although the potential clinical value of peritumoral edema assessed on T2-weighted images of TNBC is currently unclear ^{81,109,176}.

Quantitative imaging biomarkers of the PTR have also shown promise for applications in breast cancer. Radiomic features of the PTR on dynamic contrast-enhanced MRI have shown promise as predictors of sentinel node metastases ^{177,178} and treatment response ¹¹⁰. ADC metrics from the PTR have been found to correlate with lymphovascular invasion ^{169,179-181}, molecular subtype ^{96,182,183}, lymph node metastasis ^{181,183,184}, and tumor size and histological grade ¹⁸¹. However, conventional DWI is not

recommended for measurements from regions smaller than 2 cm owing to its geometric distortion and lower spatial resolution ¹⁸⁵. Advanced DWI techniques allow higher spatial resolution and less image distortion and thus have potential to improve assessment of the PTRs by providing better definition of the tumor margins and fine anatomic structures in comparison to conventional DWI ¹⁸⁶⁻¹⁸⁸. Reduced-field-of-view (rFOV) DWI in particular has shown promise for breast cancer assessment as it reduces echo planar imaging artifacts by reducing the imaging field of view and thereby shortening the readout time while maintaining the spatial resolution ^{189,190}. One preliminary report in a small group of patients ($n = 7$) showed that ADC metrics from the PTR by high-resolution rFOV DWI had promise for assessment of treatment response ¹⁸⁸.

The purpose of our study was to determine if quantitative ADC features from the PTRs, leveraging rFOV DWI for its reduced echo planar imaging artifacts, are predictive of the response to NAST in TNBC. We examined ADC features from PTRs of different thicknesses, with both inclusion and exclusion of the regions of fatty tissue, and at different imaging timepoints during the course of NAST for their predictive performance.

4.3 Methods [Peritumoral ADC for TNBC Response]

Patients

This study enrolled 108 treatment-naïve patients with biopsy-confirmed clinical stage I-III TNBC between December 2015 and September 2020 in our Institutional Review Board-approved and Health Insurance Portability and Accountability Act-compliant ongoing prospective clinical trial ARTEMIS (“A Robust TNBC Evaluation Framework to Improve Survival”; NCT02276442). All patients provided written informed consent. All patients received NAST and underwent an MRI scan at baseline and after 2 cycles (C2 scan), and 4 cycles (C4 scan) during the course of treatment. NAST consisted of dose-dense doxorubicin and cyclophosphamide for 4 cycles followed by paclitaxel every 2 weeks for 4 cycles or weekly for a total of 12 doses. The minimum tumor size in all patients at baseline was 1.0 cm. All

patients underwent surgery after the completion of NAST. Pathologic findings from surgery were used to classify patients as pCR or non-pCR, with pCR defined as having no residual invasive disease in the breast or the axillary lymph nodes.

MRI Acquisition

All MRI scans were conducted on a GE 3.0-T MR750w whole body scanner (Waukesha, WI) with an 8-channel phased array bilateral breast coil and with the patients in the prone position. Each MRI scan included an axial T2-weighted series, a dynamic contrast-enhanced MRI series, and an axial DWI series. The rFOV DWI series used the Field of view Optimized and Constrained Undistorted Single-Shot pulse sequence¹⁹¹. This sequence employs a 2D spectral-spatially selective radiofrequency (RF) pulse in the presence of an echo-planar shaped gradients for inner volume excitation. Combined with a slice selective refocusing RF pulse, the 2D RF pulse has an added advantage of fat suppression by placing the spatially-shifted fat outside the refocusing slice. A pre-excitation fat suppression pulse was also applied. Compared to conventional DWI, rFOV DWI allows a shorter echo train for a desired resolution, with reduced image blurring and reduced artifacts. Typical scan parameters for the rFOV DWI were as follows: TE/TR = 70/4000 ms, slices = 13-16, slice thickness = 4 mm, slice gap = 0 mm, FOV = 16 x 16 cm, acquisition matrix = 80 x 80, in-plane spatial resolution = 2 x 2 mm, scan duration = 5 minutes, and b-values [signal averages] = 100 [4] and either 800 [16] or 1000 [16] s/mm². A typical image from this series is presented in Figure 27A.

Image Analysis

ADC maps were generated from the acquired rFOV DWI images using a linear solution of a mono-exponential model with the signal levels at b100 and the higher b-value (either b800 or b1000). Tumor segmentation was performed using Imagel, a graphical user interface-based software developed in-house for image analyses. Imagel features importing/exporting Digital Imaging and Communications in Medicine-compatible images and manual and semi-automatic contouring of image regions of interest

¹⁶². Two fellowship-trained breast radiologists (AHA and RMM) segmented the entire tumor across all slices on ADC maps for all scans, excluding regions of necrosis or biopsy clip artifacts. Tumor segmentations were reviewed by a radiologist with 20 years of experience (GMR). If tumors were not visible on the C2 scan or the C4 scan, the tumor bed was contoured. The tumor volume on rFOV DWI (TV_{DWI}) was calculated as the summed volume of the segmented tumor voxels for each scan. PTRs were automatically generated in Imager by propagating outwards from the tumor boundaries to thicknesses of 5 mm, 10 mm, 15 mm, and 20 mm (with each of the larger PTRs including the smaller ones yet not including the tumor; Figure 27B). Additionally, fat-dominant voxels with low signal intensity on the b100 images were excluded from the PTRs using a histogram-based thresholding tool to create a set of fat-exclusive PTRs (Figure 27C).

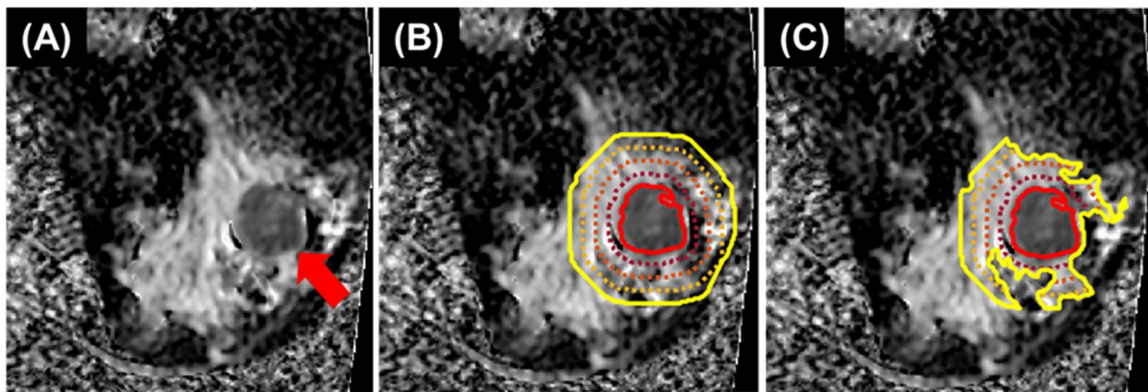


Figure 27 Peritumoral region segmentation technique in a 48-year-old woman with triple-negative breast cancer of the right breast. **A**, ADC map showing known 4.8 cm cancer at 9 o'clock position 8 cm from the nipple (red arrow). **B**, ADC maps with fat-inclusive peritumoral regions. **C**, ADC maps with fat-exclusive peritumoral regions. The solid red line in **B** and **C** show the tumor boundary; the outer lines show boundaries of different peritumoral region thicknesses: solid yellow line - 20 mm, the inner dashed orange line - 15 mm, dashed red line - 10 mm, and dashed maroon line - 5 mm.

For each scan, a set of 11 first-order histogram features were extracted from the ADC map for the tumor and each PTR thickness for fat-inclusive and fat-exclusive PTRs. These histogram features were as follows: minimum, maximum, mean, median, standard deviation, kurtosis, skewness, and 10th, 25th, 75th, and 90th percentiles. Voxels with ADC of 0 or lower were excluded from calculation of these

features. Both relative and absolute changes from the baseline scan to the C2 scan and the C4 scan were calculated for PTR ADC features and TV_{DWI} .

Statistical Analysis

The 108 patients were divided into training ($n = 77$) and testing ($n = 31$) sets. For each PTR ADC feature and TV_{DWI} , differences between pCR and non-pCR patients were tested using the Mann Whitney U test, separately for the training and the testing sets. Univariate analysis was also performed separately in the training and the testing sets to find the area under the receiver operating characteristic curve (AUC). Metrics with the lower bound of the 95% confidence interval (CI) for the AUC being at least 0.5 in both the training and the testing sets were considered significant.

TV_{DWI} measurements which reached significance by this criterion were then tested as confounders of the ADC features that reached the level of significance at the same scan. This test was performed with logistic regression using the “glm” package in R (version 3.6.3, Vienna, Austria) ¹⁹².

Training and testing sets were then combined for multivariate analyses with k-fold cross-validation. Feature selection was performed with the packages “caret” and “pROC” in R (version 3.6.3, Vienna, Austria) ¹⁹² using an elastic net algorithm for several permutations of the dataset, and average AUC and standard error were calculated for each model. Initially, PTR and tumor ADC features were considered for fat-inclusive and fat-exclusive regions separately. We then evaluated these features from both the fat-inclusive and fat-exclusive features together to investigate if the features from the different regions were complementary. These evaluations were performed for each of the scan timepoints with relative and absolute changes in ADC features from BL.

To evaluate possible redundancy between ADC features and TV_{DWI} , model feature selection was repeated with TV_{DWI} included in multivariate models. Displacement of ADC features from the model in favor of TV_{DWI} was considered an indication of redundancy between the two.

To assess the robustness of PTR ADC features with respect to the selected PTR thickness, multivariate models were fitted using ADC features exclusively from the 5-mm PTR. The AUC performance of these models was reassessed using the same PTR histogram features but selected instead from the 10-mm, 15-mm, or 20-mm PTR (e.g., 10-mm ADC kurtosis was substituted for 5-mm ADC kurtosis). The aforementioned test allowed us to evaluate the effect of inter-reader variability, specifically tumor boundary delineation, on PTR ADC features and test the potential influence of this variability on model performance.

4.4 Results [Peritumoral ADC for TNBC Response]

51 of the 108 patients (47%) had pCR and 57 had non-pCR. Characteristics of the patients in the training and the testing sets are summarized in Table 14. Not all patients underwent the scheduled MRI scans at all the timepoints. The numbers of baseline, C2, and C4 scans obtained for each patient group are shown in Table 14. The C2 scan was optional per the ARTEMIS study protocol, and only 52 of the 108 patients underwent the C2 scan.

Table 14 Characteristics of all patients and patients in the training and the testing sets.

Characteristic	All Patients N (%)	Training Set N (%)	Testing Set N (%)	P-value*
Number of patients	108	77	31	
Median age (range), y	52 (24-79)	54 (24-79)	49 (26-77)	
T-stage				0.10
1	23 (21)	12 (16)	11 (35)	
2	72 (67)	56 (73)	16 (52)	
3	10 (9)	7 (9)	3 (10)	
4	3 (3)	2 (2)	1 (3)	
N stage				0.57
0	67 (62)	49 (64)	18 (58)	
1	28 (26)	18 (23)	10 (32)	
2	3 (3)	3 (4)	0 (0)	
3	10 (9)	7 (9)	3 (10)	
Tumor histological type				0.43
Invasive ductal carcinoma	95 (88)	68 (88)	27 (87)	
Invasive lobular carcinoma	1 (1)	1 (1)	0 (0)	
Invasive mammary carcinoma	1 (1)	0 (0)	1 (3)	
Metaplastic	9 (9)	6 (8)	3 (10)	
Apocrine	2 (1)	2 (3)	0 (0)	
Type of surgery				0.17
Mastectomy	37 (34)	23 (30)	14 (45)	
Segmentectomy	71 (66)	54 (70)	17 (55)	
[Postsurgery pathology findings]				
Baseline	108	77	31	
[pCR]	51 (47)	36 (47)	15 (48)	0.99
[non-pCR]	57 (53)	41 (53)	16 (52)	
Cycle 2	52	28	24	
[pCR]	26 (50)	15 (54)	11 (46)	0.78
[non-pCR]	26 (50)	13 (46)	13 (54)	
Cycle 4	90	60	30	
[pCR]	43 (48)	28 (47)	15 (50)	0.83
[non-pCR]	47 (52)	32 (53)	15 (50)	

Note—P-values were calculated using Fisher's exact test or chi-squared test. pCR = pathologic complete response.

Univariate Analysis

By the univariate analysis, 12 PTR ADC features (Table 15, Figure 28) were significantly different between the pCR and the non-pCR groups in both the training and the testing sets. ADC features that differed significantly between the pCR and the non-pCR groups were present from each PTR thickness (5, 10, 15, and 20 mm). The top-performing ADC feature was ADC standard deviation of the fat-inclusive 20-mm PTR (Figure 28A; testing AUC: 0.84; 95% CI: 0.69, 0.98; $P = 0.0012$). Ten of the 11 remaining significant features were from the C4 scan and included maximum or high percentiles from both fat-inclusive and fat-exclusive PTRs and standard deviation from fat-inclusive PTRs. ADC maximum from the fat-inclusive 20-mm PTR was the only ADC feature that was significant from the C2 scan (Figure 28D; testing AUC: 0.71; 95% CI: 0.51, 0.91; $P = 0.041$). For all significant features, pCR patients had a lower ADC maximum/90th percentile and a lower ADC standard deviation than non-pCR patients had (Figure 28). ADC maximum features from several PTR thicknesses from the C4 scan were significant for and fat-exclusive PTRs, and their absolute measurements were similar between and fat-exclusive PTRs (Table 15). Other C2 scan features and the relative tumor volume change from the baseline scan to the C2 scan were not significant by univariate analysis. However, the analysis was likely underpowered owing to the small number of C2 scans (Table 14). No features from the baseline scan and no ADC features from the tumor were significant by the univariate analysis.

When TV_{DWI} from the C4 scan was considered as a confounder of significant ADC features as predictors, only ADC standard deviation of the 20-mm PTR and ADC standard deviation of the 15-mm PTR were independent of TV_{DWI} ($p = 0.039, 0.048$, respectively). Adjustment of the single significant ADC features from the C2 scan was not performed, as TV_{DWI} from the C2 scan did not reach significance by the univariate analysis.

Table 15 Top performing peritumoral region apparent diffusion coefficient features by univariate analysis for prediction of a pathologic complete response

Scan	PTR Thickness (mm)	Fat	Feature	Training	pCR	non-pCR	Testing	pCR	non-pCR
				AUC (95% CI) Mann Whitney U Test	ADC ($\times 10^{-3}$ mm ² /s)	ADC ($\times 10^{-3}$ mm ² /s)	AUC (95% CI) Mann Whitney U Test	ADC ($\times 10^{-3}$ mm ² /s)	ADC ($\times 10^{-3}$ mm ² /s)
Cycle 4	20	Incl.	SD	0.68 (0.53, 0.82) P = 0.020	0.51 \pm 0.096	0.57 \pm 0.096	0.84 (0.69, 0.98) P = 0.0012	0.47 \pm 0.084	0.59 \pm 0.095
Cycle 4	15	Incl.	SD	0.66 (0.52, 0.80) P = 0.034	0.51 \pm 0.093	0.56 \pm 0.093	0.83 (0.67, 0.98) P = 0.0017	0.46 \pm 0.091	0.57 \pm 0.094
Cycle 4	5	Incl.	Maximum	0.70 (0.56, 0.83) P = 0.0090	2.9 \pm 0.71	3.4 \pm 0.98	0.81 (0.65, 0.97) P = 0.0032	2.6 \pm 0.65	3.6 \pm 0.88
Cycle 4	10	Incl.	SD	0.67 (0.53, 0.81) P = 0.022	0.50 \pm 0.087	0.55 \pm 0.086	0.77 (0.60, 0.94) P = 0.011	0.46 \pm 0.087	0.55 \pm 0.088
Cycle 4	20	Incl.	Maximum	0.66 (0.52, 0.79) P = 0.040	3.4 \pm 0.75	4.0 \pm 0.12	0.77 (0.59, 0.95) P = 0.011	3.1 \pm 0.59	4.1 \pm 0.13
Cycle 4	5	Excl.	Maximum	0.71 (0.57, 0.84) P = 0.0059	2.7 \pm 0.57	3.2 \pm 0.89	0.75 (0.57, 0.93) P = 0.020	2.7 \pm 0.51	3.4 \pm 0.95
Cycle 4	15	Excl.	Maximum	0.67 (0.54, 0.81) P = 0.020	2.9 \pm 0.53	3.4 \pm 0.92	0.75 (0.56, 0.93) P = 0.021	2.8 \pm 0.74	3.8 \pm 0.14
Cycle 2	20	Incl.	Maximum	0.71 (0.51, 0.91) P = 0.058	3.5 \pm 1.0	4.6 \pm 0.18	0.75 (0.54, 0.96) P = 0.041	3.4 \pm 0.74	4.1 \pm 0.69
Cycle 4	10	Excl.	Maximum	0.70 (0.56, 0.83) P = 0.0082	2.8 \pm 0.58	3.4 \pm 0.93	0.74 (0.55, 0.93) P = 0.024	2.7 \pm 0.78	3.5 \pm 0.95
Cycle 4	20	Excl.	Maximum	0.69 (0.55, 0.82) P = 0.013	3.0 \pm 0.53	3.5 \pm 0.91	0.73 (0.54, 0.92) P = 0.033	2.9 \pm 0.65	3.9 \pm 0.14
Cycle 4	5	Incl.	SD	0.71 (0.58, 0.85) P = 0.0040	0.46 \pm 0.084	0.52 \pm 0.074	0.72 (0.53, 0.91) P = 0.041	0.46 \pm 0.092	0.54 \pm 0.092
Cycle 4	10	Excl.	90 th percentile	0.65 (0.50, 0.79) P = 0.051	1.9 \pm 0.37	2.1 \pm 0.31	0.70 (0.50, 0.90) P = 0.06	1.9 \pm 0.55	2.2 \pm 0.32

Note—Features were considered significant when the lower bound of the 95% CI exceeded 0.5 in both the training and testing tests and are ranked in that order. AUC = area under the receiver operating characteristic curve, AUC_{LL} = AUC lower limit, CI = confidence interval, FE = fat-exclusive, FI = fat-inclusive, SD = standard deviation

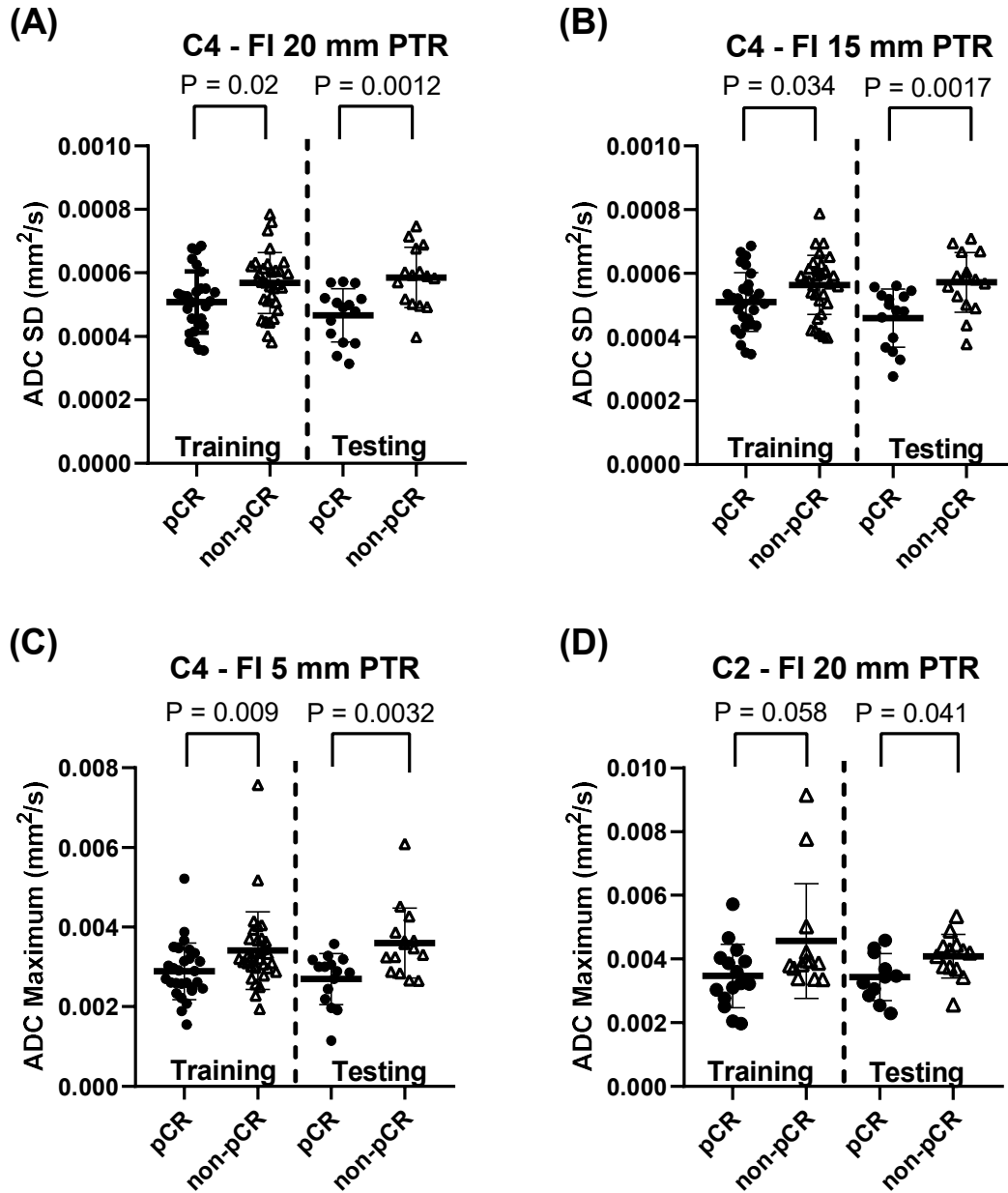


Figure 28 Dot plots and Mann Whitney p-values of the 4 top-performing peritumoral region (PTR) apparent diffusion coefficient (ADC) features compared using the area under the receiver operating characteristic curve (AUC) between patients with a pathologic complete response (pCR) and without a pCR (“non-pCR”) for both the training and testing sets. *A*, Cycle 4 fat-inclusive (FI) 20-mm ADC standard deviation (SD). *B*, Cycle 4 FI 15-mm ADC SD. *C*, Cycle 4 FI 5-mm ADC maximum. *D*, Cycle 2 FI 20-mm ADC Maximum.

Multivariate Analysis

In the multivariate analysis, the training and testing sets were combined and created patient populations (N) of 108 for the baseline scan, 52 for the C2 scan, and 90 for the C4 scan. The number of folds for each scan was chosen to include more than 15 patients in each fold, with k of 5 for the baseline scan, 3 for the C2 scan, and 4 for the C4 scan. Multivariate analysis including only ADC features revealed top performance of ADC features from fat-inclusive PTRs on the C2 scan (AUC: 0.82; standard error: 0.08) and ADC features from fat-inclusive PTRs on the C4 scan (AUC: 0.71; standard error: 0.06) (Table 16). For all scan timepoints, fat-inclusive models performed better than fat-exclusive or combined fat-inclusive and fat-exclusive models. The ADC features selected in all models typically showed good performance in the univariate analysis as well, with 7 of the 12 significant features by the univariate analysis selected as features in the multivariate models (Appendix A). Baseline ADC features, regardless of whether they were from fat-inclusive or fat-exclusive PTRs, did not show good performance in multivariate models (all AUCs were less than 0.67). Tumor ADC features were not selected by the top-performing multivariate models at any scan timepoint (Appendix A).

Multivariate analysis was repeated with TV_{DWI} included and, in all cases, model performance was not improved (Table 16). Feature selections for all models are shown in *Appendix A. Multivariate Model Parameters from Chapter 4 – Quantitative Apparent Diffusion Coefficients from Peritumoral Regions as Early Predictors of Treatment Response to Neoadjuvant Systemic Therapy in Triple Negative Breast Cancer*.

Table 16 Multivariate model results for prediction of pathologic complete response: apparent diffusion coefficient features with and without inclusion of segmented tumor volume

Scan	Cross-validation N-folds (pts)	Fat-inclusive Only AUC (SE)	Fat-exclusive Only AUC (SE)	Combined Features AUC (SE)
Baseline	5 (108)	0.66 (0.06)	0.59 (0.07)	0.64 (0.05)
+TV _{DWI}		0.65 (0.06)	0.61 (0.06)	0.63 (0.05)
Cycle 2	3 (52)	0.82 (0.08)	0.69 (0.09)	0.76 (0.09)
+TV _{DWI}		0.81 (0.07)	0.69 (0.05)	0.77 (0.07)
Cycle 4	4 (90)	0.71 (0.06)	0.65 (0.07)	0.71 (0.06)
+TV _{DWI}		0.71 (0.07)	0.66 (0.07)	0.71 (0.06)

Note—AUC = area under the receiver operating characteristic curve, FE = fat-exclusive, FI = fat-inclusive, pts = patients, SE = standard error, TV_{DWI} = tumor volume on diffusion-weighted imaging.

Robustness of Models by PTR Thickness

When fit exclusively on 5-mm PTR ADC features, multivariate models showed their top performance for the C2 scan (AUC: 0.74; 95% CI: 0.60, 0.87) and C4 scan (AUC: 0.88; 95% CI: 0.81, 0.95; Table 17). AUC performance remained robust when 10-, 15-, or 20-mm ADC features were substituted into these models (Table 17). The results from the baseline scan were consistently low (all AUC < 0.67).

Table 17 Robustness of multivariate models with respect to variation in PTR thickness.

Scan	5 mm	10 mm	15 mm	20 mm
	AUC (95% CI)	AUC (95% CI)	AUC (95% CI)	AUC (95% CI)
Baseline	0.66 (0.55, 0.76)	0.66 (0.55, 0.76)	0.66 (0.55, 0.76)	0.66 (0.55, 0.76)
Cycle 2	0.74 (0.60, 0.87)	0.72 (0.59, 0.86)	0.73 (0.59, 0.87)	0.71 (0.57, 0.86)
Cycle 4	0.88 (0.81, 0.95)	0.82 (0.73, 0.91)	0.76 (0.66, 0.86)	0.79 (0.70, 0.88)

Note— For each scan, multivariate models were fit to ADC features from the 5 mm PTR and model performance was assessed with substitution of features from the 10, 15, and 20 mm PTR thicknesses. AUC = area under the receiver operating characteristic curve, AUC_{LL} = AUC lower limit, AUC_{UL} = AUC upper limit, PTR = peritumoral region.

4.5 Discussion [Peritumoral ADC for TNBC Response]

Our study showed that quantitative apparent diffusion coefficient features from the peritumoral region on reduced-field-of-view diffusion-weighted imaging were able to predict pathologic complete response to neoadjuvant systemic therapy in triple-negative breast cancer. Top performance was by a multivariate model based on apparent diffusion coefficient features from fat-inclusive peritumoral

regions from the scan after 2 cycles of neoadjuvant systemic therapy. All multivariate models showed their best performance when using fat-inclusive apparent diffusion coefficient features for predicting pathologic complete response. The addition of tumor volume by diffusion-weighted imaging as a model feature did not improve model performance.

Higher PTR ADC maximum has been previously shown to be indicative of peritumoral edema ¹⁶⁹. Previous studies of breast cancer that included all subtypes found that the presence of peritumoral edema, as assessed by T2-weighted imaging, was associated with lower distant-metastasis-free survival ⁸¹, with more axillary lymph node metastases ¹⁷⁰, with increased aggressiveness ¹⁷⁴, and with both poor response and lower recurrence-free survival ¹⁰⁹. However, the value of peritumoral edema assessed on T2-weighted imaging as a negative prognostic finding for TNBC is not completely known. Bae et al. found a direct correlation between the presence of peritumoral edema on T2-weighted imaging and the absence of pCR in 132 TNBC patients ¹⁰⁹. Harada et al. applied a method for scoring edema across the full breast on T2-weighted imaging in 57 TNBC patients and did not find correlation with either pCR or Ki67 proliferation antigen levels ¹⁷⁶. Song et al. performed a propensity-matching study of 147 women with distant metastasis and 147 women without distant metastasis and found no correlation between the presence of peritumoral edema on T2-weighted imaging and distant-metastasis-free survival for an analysis of 86 TNBC patients ⁸¹. These studies evaluated peritumoral edema on pretreatment MRI only based on visual inspection of T2 weighted images. Our study differs since we performed quantitative evaluation of peritumoral edema based on ADC maps from rFOV DWI at longitudinal MRI during NAST. Our study did not find useful ADC features on the pretreatment scans for prediction of pCR. However, ADC maximum from the PTRs, which may indicate the presence of peritumoral edema, was significantly higher for non-pCR than pCR after 2 and 4 cycles of NAST.

Our findings of ADC features from PTRs as predictors of response to NAST are in agreement with several studies that report ADC features from PTRs to correlate with negative prognostic factors

including molecular subtype^{96,182,183}, tumor size and histological grade¹⁸¹, lymphovascular invasion^{169,179-181}, and lymph node metastasis^{181,183,184}. To our knowledge, only 1 other study evaluating ADC metrics from PTRs for assessment of treatment response with rFOV DWI, based on a small group of patients with all breast cancer subtypes ($n = 7$)¹⁸⁸. That study examined ADC features from PTRs and their change during treatment and found several metrics to be correlated with response, consistent with our findings from a larger cohort of TNBC only¹⁸⁸.

In our study, tumor ADC features were not useful for prediction of pCR by univariate or multivariate analysis. The poor performance of tumor ADC features is in line with the findings of a previous study. Li et al., in the I-SPY 2 trial, showed that although ADC was useful for prediction of treatment response in some subtypes of breast cancer, it did not show strong predictive value for the TNBC subtype when measured at early timepoints⁹⁹.

Several studies have examined quantitative radiomic imaging biomarkers from PTRs of different thicknesses in breast cancers and found that features from each thickness correlated with molecular subtype^{182,187}; nuclear grade, Ki67 expression, and lymph node metastasis¹⁸⁷; treatment response^{188,193}; and tumor-infiltrating lymphocytes¹⁸⁸. Our study also found useful features from each investigated PTR thickness for prediction of NAST response in TNBC patients.

To our knowledge, only 1 other study has examined PTR imaging metrics with both inclusion and exclusion of the regions of fat¹⁸⁴. Kettunen et al. used several methods for drawing regions of interest to extract ADC measurements from the PTR and found that ADC metrics from the contouring method that included fatty tissue were most strongly correlated with lymph node metastasis¹⁸⁴. This parallels our finding that fat-inclusive PTR ADC features showed the best performance for predicting pCR. In particular, the ADC standard deviation features from large, fat-inclusive PTRs performed well and were independent of the tumor volume. The exact cause for the correlation is unclear, although one recent study has reported that a greater volume of the tumor-fat interface is predictive of poor response

in all-comers of breast cancer ¹⁹⁴. Another study has found that tumors with a greater fraction of the tumor-fat interface were more likely to metastasize to axillary lymph nodes ¹⁹⁵.

Although the tumor volume measurement by DWI is inferior to that by dynamic contrast-enhanced MRI owing to a lack of perfusion contrast and possible distortion from echo planar imaging, tumor volume measured by rFOV DWI may still serve as an approximate measure of tumor size. We found that the addition of tumor volume by rFOV DWI did not improve performance of multivariate models for predicting pCR, suggesting that ADC features from PTRs were not redundant with tumor volume for this purpose.

Our study had some limitations. First, it was conducted using only one imaging protocol on a single MRI scanner and in a single institution. Second, we did not directly investigate the inter-reader variability of our tumor segmentation or fat-exclusion methods, although our multivariate predictive models were robust with respect to the size of the PTR.

In conclusion, quantitative apparent diffusion coefficient features by reduced-field-of-view diffusion-weighted imaging from the peritumoral region of triple-negative breast cancers after 2 and 4 cycles of treatment were predictive of pathologic complete response to neoadjuvant systemic therapy. Inclusion of fat voxels in the peritumoral regions showed the best performance for predicting response to neoadjuvant systemic therapy. Further validation of our findings in a larger population in a multi-institutional setting and correlation with long-term patient outcome are warranted.

4.6 Acknowledgements [*Peritumoral ADC for TNBC Response*]

B.C.M. would like to acknowledge partial support from the American Legion Auxiliary Fellowship in Cancer Research. We thank Stephanie P. Deming from the Scientific Publications at The University of Texas MD Anderson Cancer Center for her help in editing and proofreading this document. This research was conducted at the MD Anderson Center for Advanced Biomedical Imaging in-part with equipment support from General Electric Healthcare.

Chapter 5 – A Novel Convolutional Neural Network Inversion Algorithm for Magnetic Resonance Elastography of Breast Cancer

Magnetic Resonance Elastography (MRE) is a non-invasive MRI technique that can quantitatively measure tissue stiffness. Presently, MRE has been validated and is FDA-approved for staging of liver fibrosis, which is a diffuse pathology. MRE has also been investigated for applications in focal diseases, such as the detection and characterization of breast, liver, and prostate cancers. However, existing MRE techniques have poor spatial resolution and sometimes fail to visualize anatomy in stiffness maps. A few exceptional examples of this on *in vivo* breast MRE of TNBC from the ARTEMIS trial are shown below.

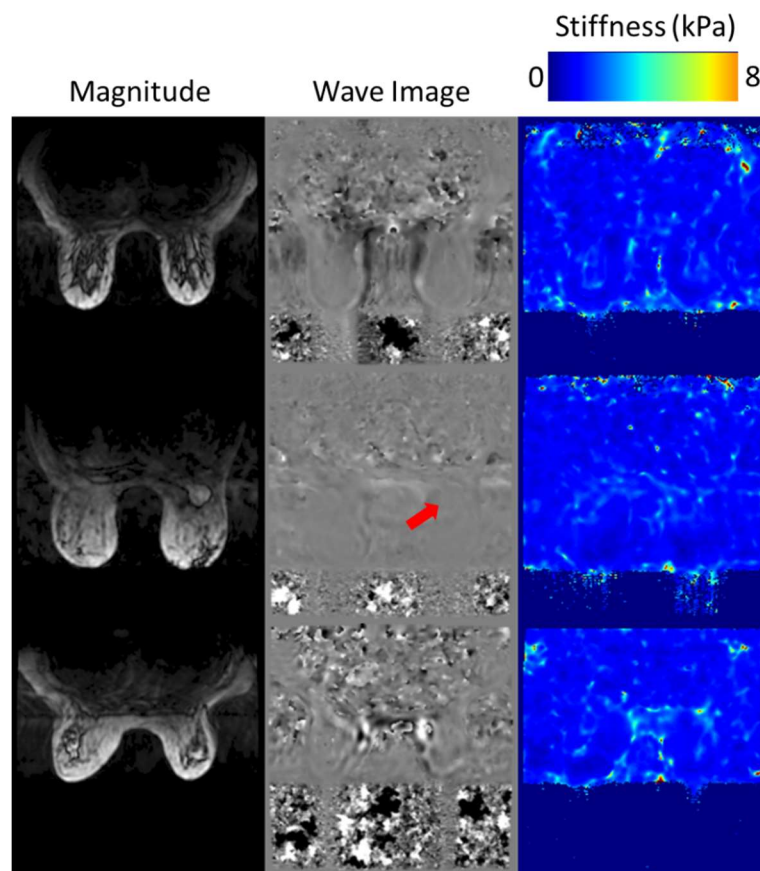


Figure 29 Examples of poor anatomy visualization in MRE stiffness maps from the vendor inversion algorithm. In row 1 and row 3, FGT is poorly visualized. In row 2, the tumor (red

arrow) does not show high stiffness in the vendor stiffness map. This is despite showing relatively homogenous grayscale values on the wave image that would correspond to a higher wavespeed and higher stiffness.

The poor spatial resolution arises from the inversion step of MRE processing, whereby the acquired MRE images are inverted into stiffness maps according to wave propagation models. An MRE inversion algorithm that circumvents this limitation will enhance the performance of MRE for cancer applications.

Convolutional neural networks (CNNs), a deep learning algorithm that shows top performance for applications in image processing, are capable of interpreting complex image features in the presence of noise or other nuisances. Like most deep learning algorithms, CNNs require training with a large set of curated data with known ground truth. Unfortunately, such a training dataset is not available for MRE applications. We therefore propose to produce the required training dataset with simulated MRE by finite volume methods (FVM) over a wide range of tissue stiffness and anatomical shapes. We hypothesize that this simulation-trained FCN will be applicable to the acquired data from *in vivo* MRE of TNBC and provide consistent stiffness measurement for better assessment of breast cancer.

5.1 Introduction [CNN-based Inversion Algorithm]

5.1.1 Magnetic Resonance Elastography in Cancer

All Cancers

Thus far, MRE has been used to assess a variety of solid cancers in humans^{52,53,196-225}. In general, tumors show increased stiffness in comparison to both surrounding tissues and benign lesions. While this contrast may hold use in some applications, the relatively high stiffness makes MRE of cancer more difficult as the long shear wavelengths are more difficult to detect for inversion. While the mechanical excitation frequency can be increased to shorten the shear wavelength, this creates a tradeoff due to increased wave attenuation at higher frequencies⁵². Despite this quandary, preliminary reports have

shown MRE-measured mechanical properties hold promise as a biomarker for a variety of oncology applications.

Mechanical properties from MRE have been shown useful for differentiating malignant lesions in the pancreas^{199,220,224}, liver^{202,207,211}, prostate²⁰⁹ and breast^{210,212-214}. MRE has shown promise for detection²¹⁸ and prediction of lymph node metastases²¹⁹ in prostate cancer. In glioma, stiffness values were shown to correlate with tumor grade and IDH1 mutation status²²⁶. In hepatocellular carcinoma, tumor stiffness showed correlation with clinical parameters⁵³ and early recurrence^{221,223}. Hepatocellular carcinoma stiffness was also seen to change in response to treatment²⁰⁰. Finally, MRE-measured mechanical properties also show potential for differentiating renal tumor subtypes²²⁵.

Breast Cancer

A number of publications have investigated MRE of the breast, either with the intent of optimizing the breast MRE technique or for characterization of breast lesions. These publications are summarized well in a recent review by Patel et al²²⁷.

A series of application studies have optimized MRE acquisition for the breast. Excitation is best performed as delivery of compression waves, which are converted to shear waves at the interface of the MRE driver with the patient²²⁸. Patients are imaged in the prone position with their breasts hanging downward into the coils. Excitation is applied to the sternum and allowing wave propagation from the chest wall. This patient and driver positioning minimizes and standardizes static compression of the breast, thereby simplifying the boundary conditions of the inversion problem²²⁹. Optimal excitation frequencies for measuring the tissue stiffnesses in breast MRE have been shown to lie between 50 and 100 Hz²³⁰.

A number of studies have published shear stiffness measurements of different breast tissues. A recent summary of these measurements can be seen in Table 2 of a review by McKnight et al²¹⁷. It is

important to recall that mechanical property measurements are dependent on frequency. Furthermore, stiffness values are dependent on measurement methods, selection of inversion algorithm, selection of elasticity model, and other acquisition factors. When the review is constrained to studies with excitation frequencies between 65-85 Hz, shear stiffnesses presented in literature have large ranges: fatty regions ~ 0.4 to 6 kPa, FGT ranges ~ 0.8 to 7 kPa, and tumors range ~ 3 to 30 kPa. These ranges are not at all encompassed by measurement variability in individual reports; however, tumors are consistently stiffer than other tissues across the reports. The variability of tissue stiffnesses presented in literature, while undoubtedly impacted by acquisition parameters, might also be impacted by the poor spatial resolution of MRE that would make ROI measurement of different tissues difficult or inconsistent.

5.1.3 Convolutional Neural Networks (CNNs)

Convolutional Neural Networks (CNNs) are a class of deep learning algorithm which specializes in processing data that is organized in elements along one or more dimensions²³¹. This might be time series data or spatial data, such as images. CNNs use convolutions to interpret the variation of data along its dimensions. Convolution is a mathematical operation which expresses the overlap of two functions as one function is shifted across another:

Equation 36: $f * g = \int_{-\infty}^{\infty} f(\tau)g(t - \tau)d\tau$

where f and g are functions varying in space and time, τ is the position in space, and t is time. It can be seen that the Fourier transform of k -space into image space (Equation 8) is simply deconvolution with a sinusoidal basis function corresponding to spatial frequency.

In 2D data processing by CNNs, convolution is performed on a local basis by applying kernels (equivalent to function g in Equation 36) to the image (equivalent to function f in Equation 36). The localization of the convolution output (also called a feature map) may be preserved by designating an

output space that conserves the dimensionality of the input. By stacking layers of convolutions and maintaining their localization, representations of complex image features can be created. In general, CNN kernels close to the input layer converge on edge-detection matrices. Collections of edges from shallow layers can be combined to create representations of complex image features in deeper layers. Importantly, the local edge detection in shallow layers can be shared between complex features in deeper layers. This sparsity is critical as it reduces the size of the CNN and allows for fast processing in comparison to other complex algorithms.

Like other supervised deep learning algorithms, CNNs can be trained for tasks with data consisting of paired inputs and a desired ground truth. For training, CNNs attempt to interpret data and are updated based on their error to improve their interpretation. Updates are calculated through backpropagation (an extension of the chain rule in calculus), which traces the error gradients between CNN predictions and ground truth through the layers of the CNN. The weights of the CNN kernels are updated using variational methods with the goal of minimize these gradients. This allows the weights of the CNN to converge upon a solution for the given task. To ensure a stable, generalizable solution, this is done in a series of iterative update steps, with each step consisting of a small batch of data.

Recently, CNNs have become more accessible to researchers due to development of programming interfaces and the cheap, widespread use of graphic processing units in computers. CNNs have shown enormous utility for medical imaging applications. The resulting popularity of CNNs has driven journals to split and form machine learning-specific categories such as *Radiology: Artificial Intelligence*. Machine learning sessions at conferences, such as the International Society of Magnetic Resonance in Medicine (ISMRM), typically fill their largest audience halls past capacity so that not even standing room is left.

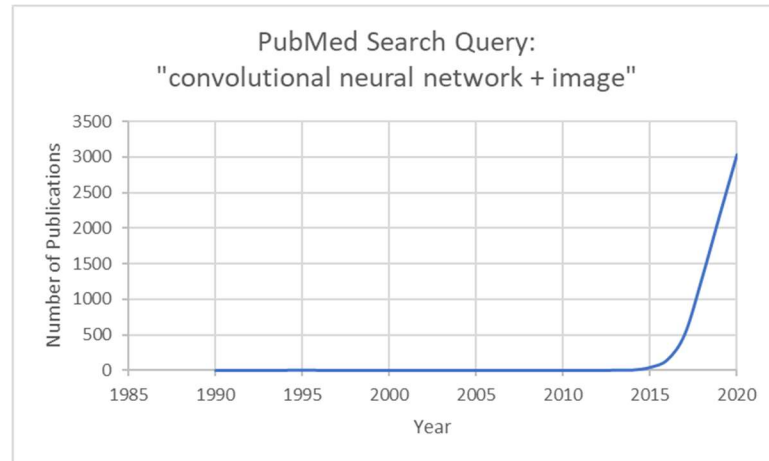


Figure 30 Number of PubMed results by year for publications mentioning CNNs and the word “image”.

Artificial neural networks have previously been proposed by one group for inversion in MRE^{232,233}. The second of these papers, a follow-up publication by Scott et al., utilizes CNNs which are trained on wave data simulated using a coupled harmonic oscillator model. This simple model discretely samples harmonic displacement in a medium with spatially varying properties; however, it neglects longitudinal waves and mode conversion at interfaces.

5.1.4 Finite Volume Methods (FVM)

Finite volume methods (FVM) are a numeric discretization method which calculate solutions to partial differential equation (PDE) across a system that is divided into discrete volumes called cells. Finite element methods (FEM), in contrast, estimate solutions to PDE for points on a grid through Taylor expansion. Rather than estimating the derivative at gridded points, FVM instead use the integral form of the PDE and solves for the value of cells by conserving flux across cell boundaries across time steps. Because FVM is an integral method and conserves flux, it shows superior performance in systems with discontinuities. FVM is covered in depth by Dr. Randall J. LeVeque in *Finite Volume Methods for Hyperbolic Problems*²³⁴. Much of the work in this chapter stems from his formulations and the software developed by his research program.

In 1D, the basic FVM for calculating the value of interest, Q , for the i^{th} cell at time t_n is:

$$\text{Equation 37: } Q_i^{n+1} = Q_i^n - \frac{\Delta x}{\Delta t} (F_{i+1/2}^n - F_{i-1/2}^n)$$

where n is the position in time, i is the spatial position, Δx is the size of the cell, Δt is the length of the time step, and $F_{i+1/2}$ is the flux at the edge of the cell.

Wave motion is a hyperbolic PDE which could be solved using an FVM formulation for elastic motion. For the scope of this dissertation, the mechanical wave motion of MRE is approximated using 2D FVM for a solid system that takes the form of a thin plate.

In 2D FVM of elastic motion in solids in a thin plate, the values which are tracked for each cell are the two normal stresses, the shear stress, and the velocities in each dimension²³⁴. These may be combined in the vector q :

$$\text{Equation 38: } q = \begin{bmatrix} \sigma^{xx} \\ \sigma^{yy} \\ \sigma^{xy} \\ u \\ v \end{bmatrix}$$

The constitutive relationships underlying this FVM algorithm are shown with derivatives in space or time as subscripts. To account for the thin plate and the necessary but small deformations in the 3rd dimension (with stress from z set to zero), an effective Lamé's first parameter may be designated:

$$\text{Equation 39: } \hat{\lambda} = \frac{2\mu\lambda}{\lambda + 2\mu}$$

The first of these constitutive relationships are the stress-strain relations for the cell. The FVM flux is the time derivative of stress (both normal and shear) applied to the cell by adjacent cells due to the differential in their velocities (spatial differential in velocity):

$$\text{Equation 40: } \sigma_t^{xx} - (\hat{\lambda} + 2\mu)u_x - (\hat{\lambda} + 2\mu)v_x = 0$$

Equation 41: $\sigma_t^{yy} - (\hat{\lambda} + 2\mu)u_y - (\hat{\lambda} + 2\mu)v_y = 0$

Equation 42: $\sigma_t^{xy} - \mu(v_x + u_y) = 0$

The remaining constitutive relations are simply Newton's Second Law for the system:

Equation 43: $\rho u_t - \sigma_x^{xx} - \sigma_y^{xy} = 0$

Equation 44: $\rho v_t - \sigma_x^{xy} - \sigma_y^{yy} = 0$

These equations may be combined into the following system:

Equation 45: $q_t + Aq_x + Bq_y = 0$

where A and B are matrices of coefficients from the constituent relations.

According to this formulation, the derivative of q with respect to time can be found by taking the spatial derivatives and relating them through the constituent relations. In Godunov's method, these spatial derivatives can be calculated exactly for a small step in time using a Riemann sum. The resulting time derivative of q can be used to update q and evolve the simulation forwards in time. In this manner, simulation of longitudinal and shear waves propagating through a media of variable material properties is possible.

The length of a simulation time step is bounded by the Courant-Friedrich-Lewis condition, which states that the simulation must be updated before the fastest wave in the stiffest cell passes halfway through that cell. The Courant number should therefore be:

Equation 46: $\frac{c_{max}\Delta t}{\Delta x} \leq 1$

In an elastic simulation with homogenous cell size, this would be the time for a longitudinal wave to travel halfway through the cell with the highest longitudinal wave speed.

5.2 Simulated MRE, CNN Inversion, and Phantom Validation [*CNN-based Inversion Algorithm*]

5.2.1 MRE Simulation by Finite Volume Analysis

During the conception of this project, several algorithms and software suites were considered for simulation. FVM, as implemented in the Clawpack Software Suite by Randall J. LeVeque and his team, were selected for the utility of the FVM algorithm and the convenient Clawpack suite²³⁵. Specifically, the “vc_elasticity_2D” module was used within the python-based API, PyClaw²³⁶. The monotized central-difference (MC) limiter, which is a second-order non-linear delimiter that enforces total variation diminishing within the numeric system, was applied to prevent oscillations:

Equation 47: $\phi(r) = \max[0, \min(2r, 0.5(1 + r), 2)]$

where ϕ is any calculated flux and r is the position. This has the effect of applying a second order flux conservation in smooth portions of the solution, while it applies first order flux conservation in regions of the solution with sharp gradients.

In all experiments, FVM was applied to a 512 x 512 grid with a designated physical size of 40 x 40 cm (0.78 mm to each side of a square cell). The left boundary was set to have periodic oscillation by adding a step source to the solver. This step source updated the q vector (Equation 38) of the left-most cells between each time step. Specifically, the y velocity of the q vector was set to oscillate in a sinusoidal manner at a given input frequency. The remaining components of the left-boundary q -vector were set to 0. The upper, lower and right boundaries were set to be sinks and therefore allowed wave propagation out of the geometry.

A few basic tests were completed to verify that wave propagation met expectations.

First, the wavespeed and wavelength for a shear wave of a given frequency in a given material were verified (Figure 31).

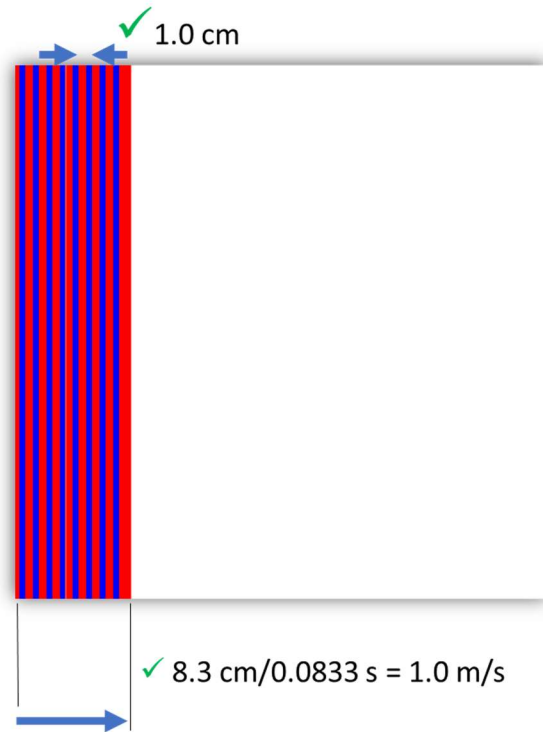


Figure 31 Y-velocity map 100 Hz shear wave propagation from the left side of a homogenous medium (40x40cm, 512x512 grid, $\rho = 1000 \text{ kg/m}^3$, $\mu = 1 \text{ kPa}$). The simulation was evolved to $t = 0.0833$ seconds. The shear wavelength and wave speed were as expected. Color scale was set with a small window to exaggerate the peaks and troughs of the waveform.

Next, for the same experiment as Figure 31, the shear stiffness was changed to verify the expected change in wavelength (Figure 32):

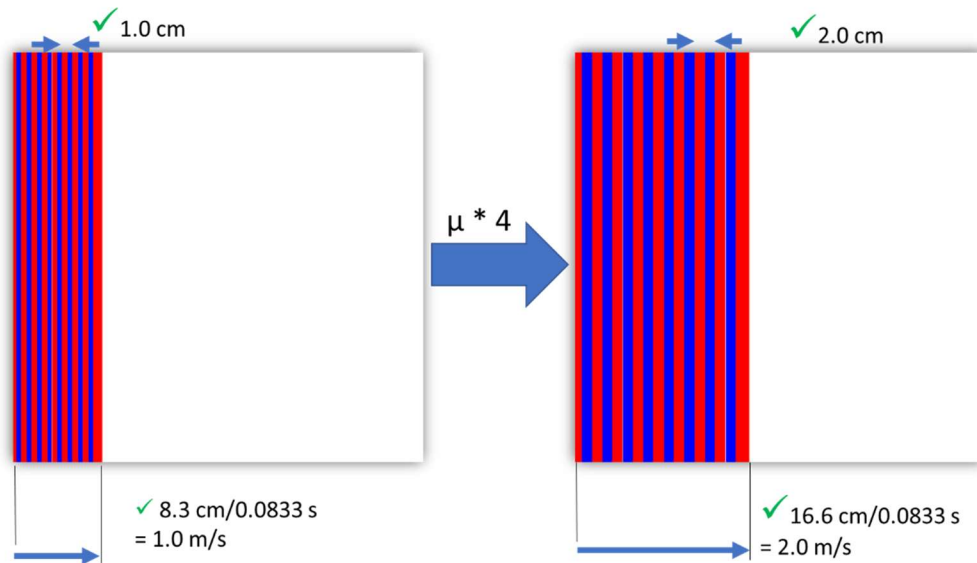


Figure 32 Y-velocity maps from 100 Hz shear wave propagation from the left side of a homogenous medium (40x40cm, 512x512 grid, $\rho = 1000 \text{ kg/m}^3$) for two shear stiffnesses: 1kPa (left) and 4 kPa (right). The simulation was evolved to $t = 0.0833$ seconds. The shear wavelength and wave speed were as expected. Color scale was set with a small window to exaggerate wave period.

Finally, the geometry was changed to have a stiff insert (6 kPa) within the 1kPa stiffness background. Change in shear stiffness wavelength between the materials is demonstrated, and longitudinal waves created by tangential reflection and refraction at the interface of the two materials can be seen (Figure 33).

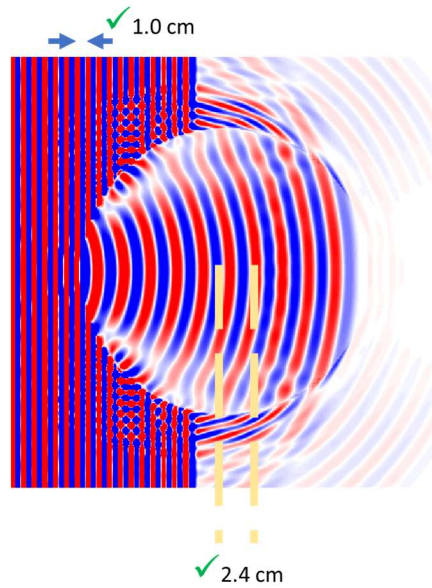


Figure 33 Y-velocity map from 100 Hz shear wave propagation from the left side of a homogenous medium (40x40cm, 512x512 grid, $\rho = 1000 \text{ kg/m}^3$, 1kPa) with a stiff circular insert (6 kPa). The shear wavelength was as expected. Color scale was set with a small window to exaggerate wave period. Longitudinal waves, which evolved from shear waves incident upon the interface of the two materials, can be seen at the right of the simulation. Reflected and refracted shear waves can also be seen.

5.2.2 Synthetic MRE Dataset

It has been shown previously shown that CNNs may learn to invert acquired MRI into underlying physical properties from a simulation with procedurally generated images²³⁷. These previous efforts created synthetic image geometries using mathematical functions. While mathematical functions create a sufficient basis for CNNs to learn voxel-specific image contrasts from simulation, MRE stiffness estimation requires interpretation of local wavelength across multiple voxels. To create a more comprehensive geometric basis of synthetic geometries, a unique method for procedural generation (PG) based on natural image shapes was developed.

Procedurally Generated Synthetic Geometries

To simulate harmonic wave behavior in geometries with sufficiently complex “anatomy,” a PG which pulls shapes from a large database of natural images was created. The image dataset, ADE20k²³⁸, contains a large variety of labeled natural images with various image labels. Segmentation labels were

pulled from the segmentation dataset randomly and overlain in a controlled random manner. The intent was to place one large object (to represent the imaged subject) and to fill it with smaller objects (to represent organs).

The steps of this procedural generation code, written in Matlab 2018b by Mathworks (Natick, MA), were as follows:

(1) Ranges of possible mechanical properties encompassing those found in normal tissue were designated:

- a. ρ (density) = 0.9-1.05 g/mL
- b. μ (shear stiffness) = 0.7-10 kPa
- c. λ (Lame's 1st parameter) = 3-75 kPa

(2) A 512x512 grid was created. A single, random set mechanical properties of each type was selected from the designated ranges and assigned across the grid.

(3) A sufficiently "round" segmented object was randomly selected from the ADE20k dataset

- a. Random object segmentations were pulled until an object fulfilling the following "roundness" condition shown in the following pseudo-code was met:

```
%Code in Matlab 2018b
[R,~] = radon(cropped_object_mask,0:2:180);
[len, ~] = size(R);
max_projection = R(round(len/2),:);
roundness = std(max_proj)./mean(max_proj);
```

Figure 34 Pseudo-code in Matlab 2018b for calculating the roundness of an object.

- b. The holes in the round object segmentation were filled.
- c. The round object was randomly scaled so that its maximum dimension was 70-85% of the 512x512 matrix dimensions.
- d. The large round object was assigned a single set of random material properties from the set ranges.

- (4) A random number (up to 30) of other segmented objects were selected and overlain on the large round object and background. Each of these were randomly rotated and then randomly scaled so that their maximum dimension fell within the maximum dimension of the round object. Each of these objects were also assigned a single set of random mechanical properties.

Examples of these synthetic geometries can be seen in Figure 35.

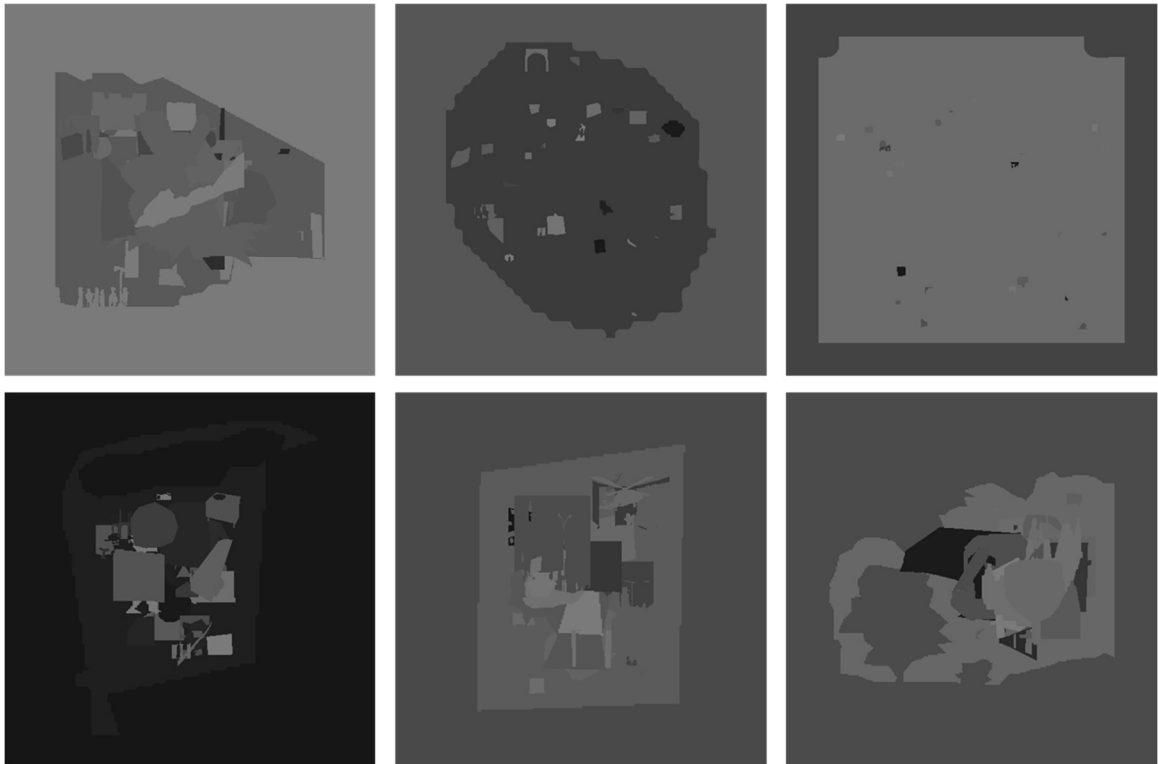


Figure 35 Procedurally generated stiffness geometries made from shapes within ADE20k.

MRE Simulation of Synthetic Geometries

Synthetic geometries were imported into PyClaw. Across all points, q -vectors were set at zero to start. To account for wave attenuation, attenuation was applied to the q -vector stress terms after each time step. The attenuation coefficient, at a value of 120 m^{-1} for a shear stiffness of 1.1 kPa at 60 Hz excitation, was taken from literature²³⁹ and was scaled inversely to shear stiffness on a cell-wise basis and proportionally to frequency in the following manner:

Equation 48: $\alpha_{cell} = (120 \text{ m}^{-1}) * \frac{f}{(60 \text{ Hz})} * \frac{\mu_{cell}}{1.1 \text{ kPa}}$

The non-oscillating boundaries (top, bottom, and right) were randomly designated to be sinks or reflective boundaries (also sometimes called “free” boundaries).

The source term on the left boundary was set to an amplitude of 100 μm and was set to oscillate sinusoidally with a frequency of 60 Hz. This frequency was chosen to match the acquired MRE datasets used in testing.

Displacements were calculated by integrating the velocity terms from the start of the simulation. After evolving the simulation to a steady-state of harmonic wave motion at 1 minute, displacement maps were saved for 6 offsets of a single excitation frequency cycle for both x and y directions. Examples of the displacement map sets can be seen for two geometries in Figure 36.

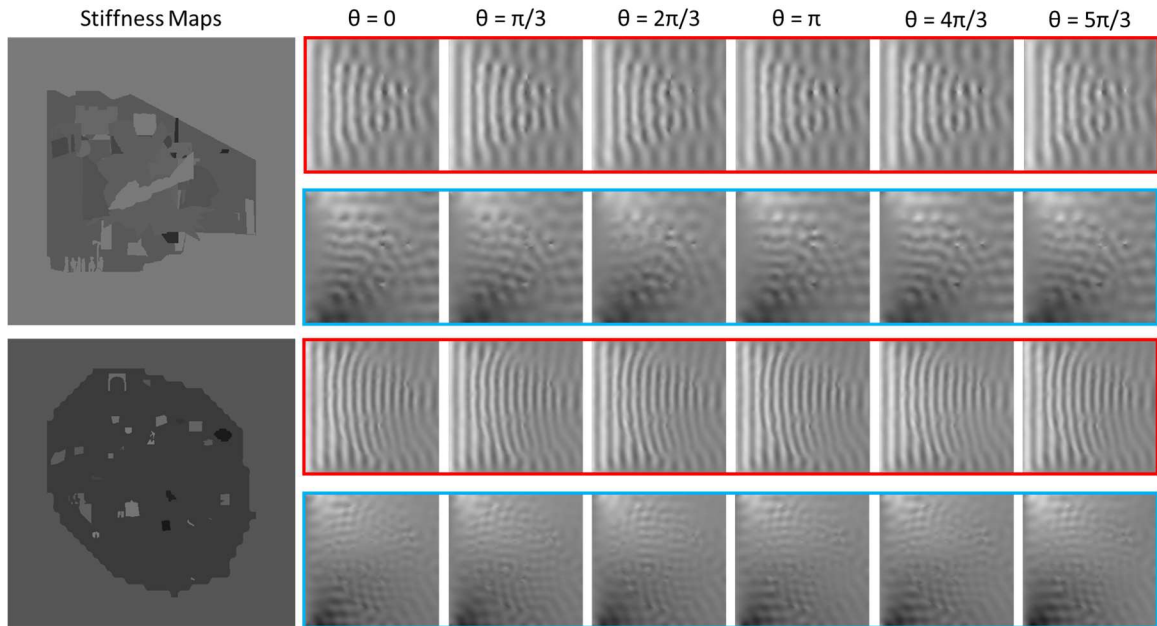


Figure 36 Examples of output displacement maps from MRE simulation for two procedurally generated geometries. Both y (red) and x (blue) displacements are shown for six offsets along one frequency cycle are shown.

5.2.3 CNN-Based Inversion

Dataset, CNN Design, and Training

A dataset consisting of paired shear stiffness maps and displacements from the MRE simulations was created. A total of 1232 geometries with 12 offsets displacement maps (6 in both x and y directions) were simulated. Each displacement map was paired with the stiffness geometry to create one data pair. The synthetic dataset was split 60:20:20 into training, validation, and testing sets so that each unique geometry was only presented in a single set. This produced to 6312, 2112, and 2124 samples for each dataset.

Using the Keras API²⁴⁰, a CNN consisting of eight 7x7-convolution layers with 20 kernels in each layer was trained to convert 512 x 512 displacement maps into 512 x 512 stiffness maps. Training was performed until validation loss was minimized. The following training parameters were used: batch size = 5, dropout = 0, learning rate = 0.001/epoch, optimizer = Adam, loss = mean-squared error. Data augmentation was performed with random flipping, shift, and rotation. Data augmentation by shearing was omitted.

Testing was carried out on both the withheld simulation testing dataset and an MRE phantom scan. Because the ground truth stiffness maps used in training were normalized, a conversion from neural network output to stiffness was calculated for the testing set.

Calibration and Results on Withheld Testing Set

Neural network label normalization is performed through subtraction of the mean value of a batch (zero-centering) and then division by the standard deviation (normalization). This process must be reversed on the CNN output to recover the true stiffness values. The optimal values were found to be multiplying by 37900 (Figure 37) and then adding the average difference with the testing ground truth, 3719.

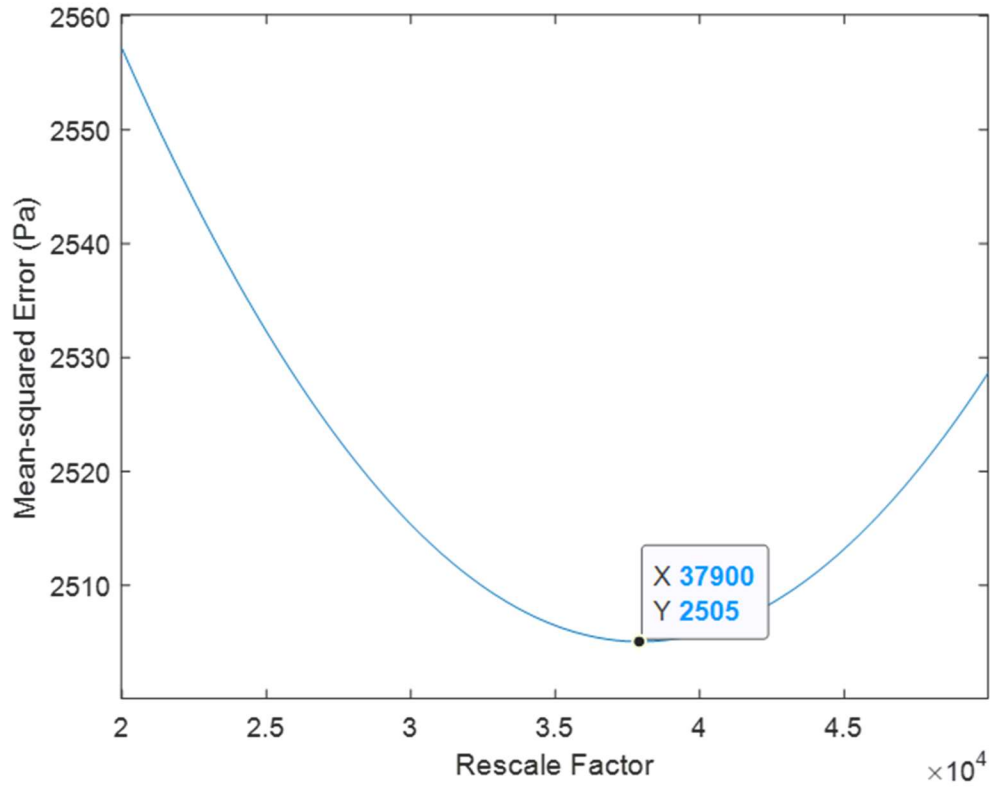


Figure 37 Optimization of rescale factor for conversion of CNN output to stiffness in Pa.

The mean-squared error of the testing set after correction by rescaling was 2505 Pa.

Phantom Scan Testing

A cylindrical MRE phantom of homogenous elastic material produced by Resoundant Inc. (Rochester, MN) was scanned with MRE using a 3.0 T MR750w scanner by General Electric Healthcare (Waukesha, WI). The exact value of the stiffness phantom is unknown, though the stiffness maps from the vendor algorithm are expected to be accurate in this simple system.

The wave images of the acquired MRE datasets were resized to maintain the pixel length of a mechanical wavelength for a given stiffness, relative to the simulation:

$$\text{Equation 49: } \textit{wavelength}(\textit{pixels})_{\textit{simulation}} \sim \left[\frac{\textit{matrix}}{\textit{FOV} * f} \right]_{\textit{simulation}} = 0.213$$

$$\text{Equation 50: } image_resize_dimension = round\left(0.213 \left[\frac{FOV * f}{matrix}\right]_{Image}\right)$$

Resulting stiffness maps from the vendor and CNN-based inversion algorithms are shown in Figure 38.

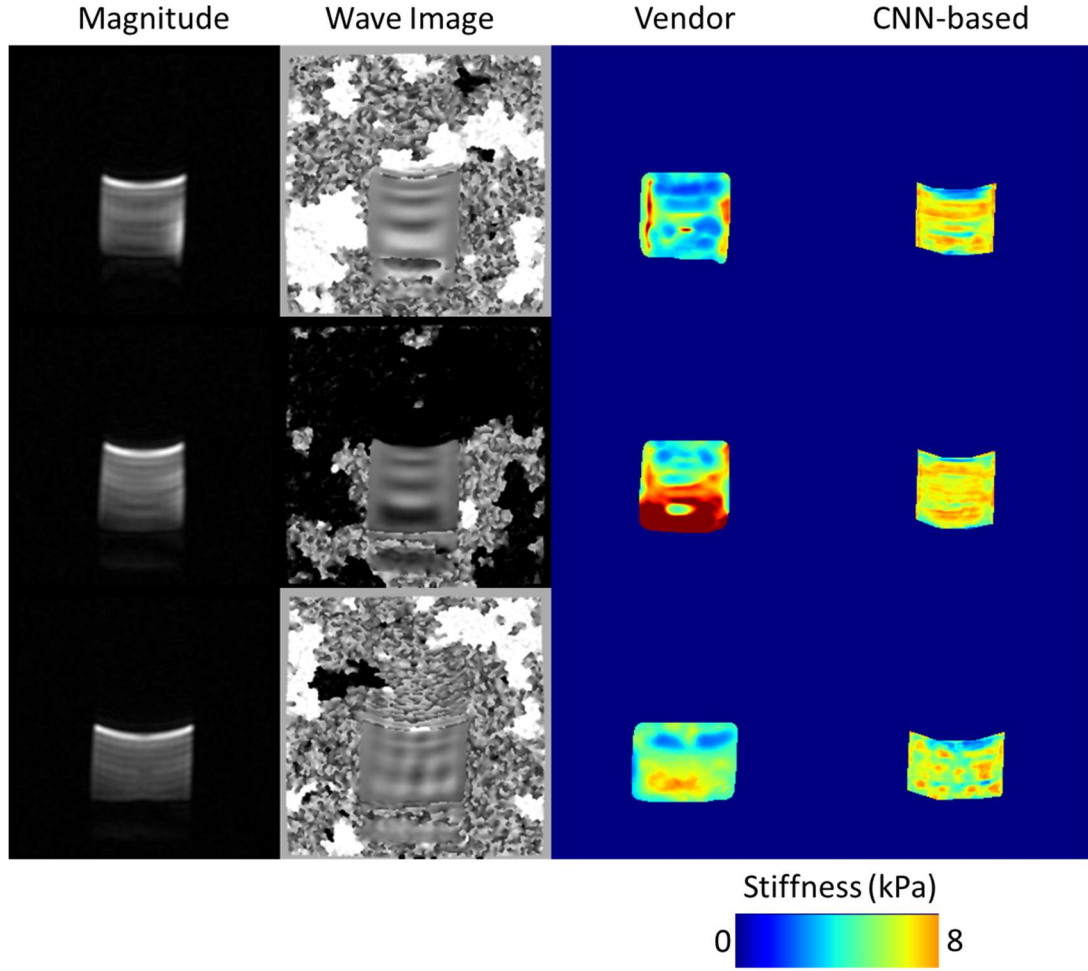


Figure 38 T1 magnitude images, unwrapped wave images, and vendor and CNN-based stiffness maps for the central three slices of the phantom scan.

Measurements were taken on the central three slices of the phantom using large regions of interest (ROIs) drawn on the T1-weighted magnitude images by an imaging scientist. Across the three slices, the average ROI stiffness values for the vendor and CNN algorithms were 4.39 ± 1.82 kPa and 4.67 ± 0.87 kPa, respectively.

5.3 In Vivo Breast Cancer MRE Validation [CNN-based Inversion Algorithm]

To test the CNN-based inversion algorithm *in vivo* and show possible improvement over the vendor algorithm, a comparison method should be developed. Because ground-truth stiffness is not known, it is not possible to evaluate the algorithms for their accuracy. Instead, stiffness measurements from different tissues were compared to ascertain if one algorithm showed more consistent contrast between the various sets of breast tissues.

5.3.1 MRE Dataset and Radiologist Interpretation

MRI Acquisition

Twenty patients with biopsy-confirmed stages I-III TNBC were enrolled in the prospective ARTEMIS trial and underwent pretreatment MRI. Patients were imaged on a 3.0 T GE MR750w scanner in the prone position. The pretreatment MRI included a T2-weighted series, a DCE series, and an MRE series. For the MRE series, harmonic wave motion was induced with a soft sternal driver. The MRE series was acquired using 3D elliptical spoiled GRE²⁴¹. Typical scan characteristics were as follows: TE/TR = 18/22 ms, flip angle = 8 degrees, slices = 12-27, slice thickness = 4 mm, slice gap = 0 mm, FOV = 38 x 38 cm, acquisition matrix = 96 x 96, in-plane pixel size = 2 x 2 mm. MRE parameters were as follows: excitation frequency = 60 Hz, number of offsets = 2, number of encoding directions = 3. Total scan duration for a patient with 19 slices was 4.10 minutes (96 frequency encoding lines * 22 ms per TR * 19 slices * 2 offsets * 3 directions) No fat-suppression was used.

Contour Measurements

A pair of experienced breast radiologists made consensus contours on the T1-weighted magnitude images. Contours were drawn in Imager, an in-house software, using a paintbrush tool and were then refined with histogram thresholding of the ROI signal intensities. Contours were made on the slice which contained the largest tumor cross-section. Contours were made on three distinct tissue

regions: the tumor, the fatty regions of the contralateral breast, and the FGT of the contralateral breast. Regions with clip artifact were avoided when placing contours.

Examples of contours for three MRE scans are shown in Figure 39.

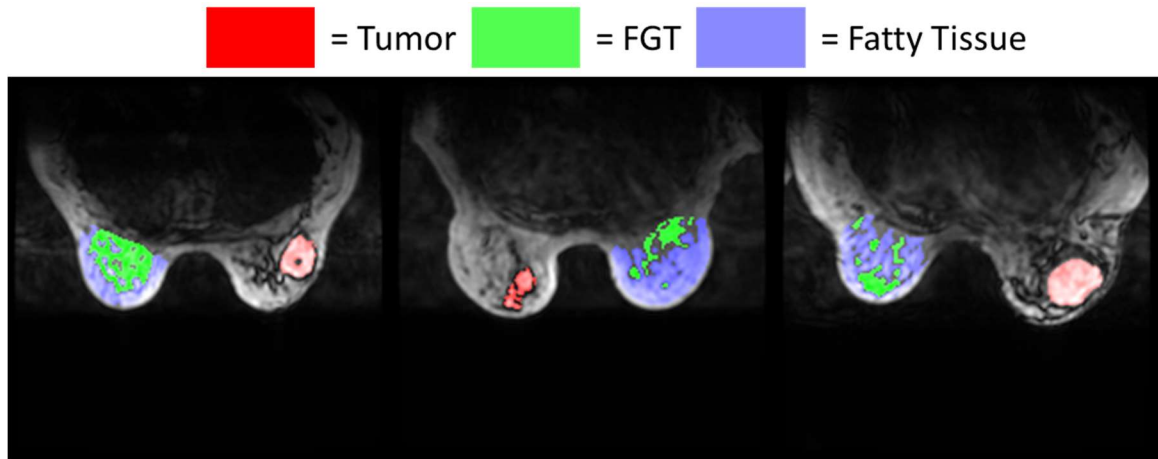


Figure 39 Examples of tissue contouring for three patient pretreatment scans on T1-weighted MRE magnitude images.

Analysis and Statistics

Wave images were resized according to Equation 50 for analysis by the CNN-based inversion algorithm. Stiffness maps were processed using both vendor and CNN algorithms. The CNN stiffness map was averaged between all offsets. Mean measurements were taken from each ROI from both stiffness maps.

For each algorithm, paired nonparametric t-tests (Wilcoxon signed-rank test) were used to compare tissue stiffnesses on a patient-wise basis. Pearson correlation was used to assess agreement between the algorithms for each of the tissue types. P-values less than 0.05 were considered significant.

5.3.2 Comparing CNN-Stiffness with Vendor Algorithm

Visual comparison between vendor and CNN-based stiffness maps for *in vivo* MRE of TNBC can be seen in Figure 40.

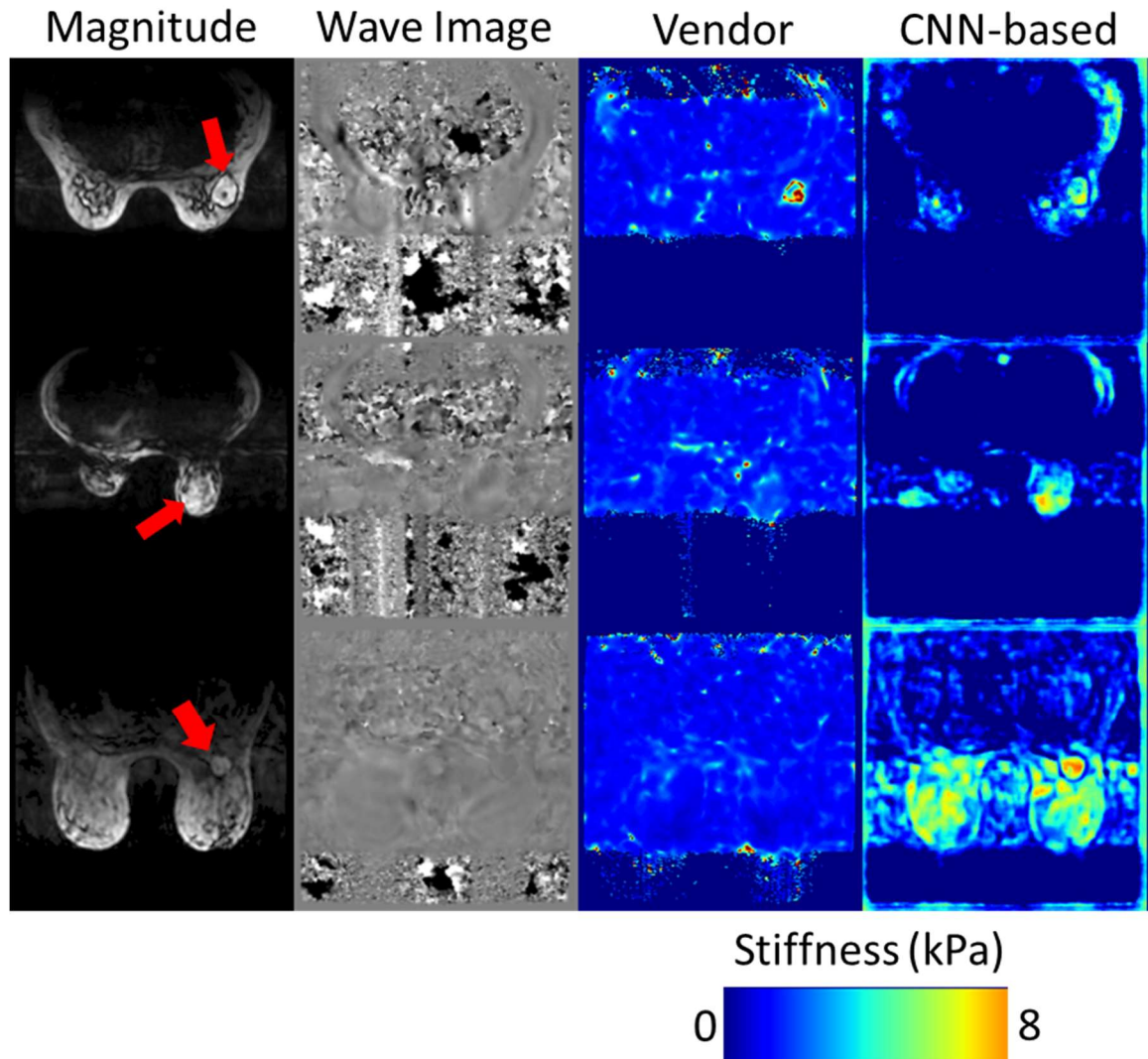
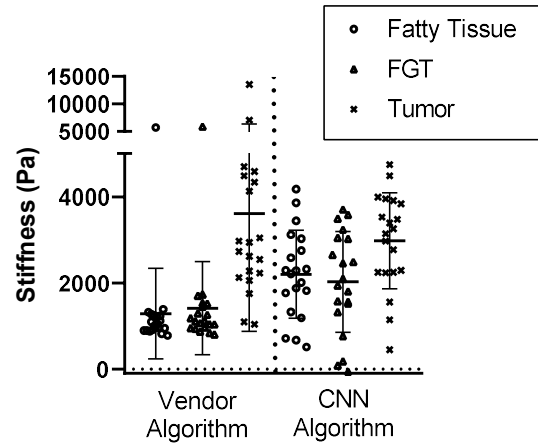


Figure 40 Comparison of vendor and CNN-based stiffness maps for three patients. Tumors are shown with red arrows. For the third patient (row 3), the tumor is not visible on vendor stiffness maps but is clearly outlined in the stiffness map output by the CNN-based algorithm.

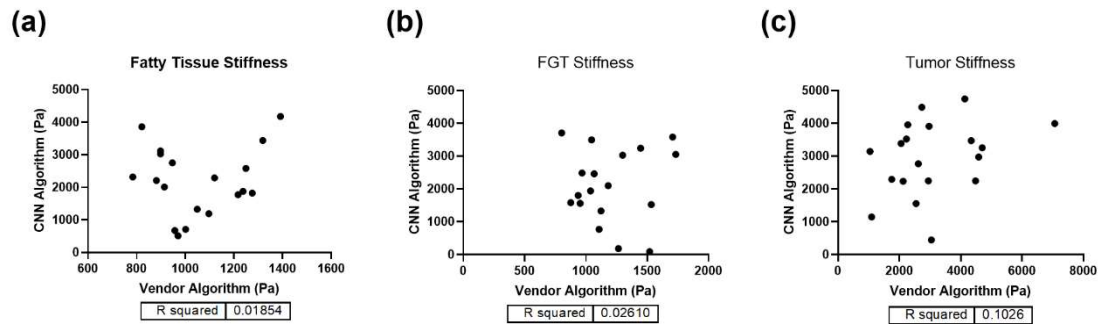
Mean values of stiffness for each tissue type and p-values for patient-wise comparison are shown in Table 18. Both algorithms showed significantly different stiffness values for fatty tissue vs tumor and FGT vs. tumor. Fatty tissue and FGT stiffnesses for the vendor algorithm were significantly different. This was not seen for the CNN algorithm.

Table 18 Comparison of tissue stiffness measurements between vendor and CNN-based algorithms.

Algorithm	Stiffness (kPa)			p-value		
	Fat	FGT	Tumor	Fat vs. FGT	Fat vs. Tumor	FGT vs. Tumor
Vendor	1.29 ± 1.05	1.42 ± 1.08	3.61 ± 2.74	0.0136	<0.0001	<0.0001
CNN-based	2.20 ± 1.02	2.03 ± 1.17	2.98 ± 1.12	0.3488	0.0121	<0.0001

**Figure 41 Dot plots showing distribution of stiffness values for vendor and CNN algorithms across different breast tissues in 20 TNBC patients.**

No correlation was seen for tissue stiffness values between the vendor algorithm and CNN algorithm. (Figure 42).

**Figure 42 Pearson correlation of tissue stiffness measurements between the vendor algorithm and the CNN algorithm. A single outlier patient with very high stiffnesses from the vendor algorithm on all tissues was excluded for correlations and plotting.**

5.4 Discussion [CNN-based Inversion Algorithm]

According to performance on the testing set, CNNs are able to learn the inversion problem from simulated MRE data and generalize to other simulated MRE data. Generalization to real-life MRE data was demonstrated in both in a homogenous gel phantom and *in vivo* MRE of TNBC. For both the CNN-based algorithm and a vendor algorithm applied to *in vivo* breast MRE, consistent differences in shear stiffness was seen between tumor vs. fatty tissue and tumor vs. FGT. However, the CNN-based algorithm was unable to distinguish fatty tissue vs. FGT by their stiffnesses, while the vendor algorithm was able to do so.

In phantom measurements, stiffness measurements from the CNN-based inversion algorithm had a lower standard deviation in comparison to stiffness measurements from the vendor algorithm. However, although the gel phantom is constructed with a homogenous gel, the stiffness distribution in the gel phantom is not known. Different regions of the phantom may have different stiffnesses due to differential cooling and other factors during phantom creation²⁴². Because of this, comparison of the two algorithms should not be considered on the basis of the standard deviation of the stiffness measurements.

Because of the wide range of stiffness measurements presented in literature²¹⁷, it is difficult to ascertain the relative accuracy of the two techniques. Tissue stiffnesses from both algorithms fall into the large ranges presented in MRE literature.

This work faces several limitations. The first is that the simulation only contains flat boundary conditions, which are not representative of *in vivo* boundary conditions. Next, the attenuation coefficient used in the simulation is highly simplified and imperfectly represents the viscoelastic behavior of tissue. Finally, the comparison of stiffnesses between tissue types is an incomplete comparison between the algorithms. A full comparison should investigate radiologist scoring of

anatomic visualization as this may impact interpretation. And, perhaps most importantly, stiffness measurements should be compared between the two algorithms in the context of some clinical application.

In conclusion, a CNN may learn inversion with FVM-simulated MRE data and show promise for generalizing to *in vivo* breast cancer MRE. CNN-based inversion algorithms may hold potential for improving MRE of breast cancer.

Chapter 6 – Future Directions

The work presented in this thesis is exploratory, with some *in vivo* validation. The predictive MRI biomarkers should be adapted for clinical use, and might undergo improvement, either through individual refinement or through combination in a shared biomarker. Suggestions for accomplishing these important items are presented in this chapter.

6.1 Potential Clinical Adaptation and Possible Refinement of Dissertation Projects

6.1.1 Potential Improvements to *Chapter 2 – Tumor Necrosis by Pretreatment Breast MRI:*

Association with Neoadjuvant Systemic Therapy Response in Triple-negative Breast Cancer

Adaptation to the Clinic

Clinically used PACS systems lack the segmentation capability that is needed for a radiologist to make tumor and necrosis segmentations. It is likely that a new generation of PACS systems will offer software scripting to assist radiologists in taking these measurements, with various tools and algorithms to assist the radiologist. This would be similar to the scripting methods offered in radiation therapy planning systems. However, the output measurements would not be subject to review and fine tuning like radiation dose plans. Because of this, the algorithms and tools would likely require FDA approval.

Segmentation time-consuming and subject to inter-reader bias. Several AI algorithms based on CNNs have shown promise for segmentation in biomedical imaging and could likely be developed for this purpose.

Evident Possible Improvements

Although the necrosis measurements explored in *Chapter 2* do not show promise for prediction of pCR, it may be that necrosis measurements correlate with long-term outcomes such as recurrence-free survival. Tumor necrosis has been shown as prognostic of these long-term outcome measures in other cancers^{243,244}. Investigation of this concept in TNBC is planned for the ARTEMIS trial once sufficient time has elapsed for assessing long-term outcome.

Speculative Improvements

It may be interesting to consider the shape or interface of the necrosis with viable tumor tissue. Some distance metric assessing how far necrosis is likely to occur from viable tissue could perhaps probe an interesting dynamic of blood supply and tumor growth. This might be accomplished through the use of 2D or shape radiomics applied at the tumor/necrosis interface.

6.1.2 Potential Improvements to *Chapter 3 – Functional Tumor Volume by Fast Dynamic Contrast-Enhanced MRI for Predicting Neoadjuvant Systemic Therapy Response in Triple-Negative Breast Cancer*

Adaptation to the Clinic

The optimal PE/SER thresholds for FTV in our TNBC-only study are similar to those optimized for TNBC in previous subtype analyses. This external validation of the TNBC-specific FTV thresholds supports their use in the clinical adaptation of FTV. Extensive adaptation work for FTV has already been done.

The improved predictive performance of FTV (measured after 4 cycles of NAST) with a 1-minute early phase timing could be easily be translated for clinical use in TNBC through simple re-selection of the early phase timing. It would be unnecessary to use fast DCE sequences to apply this FTV variant.

Evident Possible Improvements

FTV phase timings could be investigated with greater accuracy through harmonization of contrast arrival between tumors. This could be accomplished through advanced DCE acquisition and analysis techniques. Ultrafast DCE, with temporal resolution on the order of a few seconds, could be used to exquisitely determine the timing of contrast arrival to the tumor⁸³. Alternatively, detection of contrast arrival at a common vessel⁴³ might be combined with blood vessel mapping techniques⁴⁵ to estimate contrast arrival at the tumor.

All of the techniques proposed in this section are advanced and would require clinical adaptation of ultrafast DCE and/or advanced analysis algorithms.

Speculative Improvements

In essence, FTV selects regions of the tumor which show enhancement pattern three and are thought to correspond to viable tumor cells. While FTV is likely the best single volume measurement for predicting response, it is likely that there are tumor cells in regions which do not meet the FTV thresholds. It might be useful to additionally measure the volumes of the tumor which expresses the other two enhancement patterns and investigate their changes possible predictors of response.

It might also be interesting to develop a similar method to FTV that is based on ADC maps, where tumor volume below an optimized ADC threshold (corresponding to densely packed cells) is measured.

6.1.3 Potential Improvements to *Chapter 4 – Quantitative Apparent Diffusion Coefficients from Peritumoral Regions as Early Predictors of Treatment Response to Neoadjuvant Systemic Therapy in Triple Negative Breast Cancer*

Adaptation to the Clinic

Several ADC features from PTR regions were found to be useful for predicting NAST response in TNBC. Of these predictors, only the standard deviation of ADC in fat-inclusive peritumoral regions was complementary to tumor volume for predicting response. Its potential added value to FTV for predicting response will be investigated over a large group of TNBC patients in the ARTEMIS trial. If it shows value in this capacity, it will then require validation through a multi-center trial.

After validation in a large multi-institutional trial, the peritumoral region measurement technique would need to be adapted for clinical use. It should be noted that rFOV DWI is not used clinically. It would be necessary to indicate rFOV DWI for use in TNBC cancer response assessment. This would require addition of a 5-7 minute series to the MRI scan assessment.

Parallel to the clinical adaptation of the necrosis biomarkers from *Chapter 2*, peritumoral ADC measurements require tumor segmentation and software for taking measurements. A new generation of PACS systems and AI could likely serve these needs.

Evident Possible Improvements

One possible improvement in the PTR ADC experiment would be to alter the PTR so that they did not overlap (i.e. the 10 mm peritumoral region only extended from its outer edge to the outer edge of the 5 mm region). The original intent of the study was to determine a single PTR that provided useful measurements, and therefore they were assigned to overlap. It may be that outer bands of the PTR offer distinct and useful information.

Another evident improvement would be to extend the ADC features to include 2nd order or higher radiomics. A growing body of evidence shows correlation of radiomics with interesting clinicopathological parameters, which are summarized well in Table 2 of Braman et al¹¹⁰.

High resolution DWI, with voxels of 1 mm size or lower and with smaller spacing between slices, might provide a more refined assessment of ADC in the PTR for predicting response. rFOV ssEPI¹⁹¹ or with readout-segmented EPI²⁴⁵ acquisition techniques could be applied for acquisition of high-resolution DWI with reduced distortion.

Speculative Improvements

ADC standard deviation in the larger, fat-inclusive PTRs was an independent predictor of response, with consideration of tumor volume. This measurement may be indicative of the tumor location relative its surroundings, which are composed of either fatty tissue or FGT. While assessment of the tumor surroundings seems possible on ADC maps, it would be more direct to use an MRI modality which could calculate fat fraction for each voxel in the surroundings and assess its variation. Perhaps the fat fraction from the Dixon technique, available on both DCE and T2-weighted series in the ARTEMIS

trial, would provide a useful assessment of the tumor interface and offer utility as a volume-independent predictor of response.

6.1.4 Potential Improvements to *Chapter 5 – A Novel Convolutional Neural Network Inversion*

Algorithm for Magnetic Resonance Elastography of Breast Cancer

Adaptation to the Clinic

The work presented in this chapter is exploratory. While the CNN-based inversion algorithm shows potential for improved MRE of breast cancer, a large number of evident improvements should be explored before publication is considered.

Should the algorithm improve to the point that its use is desirable for use by others, it could be distributed to other groups. The open-source Github files could be downloaded for research work. Should a vendor desire use of the algorithm, they would also be free to download it and adapt it for FDA approval. Pending this, the CNN algorithm is small (<2 Mb) and fast (< 1 s per interpretation of one phase image).

Evident Possible Improvements

There are many evident improvements to this project. They are listed below categorically:

Simulation Improvements

- Simple Improvements
 - Expand number of simulations until addition of more simulated data did not result in improved CNN performance on the validation set
 - Add textures to shapes in procedurally generated geometries
 - Add sink regions within the procedurally generated geometries
 - Add non-linear boundary conditions within the FOV
- Advanced Improvements
 - Extend simulation to include viscoelastic properties
 - Extend simulation to 3D

CNN Improvements

- Test advanced CNN architectures, such as Xception²⁴⁶
- Test other data augmentation techniques and greater addition of noise to the dataset to improve robustness of network
- Test CNN performance with different combinations of wave images as input

Testing Improvements

- Check for reduced variance in repeat measurements
 - Examine variation in stiffness of large homogenous tissue between adjacent slices
 - Rescanning in test-retest format (two series acquired sequentially in the same exam)
- Compare anatomic visualization between algorithms
- Compare stiffness measurements towards some clinical purpose between algorithms

Speculative Improvements

It might be possible to make the CNN agnostic to excitation frequency, either through addition of an input parameter equal to the excitation frequency or through wave image rescaling.

6.2 Combinations of Biomarkers for Prediction of Response

Combining imaging biomarkers for response is planned for ARTEMIS patients. The imaging series in ARTEMIS are conserved between the MRI exams and each biomarker could be measured for all patients in the imaging arm. With the large (currently >200) patient population, it is possible to combine biomarkers into a refined model for predicting response. Molecular biomarkers and clinicopathological biomarkers could also be included in these models. Many algorithms exist for building predictive model from multiple features. Accuracy of these predictive models could be assessed through cross-validation, testing in a withheld validation set, or prospective testing in the continued ARTEMIS trial. After demonstrating potential, the resulting model and imaging techniques should be validated in a multi-center trial.

When optimizing a predictive model of combined biomarkers, a situation may arise where two or more biomarkers correlate and do not offer complementary information. Although complementary behavior is desirable for the performance of the predictive model, correlation of the biomarkers acquired contemporaneously with different modalities may serve as an *in vivo* validation and could help elucidate the biological meaning of imaging biomarkers of response. One potential example of this would be to correlate peritumoral regions with high ADC (possibly due to edema) with T2 relaxation measurements. T2 relaxation values would also be expected to be high in edematous regions. Intra-

patient correlation of high ADC with high T2 would support the assessment of peritumoral edema on ADC maps. Histopathologic biomarkers and other clinical measures may also be candidates for this correlation. This dissertation lacks this type of validation, representing an important limitation of this work.

A unique method for combining information from images and clinical pathology into a model of tumor growth and treatment dynamics has been proposed by several groups, notably Weis et al. for prediction of response in breast cancer²⁴⁷. This model augments and guides models of tumor growth and treatment response with imaging biomarkers.

A final, important potential use of imaging biomarkers would be to augment molecular biomarkers from biopsy samples. Intra-tumor heterogeneity limits the characterization of a tumor through biopsy. It may be that certain image measurement correlate with levels of molecular biomarkers. These measurements could be used as a support for molecular biomarkers. If, for some oncology application, a patient's molecular biomarker levels were close to a decision-making threshold, then perhaps the image biomarker correlate could be referenced for clarification. It is of particular interest to augment TIL and ki67 measurements in this manner.

Appendix A. Multivariate Model Parameters from Chapter 4 – Quantitative Apparent Diffusion Coefficients from Peritumoral Regions as Early Predictors of Treatment Response to Neoadjuvant Systemic Therapy in Triple Negative Breast Cancer

Table Key:

BL = baseline

PTR = peritumoral region

FE = fat-exclusive

FI = fat-inclusive

TV_{DWI} = tumor volume on diffusion-weighted imaging

C4 = scan after 4 cycles of therapy

C2 = scan after 2 cycles of therapy

ModelADC Features Only+ Tumor Volume**Baseline –****Fat-exclusive**

Timepoint	Region	ADC Feature	Weight
BL	Tumor	Maximum	0.18
BL	FE 15 mm PTR	Maximum	0.06
BL	Tumor	75 th Percentile	0.05
BL	FE 20 mm PTR	Standard Deviation	0.04
BL	Tumor	Mean	0.04
BL	Tumor	Median	0.03
BL	FE 20 mm PTR	90 th Percentile	0.01

Timepoint	Region	ADC Feature	Weight
BL	TV _{DWI}	N/A (Volume)	0.17
BL	Tumor	Maximum	0.14
BL	Tumor	75 th Percentile	0.07
BL	Tumor	Median	0.03
BL	Tumor	Mean	0.03
BL	FE 20 mm PTR	Standard Deviation	0.02
BL	FE 15 mm PTR	Maximum	0.01

Baseline –**Fat-inclusive**

Timepoint	Region	ADC Feature	Weight
BL	FI 15 mm PTR	Maximum	0.47
BL	FI 10 mm PTR	Kurtosis	0.34
BL	Tumor	Median	0.18
BL	Tumor	Maximum	0.15
BL	FI 5 mm PTR	Minimum	0.12
BL	Tumor	75 th Percentile	0.03

Timepoint	Region	ADC Feature	Weight
BL	FI 15 mm PTR	Maximum	0.41
BL	FI 10 mm PTR	Kurtosis	0.37
BL	TV _{DWI}	N/A (Volume)	0.21
BL	Tumor	Median	0.17
BL	FI 5 mm PTR	Minimum	0.14
BL	Tumor	Maximum	0.11
BL	Tumor	75 th Percentile	0.09
BL	FI 20 mm PTR	Skewness	0.06
BL	Tumor	25 th Percentile	0.02
BL	Tumor	Mean	0.02
BL	Tumor	Skewness	0.00
BL	FI 15 mm PTR	Skewness	0.00
BL	FI 10 mm PTR	10 th Percentile	0.00
BL	FI 10 mm PTR	Minimum	0.00

Baseline –**Combined****Fat-exclusive and****Fat-inclusive**

Timepoint	Region	ADC Feature	Weight
BL	FI 15 mm PTR	Maximum	0.54
BL	FI 10 mm PTR	Kurtosis	0.43
BL	Tumor	Median	0.28
BL	FI 5 mm PTR	Minimum	0.16
BL	Tumor	Maximum	0.10
BL	FE 20 mm PTR	Standard Deviation	0.09
BL	FI 5 mm PTR	90 th Percentile	0.00

Timepoint	Region	ADC Feature	Weight
BL	FI 15 mm PTR	Maximum	0.46
BL	FI 10 mm PTR	Kurtosis	0.42
BL	Tumor	Median	0.30
BL	TV _{DWI}	N/A (volume)	0.19
BL	FI 5 mm PTR	Minimum	0.14
BL	Tumor	Maximum	0.07
BL	FE 20 mm PTR	Standard Deviation	0.06
BL	FI 20 mm PTR	Skewness	0.03

C2 –**Fat-exclusive**

Timepoint	Region	ADC Feature	Weight
C2	FE 20 mm PTR	Standard Deviation	0.23
C2	FE 15 mm PTR	Standard Deviation	0.07
C2	FE 5 mm PTR	Standard Deviation	0.00

Timepoint	Region	ADC Feature	Weight
C2	FE 20 mm PTR	Standard Deviation	0.12
C2	TV _{DWI}	N/A (volume)	0.08
C2	FE 15 mm PTR	Standard Deviation	0.08
C2	FE 5 mm PTR	Standard Deviation	0.07

C2 –**Fat-inclusive**

Timepoint	Region	ADC Feature	Weight
(C2 – BL)/BL	FI 20 mm PTR	Kurtosis	0.23
C2	Fi 5 mm PTR	Standard Deviation	0.09

Timepoint	Region	ADC Feature	Weight
(C2 – BL)/BL	FI 20 mm PTR	Kurtosis	0.23
C2	Fi 5 mm PTR	Standard Deviation	0.09

C2 –**Combined****Fat-exclusive and****Fat-inclusive**

Timepoint	Region	ADC Feature	Weight
(C2 – BL)/BL	FI 20 mm PTR	Kurtosis	0.27
C2	FE 20 mm PTR	Standard Deviation	0.14
C2	FI 5 mm PTR	Standard Deviation	0.07

Timepoint	Region	ADC Feature	Weight
(C2 – BL)/BL	FI 20 mm PTR	Kurtosis	0.46
C2	FI 5 mm PTR	Standard Deviation	0.19
C2	FE 20 mm PTR	Standard Deviation	0.18
(C2 – BL)/BL	TV _{DWI}	N/A (volume)	0.04

C4 –

Fat-exclusive

Timepoint	Region	ADC Feature	Weight
C4	FE 5 mm PTR	Maximum	0.20
C4	FE 20 mm PTR	Standard Deviation	0.14
(C4-BL)/BL	FE 5 mm PTR	Skewness	0.14
C4-BL	FE 15 mm PTR	Maximum	0.12
(C4-BL)/BL	FE 10 mm PTR	Minimum	0.12
(C4-BL)/BL	FE 5 mm PTR	Minimum	0.12
C4-BL	FE 15 mm PTR	Standard Deviation	0.11
C4-BL	FE 20 mm PTR	Standard Deviation	0.10
C4	FE 10 mm PTR	Maximum	0.10
C4	FE 10 mm PTR	Standard Deviation	0.08
C4-BL	FE 15 mm PTR	Minimum	0.06
C4	FE 20 mm PTR	90 th Percentile	0.05
C4-BL	Tumor	Maximum	0.04
C4	FE 20 mm PTR	Maximum	0.03
C4	FE 15 mm PTR	Standard Deviation	0.02
C4	FE 15 mm PTR	90 th Percentile	0.01
C4	FE 10 mm PTR	90 th Percentile	0.00

Timepoint	Region	ADC Feature	Weight
C4	FE 5 mm PTR	Maximum	0.18
(C4-BL)/BL	Tumor	N/A (volume)	0.16
C4-BL	FE 15 mm PTR	Standard Deviation	0.16
(C4-BL)/BL	FE 10 mm PTR	Minimum	0.16
C4	FE 20 mm PTR	Standard Deviation	0.15
(C4-BL)/BL	FE 5 mm PTR	Skewness	0.14
(C4-BL)/BL	FE 5 mm PTR	Minimum	0.14
C4-BL	FE 15 mm PTR	Minimum	0.14
C4-BL	FE 20 mm PTR	Standard Deviation	0.14
C4-BL	FE 15 mm PTR	Maximum	0.13
C4	FE 10 mm PTR	Standard Deviation	0.09
C4	FE 10 mm PTR	Maximum	0.09
C4	Tumor	N/A (volume)	0.08
C4	FE 15 mm PTR	Standard Deviation	0.05
C4	FE 20 mm PTR	90 th Percentile	0.05
C4	FE 10 mm PTR	Skewness	0.03
C4	FE 20 mm PTR	Maximum	0.03
C4-BL	FE 20 mm PTR	90 th Percentile	0.03
C4	FE 20 mm PTR	75 th Percentile	0.02
C4-BL	Tumor	Maximum	0.02
C4-BL	FE 10 mm PTR	Skewness	0.01
C4	FE 15 mm PTR	90 th Percentile	0.01
C4	FE 10 mm PTR	90 th Percentile	0.01
C4	FE 5 mm PTR	Standard Deviation	0.00

C4 –**Fat-inclusive**

Timepoint	Region	ADC Feature	Weight
C4	FI 5 mm PTR	Standard Deviation	0.54
C4 - BL	FI 15 mm PTR	Maximum	0.52
(C4 - BL)/BL	FI 10 mm PTR	Skewness	0.09
C4	FI 20 mm PTR	Standard Deviation	0.02

Timepoint	Region	ADC Feature	Weight
C4 - BL	FI 15 mm PTR	Maximum	0.54
C4	FI 5 mm PTR	Standard Deviation	0.50
(C4-BL)/BL	Tumor	N/A (volume)	0.15
(C4-BL)/BL	Fi 10 mm PTR	Skewness	0.08

C4 –**Combined****Fat-exclusive and****Fat-inclusive**

Timepoint	Region	ADC Feature	Weight
C4 - BL	FI 15 mm PTR	Maximum	0.35
C4	FI 5 mm PTR	Standard Deviation	0.34
C4	FE 5 mm PTR	Maximum	0.14
(C4 - BL)/BL	FE 5 mm PTR	Minimum	0.11
(C4 - BL)/BL	FE 5 mm PTR	Skewness	0.10
C4 - BL	FE 15 mm PTR	Standard Deviation	0.01
(C4 - BL)/BL	FE 10 mm PTR	Minimum	0.01

Timepoint	Region	ADC Feature	Weight
C4 - BL	FI 15 mm PTR	Maximum	0.35
C4	FI 5 mm PTR	Standard Deviation	0.33
C4	FE 5 mm PTR	Maximum	0.13
(C4 - BL)/BL	FE 5 mm PTR	Minimum	0.11
(C4 - BL)/BL	FE 5 mm PTR	Skewness	0.09
(C4 - BL)/BL	Tumor	N/A (volume)	0.04
C4 - BL	FE 15 mm PTR	Standard Deviation	0.02
(C4 - BL)/BL	FE 10 mm PTR	Minimum	0.01

References

1. Sawyers CL, Van't Veer LJ. Reliable and effective diagnostics are keys to accelerating personalized cancer medicine and transforming cancer care: a policy statement from the American Association for Cancer Research. *Clin Cancer Res.* 2014;20(19):4978-4981.
2. Agostinetto E, Eiger D, Punie K, de Azambuja E. Emerging therapeutics for patients with triple-negative breast cancer. *Curr Oncol Rep.* 2021;23(5):57.
3. Seth S, Huo L, Rauch GM, Adrada B, Piwnica-Worms H, Lim B, Thompson AM, Mittendorf EA, Heffernan T, Litton JK, Symmans WF, Draetta GF, Futreal AP, Chang JT, Moulder SL. Abstract 1497: Longitudinal response and selection under neoadjuvant systemic therapy (NAST) in triple-negative breast cancer (TNBC): profiling results from a randomized trial (ARTEMIS; NCT02276443). *Cancer Res.* 2020;80(16 Supplement):1497.
4. Kos Z, Roblin E, Kim RS, Michiels S, Gallas BD, Chen W, van de Vijver KK, Goel S, Adams S, Demaria S, Viale G, Nielsen TO, Badve SS, Symmans WF, Sotiriou C, Rimm DL, Hewitt S, Denkert C, Loibl S, Luen SJ, Bartlett JMS, Savas P, Pruneri G, Dillon DA, Cheang MCU, Tutt A, Hall JA, Kok M, Horlings HM, Madabhushi A, van der Laak J, Ciompi F, Laenkholm A-V, Bellolio E, Gruosso T, Fox SB, Araya JC, Floris G, Hudeček J, Voorwerk L, Beck AH, Kerner J, Larsimont D, Declercq S, Van den Eynden G, Pusztai L, Ehinger A, Yang W, AbdulJabbar K, Yuan Y, Singh R, Hiley C, Bakir Ma, Lazar AJ, Naber S, Wienert S, Castillo M, Curigliano G, Dieci M-V, André F, Swanton C, Reis-Filho J, Sparano J, Balslev E, Chen IC, Stovgaard EIS, Pogue-Geile K, Blenman KRM, Penault-Llorca F, Schnitt S, Lakhani SR, Vincent-Salomon A, Rojo F, Braybrooke JP, Hanna MG, Soler-Monsó MT, Bethmann D, Castaneda CA, Willard-Gallo K, Sharma A, Lien H-C, Fineberg S, Thagaard J, Comerma L, Gonzalez-Ericsson P, Brogi E, Loi S, Saltz J, Klauschen F, Cooper L, Amgad M, Moore DA, Salgado R, Hyytiäinen A, Hida AI, Thompson A, Lefevre A, Gown A, Lo A, Sapino A, Moreira

- AM, Richardson A, Vingiani A, Bellizzi AM, Guerrero A, Grigoriadis A, Garrido-Castro AC, Cimino-Mathews A, Srinivasan A, Acs B, Singh B, Calhoun B, Haibe-Kans B, Solomon B, Thapa B, Nelson BH, Ballesteros-Merino C, Criscitiello C, Boeckx C, Colpaert C, Quinn C, Chennubhotla CS, Solinas C, Drubay D, Sabanathan D, Peeters D, Zardavas D, Höflmayer D, Johnson DB, Thompson EA, Perez E, ElGabry EA, Blackley EF, Reisenbichler E, Chmielik E, Gaire F, Lu F-I, Azmoudeh-Ardalan F, Peale F, Hirsch FR, Acosta-Haab G, Farshid G, Broeckx G, Koeppen H, Haynes HR, McArthur H, Joensuu H, Olofsson H, Cree I, Nederlof I, Frahm I, Brcic I, Chan J, Ziai J, Brock J, Weseling J, Giltane J, Lemonnier J, Zha J, Ribeiro J, Lennerz JK, Carter JM, Hartman J, Hainfellner J, Le Quesne J, Juco JW, van den Berg J, Sanchez J, Cucherousset J, Adam J, Balko JM, Saeger K, Siziopikou K, Sikorska K, Weber K, Steele KE, Emancipator K, El Bairi K, Allison KH, Korski K, Buisseret L, Shi L, Kooreman LFS, Molinero L, Estrada MV, Van Seijen M, Lacroix-Triki M, Sebastian MM, Balancin ML, Mathieu M-C, van de Vijver M, Rebelatto MC, Piccart M, Goetz MP, Preusser M, Khojasteh M, Sanders ME, Regan MM, Barnes M, Christie M, Misialek M, Ignatiadis M, de Maaker M, Van Bockstal M, Harbeck N, Tung N, Laudus N, Sirtaine N, Burchardi N, Ternes N, Radošević-Robin N, Gluz O, Grimm O, Nuciforo P, Jank P, Kirtani P, Watson PH, Jelinic P, Francis PA, Russell PA, Pierce RH, Hills R, Leon-Ferre R, de Wind R, Shui R, Leung S, Tabbarah S, Souza SC, O'Toole S, Swain S, Dudgeon S, Willis S, Ely S, Bedri S, Irshad S, Liu S, Hendry S, Bianchi S, Bragança S, Paik S, Luz S, Gevaert T, d'Alfons T, John T, Sugie T, Kurkure U, Bossuyt V, Manem V, Cámaea VP, Tong W, Tran WT, Wang Y, Allory Y, Husain Z, Bago-Horvath Z, the International Immuno-Oncology Biomarker Working G. Pitfalls in assessing stromal tumor infiltrating lymphocytes (sTILs) in breast cancer. *npj Breast Cancer*. 2020;6(1):17.
5. Nofech-Mozes S, Trudeau M, Kahn HK, Dent R, Rawlinson E, Sun P, Narod SA, Hanna WM. Patterns of recurrence in the basal and non-basal subtypes of triple-negative breast cancers. *Breast Cancer Res Treat*. 2009;118(1):131-137.

6. Plasilova ML, Hayse B, Killelea BK, Horowitz NR, Chagpar AB, Lannin DR. Features of triple-negative breast cancer: Analysis of 38,813 cases from the national cancer database. *Medicine (Baltimore)*. 2016;95(35):e4614.

7. Perou CM, Sørli T, Eisen MB, van de Rijn M, Jeffrey SS, Rees CA, Pollack JR, Ross DT, Johnsen H, Akslen LA, Fluge Ø, Pergamenschikov A, Williams C, Zhu SX, Lønning PE, Børresen-Dale A-L, Brown PO, Botstein D. Molecular portraits of human breast tumours. *Nature*. 2000;406(6797):747-752.

8. Koboldt DC, Fulton RS, McLellan MD, Schmidt H, Kalicki-Veizer J, McMichael JF, Fulton LL, Dooling DJ, Ding L, Mardis ER, Wilson RK, Ally A, Balasundaram M, Butterfield YSN, Carlsen R, Carter C, Chu A, Chuah E, Chun H-JE, Coope RJN, Dhalla N, Guin R, Hirst C, Hirst M, Holt RA, Lee D, Li HI, Mayo M, Moore RA, Mungall AJ, Pleasance E, Gordon Robertson A, Schein JE, Shafiei A, Sipahimalani P, Slobodan JR, Stoll D, Tam A, Thiessen N, Varhol RJ, Wye N, Zeng T, Zhao Y, Birol I, Jones SJM, Marra MA, Cherniack AD, Saksena G, Onofrio RC, Pho NH, Carter SL, Schumacher SE, Tabak B, Hernandez B, Gentry J, Nguyen H, Crenshaw A, Ardlie K, Beroukhim R, Winckler W, Getz G, Gabriel SB, Meyerson M, Chin L, Park PJ, Kucherlapati R, Hoadley KA, Todd Auman J, Fan C, Turman YJ, Shi Y, Li L, Topal MD, He X, Chao H-H, Prat A, Silva GO, Iglesia MD, Zhao W, Usary J, Berg JS, Adams M, Booker J, Wu J, Gulabani A, Bodenheimer T, Hoyle AP, Simons JV, Soloway MG, Mose LE, Jefferys SR, Balu S, Parker JS, Neil Hayes D, Perou CM, Malik S, Mahurkar S, Shen H, Weisenberger DJ, Triche Jr T, Lai PH, Bootwalla MS, Maglinte DT, Berman BP, Van Den Berg DJ, Baylin SB, Laird PW, Creighton CJ, Donehower LA, Getz G, Noble M, Voet D, Saksena G, Gehlenborg N, DiCara D, Zhang J, Zhang H, Wu C-J, Yingchun Liu S, Lawrence MS, Zou L, Sivachenko A, Lin P, Stojanov P, Jing R, Cho J, Sinha R, Park RW, Nazaire M-D, Robinson J, Thorvaldsdottir H, Mesirov J, Park PJ, Chin L, Reynolds S, Kreisberg RB, Bernard B, Bressler R, Erkkila T, Lin J, Thorsson V, Zhang W, Shmulevich I, Ciriello G, Weinhold N, Schultz N, Gao J,

Cerami E, Gross B, Jacobsen A, Sinha R, Arman Aksoy B, Antipin Y, Reva B, Shen R, Taylor BS, Ladanyi M, Sander C, Anur P, Spellman PT, Lu Y, Liu W, Verhaak RRG, Mills GB, Akbani R, Zhang N, Broom BM, Casasent TD, Wakefield C, Unruh AK, Baggerly K, Coombes K, Weinstein JN, Haussler D, Benz CC, Stuart JM, Benz SC, Zhu J, Szeto CC, Scott GK, Yau C, Paull EO, Carlin D, Wong C, Sokolov A, Thusberg J, Mooney S, Ng S, Goldstein TC, Ellrott K, Grifford M, Wilks C, Ma S, Craft B, Yan C, Hu Y, Meerzaman D, Gastier-Foster JM, Bowen J, Ramirez NC, Black AD, Pyatt RE, White P, Zmuda EJ, Frick J, Lichtenberg TM, Brookens R, George MM, Gerken MA, Harper HA, Leraas KM, Wise LJ, Tabler TR, McAllister C, Barr T, Hart-Kothari M, Tarvin K, Saller C, Sandusky G, Mitchell C, Iacocca MV, Brown J, Rabeno B, Czerwinski C, Petrelli N, Dolzhansky O, Abramov M, Voronina O, Potapova O, Marks JR, Suchorska WM, Murawa D, Kycler W, Ibbs M, Korski K, Spychała A, Murawa P, Brzeziński JJ, Perz H, Łażniak R, Teresiak M, Tatka H, Leporowska E, Bogusz-Czerniewicz M, Malicki J, Mackiewicz A, Wiznerowicz M, Van Le X, Kohl B, Viet Tien N, Thorp R, Van Bang N, Sussman H, Duc Phu B, Hajek R, Phi Hung N, Viet The Phuong T, Quyet Thang H, Zaki Khan K, Penny R, Mallery D, Curley E, Shelton C, Yena P, Ingle JN, Couch FJ, Lingle WL, King TA, Maria Gonzalez-Angulo A, Mills GB, Dyer MD, Liu S, Meng X, Patangan M, The Cancer Genome Atlas N, Genome sequencing centres: Washington University in St L, Genome characterization centres BCCA, Broad I, Brigham, Women's H, Harvard Medical S, University of North Carolina CH, University of Southern California/Johns H, Genome data analysis: Baylor College of M, Institute for Systems B, Memorial Sloan-Kettering Cancer C, Oregon H, Science U, The University of Texas MDACC, University of California SCBI, Nci, Biospecimen core resource: Nationwide Children's Hospital Biospecimen Core R, Tissue source sites A-I, Christiana, Cureline, Duke University Medical C, The Greater Poland Cancer C, IIsbio, International Genomics C, Mayo C, Mskcc, Center MDAC. Comprehensive molecular portraits of human breast tumours. *Nature*. 2012;490(7418):61-70.

9. Bertucci F, Finetti P, Cervera N, Esterni B, Hermitte F, Viens P, Birnbaum D. How basal are triple-negative breast cancers? *Int J Cancer*. 2008;123(1):236-240.
10. Prat A, Pineda E, Adamo B, Galván P, Fernández A, Gaba L, Díez M, Viladot M, Arance A, Muñoz M. Clinical implications of the intrinsic molecular subtypes of breast cancer. *Breast*. 2015;24:S26-S35.
11. Dent R, Trudeau M, Pritchard KI, Hanna WM, Kahn HK, Sawka CA, Lickley LA, Rawlinson E, Sun P, Narod SA. Triple-negative breast cancer: clinical features and patterns of recurrence. *Clin Cancer Res*. 2007;13(15):4429-4434.
12. Gluz O, Liedtke C, Gottschalk N, Pusztai L, Nitz U, Harbeck N. Triple-negative breast cancer—current status and future directions. *Ann Oncol*. 2009;20(12):1913-1927.
13. Öztürk VS, Polat YD, Soyder A, Tanyeri A, Karaman CZ, Taşkın F. The Relationship Between MRI Findings and Molecular Subtypes in Women With Breast Cancer. *Curr Probl Diagn Radiol*. 2020;49(6):417-421.
14. National Cancer Institute D, Surveillance Research Program. Surveillance, Epidemiology, and End Results (SEER) Program (www.seer.cancer.gov) SEER*Stat Database.
15. Jordan VC, Brodie AMH. Development and evolution of therapies targeted to the estrogen receptor for the treatment and prevention of breast cancer. *Steroids*. 2007;72(1):7-25.
16. Vu T, Claret FX. Trastuzumab: updated mechanisms of action and resistance in breast cancer. *Front Oncol*. 2012;2:62-62.
17. Pienkowski T, Zielinski CC. Trastuzumab treatment in patients with breast cancer and metastatic CNS disease. *Ann Oncol*. 2010;21(5):917-924.
18. da Silva JL, Cardoso Nunes NC, Izetti P, de Mesquita GG, de Melo AC. Triple negative breast cancer: a thorough review of biomarkers. *Crit Rev Oncol Hematol*. 2020;145:102855.

19. Yam C, Mani SA, Moulder SL. Targeting the molecular subtypes of triple negative breast cancer: understanding the diversity to progress the field. *Oncologist*. 22(9):1086-1093.
20. Lehmann BD, Bauer JA, Chen X, Sanders ME, Chakravarthy AB, Shyr Y, Pietersenpol JA. Identification of human triple-negative breast cancer subtypes and preclinical models for selection of targeted therapies. *J Clin Invest*. 2011;121(7):2750-2767.
21. Burstein MD, Tsimelzon A, Poage GM, Covington KR, Contreras A, Fuqua SA, Savage MI, Osborne CK, Hilsenbeck SG, Chang JC, Mills GB, Lau CC, Brown PH. Comprehensive genomic analysis identifies novel subtypes and targets of triple-negative breast cancer. *Clin Cancer Res*. 2015;21(7):1688-1698.
22. Lehmann BD, Jovanović B, Chen X, Estrada MV, Johnson KN, Shyr Y, Moses HL, Sanders ME, Pietersenpol JA. Refinement of triple-negative breast cancer molecular subtypes: implications for neoadjuvant chemotherapy selection. *PLoS One*. 2016;11(6):e0157368.
23. Cardoso F, Kyriakides S, Ohno S, Penault-Llorca F, Poortmans P, Rubio IT, Zackrisson S, Senkus E, Committee EG. Early breast cancer: ESMO Clinical Practice Guidelines for diagnosis, treatment and follow-up. *Ann Oncol*. 2019;30(10):1674.
24. Bakker MF, de Lange SV, Pijnappel RM, Mann RM, Peeters PHM, Monninkhof EM, Emaus MJ, Loo CE, Bisschops RHC, Lobbjes MBI, de Jong MDF, Duvivier KM, Veltman J, Karssemeijer N, de Koning HJ, van Diest PJ, Mali W, van den Bosch M, Veldhuis WB, van Gils CH, Group DTS. Supplemental MRI screening for women with extremely dense breast tissue. *N Engl J Med*. 2019;381(22):2091-2102.
25. Giuliano AE, Connolly JL, Edge SB, Mittendorf EA, Rugo HS, Solin LJ, Weaver DL, Winchester DJ, Hortobagyi GN. Breast Cancer-Major changes in the American Joint Committee on Cancer eighth edition cancer staging manual. *CA Cancer J Clin*. 2017;67(4):290-303.

26. Pecorino L. *Molecular biology of cancer : mechanisms, targets, and therapeutics*. 3rd ed. Oxford: Oxford University Press; 2012.
27. Cortazar P, Zhang L, Untch M, Mehta K, Costantino JP, Wolmark N, Bonnefoi H, Cameron D, Gianni L, Valagussa P, Swain SM, Prowell T, Loibl S, Wickerham DL, Bogaerts J, Baselga J, Perou C, Blumenthal G, Blohmer J, Mamounas EP, Bergh J, Semiglazov V, Justice R, Eidtmann H, Paik S, Piccart M, Sridhara R, Fasching PA, Slaets L, Tang S, Gerber B, Geyer CE, Jr., Pazdur R, Ditsch N, Rastogi P, Eiermann W, von Minckwitz G. Pathological complete response and long-term clinical benefit in breast cancer: the CTNeoBC pooled analysis. *Lancet*. 2014;384(9938):164-172.
28. Goorts B, van Nijnatten TJA, de Munck L, Moosdorff M, Heuts EM, de Boer M, Lobbes MBI, Smidt ML. Clinical tumor stage is the most important predictor of pathological complete response rate after neoadjuvant chemotherapy in breast cancer patients. *Breast Cancer Res Treat*. 2017;163(1):83-91.
29. Zhang G, Xie W, Liu Z, Lin C, Piao Y, Xu L, Guo F, Xie X. Prognostic function of Ki-67 for pathological complete response rate of neoadjuvant chemotherapy in triple-negative breast cancer. *Tumori*. 2014;100(2):136-142.
30. Gluz O, Kolberg-Liedtke C, Prat A, Christgen M, Gebauer D, Kates R, Paré L, Grischke EM, Forstbauer H, Braun M, Warm M, Hackmann J, Uleer C, Aktas B, Schumacher C, Kuemmel S, Wuerstlein R, Pelz E, Nitz U, Kreipe HH, Harbeck N. Efficacy of deescalated chemotherapy according to PAM50 subtypes, immune and proliferation genes in triple-negative early breast cancer: primary translational analysis of the WSG-ADAPT-TN trial. *Int J Cancer*. 2020;146(1):262-271.
31. Denkert C, von Minckwitz G, Darb-Esfahani S, Lederer B, Heppner BI, Weber KE, Budczies J, Huober J, Klauschen F, Furlanetto J, Schmitt WD, Blohmer JU, Karn T, Pfitzner BM, Kümmel S, Engels K, Schneeweiss A, Hartmann A, Noske A, Fasching PA, Jackisch C, van Mackelenbergh M,

- Sinn P, Schem C, Hanusch C, Untch M, Loibl S. Tumour-infiltrating lymphocytes and prognosis in different subtypes of breast cancer: a pooled analysis of 3771 patients treated with neoadjuvant therapy. *Lancet Oncol.* 2018;19(1):40-50.
32. Cerbelli B, Botticelli A, Pisano A, Pernazza A, Campagna D, De Luca A, Ascierto PA, Pignataro MG, Pelullo M, Rocca CD, Marchetti P, Fortunato L, Costarelli L, d'Amati G. CD73 expression and pathologic response to neoadjuvant chemotherapy in triple negative breast cancer. *Virchows Arch.* 2020;476(4):569-576.
 33. Prat A, Lluch A, Albanell J, Barry WT, Fan C, Chacón JI, Parker JS, Calvo L, Plazaola A, Arcusa A, Seguí-Palmer MA, Burgues O, Ribelles N, Rodriguez-Lescure A, Guerrero A, Ruiz-Borrego M, Munarriz B, López JA, Adamo B, Cheang MC, Li Y, Hu Z, Gulley ML, Vidal MJ, Pitcher BN, Liu MC, Citron ML, Ellis MJ, Mardis E, Vickery T, Hudis CA, Winer EP, Carey LA, Caballero R, Carrasco E, Martín M, Perou CM, Alba E. Predicting response and survival in chemotherapy-treated triple-negative breast cancer. *Br J Cancer.* 2014;111(8):1532-1541.
 34. Chica-Parrado MR, Godoy-Ortiz A, Jiménez B, Ribelles N, Barragan I, Alba E. Resistance to neoadjuvant treatment in breast cancer: clinicopathological and molecular predictors. *Cancers.* 2020;12(8):2012.
 35. Papanicolas I, Woskie LR, Jha AK. Health care spending in the United States and other high-income countries. *JAMA.* 2018;319(10):1024-1039.
 36. Breit G, Rabi II. Measurement of nuclear spin. *Physical Review.* 1931;38(11):2082-2083.
 37. Haase A, Frahm J, Hänicke W, Matthaei D. 1H NMR chemical shift selective (CHESS) imaging. *Phys Med Biol.* 1985;30(4):341-344.
 38. Dixon WT. Simple proton spectroscopic imaging. *Radiology.* 1984;153(1):189-194.
 39. Ma J. Dixon techniques for water and fat imaging. *J Magn Reson Imaging.* 2008;28(3):543-558.

40. Pintaske J, Martirosian P, Graf H, Erb G, Lodemann KP, Claussen CD, Schick F. Relaxivity of Gadopentetate Dimeglumine (Magnevist), Gadobutrol (Gadovist), and Gadobenate Dimeglumine (MultiHance) in human blood plasma at 0.2, 1.5, and 3 Tesla. *Invest Radiol.* 2006;41(3):213-221.
41. Tofts PS, Berkowitz B, Schnall MD. Quantitative analysis of dynamic Gd-DTPA enhancement in breast tumors using a permeability model. *Magn Reson Med.* 1995;33(4):564-568.
42. Sourbron SP, Buckley DL. On the scope and interpretation of the Tofts models for DCE-MRI. *Magn Reson Med.* 2011;66(3):735-745.
43. Parker GJ, Roberts C, Macdonald A, Buonaccorsi GA, Cheung S, Buckley DL, Jackson A, Watson Y, Davies K, Jayson GC. Experimentally-derived functional form for a population-averaged high-temporal-resolution arterial input function for dynamic contrast-enhanced MRI. *Magn Reson Med.* 2006;56(5):993-1000.
44. Woolf DK, Taylor NJ, Makris A, Tunariu N, Collins DJ, Li SP, Ah-See ML, Beresford M, Padhani AR. Arterial input functions in dynamic contrast-enhanced magnetic resonance imaging: which model performs best when assessing breast cancer response? *Br J Radiol.* 2016;89(1063):20150961.
45. Yankeelov TE, Cron GO, Addison CL, Wallace JC, Wilkins RC, Pappas BA, Santyr GE, Gore JC. Comparison of a reference region model with direct measurement of an AIF in the analysis of DCE-MRI data. *Magn Reson Med.* 2007;57(2):353-361.
46. Kovar DA, Lewis M, Karczmar GS. A new method for imaging perfusion and contrast extraction fraction: input functions derived from reference tissues. *J Magn Reson Imaging.* 1998;8(5):1126-1134.

47. Cárdenas-Rodríguez J, Howison CM, Pagel MD. A linear algorithm of the reference region model for DCE-MRI is robust and relaxes requirements for temporal resolution. *Magn Reson Imaging*. 2013;31(4):497-507.
48. Wu C, Pineda F, Hormuth DA, 2nd, Karczmar GS, Yankeelov TE. Quantitative analysis of vascular properties derived from ultrafast DCE-MRI to discriminate malignant and benign breast tumors. *Magn Reson Med*. 2019;81(3):2147-2160.
49. Muthupillai R, Lomas DJ, Rossman PJ, Greenleaf JF, Manduca A, Ehman RL. Magnetic resonance elastography by direct visualization of propagating acoustic strain waves. *Science*. 1995;269(5232):1854-1857.
50. Venkatesh S, Yin M, Talwalkar J, Ehman R. Application of liver MR elastography in clinical practice. Paper presented at: Annual Meeting of the International Society of Magnetic Resonance in Medicine 2008.
51. Mariappan YK, Glaser KJ, Ehman RL. Magnetic resonance elastography: a review. *Clinical anatomy (New York, NY)*. 2010;23(5):497-511.
52. Pepin KM, Ehman RL, McGee KP. Magnetic resonance elastography (MRE) in cancer: technique, analysis, and applications. *Progress in nuclear magnetic resonance spectroscopy*. 2015;90-91:32-48.
53. Thompson SM, Wang J, Chandan VS, Glaser KJ, Roberts LR, Ehman RL, Venkatesh SK. MR elastography of hepatocellular carcinoma: correlation of tumor stiffness with histopathology features-preliminary findings. *Magn Reson Imaging*. 2017;37:41-45.
54. Qayyum A, Avritscher R, Morani A, Sun J, Bhosale P, Hwang K-P, Stafford J, Abugabal YI, Ma J, Kaseb AO. Immunotherapy response evaluation with MR elastography (MRE) in advanced HCC. *J Clin Oncol*. 2019;37(4):230-230.

55. Jiang YU, Fujiwara H, Nakamura GEN. Approximate steady state models for magnetic resonance elastography. *SIAM J Appl Math.* 2011;71(6):1965-1989.
56. Parker KJ, Szabo T, Holm S. Towards a consensus on rheological models for elastography in soft tissues. *Phys Med Biol.* 2019;64(21):215012.
57. Schmidt JL, Tweten DJ, Badachhane AA, Reiter AJ, Okamoto RJ, Garbow JR, Bayly PV. Measurement of anisotropic mechanical properties in porcine brain white matter ex vivo using magnetic resonance elastography. *J Mech Behav Biomed Mater.* 2018;79:30-37.
58. Smith D, Guertler CA, Okamoto RJ, Romano A, Bayly PV, Johnson CL. Multi-excitation MR elastography of the brain: wave propagation in anisotropic white matter. *J Biomech Eng.* 2020;142(7):0710051-0710059.
59. Fovargue D, Nordsletten D, Sinkus R. Stiffness reconstruction methods for MR elastography. *NMR Biomed.* 2018;31(10):e3935-e3935.
60. Oberai AA, Gokhale NH, Feijóo GR. Solution of inverse problems in elasticity imaging using the adjoint method. *Inverse Probl.* 2003;19(2):297.
61. Tan L, McGarry MD, Van Houten EE, Ji M, Solamen L, Weaver JB, Paulsen KD. Gradient-based optimization for poroelastic and viscoelastic MR elastography. *IEEE Trans Med Imaging.* 2017;36(1):236-250.
62. Van Houten EE, Paulsen KD, Miga MI, Kennedy FE, Weaver JB. An overlapping subzone technique for MR-based elastic property reconstruction. *Magn Reson Med.* 1999;42(4):779-786.
63. Knutsson H, Westin C, Granlund G. Local multiscale frequency and bandwidth estimation. Paper presented at: Proceedings of 1st International Conference on Image Processing; Nov. 13, 1994.
64. Manduca A, Lake DS, Kruse SA, Ehman RL. Spatio-temporal directional filtering for improved inversion of MR elastography images. *Med Image Anal.* 2003;7(4):465-473.

65. Morris E, Comstock C, Lee C. ACR BI-RADS® Magnetic Resonance Imaging. . *ACR BI-RADS® Atlas, Breast Imaging Reporting and Data System*. Reston, VA: American College of Radiology; 2013.
66. Ha R, Mango V, Al-Khalili R, Mema E, Friedlander L, Desperito E, Wynn RT. Evaluation of association between degree of background parenchymal enhancement on MRI and breast cancer subtype. *Clin Imaging*. 2018;51:307-310.
67. Delille J-P, Slanetz PJ, Yeh ED, Kopans DB, Garrido L. Physiologic changes in breast magnetic resonance imaging during the menstrual cycle: perfusion imaging, signal enhancement, and influence of the T1 relaxation time of breast tissue. *Breast J*. 2005;11(4):236-241.
68. Delille J-P, Slanetz PJ, Yeh ED, Kopans DB, Halpern EF, Garrido L. Hormone replacement therapy in postmenopausal women: breast tissue perfusion determined with MR imaging—initial observations. *Radiology*. 2005;235(1):36-41.
69. Müller-Schimpfle M, Ohmenhäuser K, Stoll P, Dietz K, Claussen CD. Menstrual cycle and age: influence on parenchymal contrast medium enhancement in MR imaging of the breast. *Radiology*. 1997;203(1):145-149.
70. King V, Brooks JD, Bernstein JL, Reiner AS, Pike MC, Morris EA. Background parenchymal enhancement at breast MR imaging and breast cancer risk. *Radiology*. 2011;260(1):50-60.
71. Dontchos BN, Rahbar H, Partridge SC, Korde LA, Lam DL, Scheel JR, Peacock S, Lehman CD. Are qualitative assessments of background parenchymal enhancement, amount of fibroglandular tissue on MR images, and mammographic density associated with breast cancer risk? *Radiology*. 2015;276(2):371-380.
72. Uematsu T, Kasami M, Yuen S. Triple-negative breast cancer: correlation between MR imaging and pathologic findings. *Radiology*. 2009;250(3):638-647.

73. Mema E, Schnabel F, Chun J, Kaplowitz E, Price A, Goodgal J, Moy L. The relationship of breast density in mammography and magnetic resonance imaging in women with triple negative breast cancer. *Eur J Radiol.* 2020;124:108813.
74. Huang Y, Zheng C, Zhang X, Cheng Z, Yang Z, Hao Y, Shen J. The usefulness of Bayesian network in assessing the risk of triple-negative breast cancer. *Acad Radiol.* 2020;27(12):e282-e291.
75. Angelini G, Marini C, Iacconi C, Mazzotta D, Moretti M, Picano E, Morganti R. Magnetic resonance (MR) features in triple negative breast cancer (TNBC) vs receptor positive cancer (nTNBC). *Clin Imaging.* 2018;49:12-16.
76. Kim JY, Kim SH, Kim YJ, Kang BJ, An YY, Lee AW, Song BJ, Park YS, Lee HB. Enhancement parameters on dynamic contrast enhanced breast MRI: do they correlate with prognostic factors and subtypes of breast cancers? *Magn Reson Imaging.* 2015;33(1):72-80.
77. Dogan S, Ozmen S, Oz B, Imamoglu H, Kahriman G, Zararsiz G, Ozturk M. Comparison of different dynamic contrast enhanced-magnetic resonance imaging descriptors and clinical findings among breast cancer subtypes determined based on molecular assessment. *Iran J Radiol.* 2018;15(4):e64889.
78. Negrão EMS, Souza JA, Marques EF, Bitencourt AGV. Breast cancer phenotype influences MRI response evaluation after neoadjuvant chemotherapy. *Eur J Radiol.* 2019;120:108701.
79. Du S, Gao S, Zhang L, Yang X, Qi X, Li S. Improved discrimination of molecular subtypes in invasive breast cancer: comparison of multiple quantitative parameters from breast MRI. *Magn Reson Imaging.* 2021;77:148-158.
80. Yuen S, Monzawa S, Yanai S, Matsumoto H, Yata Y, Ichinose Y, Deai T, Hashimoto T, Tashiro T, Yamagami K. The association between MRI findings and breast cancer subtypes: focused on the combination patterns on diffusion-weighted and T2-weighted images. *Breast Cancer.* 2020;27(5):1029-1037.

81. Song SE, Shin SU, Moon HG, Ryu HS, Kim K, Moon WK. MR imaging features associated with distant metastasis-free survival of patients with invasive breast cancer: a case-control study. *Breast Cancer Res Treat.* 2017;162(3):559-569.
82. Costantini M, Belli P, Distefano D, Bufi E, Matteo MD, Rinaldi P, Giuliani M, Petrone G, Magno S, Bonomo L. Magnetic resonance imaging features in triple-negative breast cancer: comparison with luminal and HER2-overexpressing tumors. *Clin Breast Cancer.* 2012;12(5):331-339.
83. Onishi N, Sadinski M, Hughes MC, Ko ES, Gibbs P, Gallagher KM, Fung MM, Hunt TJ, Martinez DF, Shukla-Dave A, Morris EA, Sutton EJ. Ultrafast dynamic contrast-enhanced breast MRI may generate prognostic imaging markers of breast cancer. *Breast Cancer Res.* 2020;22(1):58.
84. Shin SU, Cho N, Kim SY, Lee SH, Chang JM, Moon WK. Time-to-enhancement at ultrafast breast DCE-MRI: potential imaging biomarker of tumour aggressiveness. *Eur Radiol.* 2020;30(7):4058-4068.
85. Li SP, Padhani AR, Taylor NJ, Beresford MJ, Ah-See M-LW, Stirling JJ, d'Arcy JA, Collins DJ, Makris A. Vascular characterisation of triple negative breast carcinomas using dynamic MRI. *Eur Radiol.* 2011;21(7):1364-1373.
86. Koo HR, Cho N, Song IC, Kim H, Chang JM, Yi A, Yun BL, Moon WK. Correlation of perfusion parameters on dynamic contrast-enhanced MRI with prognostic factors and subtypes of breast cancers. *J Magn Reson Imaging.* 2012;36(1):145-151.
87. Lee HS, Kim SH, Kang BJ, Baek JE, Song BJ. Perfusion parameters in dynamic contrast-enhanced MRI and apparent diffusion coefficient value in diffusion-weighted MRI: association with prognostic factors in breast cancer. *Acad Radiol.* 2016;23(4):446-456.
88. El Khouli RH, Macura KJ, Kamel IR, Jacobs MA, Bluemke DA. 3-T dynamic contrast-enhanced MRI of the breast: pharmacokinetic parameters versus conventional kinetic curve analysis. *AJR Am J Roentgenol.* 2011;197(6):1498-1505.

89. Fan M, Zhang P, Wang Y, Peng W, Wang S, Gao X, Xu M, Li L. Radiomic analysis of imaging heterogeneity in tumours and the surrounding parenchyma based on unsupervised decomposition of DCE-MRI for predicting molecular subtypes of breast cancer. *Eur Radiol*. 2019;29(8):4456-4467.
90. Chang RF, Chen HH, Chang YC, Huang CS, Chen JH, Lo CM. Quantification of breast tumor heterogeneity for ER status, HER2 status, and TN molecular subtype evaluation on DCE-MRI. *Magn Reson Imaging*. 2016;34(6):809-819.
91. Fox MJ, Gibbs P, Pickles MD. Minkowski functionals: An MRI texture analysis tool for determination of the aggressiveness of breast cancer. *J Magn Reson Imaging*. 2016;43(4):903-910.
92. Wang Q, Mao N, Liu M, Shi Y, Ma H, Dong J, Zhang X, Duan S, Wang B, Xie H. Radiomic analysis on magnetic resonance diffusion weighted image in distinguishing triple-negative breast cancer from other subtypes: a feasibility study. *Clin Imaging*. 2021;72:136-141.
93. Horvat JV, Iyer A, Morris EA, Apte A, Bernard-Davila B, Martinez DF, Leithner D, Sutton OM, Ochoa-Albiztegui RE, Giri D, Pinker K, Thakur SB. Histogram analysis and visual heterogeneity of diffusion-weighted imaging with apparent diffusion coefficient mapping in the prediction of molecular subtypes of invasive breast cancers. *Contrast Media Mol Imaging*. 2019;2019:2972189-2972189.
94. Surov A, Chang YW, Li L, Martincich L, Partridge SC, Kim JY, Wienke A. Apparent diffusion coefficient cannot predict molecular subtype and lymph node metastases in invasive breast cancer: a multicenter analysis. *BMC Cancer*. 2019;19(1):1043.
95. Uslu H, Önal T, Tosun M, Arslan AS, Ciftci E, Utkan NZ. Intravoxel incoherent motion magnetic resonance imaging for breast cancer: a comparison with molecular subtypes and histological grades. *Magn Reson Imaging*. 2021;78:35-41.

96. Zhao M, Fu K, Zhang L, Guo W, Wu Q, Bai X, Li Z, Guo Q, Tian J. Intravoxel incoherent motion magnetic resonance imaging for breast cancer: a comparison with benign lesions and evaluation of heterogeneity in different tumor regions with prognostic factors and molecular classification. *Oncol Lett.* 2018;16(4):5100-5112.
97. Leithner D, Mayerhoefer ME, Martinez DF, Jochelson MS, Morris EA, Thakur SB, Pinker K. Non-invasive assessment of breast cancer molecular subtypes with multiparametric magnetic resonance imaging radiomics. *Journal of clinical medicine.* 2020;9(6):1853.
98. Leithner D, Bernard-Davila B, Martinez DF, Horvat JV, Jochelson MS, Marino MA, Avendano D, Ochoa-Albiztegui RE, Sutton EJ, Morris EA, Thakur SB, Pinker K. Radiomic signatures derived from diffusion-weighted imaging for the assessment of breast cancer receptor status and molecular subtypes. *Molecular imaging and biology.* 2020;22(2):453-461.
99. Li W, Newitt DC, Wilmes LJ, Jones EF, Arasu V, Gibbs J, La Yun B, Li E, Partridge SC, Kornak J, Consortium IS, Esserman LJ, Hylton NM. Additive value of diffusion-weighted MRI in the I-SPY 2 TRIAL. *J Magn Reson Imaging.* 2019;50(6):1742-1753.
100. Chamming's F, Ueno Y, Ferré R, Kao E, Jannot AS, Chong J, Omeroglu A, Mesurolle B, Reinhold C, Gallix B. Features from computerized texture analysis of breast cancers at pretreatment MR imaging are associated with response to neoadjuvant chemotherapy. *Radiology.* 2018;286(2):412-420.
101. Li W, Newitt DC, Gibbs J, Wilmes LJ, Jones EF, Arasu VA, Strand F, Onishi N, Nguyen AA-T, Kornak J, Joe BN, Price ER, Ojeda-Fournier H, Eghtedari M, Zamora KW, Woodard SA, Umphrey H, Bernreuter W, Nelson M, Church AL, Bolan P, Kuritza T, Ward K, Morley K, Wolverton D, Fountain K, Lopez-Paniagua D, Hardesty L, Brandt K, McDonald ES, Rosen M, Kontos D, Abe H, Sheth D, Crane EP, Dillis C, Sheth P, Hovanessian-Larsen L, Bang DH, Porter B, Oh KY, Jafarian N, Tudorica A, Niell BL, Drukeinis J, Newell MS, Cohen MA, Giurescu M, Berman E, Lehman C,

- Partridge SC, Fitzpatrick KA, Borders MH, Yang WT, Dogan B, Goudreau S, Chenevert T, Yau C, DeMichele A, Berry D, Esserman LJ, Hylton NM. Predicting breast cancer response to neoadjuvant treatment using multi-feature MRI: results from the I-SPY 2 TRIAL. *npj Breast Cancer*. 2020;6(1):63.
102. Musall BC, Abdelhafez AH, Adrada BE, Candelaria RP, Mohamed RMM, Boge M, Le-Petross H, Arribas E, Lane DL, Spak DA, Leung JWT, Hwang K-P, Son JB, Elshafeey NA, Mahmoud HS, Wei P, Sun J, Zhang S, White JB, Ravenberg EE, Litton JK, Damodaran S, Thompson AM, Moulder SL, Yang WT, Pagel MD, Rauch GM, Ma J. Functional tumor volume by fast dynamic contrast-enhanced MRI for predicting neoadjuvant systemic therapy response in triple-negative breast cancer. *J Magn Reson Imaging*. 2021;n/a(n/a).
 103. Dave RV, Millican-Slater R, Dodwell D, Horgan K, Sharma N. Neoadjuvant chemotherapy with MRI monitoring for breast cancer. *Br J Surg*. 2017;104(9):1177-1187.
 104. Schmitz AMT, Teixeira SC, Pengel KE, Loo CE, Vogel WV, Wesseling J, Rutgers EJT, Valdés Olmos RA, Sonke GS, Rodenhuis S, Vrancken Peeters MJTFD, Gilhuijs KGA. Monitoring tumor response to neoadjuvant chemotherapy using MRI and 18F-FDG PET/CT in breast cancer subtypes. *PLoS One*. 2017;12(5):e0176782-e0176782.
 105. Eom HJ, Cha JH, Choi WJ, Chae EY, Shin HJ, Kim HH. Predictive clinicopathologic and dynamic contrast-enhanced MRI findings for tumor response to neoadjuvant chemotherapy in triple-negative breast cancer. *AJR Am J Roentgenol*. 2017;208(6):W225-w230.
 106. Bansal GJ, Santosh D. Accuracy of MRI for prediction of response to neo-adjuvant chemotherapy in triple negative breast cancer compared to other subtypes of breast cancer. *Indian J Radiol Imaging*. 2016;26(4):475-481.
 107. De Los Santos JF, Cantor A, Amos KD, Forero A, Golshan M, Horton JK, Hudis CA, Hylton NM, McGuire K, Meric-Bernstam F, Meszoely IM, Nanda R, Hwang ES. Magnetic resonance imaging as

- a predictor of pathologic response in patients treated with neoadjuvant systemic treatment for operable breast cancer: translational breast cancer research consortium trial 017. *Cancer*. 2013;119(10):1776-1783.
108. Golshan M, Wong SM, Loibl S, Huober JB, O'Shaughnessy J, Rugo HS, Wolmark N, Ansell P, Maag D, Sullivan DM, Metzger-Filho O, Von Minckwitz G, Geyer CE, Jr., Sikov WM, Untch M. Early assessment with magnetic resonance imaging for prediction of pathologic response to neoadjuvant chemotherapy in triple-negative breast cancer: results from the phase III BrighTNess trial. *Eur J Surg Oncol*. 2020;46(2):223-228.
 109. Bae MS, Shin SU, Ryu HS, Han W, Im SA, Park IA, Noh DY, Moon WK. Pretreatment MR imaging features of triple-negative breast cancer: association with response to neoadjuvant chemotherapy and recurrence-free survival. *Radiology*. 2016;281(2):392-400.
 110. Braman NM, Etesami M, Prasanna P, Dubchuk C, Gilmore H, Tiwari P, Plecha D, Madabhushi A. Intratumoral and peritumoral radiomics for the pretreatment prediction of pathological complete response to neoadjuvant chemotherapy based on breast DCE-MRI. *Breast Cancer Res*. 2017;19(1):57.
 111. Bufi E, Belli P, Di Matteo M, Terribile D, Franceschini G, Nardone L, Petrone G, Bonomo L. Effect of breast cancer phenotype on diagnostic performance of MRI in the prediction to response to neoadjuvant treatment. *Eur J Radiol*. 2014;83(9):1631-1638.
 112. Liu Z, Li Z, Qu J, Zhang R, Zhou X, Li L, Sun K, Tang Z, Jiang H, Li H, Xiong Q, Ding Y, Zhao X, Wang K, Liu Z, Tian J. Radiomics of multiparametric MRI for pretreatment prediction of pathologic complete response to neoadjuvant chemotherapy in breast cancer: a multicenter study. *Clin Cancer Res*. 2019;25(12):3538-3547.
 113. Abdelhafez AH, Musall BC, Adrada BE, Hess K, Son JB, Hwang KP, Candelaria RP, Santiago L, Whitman GJ, Le-Petross HT, Moseley TW, Arribas E, Lane DL, Scoggins ME, Leung JWT,

- Mahmoud HS, White JB, Ravenberg EE, Litton JK, Valero V, Wei P, Thompson AM, Moulder SL, Pagel MD, Ma J, Yang WT, Rauch GM. Tumor necrosis by pretreatment breast MRI: association with neoadjuvant systemic therapy (NAST) response in triple-negative breast cancer (TNBC). *Breast Cancer Res Treat.* 2020.
114. Bao C, Lu Y, Chen J, Chen D, Lou W, Ding B, Xu L, Fan W. Exploring specific prognostic biomarkers in triple-negative breast cancer. *Cell Death Dis.* 2019;10(11):807.
 115. Maiorano E, Regan MM, Viale G, Mastropasqua MG, Colleoni M, Castiglione-Gertsch M, Price KN, Gelber RD, Goldhirsch A, Coates AS. Prognostic and predictive impact of central necrosis and fibrosis in early breast cancer: results from two International Breast Cancer Study Group randomized trials of chemoendocrine adjuvant therapy. *Breast Cancer Res Treat.* 2010;121(1):211-218.
 116. Bauer KR, Brown M, Cress RD, Parise CA, Caggiano V. Descriptive analysis of estrogen receptor (ER)-negative, progesterone receptor (PR)-negative, and HER2-negative invasive breast cancer, the so-called triple-negative phenotype: a population-based study from the California Cancer Registry. *Cancer.* 2007;109(9):1721-1728.
 117. Richards CH, Mohammed Z, Qayyum T, Horgan PG, McMillan DC. The prognostic value of histological tumor necrosis in solid organ malignant disease: a systematic review. *Future Oncol.* 2011;7(10):1223-1235.
 118. Vayrynen SA, Vayrynen JP, Klintrup K, Makela J, Karttunen TJ, Tuomisto A, Makinen MJ. Clinical impact and network of determinants of tumour necrosis in colorectal cancer. *Br J Cancer.* 2016;114(12):1334-1342.
 119. Fujisaki A, Aoki T, Kasai T, Kinoshita S, Tomoda Y, Tanaka F, Yatera K, Mukae H, Korogi Y. Pleomorphic carcinoma of the lung: relationship between CT findings and prognosis. *AJR Am J Roentgenol.* 2016;207(2):289-294.

120. Zhang L, Zha Z, Qu W, Zhao H, Yuan J, Feng Y, Wu B. Tumor necrosis as a prognostic variable for the clinical outcome in patients with renal cell carcinoma: a systematic review and meta-analysis. *BMC Cancer*. 2018;18(1):870.
121. Dietzel M, Baltzer PA, Vag T, Herzog A, Gajda M, Camara O, Kaiser WA. The necrosis sign in magnetic resonance-mammography: diagnostic accuracy in 1,084 histologically verified breast lesions. *Breast J*. 2010;16(6):603-608.
122. Jimenez RE, Wallis T, Visscher DW. Centrally necrotizing carcinomas of the breast: a distinct histologic subtype with aggressive clinical behavior. *Am J Surg Pathol*. 2001;25(3):331-337.
123. Zhang Y, Ou Y, Yu D, Yong X, Wang X, Zhu B, Zhang Q, Zhou L, Cai Z, Cheng Z. Clinicopathological study of centrally necrotizing carcinoma of the breast. *BMC Cancer*. 2015;15:282.
124. Pu RT, Schott AF, Sturtz DE, Griffith KA, Kleer CG. Pathologic features of breast cancer associated with complete response to neoadjuvant chemotherapy: importance of tumor necrosis. *Am J Surg Pathol*. 2005;29(3):354-358.
125. Masood S. Neoadjuvant chemotherapy in breast cancers. *Womens Health*. 2016;12(5):480-491.
126. Lee AH, Gillett CE, Ryder K, Fentiman IS, Miles DW, Millis RR. Different patterns of inflammation and prognosis in invasive carcinoma of the breast. *Histopathology*. 2006;48(6):692-701.
127. Kato T, Kimura T, Miyakawa R, Tanaka S, Fujii A, Yamamoto K, Kameoka S, Hamano K, Kawakami M, Aiba M. Clinicopathologic study of angiogenesis in Japanese patients with breast cancer. *World J Surg*. 1997;21(1):49-56.
128. Urru SAM, Gallus S, Bosetti C, Moi T, Medda R, Sollai E, Murgia A, Sanges F, Pira G, Manca A, Palmas D, Floris M, Asunis AM, Atzori F, Carru C, D'Incalci M, Ghiani M, Marras V, Onnis D, Santona MC, Sarobba G, Valle E, Canu L, Cossu S, Bulfone A, Rocca PC, De Miglio MR, Orru S. Clinical and pathological factors influencing survival in a large cohort of triple-negative breast cancer patients. *BMC Cancer*. 2018;18(1):56.

129. Walsh EM, Keane MM, Wink DA, Callagy G, Glynn SA. Review of triple negative breast cancer and the impact of inducible nitric oxide synthase on tumor biology and patient outcomes. *Crit Rev Oncog*. 2016;21(5-6):333-351.
130. Keam B, Im SA, Lee KH, Han SW, Oh DY, Kim JH, Lee SH, Han W, Kim DW, Kim TY, Park IA, Noh DY, Heo DS, Bang YJ. Ki-67 can be used for further classification of triple negative breast cancer into two subtypes with different response and prognosis. *Breast Cancer Res*. 2011;13(2):R22.
131. Fulford LG, Easton DF, Reis-Filho JS, Sofronis A, Gillett CE, Lakhani SR, Hanby A. Specific morphological features predictive for the basal phenotype in grade 3 invasive ductal carcinoma of breast. *Histopathology*. 2006;49(1):22-34.
132. Ryu DW, Jung MJ, Choi WS, Lee CH. Clinical significance of morphologic characteristics in triple negative breast cancer. *J Korean Surg Soc*. 2011;80(5):301-306.
133. Kawashima H, Inokuchi M, Furukawa H, Kitamura S. Triple-negative breast cancer: are the imaging findings different between responders and nonresponders to neoadjuvant chemotherapy? *Acad Radiol*. 2011;18(8):963-969.
134. Fang P, Musall BC, Son JB, Moreno AC, Hobbs BP, Carter BW, Fellman BM, Mawlawi O, Ma J, Lin SH. Multimodal imaging of pathologic response to chemoradiation in esophageal cancer. *Int J Radiat Oncol Biol Phys*. 2018.
135. Collins J, Epstein JI. Prognostic significance of extensive necrosis in renal cell carcinoma. *Hum Pathol*. 2017;66:108-114.
136. Rilke F, Colnaghi MI, Cascinelli N, Andreola S, Baldini MT, Bufalino R, Della Porta G, Menard S, Pierotti MA, Testori A. Prognostic significance of HER-2/neu expression in breast cancer and its relationship to other prognostic factors. *Int J Cancer*. 1991;49(1):44-49.

137. Liu YX, Wang KR, Xing H, Zhai XJ, Wang LP, Wang W. Attempt towards a novel classification of triple-negative breast cancer using immunohistochemical markers. *Oncol Lett*. 2016;12(2):1240-1256.
138. Pistelli M, Pagliacci A, Battelli N, Santinelli A, Biscotti T, Ballatore Z, Berardi R, Cascinu S. Prognostic factors in early-stage triple-negative breast cancer: lessons and limits from clinical practice. *Anticancer Res*. 2013;33(6):2737-2742.
139. Hudis CA, Barlow WE, Costantino JP, Gray RJ, Pritchard KI, Chapman JA, Sparano JA, Hunsberger S, Enos RA, Gelber RD, Zujewski JA. Proposal for standardized definitions for efficacy end points in adjuvant breast cancer trials: the STEEP system. *J Clin Oncol*. 2007;25(15):2127-2132.
140. Moulder S, Moroney J, Helgason T, Wheler J, Booser D, Albarracin C, Morrow PK, Koenig K, Kurzrock R. Responses to liposomal Doxorubicin, bevacizumab, and temsirolimus in metaplastic carcinoma of the breast: biologic rationale and implications for stem-cell research in breast cancer. *J Clin Oncol*. 2011;29(19):e572-575.
141. Houssami N, Macaskill P, von Minckwitz G, Marinovich ML, Mamounas E. Meta-analysis of the association of breast cancer subtype and pathologic complete response to neoadjuvant chemotherapy. *Eur J Cancer*. 2012;48(18):3342-3354.
142. Sharma P, Lopez-Tarruella S, Garcia-Saenz JA, Khan QJ, Gomez HL, Prat A, Moreno F, Jerez-Gilarranz Y, Barnadas A, Picornell AC, Monte-Millan MD, Gonzalez-Rivera M, Massarrah T, Pelaez-Lorenzo B, Palomero MI, Gonzalez Del Val R, Cortes J, Fuentes-Rivera H, Morales DB, Marquez-Rodas I, Perou CM, Lehn C, Wang YY, Klemp JR, Mammen JV, Wagner JL, Amin AL, O'Dea AP, Heldstab J, Jensen RA, Kimler BF, Godwin AK, Martin M. Pathological response and survival in triple-negative breast cancer following neoadjuvant carboplatin plus docetaxel. *Clin Cancer Res*. 2018;24(23):5820-5829.

143. de Ruijter TC, Veeck J, de Hoon JPJ, van Engeland M, Tjan-Heijnen VC. Characteristics of triple-negative breast cancer. *Journal of cancer research and clinical oncology*. 2011;137(2):183-192.
144. Turnbull LW. Dynamic contrast-enhanced MRI in the diagnosis and management of breast cancer. *NMR Biomed*. 2009;22(1):28-39.
145. Jafri NF, Newitt DC, Kornak J, Esserman LJ, Joe BN, Hylton NM. Optimized breast MRI functional tumor volume as a biomarker of recurrence-free survival following neoadjuvant chemotherapy. *J Magn Reson Imaging*. 2014;40(2):476-482.
146. Drukker K, Li H, Antropova N, Edwards A, Papaioannou J, Giger ML. Most-enhancing tumor volume by MRI radiomics predicts recurrence-free survival "early on" in neoadjuvant treatment of breast cancer. *Cancer Imaging*. 2018;18(1):12.
147. Partridge SC, Gibbs JE, Lu Y, Esserman LJ, Tripathy D, Wolverton DS, Rugo HS, Hwang ES, Ewing CA, Hylton NM. MRI measurements of breast tumor volume predict response to neoadjuvant chemotherapy and recurrence-free survival. *AJR Am J Roentgenol*. 2005;184(6):1774-1781.
148. Hylton NM, Gatsonis CA, Rosen MA, Lehman CD, Newitt DC, Partridge SC, Bernreuter WK, Pisano ED, Morris EA, Weatherall PT, Polin SM, Newstead GM, Marques HS, Esserman LJ, Schnall MD. Neoadjuvant chemotherapy for breast cancer: functional tumor volume by MR imaging predicts recurrence-free survival-results from the ACRIN 6657/CALGB 150007 I-SPY 1 TRIAL. *Radiology*. 2016;279(1):44-55.
149. Li W, Arasu V, Newitt DC, Jones EF, Wilmes L, Gibbs J, Kornak J, Joe BN, Esserman LJ, Hylton NM, Team AT, Network ISI. Effect of MR imaging contrast thresholds on prediction of neoadjuvant chemotherapy response in breast cancer subtypes: a subgroup analysis of the ACRIN 6657/I-SPY 1 TRIAL. *Tomography (Ann Arbor, Mich)*. 2016;2(4):378-387.

150. Lo WC, Li W, Jones EF, Newitt DC, Kornak J, Wilmes LJ, Esserman LJ, Hylton NM. Effect of imaging parameter thresholds on MRI prediction of neoadjuvant chemotherapy response in breast cancer subtypes. *PLoS One*. 2016;11(2):e0142047.
151. Mori N, Abe H, Mugikura S, Takasawa C, Sato S, Miyashita M, Mori Y, Pineda FD, Karczmar GS, Tamura H, Takahashi S, Takase K. Ultrafast dynamic contrast-enhanced breast MRI: kinetic curve assessment using empirical mathematical model validated with histological microvessel density. *Acad Radiol*. 2019;26(7):e141-e149.
152. Mori N, Pineda FD, Tsuchiya K, Mugikura S, Takahashi S, Karczmar GS, Abe H. Fast temporal resolution dynamic contrast-enhanced MRI: histogram analysis versus visual analysis for differentiating benign and malignant breast lesions. *AJR Am J Roentgenol*. 2018;211(4):933-939.
153. Verburg E, van Gils CH, Bakker MF, Viergever MA, Pijnappel RM, Veldhuis WB, Gilhuijs KGA. Computer-aided diagnosis in multiparametric magnetic resonance imaging screening of women with extremely dense breasts to reduce false-positive diagnoses. *Invest Radiol*. 2020;55(7):438-444.
154. Kuhl CK, Schild HH, Morakkabati N. Dynamic bilateral contrast-enhanced MR imaging of the breast: trade-off between spatial and temporal resolution. *Radiology*. 2005;236(3):789-800.
155. Stoutjesdijk MJ, Fütterer JJ, Boetes C, van Die LE, Jager G, Barentsz JO. Variability in the description of morphologic and contrast enhancement characteristics of breast lesions on magnetic resonance imaging. *Invest Radiol*. 2005;40(6):355-362.
156. Wu C, Pineda F, Hormuth li DA, Karczmar GS, Yankeelov TE. Quantitative analysis of vascular properties derived from ultrafast DCE-MRI to discriminate malignant and benign breast tumors. *Magn Reson Med*. 2019;81(3):2147-2160.

157. Pineda FD, Medved M, Wang S, Fan X, Schacht DV, Sennett C, Oto A, Newstead GM, Abe H, Karczmar GS. Ultrafast bilateral DCE-MRI of the breast with conventional fourier sampling: preliminary evaluation of semi-quantitative analysis. *Acad Radiol*. 2016;23(9):1137-1144.
158. Milon A, Wahab CA, Kermarrec E, Bekhouche A, Taourel P, Thomassin-Naggara I. Breast MRI: is faster better? *AJR Am J Roentgenol*. 2020;214(2):282-295.
159. Saranathan M, Rettmann DW, Hargreaves BA, Clarke SE, Vasanawala SS. Differential Subsampling with Cartesian Ordering (DISCO): a high spatio-temporal resolution Dixon imaging sequence for multiphasic contrast enhanced abdominal imaging. *J Magn Reson Imaging*. 2012;35(6):1484-1492.
160. Luo J, Johnston BS, Kitsch AE, Hippe DS, Korde LA, Javid S, Lee JM, Peacock S, Lehman CD, Partridge SC, Rahbar H. Ductal carcinoma in situ: quantitative preoperative breast MR imaging features associated with recurrence after treatment. *Radiology*. 2017;285(3):788-797.
161. Henderson SA, Muhammad Gowdh N, Purdie CA, Jordan LB, Evans A, Brunton T, Thompson AM, Vinnicombe S. Breast cancer: influence of tumour volume estimation method at MRI on prediction of pathological response to neoadjuvant chemotherapy. *Br J Radiol*. 2018;91(1087):20180123.
162. Musall BC. Quantitative DWI as an early imaging biomarker of the response to chemoradiation in esophageal cancer. *UT GSBS dissertations and theses (Open Access)*. 2017.
163. Newitt DC, Aliu SO, Witcomb N, Sela G, Kornak J, Esserman L, Hylton NM. Real-time measurement of functional tumor volume by MRI to assess treatment response in breast cancer neoadjuvant clinical trials: validation of the Aegis SER software platform. *Transl Oncol*. 2014;7(1):94-100.
164. Onishi N, Li W, Gibbs J, Wilmes LJ, Nguyen A, Jones EF, Arasu V, Kornak J, Joe BN, Esserman LJ, Newitt DC, Hylton NM. Impact of MRI protocol adherence on prediction of pathological

- complete response in the I-SPY 2 neoadjuvant breast cancer trial. *Tomography (Ann Arbor, Mich)*. 2020;6(2):77-85.
165. Jones KM, Pagel MD, Cárdenas-Rodríguez J. Linearization improves the repeatability of quantitative dynamic contrast-enhanced MRI. *Magn Reson Imaging*. 2018;47:16-24.
 166. Galbraith SM, Lodge MA, Taylor NJ, Rustin GJ, Bentzen S, Stirling JJ, Padhani AR. Reproducibility of dynamic contrast-enhanced MRI in human muscle and tumours: comparison of quantitative and semi-quantitative analysis. *NMR Biomed*. 2002;15(2):132-142.
 167. Anders C, Carey LA. Understanding and treating triple-negative breast cancer. *Oncology*. 2008;22(11):1233-1239.
 168. von Minckwitz G, Untch M, Blohmer JU, Costa SD, Eidtmann H, Fasching PA, Gerber B, Eiermann W, Hilfrich J, Huober J, Jackisch C, Kaufmann M, Konecny GE, Denkert C, Nekljudova V, Mehta K, Loibl S. Definition and impact of pathologic complete response on prognosis after neoadjuvant chemotherapy in various intrinsic breast cancer subtypes. *J Clin Oncol*. 2012;30(15):1796-1804.
 169. Moradi B, Gity M, Etesam F, Borhani A, Ahmadinejad N, Kazemi MA. Correlation of apparent diffusion coefficient values and peritumoral edema with pathologic biomarkers in patients with breast cancer. *Clin Imaging*. 2020;68:242-248.
 170. Ahn HS, Jang M, Kim SM, La Yun B, Lee SH. Usefulness of preoperative breast magnetic resonance imaging with a dedicated axillary sequence for the detection of axillary lymph node metastasis in patients with early ductal breast cancer. *Radiol Med*. 2019;124(12):1220-1228.
 171. Uematsu T. Focal breast edema associated with malignancy on T2-weighted images of breast MRI: peritumoral edema, prepectoral edema, and subcutaneous edema. *Breast Cancer*. 2015;22(1):66-70.

172. Baltzer PA, Yang F, Dietzel M, Herzog A, Simon A, Vag T, Gajda M, Camara O, Kaiser WA. Sensitivity and specificity of unilateral edema on T2w-TSE sequences in MR-Mammography considering 974 histologically verified lesions. *Breast J.* 2010;16(3):233-239.
173. Yili Z, Xiaoyan H, Hongwen D, Yun Z, Xin C, Peng W, Youmin G. The value of diffusion-weighted imaging in assessing the ADC changes of tissues adjacent to breast carcinoma. *BMC Cancer.* 2009;9(1):18.
174. Panzironi G, Moffa G, Galati F, Marzocca F, Rizzo V, Pediconi F. Peritumoral edema as a biomarker of the aggressiveness of breast cancer: results of a retrospective study on a 3 T scanner. *Breast Cancer Res Treat.* 2020;181(1):53-60.
175. Cheon H, Kim HJ, Kim TH, Ryeom HK, Lee J, Kim GC, Yuk JS, Kim WH. Invasive breast cancer: prognostic value of peritumoral edema identified at preoperative MR imaging. *Radiology.* 2018;287(1):68-75.
176. Harada TL, Uematsu T, Nakashima K, Sugino T, Nishimura S, Takahashi K, Hayashi T, Tadokoro Y, Watanabe J, Nakamoto S, Ito T. Is the presence of edema and necrosis on T2WI pretreatment breast MRI the key to predict pCR of triple negative breast cancer? *Eur Radiol.* 2020;30(6):3363-3370.
177. Liu C, Ding J, Spuhler K, Gao Y, Serrano Sosa M, Moriarty M, Hussain S, He X, Liang C, Huang C. Preoperative prediction of sentinel lymph node metastasis in breast cancer by radiomic signatures from dynamic contrast-enhanced MRI. *J Magn Reson Imaging.* 2019;49(1):131-140.
178. Choi EJ, Youk JH, Choi H, Song JS. Dynamic contrast-enhanced and diffusion-weighted MRI of invasive breast cancer for the prediction of sentinel lymph node status. *J Magn Reson Imaging.* 2020;51(2):615-626.
179. Mori N, Mugikura S, Takasawa C, Miyashita M, Shimauchi A, Ota H, Ishida T, Kasajima A, Takase K, Kodama T, Takahashi S. Peritumoral apparent diffusion coefficients for prediction of

- lymphovascular invasion in clinically node-negative invasive breast cancer. *Eur Radiol.* 2016;26(2):331-339.
180. Igarashi T, Furube H, Ashida H, Ojiri H. Breast MRI for prediction of lymphovascular invasion in breast cancer patients with clinically negative axillary lymph nodes. *Eur J Radiol.* 2018;107:111-118.
 181. Okuma H, Sudah M, Kettunen T, Niukkanen A, Sutela A, Masarwah A, Kosma VM, Auvinen P, Mannermaa A, Vanninen R. Peritumor to tumor apparent diffusion coefficient ratio is associated with biologically more aggressive breast cancer features and correlates with the prognostication tools. *PLoS One.* 2020;15(6):e0235278.
 182. Fan M, He T, Zhang P, Cheng H, Zhang J, Gao X, Li L. Diffusion-weighted imaging features of breast tumours and the surrounding stroma reflect intrinsic heterogeneous characteristics of molecular subtypes in breast cancer. *NMR Biomed.* 2018;31(2):e3869.
 183. Kim EJ, Kim SH, Park GE, Kang BJ, Song BJ, Kim YJ, Lee D, Ahn H, Kim I, Son YH, Grimm R. Histogram analysis of apparent diffusion coefficient at 3.0T: Correlation with prognostic factors and subtypes of invasive ductal carcinoma. *J Magn Reson Imaging.* 2015;42(6):1666-1678.
 184. Kettunen T, Okuma H, Auvinen P, Sudah M, Tiainen S, Sutela A, Masarwah A, Tammi M, Tammi R, Oikari S, Vanninen R. Peritumoral ADC values in breast cancer: region of interest selection, associations with hyaluronan intensity, and prognostic significance. *Eur Radiol.* 2020;30(1):38-46.
 185. Padhani AR, Liu G, Koh DM, Chenevert TL, Thoeny HC, Takahara T, Dzik-Jurasz A, Ross BD, Van Cauteren M, Collins D, Hammoud DA, Rustin GJ, Taouli B, Choyke PL. Diffusion-weighted magnetic resonance imaging as a cancer biomarker: consensus and recommendations. *Neoplasia.* 2009;11(2):102-125.

186. Barentsz MW, Taviani V, Chang JM, Ikeda DM, Miyake KK, Banerjee S, van den Bosch MA, Hargreaves BA, Daniel BL. Assessment of tumor morphology on diffusion-weighted (DWI) breast MRI: diagnostic value of reduced field of view DWI. *J Magn Reson Imaging*. 2015;42(6):1656-1665.
187. Shin HJ, Park JY, Shin KC, Kim HH, Cha JH, Chae EY, Choi WJ. Characterization of tumor and adjacent peritumoral stroma in patients with breast cancer using high-resolution diffusion-weighted imaging: correlation with pathologic biomarkers. *Eur J Radiol*. 2016;85(5):1004-1011.
188. McLaughlin RL, Newitt DC, Wilmes LJ, Jones EF, Wisner DJ, Kornak J, Proctor E, Joe BN, Hylton NM. High resolution in vivo characterization of apparent diffusion coefficient at the tumor-stromal boundary of breast carcinomas: a pilot study to assess treatment response using proximity-dependent diffusion-weighted imaging. *J Magn Reson Imaging*. 2014;39(5):1308-1313.
189. Singer L, Wilmes LJ, Saritas EU, Shankaranarayanan A, Proctor E, Wisner DJ, Chang B, Joe BN, Nishimura DG, Hylton NM. High-resolution diffusion-weighted magnetic resonance imaging in patients with locally advanced breast cancer. *Acad Radiol*. 2012;19(5):526-534.
190. Park JY, Shin HJ, Shin KC, Sung YS, Choi WJ, Chae EY, Cha JH, Kim HH. Comparison of readout segmented echo planar imaging (EPI) and EPI with reduced field-of-view diffusion-weighted imaging at 3T in patients with breast cancer. *J Magn Reson Imaging*. 2015;42(6):1679-1688.
191. Saritas EU, Cunningham CH, Lee JH, Han ET, Nishimura DG. DWI of the spinal cord with reduced FOV single-shot EPI. *Magn Reson Med*. 2008;60(2):468-473.
192. *R: A language and environment for statistical computing* [computer program]. Vienna, Austria: R Foundation for Statistical Computing; 2010.
193. Braman N, Prasanna P, Whitney J, Singh S, Beig N, Etesami M, Bates DDB, Gallagher K, Bloch BN, Vulchi M, Turk P, Bera K, Abraham J, Sikov WM, Somlo G, Harris LN, Gilmore H, Plecha D,

- Varadan V, Madabhushi A. Association of peritumoral radiomics with tumor biology and pathologic response to preoperative targeted therapy for HER2 (ERBB2)-positive breast cancer. *JAMA Netw Open*. 2019;2(4):e192561.
194. Cho HH, Park M, Park H, Ko ES, Hwang NY, Im YH, Ko K, Sim SH. The tumor-fat interface volume of breast cancer on pretreatment MRI is associated with a pathologic response to neoadjuvant chemotherapy. *Biology*. 2020;9(11).
 195. Obeid JP, Stoyanova R, Kwon D, Patel M, Padgett K, Slingerland J, Takita C, Alperin N, Yepes M, Zeidan YH. Multiparametric evaluation of preoperative MRI in early stage breast cancer: prognostic impact of peri-tumoral fat. *Clin Transl Oncol*. 2017;19(2):211-218.
 196. Balleyguier C, Lakhdar AB, Dunant A, Mathieu MC, Delaloge S, Sinkus R. Value of whole breast magnetic resonance elastography added to MRI for lesion characterization. *NMR Biomed*. 2018;31(1).
 197. Dittmann F, Reiter R, Guo J, Haas M, Asbach P, Fischer T, Braun J, Sack I. Tomoelastography of the prostate using multifrequency MR elastography and externally placed pressurized-air drivers. *Magn Reson Med*. 2018;79(3):1325-1333.
 198. Vogl TJ, Martin SS, Johnson AA, Haas Y. Evaluation of MR elastography as a response parameter for transarterial chemoembolization of colorectal liver metastases. *Eur Radiol*. 2020;30(7):3900-3907.
 199. Shi Y, Gao F, Li Y, Tao S, Yu B, Liu Z, Liu Y, Glaser KJ, Ehman RL, Guo Q. Differentiation of benign and malignant solid pancreatic masses using magnetic resonance elastography with spin-echo echo planar imaging and three-dimensional inversion reconstruction: a prospective study. *Eur Radiol*. 2018;28(3):936-945.

200. Gordic S, Ayache JB, Kennedy P, Besa C, Wagner M, Bane O, Ehman RL, Kim E, Taouli B. Value of tumor stiffness measured with MR elastography for assessment of response of hepatocellular carcinoma to locoregional therapy. *Abdom Radiol (NY)*. 2017;42(6):1685-1694.
201. Yin Z, Hughes JD, Trzasko JD, Glaser KJ, Manduca A, Van Gompel J, Link MJ, Romano A, Ehman RL, Huston J, 3rd. Slip interface imaging based on MR-elastography preoperatively predicts meningioma-brain adhesion. *J Magn Reson Imaging*. 2017;46(4):1007-1016.
202. Hennedige TP, Hallinan JT, Leung FP, Teo LL, Iyer S, Wang G, Chang S, Madhavan KK, Wee A, Venkatesh SK. Comparison of magnetic resonance elastography and diffusion-weighted imaging for differentiating benign and malignant liver lesions. *Eur Radiol*. 2016;26(2):398-406.
203. Sahebjavaher RS, Nir G, Honarvar M, Gagnon LO, Ischia J, Jones EC, Chang SD, Fazli L, Goldenberg SL, Rohling R, Kozlowski P, Sinkus R, Salcudean SE. MR elastography of prostate cancer: quantitative comparison with histopathology and repeatability of methods. *NMR Biomed*. 2015;28(1):124-139.
204. Sahebjavaher RS, Nir G, Gagnon LO, Ischia J, Jones EC, Chang SD, Yung A, Honarvar M, Fazli L, Goldenberg SL, Rohling R, Sinkus R, Kozlowski P, Salcudean SE. MR elastography and diffusion-weighted imaging of ex vivo prostate cancer: quantitative comparison to histopathology. *NMR Biomed*. 2015;28(1):89-100.
205. Reiss-Zimmermann M, Streitberger KJ, Sack I, Braun J, Arlt F, Fritzsche D, Hoffmann KT. High resolution imaging of viscoelastic properties of intracranial tumours by multi-frequency magnetic resonance elastography. *Clin Neuroradiol*. 2015;25(4):371-378.
206. Arani A, Da Rosa M, Ramsay E, Plewes DB, Haider MA, Chopra R. Incorporating endorectal MR elastography into multi-parametric MRI for prostate cancer imaging: Initial feasibility in volunteers. *J Magn Reson Imaging*. 2013;38(5):1251-1260.

207. Garteiser P, Doblas S, Daire JL, Wagner M, Leitaio H, Vilgrain V, Sinkus R, Van Beers BE. MR elastography of liver tumours: value of viscoelastic properties for tumour characterisation. *Eur Radiol.* 2012;22(10):2169-2177.
208. Arani A, Plewes D, Krieger A, Chopra R. The feasibility of endorectal MR elastography for prostate cancer localization. *Magn Reson Med.* 2011;66(6):1649-1657.
209. Li S, Chen M, Wang W, Zhao W, Wang J, Zhao X, Zhou C. A feasibility study of MR elastography in the diagnosis of prostate cancer at 3.0T. *Acta Radiol.* 2011;52(3):354-358.
210. Siegmann KC, Xydeas T, Sinkus R, Kraemer B, Vogel U, Claussen CD. Diagnostic value of MR elastography in addition to contrast-enhanced MR imaging of the breast-initial clinical results. *Eur Radiol.* 2010;20(2):318-325.
211. Venkatesh SK, Yin M, Glockner JF, Takahashi N, Araoz PA, Talwalkar JA, Ehman RL. MR elastography of liver tumors: preliminary results. *AJR Am J Roentgenol.* 2008;190(6):1534-1540.
212. Sinkus R, Siegmann K, Xydeas T, Tanter M, Claussen C, Fink M. MR elastography of breast lesions: understanding the solid/liquid duality can improve the specificity of contrast-enhanced MR mammography. *Magn Reson Med.* 2007;58(6):1135-1144.
213. Xydeas T, Siegmann K, Sinkus R, Krainick-Strobel U, Miller S, Claussen CD. Magnetic resonance elastography of the breast: correlation of signal intensity data with viscoelastic properties. *Invest Radiol.* 2005;40(7):412-420.
214. Sinkus R, Tanter M, Xydeas T, Catheline S, Bercoff J, Fink M. Viscoelastic shear properties of in vivo breast lesions measured by MR elastography. *Magn Reson Imaging.* 2005;23(2):159-165.
215. Sinkus R, Tanter M, Catheline S, Lorenzen J, Kuhl C, Sondermann E, Fink M. Imaging anisotropic and viscous properties of breast tissue by magnetic resonance-elastography. *Magn Reson Med.* 2005;53(2):372-387.

216. Lorenzen J, Sinkus R, Lorenzen M, Dargatz M, Leussler C, Roschmann P, Adam G. MR elastography of the breast: preliminary clinical results. *Rofo*. 2002;174(7):830-834.
217. McKnight AL, Kugel JL, Rossman PJ, Manduca A, Hartmann LC, Ehman RL. MR elastography of breast cancer: preliminary results. *AJR Am J Roentgenol*. 2002;178(6):1411-1417.
218. Li M, Guo J, Hu P, Jiang H, Chen J, Hu J, Asbach P, Sack I, Li W. Tomoelastography based on multifrequency MR elastography for prostate cancer detection: comparison with multiparametric MRI. *Radiology*. 2021:201852.
219. Hu B, Deng Y, Chen J, Kuang S, Tang W, He B, Zhang L, Xiao Y, Chen J, Rossman P, Arani A, Yin Z, Glaser KJ, Yin M, Venkatesh SK, Ehman RL, Wang J. Evaluation of MR elastography for prediction of lymph node metastasis in prostate cancer. *Abdom Radiol (NY)*. 2021.
220. Zhu L, Guo J, Jin Z, Xue H, Dai M, Zhang W, Sun Z, Xu J, Marticorena Garcia SR, Asbach P, Hamm B, Sack I. Distinguishing pancreatic cancer and autoimmune pancreatitis with in vivo tomoelastography. *Eur Radiol*. 2021;31(5):3366-3374.
221. Cho HJ, Kim B, Kim HJ, Huh J, Kim JK, Lee JH, Seo CW, Ahn HR, Eun JW, Kim SS, Cho SW, Cheong JY. Liver stiffness measured by MR elastography is a predictor of early HCC recurrence after treatment. *Eur Radiol*. 2020;30(8):4182-4192.
222. Reiter R, Majumdar S, Kearney S, Kajdacsy-Balla A, Macias V, Crivellaro S, Caldwell B, Abern M, Royston TJ, Klatt D. Prostate cancer assessment using MR elastography of fresh prostatectomy specimens at 9.4 T. *Magn Reson Med*. 2019.
223. Wang J, Shan Q, Liu Y, Yang H, Kuang S, He B, Zhang Y, Chen J, Zhang T, Glaser KJ, Zhu C, Chen J, Yin M, Venkatesh SK, Ehman RL. 3D MR elastography of hepatocellular carcinomas as a potential biomarker for predicting tumor recurrence. *J Magn Reson Imaging*. 2019;49(3):719-730.

224. Shi Y, Cang L, Zhang X, Cai X, Wang X, Ji R, Wang M, Hong Y. The use of magnetic resonance elastography in differentiating autoimmune pancreatitis from pancreatic ductal adenocarcinoma: a preliminary study. *Eur J Radiol.* 2018;108:13-20.
225. Prezzi D, Neji R, Kelly-Morland C, Verma H, O'Brien T, Challacombe B, Fernando A, Chandra A, Sinkus R, Goh V. Characterization of small renal tumors with magnetic resonance elastography: a feasibility study. *Invest Radiol.* 2018;53(6):344-351.
226. Pepin KM, McGee KP, Arani A, Lake DS, Glaser KJ, Manduca A, Parney IF, Ehman RL, Huston J, 3rd. MR elastography analysis of glioma stiffness and IDH1-mutation Status. *AJNR Am J Neuroradiol.* 2018;39(1):31-36.
227. Patel BK, Samreen N, Zhou Y, Chen J, Brandt K, Ehman R, Pepin K. MR elastography of the breast: evolution of technique, case examples, and future directions. *Clin Breast Cancer.* 2021;21(1):e102-e111.
228. Sinkus R, Lorenzen J, Schrader D, Lorenzen M, Dargatz M, Holz D. High-resolution tensor MR elastography for breast tumour detection. *Phys Med Biol.* 2000;45(6):1649-1664.
229. Hawley JR, Kalra P, Mo X, Raterman B, Yee LD, Kolipaka A. Quantification of breast stiffness using MR elastography at 3 Tesla with a soft sternal driver: a reproducibility study. *J Magn Reson Imaging.* 2017;45(5):1379-1384.
230. Lawrence A, Muthupillai R, Rossman P, Smith J, Manduca A, Ehman R. Magnetic resonance elastography of the breast: preliminary experience. *Proc Int Soc Magn Reson.* 1998.
231. LeCun Y. Generalization and network design strategies. *Connectionism in perspective.* 1989;19:143-155.
232. Murphy MC, Manduca A, Trzasko JD, Glaser KJ, Huston J, 3rd, Ehman RL. Artificial neural networks for stiffness estimation in magnetic resonance elastography. *Magn Reson Med.* 2018;80(1):351-360.

233. Scott JM, Arani A, Manduca A, McGee KP, Trzasko JD, Huston J, Ehman RL, Murphy MC. Artificial neural networks for magnetic resonance elastography stiffness estimation in inhomogeneous materials. *Med Image Anal.* 2020;63:101710.
234. LeVeque RJ. *Finite volume methods for hyperbolic problems*. Cambridge: Cambridge University Press; 2002.
235. LeVeque RJ. Wave propagation algorithms for multidimensional hyperbolic systems. *Journal of Computational Physics.* 1997;131(2):327-353.
236. Ketcheson D, Mandli K, Ahmadi A, Alghamdi A, Luna MQD, Parsani M, Knepley M, Emmett M. PyClaw: accessible, extensible, scalable tools for wave propagation problems. *SIAM J Sci Comput.* 2012;34.
237. Cai C, Zeng Y, Wang C, Cai S, Zhang J, Chen Z, Ding X, Zhong J. High efficient reconstruction of single-shot T2 mapping from overlapping-echo detachment planar imaging based on deep residual network. *arXiv preprint arXiv:170805170.* 2017.
238. Zhou B, Zhao H, Puig X, Fidler S, Barriuso A, Torralba A. Scene parsing through ADE20k dataset. Paper presented at: IEEE conference on computer vision and pattern recognition 2017.
239. Yin M, Venkatesh S, Mariappan Y, Glaser K, Grimm R, Manduca A, Romano A, Ehman R. Value of shear wave attenuation as a tissue characterization parameter in MR elastography of the liver. 2008.
240. Keras [computer program]. GitHub repository: GitHub; 2015.
241. Lin C, Bernstein MA. 3D magnetization prepared elliptical centric fast gradient echo imaging. *Magn Reson Med.* 2008;59(2):434-439.
242. Solamen LM, McGarry MD, Tan L, Weaver JB, Paulsen KD. Phantom evaluations of nonlinear inversion MR elastography. *Phys Med Biol.* 2018;63(14):145021-145021.

243. Yi M, Xia L, Zhou Y, Wu X, Zhuang W, Chen Y, Zhao R, Wan Q, Du L, Zhou Y. Prognostic value of tumor necrosis in gastrointestinal stromal tumor: a meta-analysis. *Medicine*. 2019;98(17).
244. Ling Y-h, Chen J-w, Wen S-h, Huang C-y, Li P, Lu L-h, Mei J, Li S-h, Wei W, Cai M-y, Guo R-p. Tumor necrosis as a poor prognostic predictor on postoperative survival of patients with solitary small hepatocellular carcinoma. *BMC Cancer*. 2020;20(1):607.
245. Robson MD, Anderson AW, Gore JC. Diffusion-weighted multiple shot echo planar imaging of humans without navigation. *Magn Reson Med*. 1997;38(1):82-88.
246. Chollet F. Xception: deep learning with depthwise separable convolutions. Paper presented at: Proceedings of the IEEE conference on computer vision and pattern recognition. 2017.
247. Weis JA, Miga MI, Arlinghaus LR, Li X, Chakravarthy AB, Abramson V, Farley J, Yankeelov TE. A mechanically coupled reaction-diffusion model for predicting the response of breast tumors to neoadjuvant chemotherapy. *Phys Med Biol*. 2013;58(17):5851-5866.

Vita

Benjamin C. Musall was born in Augusta, Georgia to his parents, John and Jacqueline Musall, and was later joined by his sister, Hannah. He began his secondary education in August of 2011 at the Georgia Institute of Technology in Atlanta, Georgia, where he earned a Bachelor of Science in nuclear and radiological engineering with summa cum laude. He moved to Houston, Texas in August of 2015 to pursue his Specialized Master of Science degree in Medical Physics and was mentored by Steven H. Lin and Jingfei Ma. In the summer of 2017, he defended his thesis, “Quantitative DWI as an Early Imaging Biomarker of the Response to Chemoradiation in Esophageal Cancer”, and then continued his study under Jingfei Ma in pursuit of his Doctorate of Philosophy in medical physics. After completing his Ph.D., and beginning in July of 2021, he will take on a 3-year residency at UTHealth McGovern Medical School in Houston, TX to be trained as a medical physicist in both Diagnostic Imaging and Nuclear Medicine.